

# **Novel Cathode and Anode Materials for Rechargeable Lithium-ion Batteries**

**A thesis presented for the Doctor of Philosophy at the University of  
Sheffield**



**Nik Reeves, BSc (University of Aberdeen)**

**2003**

## **Declaration**

This thesis has been composed by myself and has not been submitted or accepted in any previous degree application. The work has been conducted by myself, except where due acknowledgement has been given.

Part of this work has been published as a paper in a scientific journal:

Reeves, N.; Kirk, C. A.; West, A. R. *Journal of Materials Chemistry* 2001, 11, 249.

Nik Reeves

September 2003.

## **Acknowledgements**

I would like to thank my supervisor, Professor Tony West, for his guidance, continuing patience, and financial support.

I also thank EPSRC for their financial backing.

I would like to thank my fiancée Lorraine for her unending support; this work is dedicated to her.

Thanks to Edd Abram for taking part in countless general discussions and for his patience in explaining ac Impedance – again. Also, thanks to Denis Pasero for his support, assistance with the battery work and input over the past two years.

Thanks to Gabrielle Miles for the help during my honours project that got me started on this road, and for convincing Lorraine to go out with me in the first place.

Finally, thanks to the Electroceramics group here in Sheffield for many memorable times and for their support. It would have been easier on me if they'd all known how to use computers properly themselves, but I guess you have to make some trades...

## Summary

A number of compositions from the  $\text{Li}_2\text{O}-\text{CoO}_x-\text{MnO}_y$  ternary phase diagram have been studied. Samples have been studied by *X-ray powder diffraction*. Property characterisation has been conducted using a variety of techniques (Chapter 2): *thermal analysis* has been carried out using thermogravimetry (TG), differential thermal analysis (DTA) and differential scanning calorimetry (DSC), *electrical measurements* have been made using ac impedance, *battery testing* has been carried out using galvanostatic cycling with potential limitation (GCPL).

The pseudo-binary join between cobalt oxide and manganese oxide has been studied (Chapter 3); the phase diagram has been established from room temperature to  $\sim 1400$  °C. It was found that single phase samples with the spinel structure (with either cubic ( $0.00 \leq x \leq 1.30$ ) or tetragonal (for  $1.30 < x \leq 3.00$ ) symmetry could be isolated. These phases were studied using GCPL (Chapter 4) for possible application as anodes in Li-ion batteries, and were found to be able to reversibly accept Li by a reduction/re-oxidation process. On first discharge, the spinel was fully reduced to a discrete mixture of Co and Mn metal particles; these could be re-oxidised to CoO and MnO on subsequent charging. The best performance found was for  $\text{Co}_{0.4}\text{Mn}_{2.6}\text{O}_4$ , which showed good capacity retention, better specific capacity than the graphite anode materials currently used, and the lowest potential vs. Li metal, while also replacing most of the expensive and toxic Co with Mn.

The ternary  $\text{Li}_2\text{O}-\text{CoO}_x-\text{MnO}_y$  phase diagram has also been studied (Chapter 5), with particular attention paid to three solid solutions:

- (i) The reported cubic spinel solid solution between  $\text{LiMn}_2\text{O}_4$  and  $\text{LiCoMnO}_4$ .  
(i.e.  $\text{LiCo}_x\text{Mn}_{2-x}\text{O}_4$ ).
- (ii) A previously unreported join between  $\text{LiCoMnO}_4$  and  $\text{Co}_3\text{O}_4$ .  
(i.e.  $\text{Li}_{1-x}\text{Co}_{1+2x}\text{Mn}_{1-x}\text{O}_4$ ).
- (iii) A previously unreported join between  $\text{Li}_2\text{CoMn}_3\text{O}_8$  and  $\text{Co}_{1.7}\text{Mn}_{1.3}\text{O}_4$ .  
(i.e.  $\text{Li}_{1-x}\text{Co}_{1/2+6x/5}\text{Mn}_{1.5-x/5}\text{O}_4$ ).

It is most likely that these joins are, in fact, three sections through a solid solution area. It was noted that upon heating these cubic spinels, oxygen volatilization occurred. For a limited range of cubic spinel compositions, the equivalent of  $\sim 1$  oxygen atom could be lost from the structure, resulting in the formation of a high temperature rock salt solid solution area.

Battery testing (Chapter 6) was conducted on phases from two of these cubic spinel solid solutions ( $\text{Li}_{1-x}\text{Co}_{1+2x}\text{Mn}_{1-x}\text{O}_4$  and  $\text{Li}_{1-x}\text{Co}_{1/2+6x/5}\text{Mn}_{3/2-x/5}\text{O}_4$ ).  $\text{LiCoMnO}_4$  has the greatest potential applicability as a cathode material for the next generation of Li-ion batteries. Two plateaux are observed in the electrochemical data; a short plateau at 4.0 V (possibly due to a  $\text{Mn}^{3+} \rightleftharpoons \text{Mn}^{4+}$  redox couple brought about by a small degree of oxygen non-stoichiometry) and at  $\sim 5.0$  V (most likely due to the  $\text{Co}^{3+} \rightleftharpoons \text{Co}^{4+}$  redox couple). It has also been found that phases with compositions on the  $\text{Li}_{1-x}\text{Co}_{1+2x}\text{Mn}_{1-x}\text{O}_4$  and  $\text{Li}_{1-x}\text{Co}_{1/2+6x/5}\text{Mn}_{3/2-x/5}\text{O}_4$  solid solutions performed well as anode materials. The best anode performance was observed for  $x = 0.51$  on the  $\text{Li}_{1-x}\text{Co}_{1+2x}\text{Mn}_{1-x}\text{O}_4$  solid solution, where specific capacities of  $\sim 750 \text{ mAh g}^{-1}$  were obtained. This is acceptable for use as an anode material.

The low temperature phase diagram of  $\text{LiMn}_2\text{O}_4$  was investigated by DSC (Chapter 7); two low temperature phase transitions were observed. An ' $\alpha \rightarrow \beta$ ' transition, at  $\sim 23$  °C on heating, has been widely reported, though the symmetry changes involved are not yet satisfactorily understood. A second transition (' $\beta \rightarrow \gamma$ ') occurred at  $\sim -140$  °C on cooling, and  $\sim 15$  °C on heating. This second transition could be stabilised over the  $\text{Li}_{1+x}\text{Mn}_{2-x}\text{O}_4$  solid solution for compositions with  $0.04 \leq x \leq 0.12$  by introducing oxygen vacancies such that the average Mn valence fell to  $\leq 3.5+$ . This second transition has not been clearly identified in the literature, and has not been studied by DSC previously.

## Table of contents

<b>Chapter 1 – Introduction and Literature Review.....</b>	<b>1</b>
1.1 Background Theory	1
1.1.1 Crystal Field Theory	1
1.1.2 Jahn-Teller Effect	4
1.1.3 Intercalation Chemistry	5
1.1.3a What is intercalation?	5
1.1.3b Existing Nickel-based battery systems	6
1.1.3c Lithium rocking chair batteries	7
1.1.4 Why lithium?	9
1.2 Cathode materials	10
1.2.1 Layered compounds	11
1.2.1a LiCoO <sub>2</sub>	11
1.2.1b LiNiO <sub>2</sub>	12
1.2.1c LiMnO <sub>2</sub>	13
1.2.1d LiFeO <sub>2</sub>	15
1.2.2 Spinel	17
1.2.2a LiMn <sub>2</sub> O <sub>4</sub>	19
1.2.2b Five-volt materials	23
1.2.3 Olivines	27
1.2.4 PLiON	29
1.2.5 Theoretical capacities for cathode materials	30
1.3 Anode materials	31
1.3.1 Graphite	32
1.3.2 Tin-based amorphous oxides	33
1.3.3 Transition metal oxides	34
1.3.4 Lithium-containing metal oxides	36
1.3.5 Intermetallic alloys	36
1.4 References	39
<b>Chapter 2 – Experimental Techniques.....</b>	<b>47</b>
2.1 Sample Preparation	47
2.2 X-ray Powder Diffraction	50
2.2.1 Background Theory	50
2.2.2 Instrumentation	51
2.2.3 Fluorescence problems	52
2.2.4 Scanning conditions used	52
2.3 Thermogravimetry (TG), Differential Thermal Analysis (DTA) and Differential Scanning Calorimetry (DSC)	53
2.3.1 Thermogravimetry (TG)	53
2.3.2 Differential Thermal Analysis (DTA)	53
2.3.3 Differential Scanning Calorimetry (DSC)	54
2.4 ac Impedance Spectroscopy	55
2.4.1 Sample preparation for ac Impedance	59
2.5 Electrochemical measurements	60
2.5.1 Battery construction	60
2.5.1a Electrode film preparation	60
2.5.1b Electrolyte preparation	61
2.5.1c Coin cell construction	61
2.5.2 Battery Testing	64

	2.5.2a Cyclic voltammetry	64
	2.5.2b Galvanostatic Cycling with Potential Limitation (GCPL)	66
2.6	References	69

**Chapter 3 - 'Co<sub>3-x</sub>Mn<sub>x</sub>O<sub>4</sub>' – phase relations in the Co<sub>3</sub>O<sub>4</sub> – Mn<sub>3</sub>O<sub>4</sub> system.....70**

3.1	Literature review	70
3.2	Experimental	73
3.3	Results	74
	3.3.1 X-ray diffraction	74
	3.3.2 High temperature structures in Co <sub>3-x</sub> Mn <sub>x</sub> O <sub>4</sub>	77
	3.3.3 TG data	83
	3.3.4 DTA data	85
3.4	Discussion	87
	3.4.1 Phase diagram construction	87
	3.4.2 Deviations from Vegard's Law in Co <sub>3-x</sub> Mn <sub>x</sub> O <sub>4</sub> spinels ( $x \leq 1.30$ )	89
	3.4.3 Substitution mechanisms in Co <sub>3-x</sub> Mn <sub>x</sub> O <sub>4</sub> spinels	89
	3.4.4 Oxygen non-stoichiometry in Co <sub>3-x</sub> Mn <sub>x</sub> O <sub>4</sub> spinels	90
3.5	Conclusion	92
3.6	References	93

	Appendix to Chapter 3 – TG-DTA data for Co <sub>3-x</sub> Mn <sub>x</sub> O <sub>4</sub>	94
--	--	----

**Chapter 4 - Electrochemical properties of 'Co<sub>3-x</sub>Mn<sub>x</sub>O<sub>4</sub>' spinels.....102**

4.1	Literature review	102
4.2	Experimental	105
4.3	Galvanostatic Cycling with Potential Limitation	106
	4.3.1 Charge / Discharge profiles for Co <sub>3</sub> O <sub>4</sub>	106
	4.3.2 Discharge / Charge Profiles for Co <sub>3-x</sub> Mn <sub>x</sub> O <sub>4</sub> ( $0.30 \leq x \leq 3.00$ )	110
	4.3.3 Differential potentiometry	120
	4.3.4 Discussion of GCPL results	125
4.4	Conclusions	129
4.4	References	130

**Chapter 5 - Cubic spinel and rock salt materials in the Li<sub>2</sub>O-CoO<sub>x</sub>-MnO<sub>y</sub> phase diagram.....131**

5.1	Introduction	131
5.2	Experimental	134
5.3	'LiCo <sub>x</sub> Mn <sub>2-x</sub> O <sub>4</sub> ' – Phase relations in the LiMn <sub>2</sub> O <sub>4</sub> - LiCoMnO <sub>4</sub> system	135
	5.3.1 Solid solution studies	135
	5.3.2 Thermal behaviour studies	136
	5.3.2a Thermogravimetry results	136
	5.3.2b DTA results	140
	5.3.2c DSC results	141
5.3.3	Binary phase diagram for LiCo <sub>x</sub> Mn <sub>2-x</sub> O <sub>4</sub> join	141

5.3.4	Conclusions	145
5.4	' $\text{Li}_{1-x}\text{Co}_{1+2x}\text{Mn}_{1-x}\text{O}_4$ ' – phase relations in the $\text{LiCoMnO}_4 - \text{Co}_3\text{O}_4$ system	146
5.4.1	Solid solution studies	146
5.4.2	Thermal behaviour studies	148
5.4.2a	Thermogravimetry results	148
5.4.2b	DTA results	152
5.4.3	Binary Phase Diagram for $\text{Li}_{1-x}\text{Co}_{1+2x}\text{Mn}_{1-x}\text{O}_4$ join	153
5.4.4	Conclusions	157
5.5	' $\text{Li}_{1-x}\text{Co}_{1/2+6x/5}\text{Mn}_{1.5-x/5}\text{O}_4$ ' – phase relations in the $\text{LiCo}_{0.5}\text{Mn}_{1.5}\text{O}_4 - \text{Co}_{1.7}\text{Mn}_{1.3}\text{O}_4$ system	158
5.5.1	Solid solution studies	158
5.5.2	Thermal behaviour studies	159
5.5.2a	Thermogravimetry results	159
5.5.2b	DTA results	162
5.5.3	Binary Phase Diagram for $\text{Li}_{1-x}\text{Co}_{1/2+6x/5}\text{Mn}_{1.5-x/5}\text{O}_4$ join	163
5.5.4	Conclusions	164
5.6	Cubic spinel and rock salt solid solution areas in the $\text{Li}_2\text{O}-\text{CoO}_x-\text{MnO}_y$ phase diagram	165
5.6.1	Ternary $\text{Li}_2\text{O}-\text{CoO}_x-\text{MnO}_y$ phase diagram at 550 °C	165
5.6.2	Effect of temperature on spinel solid solution area	166
5.6.3	Effect of temperature on rock salt solid solution area	170
5.6.4	Variation of lattice parameter across spinel solid solution area	173
5.7	References	176

**Chapter 6 – Electrical and Electrochemical Responses of  $\text{Li}_{1-x}\text{Co}_{1+2x}\text{Mn}_{1-x}\text{O}_4$  ( $0.00 \leq x \leq 1.00$ ) and  $\text{Li}_{1-x}\text{Co}_{1/2+6x/5}\text{Mn}_{1.5-x/5}\text{O}_4$  ( $0.00 \leq x \leq 1.00$ ) cubic spinels.....177**

6.1	Experimental	177
6.2	ac Impedance	178
6.2.1	$\text{Li}_{1-x}\text{Co}_{1+2x}\text{Mn}_{1-x}\text{O}_4$	178
6.2.2	$\text{Li}_{1-x}\text{Co}_{1/2+6x/5}\text{Mn}_{1.5-x/5}\text{O}_4$	180
6.3	Galvanostatic Cycling	182
6.3.1	Results for $\text{Li}_{1-x}\text{Co}_{1+2x}\text{Mn}_{1-x}\text{O}_4$	182
6.3.2	Discussion of results for $\text{Li}_{1-x}\text{Co}_{1+2x}\text{Mn}_{1-x}\text{O}_4$	189
6.3.3	Results for $\text{Li}_{1-x}\text{Co}_{1/2+6x/5}\text{Mn}_{3/2-x/5}\text{O}_4$	192
6.3.4	Discussion of results for $\text{Li}_{1-x}\text{Co}_{1/2+6x/5}\text{Mn}_{3/2-x/5}\text{O}_4$	199
6.4	Conclusions	200
6.5	References	201

**Chapter 7 – Low temperature polymorphism of  $\text{LiMn}_2\text{O}_4$ ....202**

7.1	Background	202
7.2	Experimental	204
7.3	Results and Discussion	205
7.3.1	Solid solution formation in $\text{Li}_{1+x}\text{Mn}_{2-x}\text{O}_4$ .	205
7.3.2	High temperature behaviour	205
7.3.3	Low temperature Differential Scanning Calorimetry (DSC)	209
7.3.3a	Untreated, stoichiometric $\text{LiMn}_2\text{O}_4$	209
7.3.3b	Untreated $\text{Li}_{1+x}\text{Mn}_{2-x}\text{O}_4$	213

7.3.3c	Heat-treated $\text{Li}_{1+x}\text{Mn}_{2-x}\text{O}_4$	214
7.4	Conclusion	217
7.5	References	218
<b>Chapter 8 – Conclusions and Further Work.....</b>		<b>219</b>
8.1	Conclusions	219
8.2	Further Work	221

# Chapter 1

## Introduction and Literature Survey

In 1800, Alessandro Volta made history by developing the first battery.<sup>1</sup> His design generated electrical current from the chemical reaction between two metals; Volta stacked disks of zinc and silver together, with a porous membrane soaked in sea water separating the two.

In 1991, Sony released the first commercial rechargeable Li-ion cell, incorporating a  $\text{LiCoO}_2$  intercalation cathode. Until this time, battery technology was still largely based on the initial discovery of Alessandro Volta in 1800, and the release of the Sony cell was arguably the start of the biggest revolution in battery technology since Volta.

### 1.1 Background Theory

The aim of this section is to pick out some of the important areas of theory for lithium-ion batteries. The relevance and importance of these areas will become clear in later sections.

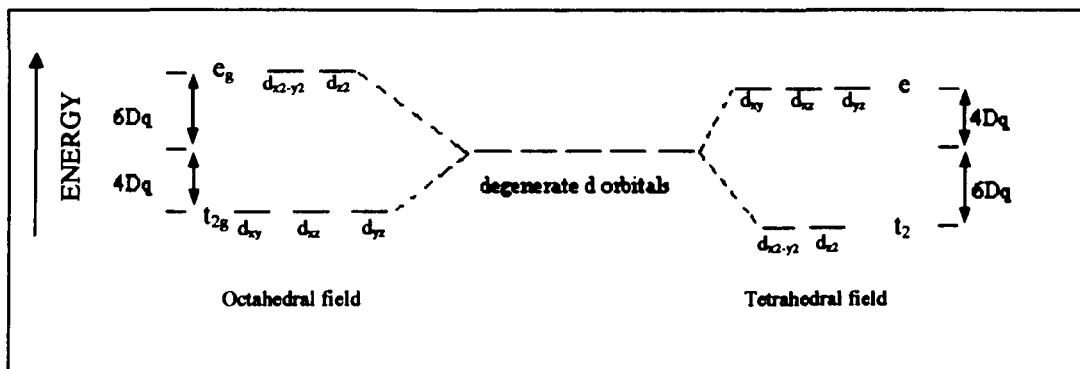
#### 1.1.1 Crystal Field Theory (CFT)

The  $d$  orbital electrons of transition metal cations play a vital role in the coordination environment of the metal atom and the properties of their compounds. Normally the  $d$  orbitals are degenerate, *i.e.* all five are of equal energy. However, when the metal atom is placed into either an octahedral or tetrahedral field, crystal field splitting occurs, as shown in Figure 1.1.

Electrons fill these orbitals according to Hund's rule, *i.e.* the low energy orbitals are filled singly first. For  $d^4$  to  $d^7$  cations there are two possible configurations: low and high spin. For low spin arrangements, all of the low energy orbitals (*e.g.* for octahedral field splitting, the  $t_{2g}$  orbitals) are doubly filled before filling of the high energy orbitals (*e.g.* for octahedral field splitting, the  $e_g$  orbitals) commences. For the high spin state,

filling of orbitals commences by first filling the low energy orbitals singly, then the high energy orbitals singly, then double filling of low energy orbitals.

**Figure 1.1 – Splitting of  $d$  orbital energy levels in octahedral or tetrahedral field.**

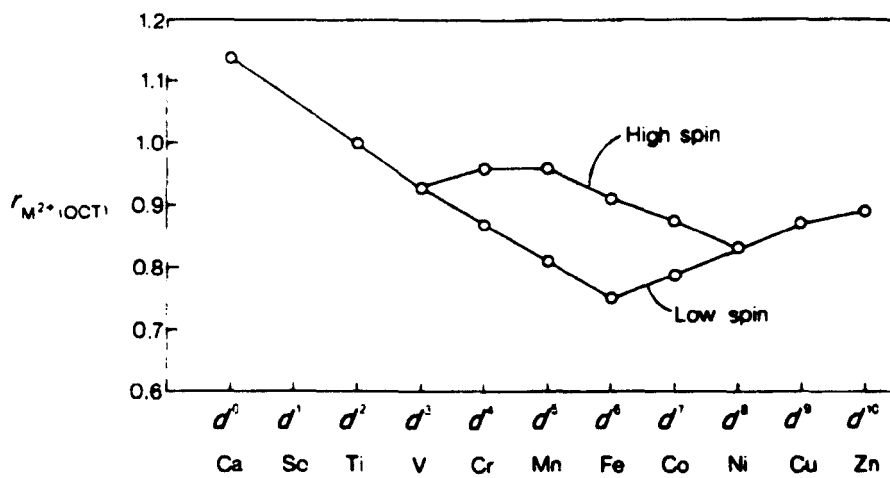


The cationic radii of transition metals depend upon their  $d$  electron configuration (see Figure 1.2). Assuming low spin configuration and an octahedral field where appropriate, ionic radii decrease as filling of the orbitals proceeds from  $d^0$  (e.g.  $\text{Ca}^{2+}$ ,  $\text{Sc}^{3+}$ ) to  $d^6$  (e.g.  $\text{Fe}^{2+}$ ,  $\text{Co}^{3+}$ ). This is explained by the poor shielding of the outer electrons from the nuclear charge, so the electron cloud is effectively pulled in. When filling from  $d^6$  to  $d^{10}$  (e.g.  $\text{Zn}^{2+}$ ) the ionic radii increase, as the electrons enter the  $e_g$  orbitals and begin to shield the nuclear charge more effectively.

This general pattern is not followed by the high spin state metal cations. For  $d^4$  and  $d^6$  cations, the  $e_g$  orbitals (assuming an octahedral field) get singly filled and hence offer some shielding from the nuclear charge; the ionic radii therefore increase. Filling of  $d^6$  to  $d^8$  orbitals again fills the  $t_{2g}$  levels, and so ionic radii decrease slightly, since extra positive and negative charges are added with little extra shielding and so the electron cloud gets pulled in tighter. Then for  $d^9$  and  $d^{10}$  orbital filling, again the ionic radii increase on the addition of electrons to the  $e_g$  levels.

Crystal field stabilization energies (CFSE) may be calculated from 'Dq' values. The energy difference,  $\Delta$ , between high and low energy orbitals is fixed at  $10 Dq$ ; the  $t_{2g}$  and  $e_g$  orbitals are stabilized/destabilized by  $4 Dq$  or  $6 Dq$ , depending on the splitting (see Figure 1.1 for clarification). CFSE can clarify whether a transition metal cation will occupy high or low spin state and play roles in choice of site occupation and lattice enthalpies. Ions of  $d^0$ ,  $d^5$  and  $d^{10}$  configurations do not exhibit CFSE.

**Figure 1.2 – Ionic radii for divalent transition metal cations.<sup>2,3</sup>**



### 1.1.2 Jahn-Teller Effect

In the case of  $d^9$ ,  $d^7$  (LS) and  $d^4$  (HS) transition metal ions, filling of the  $d$  orbitals leaves the higher energy  $e_g$  orbitals unevenly occupied, e.g. in the case of a  $d^9$  ion, we have two electrons in one  $e_g$  orbital, and one in the other; for  $d^7$  (LS) and  $d^4$  (HS) ions we have only one electron in one  $e_g$  orbital. The  $e_g$  orbitals are no longer degenerate.

Since  $d$  orbitals are not spherical, this uneven filling of the higher energy levels results in uneven repulsion of negatively charged ligands around the metal cation. For example, for high spin  $Mn^{3+}$  the three  $t_{2g}$  orbitals are singly filled, and then one of the  $e_g$  orbitals (the  $d_{z^2}$ ) will be singly filled. This means that a ligand approaching the metal atom along the  $z$ -axis will experience greater repulsion than one approaching along the  $x$ - and  $y$ -axes. The net result is lengthening of the metal-ligand bond along the  $z$ -axis, and a distortion in the local crystal structure.

## 1.1.3 Intercalation Chemistry

### 1.1.3a What is intercalation?

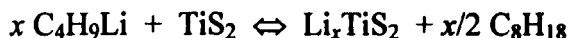
Intercalation<sup>2</sup> is the addition of an ion or molecule into a host structure, without altering the basic structure of the host, *i.e.* a topotactic reaction. The classic example<sup>4-6</sup> is the reversible electrochemical insertion of an alkali metal cation into the layered TiS<sub>2</sub> structure:



There are two processes that allow for this reaction to occur.

#### (i) Chemical

A lithiating agent is used, *e.g.* *n*-butyl lithium (C<sub>4</sub>H<sub>9</sub>Li) dissolved in hexane:



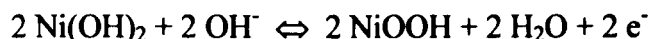
#### (ii) Electrochemical

An electrochemical cell is constructed with polycrystalline TiS<sub>2</sub> as the cathode, an electrolyte (*e.g.* an organic solvent mixed with lithium chlorate), and a Li metal anode. On shorting the circuit, lithium ions intercalate into the host TiS<sub>2</sub> structure, while the electrons pass through an external circuit. This was the approach of Exxon<sup>7</sup> in 1972, but dendrites formed as the Li anode was repeatedly replated, which ultimately led to a risk of short-circuit and explosion.

In either case, the layered character of the TiS<sub>2</sub> host structure is unchanged by the process. Since Li<sub>1-x</sub>TiS<sub>2</sub> is a solid solution with the same structure present for the entire range of reaction, there are no intermediate phases to nucleate.<sup>6</sup> The reaction is fully reversible and close to 100 % efficient. The voltage from the cell vs. Li is too low to be of significant use, though reported energy densities for this system of ~ 480 Wh/kg are still among the highest known.

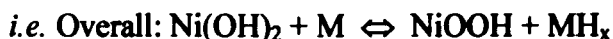
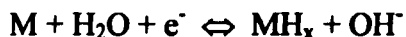
### 1.1.3b Existing Nickel-based battery systems

Other examples of intercalation compounds include the cathode materials used in Nickel-Cadmium ('Ni-Cd') and Nickel-Metal Hydride (NiMH) cells. Both utilise the (de)intercalation of hydrogen ions into (and out of) the electrode materials, as indicated by the following redox reactions for a Ni-Cd cell:



Dendritic growth of 'cadmium needles' occurs on repeated dissolution/precipitation of cadmium, which eventually results in short-circuit and cell failure. There are also memory effect problems after partial charges/discharges. Production of Ni-Cd cells accounts for approximately two-thirds of the global use of cadmium; however, the European Commission has proposed a ban on all nickel-cadmium batteries by 2008, due to environmental and health concerns over the use of cadmium.<sup>8</sup> NiMH technology offers one alternative.

NiMH cells use a NiOOH cathode, an aqueous electrolyte and a metal hydride (MH) anode. Energy densities are reasonable, but capacity losses on storage are significant (up to 25 % of the capacity can be lost in the first month of storage) due to self-discharge reactions.<sup>9</sup> NiMH cells work via the following reaction – note that the chemistry of the Ni electrode is the same as for the NiCd cell:



In theory, these cells have less chance of overcharging than NiCd batteries. They also have the obvious benefit of not containing cadmium, while retaining similar properties.

### 1.1.3c Lithium rocking chair batteries

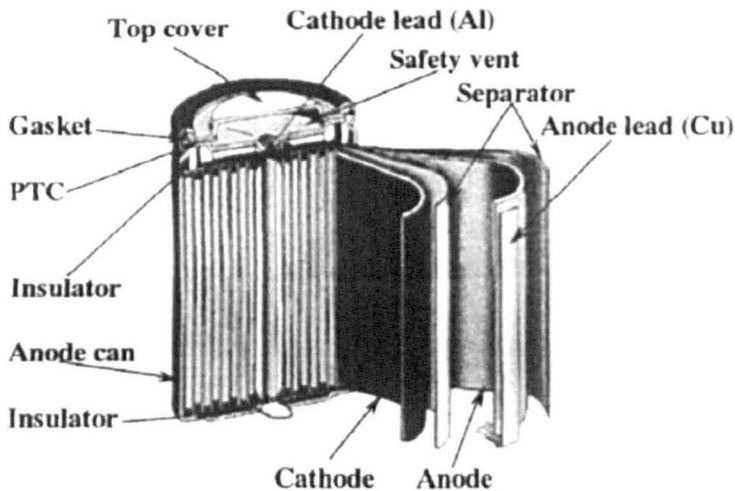
Rocking chair or shuttlecock batteries are so called because the mobile species, e.g.  $\text{Li}^+$  ions, in the cell rocks, or shuttles, to and fro from one side to the other, as indicated in Figure 1.3.

*Figure 1.3 – Schematic of a rocking chair battery using  $\text{LiCoO}_2$  and graphite as the active electrode materials.<sup>10</sup>*



This can be shown in the form of a real battery in Figure 1.4.

*Figure 1.4 – Diagram showing real battery construction.<sup>11</sup>*



The source of the voltage from these topotactic reactions at the cathode and anode is due to redox processes in the active material, e.g.:



The energy involved in the (de)intercalation of Li into/from the active material here is given by the Nernst Equation:

$$E = E_0 + \frac{RT}{nF} \cdot \log \frac{[\text{Oxidised}]}{[\text{Reduced}]}$$

Where: E = operating voltage, in volts.

$E_0$  = ideal voltage for the reaction, in volts.

R = gas constant, 8.3143 J mol<sup>-1</sup> K<sup>-1</sup>.

T = temperature, in Kelvin.

n = number of electrons involved in the reduction/oxidation process.

F = Faraday constant, 9.469 x 10<sup>4</sup> C mol<sup>-1</sup>.

As the deintercalation reaction begins, the concentration of oxidised species (*e.g.* Me<sup>4+</sup>) is very low, so the log term in the Nernst equation is negative; the operating voltage, E, is less than  $E_0$ . As the reaction proceeds, the concentration of reduced (*e.g.* Me<sup>3+</sup>) and oxidised species (*e.g.* Me<sup>4+</sup>) becomes equal, and the log term cancels to unity. A cyclic voltammogram will show a peak at a voltage slightly higher than  $E_0$ . On further deintercalation, the concentration of the oxidised species becomes dominant, and so the log term will become positive. The operating voltage increases further, until the concentration of the reduced species (*e.g.* Me<sup>3+</sup>) reaches zero.

The physical processes occurring can be broken into four steps:

- (i) Formation of a Li-ion:  $\text{Li} \rightarrow \text{Li}^+ + e^-$
- (ii) Transfer of electron to transition metal:  $\text{Me}^{\text{IV}} \text{O}_6^{8-} + e^- \longrightarrow \text{Me}^{\text{III}} \text{O}_6^{9-}$
- (iii) Transfer of lithium into octahedral hole in anion array:  $\square_{(\text{oh})} + \text{Li}^+ \rightarrow \text{Li}^+_{(\text{oh})}$
- (iv) Distribution of charge carriers (*i.e.* Li<sup>+</sup>, e<sup>-</sup>) through matrix and into 'circuit'.

## 1.2 Cathode materials

As discussed in section 1.1.4, there has been massive industrial interest in the development of new materials for use as cathodes in rechargeable lithium-ion batteries. However, further development is required if new applications, such as zero emission vehicles (ZEVs), are to be realised. Existing applications also demand ever improving properties from batteries, and the demands made for the next generation of batteries can be summarised:<sup>10</sup>

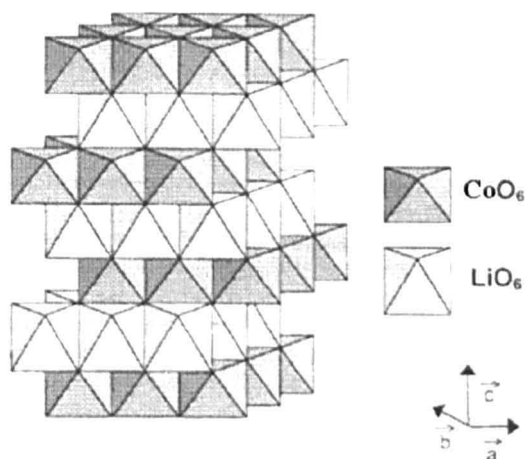
- must act as an intercalation host for lithium.
- be capable of sustaining high lithium (de)intercalation.
- lithium intercalation must be highly reversible.
- low Fermi level to allow for high operating voltage.
- flat (dis)charge plateau – *i.e.* cell potential constant with state of charge.
- high capacity.
- low formula weight (high gravimetric energy density).
- low molar volume (high volumetric energy density).
- minimal volume changes during intercalation.
- avoid reactions with the electrolyte.
- good electrical conductivity (less additives needed).
- easily fabricated into composite electrodes.
- low cost.
- low toxicity.
- environmentally friendly.

## 1.2.1 Layered Compounds

### 1.2.1a LiCoO<sub>2</sub>

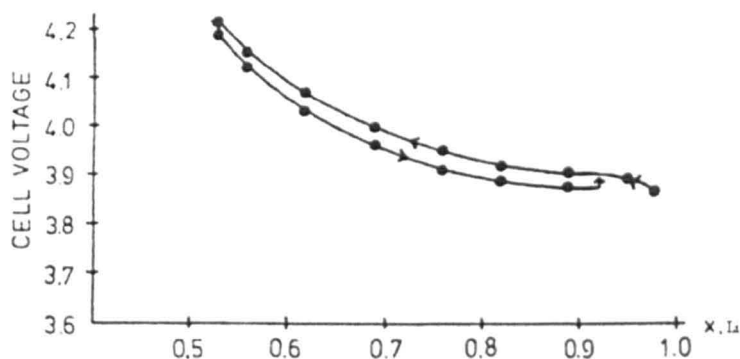
Goodenough *et al.*<sup>13,14</sup> first outlined the high energy density of LiCoO<sub>2</sub> in 1980. LiCoO<sub>2</sub> has the NaFeO<sub>2</sub> structure (R-3m space group), which can be described (Figure 1.6) as a layered rock salt structure with Li<sup>+</sup> and Co<sup>3+</sup> in alternating (111) layers of octahedral sites.

**Figure 1.6** –  $\alpha$ -NaFeO<sub>2</sub> type structure of LiCoO<sub>2</sub>.



This was the cathode used in the first commercial Li-ion battery, released by Sony Corporation in June 1991.<sup>9,15</sup> The potential of LiCoO<sub>2</sub>, resulting from the Co<sup>3+/4+</sup> redox couple, exceeds 3.6 V (more than three times that of alkaline batteries). The practical gravimetric energy density is  $\sim 140 \text{ W h kg}^{-1}$  (NiCd batteries have energy densities at best  $\frac{1}{2}$  of this). Figure 1.7 shows an example voltammogram for a cell using LiCoO<sub>2</sub> as the active cathode material.

**Figure 1.7** – Voltage vs. composition,  $x$ , for Li <sub>$x$</sub> CoO<sub>2</sub>.<sup>16</sup>



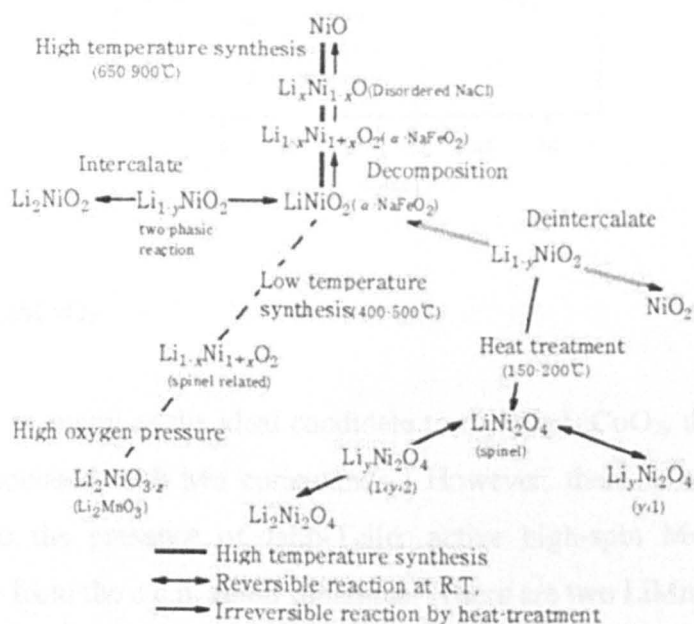
However, there are concerns over the toxicity and expense of cobalt – it has been suggested that already the lithium battery market has used 10 % of the Earth’s supply of cobalt,<sup>17</sup> and indeed some initial attempts are being made to recycle old battery cathodes.<sup>18</sup> Furthermore,  $\text{Co}^{4+}$  is unstable and attacks the electrolyte, with resulting safety concerns, so delithiation is restricted to  $\sim 0.5$  Li (hence the theoretical capacity of  $\sim 269 \text{ mAh.g}^{-1}$  is not reached). There is, therefore, great demand for alternative materials with improved properties that avoid the use of expensive or toxic materials.

Other properties (*e.g.* any order-disorder phenomena at high temperature, or thermal behaviour in general) of  $\text{LiCoO}_2$  appeared to have been either poorly studied or, more likely, often unreported. Wang *et al.*<sup>19</sup> studied the thermogravimetric response of  $\text{LiCoO}_2$ , showing small amounts of  $\text{Li}_2\text{O}$  loss ( $< 1 \text{ wt } \%$ ) on heating to  $1000 \text{ }^\circ\text{C}$ .

### 1.2.1b $\text{LiNiO}_2$

$\text{LiNiO}_2$  is isostructural with  $\text{LiCoO}_2$ , *i.e.* it has the same layered structure in the R-3m space group. However,  $\text{LiNiO}_2$  is difficult to prepare as the stoichiometric phase. Kanno<sup>20</sup> proposes the cause of this to be lithia volatilization at the calcination temperature, resulting in a true stoichiometry of  $\text{Li}_{1-x}\text{Ni}_{1+x}\text{O}_2$ . Obtained values of  $x$  can vary greatly; the interrelation of phases that can be obtained for lithium nickelates is described in Figure 1.8.

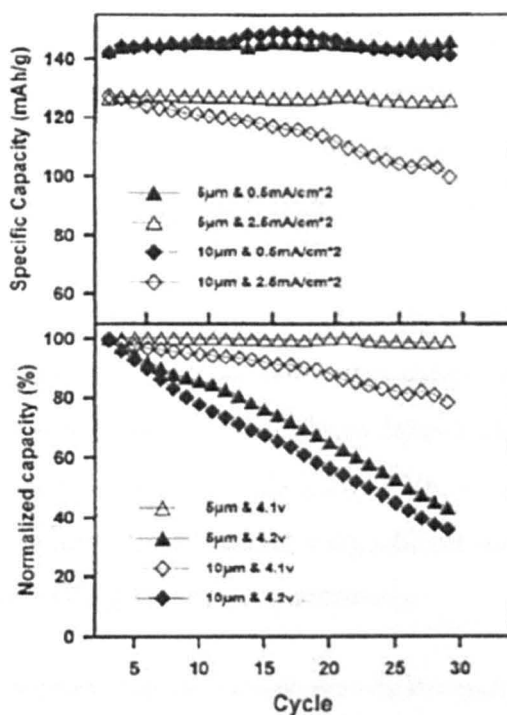
**Figure 1.8** – Phase relationships in  $\text{LiNiO}_2$ .<sup>20</sup>



Phases with the stoichiometry  $\text{Li}_{1-x}\text{Ni}_{1+x}\text{O}_2$  are shown to have partially disordered cation distribution on the Li site, *i.e.* Ni ions migrate into the lithium layers. The reverse is generally not true, with Ni layers remaining Li-free except when relatively large values of  $x$  are obtained.

Sheu *et al.*<sup>21</sup> studied the effect of particle size, charge rate and charge-end voltage for  $\text{LiNiO}_2$  (Figure 1.9). All three parameters were shown to influence battery performance, with the highest specific capacity ( $\sim 140 \text{ mAh.g}^{-1}$ ) and capacity retention obtained for cells cycled at a current density of  $0.4 \text{ mA.cm}^{-2}$  and charge-end voltage 4.1 V, with the active material of average particle size  $\sim 5 \mu\text{m}$ . This maximum capacity is approximately half of the theoretical maximum of  $269 \text{ mAh.g}^{-1}$ .

**Figure 1.9** – Effect of particle size and cycle rate (upper) and charge-end voltage effect (cycled at  $2.5 \text{ mA cm}^{-2}$ ) on battery performance of  $\text{LiNiO}_2$ .<sup>21</sup>



### 1.2.1c $\text{LiMnO}_2$

$\text{LiMnO}_2$  is seen by many as the ideal candidate to replace  $\text{LiCoO}_2$ , due to the low cost and toxicity associated with Mn compounds. However, there is no direct structural analogue due to the presence of Jahn-Teller active high-spin  $\text{Mn}^{3+}$ , which causes distortions away from the c.c.p. anion sublattice. There are two  $\text{LiMnO}_2$  polymorphs.<sup>22</sup>

Synthesis by high temperature solid state reaction routes yields o-LiMnO<sub>2</sub>, belonging to the orthorhombic Pmm space group. This is an ordered rocksalt, with LiO<sub>6</sub> and MnO<sub>6</sub> octahedra arranged in corrugated layers.

The m-LiMnO<sub>2</sub> has a monoclinic structure, belonging to the C2/m space group, and can only be prepared by ion exchange and hydrothermal reactions. This phase is generally considered unstable relative to the orthorhombic phase. It may be viewed as having a distorted NaFeO<sub>2</sub> (*i.e.* LiCoO<sub>2</sub>) structure. Lithium occupies octahedral sites between MnO<sub>6</sub> sheets. Doping with various cations<sup>23</sup> (*e.g.* Al, Cr, Co, V, Ti, Mg) in place of Mn<sup>3+</sup> can stabilise this polymorph by reducing the distorting effect of the Jahn-Teller active cation, and allow preparation by high temperature methods.

The electrochemistry of layered LiMnO<sub>2</sub> has been studied by Bruce *et al.*,<sup>10</sup> and an example cyclic voltammogram is presented in Figure 1.10. On first cycle, peaks can be observed at ~ 3.5 and 4.0 V; however, on subsequent charges the 4.0 V peak has diminished in size and the 3.5 V peak has been replaced by a peak at ~ 3.25 V. The specific capacity drops from 230 mAh.g<sup>-1</sup> on the first cycle to 130 mAh.g<sup>-1</sup> thereafter; these values are well short of the theoretical maximum of 280 mAh.g<sup>-1</sup> for LiMnO<sub>2</sub>.

On deintercalation of 0.5 Li, displacement of Mn ions into the lithium layers occurs, forming localised regions with the composition and structure of spinel, *i.e.* LiMn<sub>2</sub>O<sub>4</sub>; this is responsible for the 4 V peak. Problems with Jahn-Teller active Mn<sup>3+</sup> cations are also detrimental to capacity retention. Doping with ~ 10 % Co eliminates the cooperative Jahn-Teller distortion, and causes a significant improvement in the specific capacity to ~ 200 mAh.g<sup>-1</sup> with good capacity retention.

**Figure 1.10** – Cyclic voltammogram of layered LiMnO<sub>2</sub> showing five cycles at 10 μV s<sup>-1</sup> within range 2.0 to 4.6 V vs. Li.<sup>10</sup>

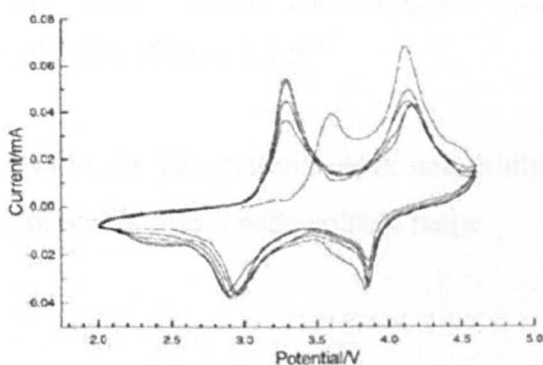
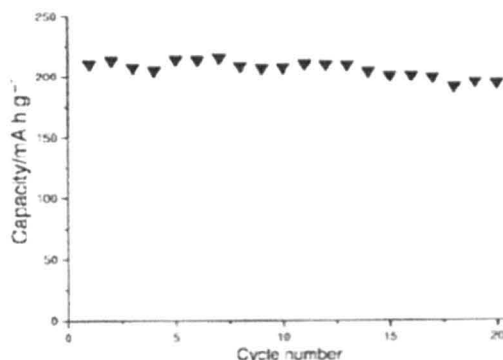


**Figure 1.11** – Specific discharge capacity as a function of cycle number for layered  $\text{Li}(\text{Mn}_{0.9}\text{Co}_{0.1})\text{O}_2$  at  $100 \text{ mA cm}^{-2}$  and  $2.6 - 4.8 \text{ V}$ .<sup>10</sup>



### 1.2.1d $\text{LiFeO}_2$

$\text{LiFeO}_2$  is an ideal, low cost, candidate to replace  $\text{LiCoO}_2$ . However, there are three polymorphs of  $\text{LiFeO}_2$ :  $\alpha$  (cubic, space group  $\text{Fm}\bar{3}\text{m}$ ),  $\beta$  (monoclinic, space group  $\text{C2/c}$ ) and  $\gamma$  (tetragonal, space group  $\text{I4}_1/\text{amd}$ ). The transition between the polymorphs proceeds via ordering of the  $\text{Li}^+$  and  $\text{Fe}^{3+}$  cations on the octahedral sites; the cubic phase is fully disordered and the tetragonal phase is fully ordered. These polymorphs, and more exotic structure types (e.g. hollandite and corrugated layer-structured types<sup>20</sup>) have been studied in numerous reports,<sup>24-31</sup> but electrochemical properties have fallen well short of the theoretical maximum: specific capacities of  $\sim 120 \text{ mAh.g}^{-1}$  (vs.  $277 \text{ mAh.g}^{-1}$  for full Li extraction in theory)<sup>26</sup> and poor capacity retention have been reported.

Poor capacity retention in  $\text{LiFeO}_2$  appears to be linked, as in  $\text{LiMnO}_2$ , to the formation of localised regions of spinel phase on Li deintercalation. The limitation in terms of capacity is poorly explained in much of the literature, but appears to be linked to the electrochemical inactivity of some of the polymorphs (the  $\alpha$  and  $\beta$  phases), and work has focussed on low temperature methods to prepare new structure types of  $\text{LiFeO}_2$ . Doping with Mn has also been reported, and brought a significant improvement in specific capacity and cyclability (Figure 1.12).<sup>32</sup>

However, the charge profile for this material does not exhibit a flat plateau (Figure 1.13); instead, charging proceeds over a wide voltage range.

**Figure 1.12** – Specific discharge capacity vs. cycle number for  $\text{LiMn}_x\text{Fe}_{1-x}\text{O}_2$ , (a)  $x = 0.1$ , (b)  $x = 0.3$  and (c)  $x = 0.5$ . Current density  $0.4 \text{ mA cm}^{-2}$ , cycling range  $1.5 - 4.5 \text{ V}$  at  $25 \text{ }^\circ\text{C}$ .<sup>32</sup>

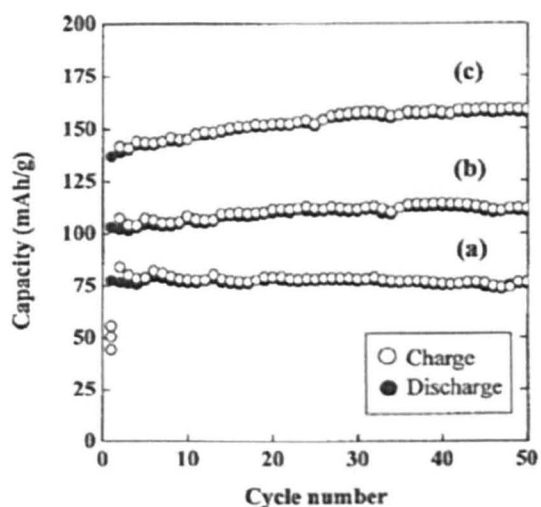
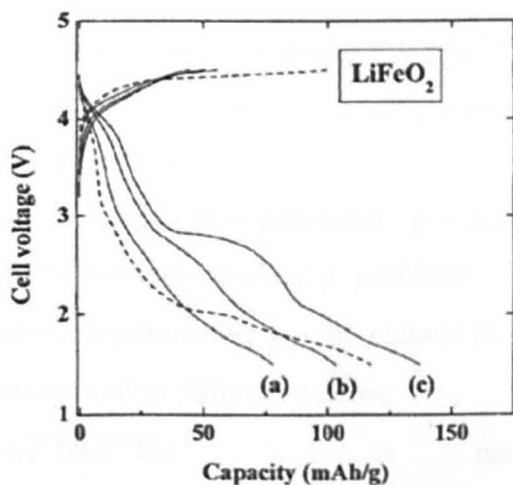


**Figure 1.13** – Initial charge/discharge curves for  $\text{LiMn}_x\text{Fe}_{1-x}\text{O}_2$ , (a)  $x = 0.1$ , (b)  $x = 0.3$  and (c)  $x = 0.5$ . Current density  $0.4 \text{ mA cm}^{-2}$ , cycling range  $1.5 - 4.5 \text{ V}$  at  $25 \text{ }^\circ\text{C}$ .<sup>32</sup>



## 1.2.2 Spinel

The spinel crystal structure was determined independently by Bragg<sup>33</sup> and Nishikawa<sup>34</sup> in 1915. Spinel compounds exhibit many interesting properties, amongst which the ability of some lithium-containing materials to (de)intercalate lithium ions is of interest here.

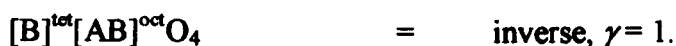
Most spinel compounds have the space group Fd3m. The primitive tetragonal unit cell, containing two molecular AB<sub>2</sub>X<sub>4</sub> units, is shown in Figure 1.14.<sup>35</sup> Four of these units combine to form the cubic spinel unit cell, *i.e.* there are Z = 8 formula units per unit cell. Another projection of the unit cell is given in Figure 1.15.

Each face-centred cubic (f.c.c.) unit cell contains 32 anions and 24 cations. The anion sublattice is cubic-close packed, with 96 interstices. There are 64 tetrahedral sites, which are filled by 8 cations (*i.e.* 1/8<sup>th</sup> filled), and 32 octahedral sites, filled by 16 cations (*i.e.* half full). The filled tetrahedral and octahedral sites are labelled 8a and 16d respectively.

Many different cations can be introduced into the spinel structure, with different charge combinations possible (Table 1.1).<sup>2</sup>

Spinel also have a number of structural degrees of freedom<sup>2,35,36</sup>:

- (i) lattice parameter,  $\underline{a}$  - spinel lattice parameters are quite large, as indicated in Table 1.1.
- (ii) generalised anion position parameter,  $\underline{u}$  - anions in spinel are usually dilated away from their ideal c.c.p. positions.
- (iii) cation inversion parameter,  $\gamma$  - the cations in spinel may be ordered in different ways and to different extents:



$\gamma$  is determined by several factors, including cation size, covalent bonding effects and crystal field stabilization energies.

Figure 1.14 – The cubic unit cell of spinel, with atom positions indicated for two octants.<sup>35</sup>

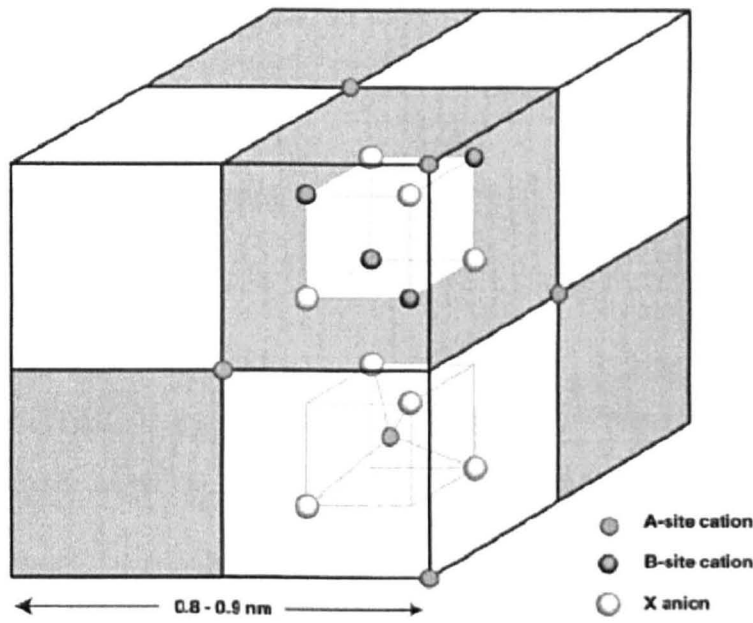
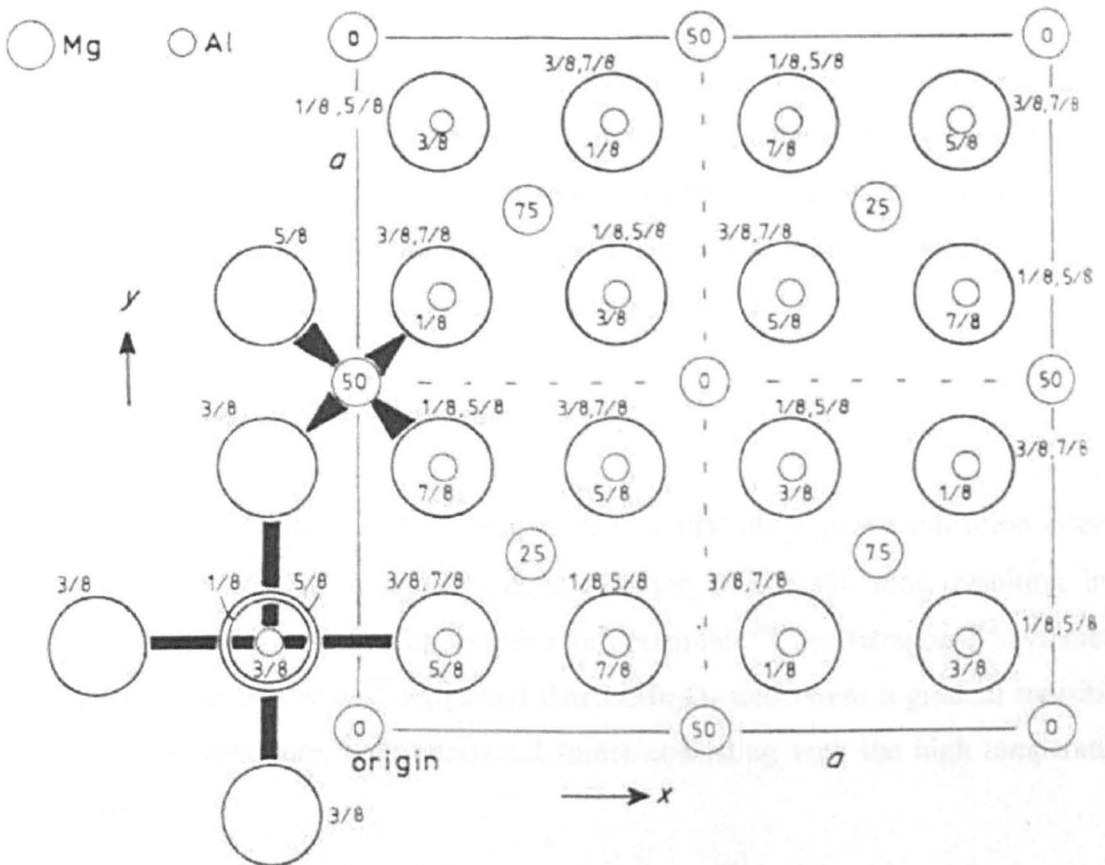


Figure 1.15 – The spinel structure: atom heights given as fractions/percentages of  $c$ .<sup>2</sup>



The anion parameter,  $u$ , is largely dependent on  $\gamma$ . The lattice parameter is dependent on the effective cationic radii, with no significant dependence on cation arrangement.

*Table 1.1 – Some oxide compounds with the spinel structure.<sup>2</sup>*

Crystal	Charge combination	$a / \text{Å}$	Structure
MgAl <sub>2</sub> O <sub>4</sub>	2,3	8.080	Normal
CoGe <sub>2</sub> O <sub>4</sub>	2,4	8.318	Normal
MgFe <sub>2</sub> O <sub>4</sub>	2,3	8.398	Inverse
Mg <sub>2</sub> TiO <sub>4</sub>	2,4	8.440	Inverse
Li <sub>0.5</sub> Al <sub>2.5</sub> O <sub>4</sub>	1,3	7.909	Inverse
LiMnTiO <sub>4</sub>	1,3,4	8.300	Li in 8a
LiCoSbO <sub>4</sub>	1,2,5	8.560	Li in 8a
Na <sub>2</sub> WO <sub>4</sub>	1,6	9.130	

### 1.2.2a LiMn<sub>2</sub>O<sub>4</sub>

LiMn<sub>2</sub>O<sub>4</sub> is one of the leading candidates for the next generation of Li-ion battery cathode materials due to the economical and environmental benefits it has over LiCoO<sub>2</sub>. LiMn<sub>2</sub>O<sub>4</sub> has the normal cubic spinel structure, Li<sub>8a</sub>[Mn<sub>2</sub>]<sub>16d</sub>O<sub>4</sub>, where 8a and 16d refer to the tetrahedral and octahedral sites in the Fd3m space group respectively.<sup>37,14</sup> In general, the phase is prepared at ~ 800 °C, with  $a \approx 8.246 \text{ Å}$ .

#### *Low temperature phase transitions*

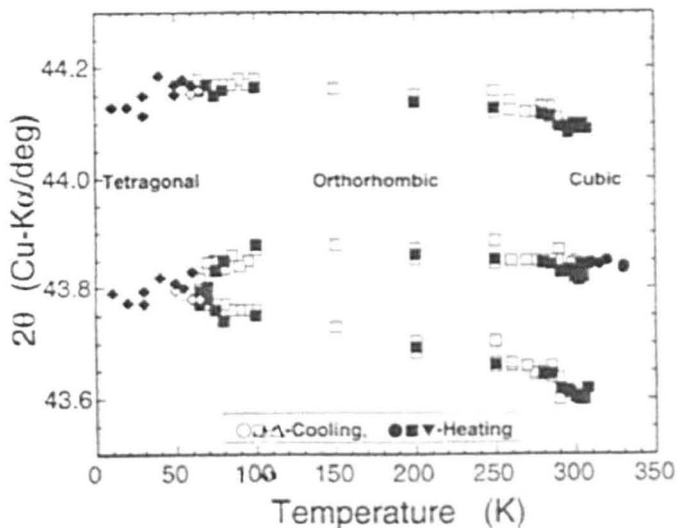
On cooling LiMn<sub>2</sub>O<sub>4</sub> below room temperature, a first-order phase transition occurs. This appears to be due to partial charge ordering of the Mn ions, resulting in a cooperative Jahn-Teller distortion to either orthorhombic<sup>38-41</sup> or tetragonal<sup>42</sup> symmetry at ~ 280 K. Yamada *et al.*<sup>43</sup> suggested that LiMn<sub>2</sub>O<sub>4</sub> underwent a gradual transition below room temperature, with tetragonal spinel coexisting with the high temperature cubic form.

Charge ordering may continue to give a fully ordered state at lower temperatures,<sup>40,44</sup> (Figure 1.16) with a tetragonal unit cell belonging to the I4<sub>1</sub>/amd space group. Patterns

(recorded as low as 1.5 K) reported by Rouse *et al.*<sup>38</sup> were indexed only on the orthorhombic space group. Similar findings were reported by Tabuchi *et al.*<sup>45</sup>

As yet, the low temperature polymorphism of  $\text{LiMn}_2\text{O}_4$  is still poorly understood.

**Figure 1.16** – Possible low temperature phase diagram of  $\text{LiMn}_2\text{O}_4$ . Takada *et al.*<sup>40</sup>

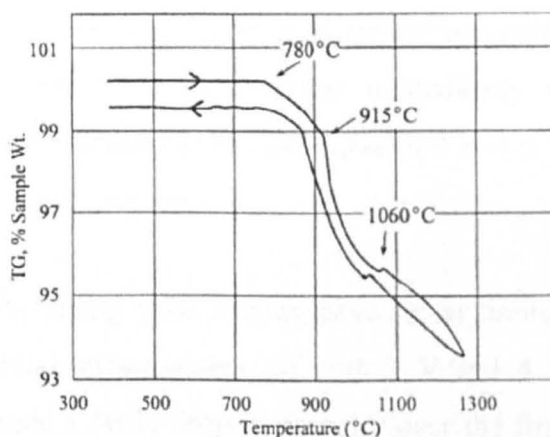


### High temperature phase transitions

$\text{LiMn}_2\text{O}_4$  has also been widely studied to high temperatures by thermal methods, such as thermogravimetry (TG) and differential thermal analysis (DTA). A number of noteworthy features are reported.

TG work (Figure 1.17) indicates a reversible weight loss of  $\sim 6\%$  on heating to 1200 °C. This weight loss is due to oxygen loss, as confirmed by Mandal *et al.*<sup>47</sup>

**Figure 1.17** – TGA plot of  $\text{LiMn}_2\text{O}_4$ .<sup>46</sup>



Oxygen loss begins at  $\sim 780$  °C, and the spinel retains cubic symmetry until the stoichiometry reaches  $\text{LiMn}_2\text{O}_{3.86}$ , at  $\sim 880$  °C,<sup>48,49</sup> where a tetragonal symmetry is observed (evident principally due to the splitting of the  $\{311\}$  peak into (311) and (113) peaks).<sup>50</sup>

Between  $\sim 880$  °C and 915 °C segregation of the monoclinic rocksalt phase  $\text{Li}_2\text{MnO}_3$  occurs, and up to 1000 °C this phase then reacts with some of the remaining Mn-rich spinel phase to form the orthorhombic rocksalt  $\text{LiMnO}_2$ . Oxygen loss during this stage has become very rapid. Thackeray<sup>46</sup> reports that, above 1100 °C, this rocksalt phase recombines with the spinel to give a single phase cubic spinel product. This product phase exhibits Hausmannite  $\text{Mn}_3\text{O}_4$ -type behaviour, with the nominal stoichiometry ' $\text{Li}_{0.6}\text{Mn}_{2.4}\text{O}_4$ ', though this requires lithia loss. However, Sugiyama<sup>51</sup> reports a straight reaction of:



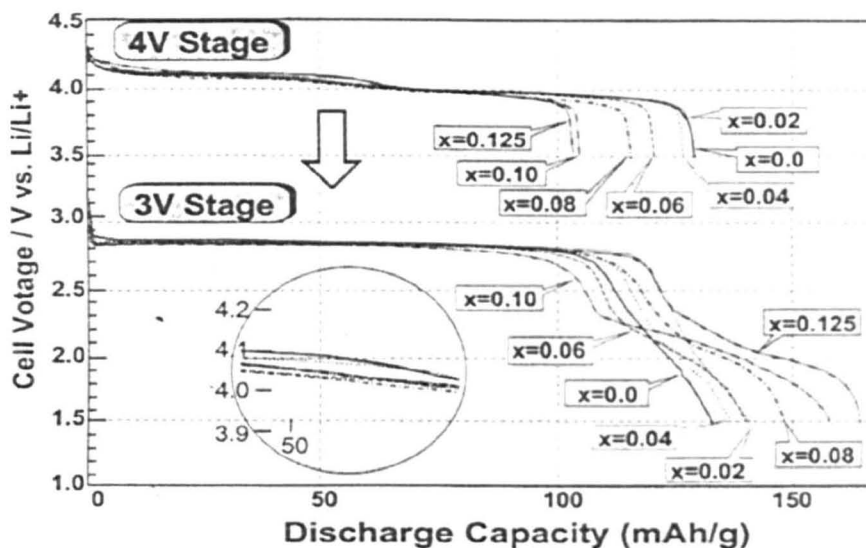
However, little evidence exists of any extensive lithia loss, barring a small degree of irreversible weight loss which could easily be attributed to less than complete re-oxidation of the transition metal back to the average oxidation state of  $3.5^+$ .

### *Electrochemical properties*

The (de)intercalation of lithium (from)/into  $\text{LiMn}_2\text{O}_4$  was first demonstrated by Thackeray *et al.*<sup>14</sup> in 1983. Extraction of lithium proceeds, utilising the  $\text{Mn}^{3+/4+}$  redox couple, via a two-step process at  $\sim 4.1$  V, with  $\sim 0.1$  V separating the two processes.<sup>52,53</sup> This 0.1 V step is attributed to ordering of Li ions over half of the tetrahedral sites when  $x = \frac{1}{2}$  in  $\text{Li}_x\text{Mn}_2\text{O}_4$ . Insertion of Li into  $\text{LiMn}_2\text{O}_4$  is also possible, and proceeds at  $\sim 3.0$  V, reaching an  $\text{Li}_2\text{Mn}_2\text{O}_4$  end-member with tetragonal symmetry. The first-order cubic  $\rightarrow$  tetragonal phase transition occurs almost immediately upon lithium insertion. Example first discharge profiles for  $\text{Li}_{1+x}\text{Mn}_{2-x}\text{O}_4$  ( $0.0 \leq x \leq 0.125$ ) are presented in Figure 1.18.

Problems with capacity fading upon cycling have so far limited the performance, and therefore the commercial attractiveness, of both 3 V and 4 V steps. In particular, Thackeray *et al.* reported a 50 % drop in capacity over the first 10 cycles for the 3 V process.

**Figure 1.18** – First discharge profiles of cells  $\text{Li}/\text{Li}_{1-x}\text{Mn}_{2-x}\text{O}_4$  ( $0.0 \leq x \leq 0.125$ ) in the 4 V (4.5 – 3.6 V) and 3 V (3.6 – 1.5 V) regions.<sup>40</sup>



Three possible mechanisms for capacity fading have been proposed:

- (i) dissolution of Mn into the electrolyte following a disproportionation reaction of the type:



- (ii) electrolyte instability at high voltages
- (iii) cooperative Jahn-Teller distortion due to high spin  $\text{Mn}^{3+}$  ions. Phase transitions between the cubic and tetragonal phase can be accompanied by  $\sim 7\%$  volume change in the cathode. This could essentially rip the cathode apart, and the gradually decreasing connectivity of the particles to each other and the neighbouring battery pieces could cause capacity fading.

The first of these reasons is generally considered most likely. Much work has been conducted to try to improve the electrochemical performance. Some notable studies shall be discussed here.

Kang and Goodenough<sup>54</sup> attempted to prepare  $\text{LiMn}_2\text{O}_4$  by a novel sol-gel route, using  $\text{MnCl}_2$  as a reagent to attempt to leave a Cl-coated particle surface. No evidence of chlorine coating was reported, but the resulting product showed excellent cyclability in the 3 V range – capacities of  $\sim 138 \text{ mAh g}^{-1}$  were observed ( $\sim 93\%$  of the theoretical capacity). No improvement was witnessed in the 4 V range. This author suspects that

traces of a second phase, namely  $\text{Li}_2\text{MnO}_3$ , may have contaminated some of the samples.

Low level doping ( $< 10\%$ ) of  $\text{Mn}^{3+}$  by a range of other cations (*e.g.* Al,<sup>55</sup> Co,<sup>56,57</sup> Cr,<sup>58</sup> Mg<sup>59</sup>) has been attempted as one way of improving battery performance, both in terms of capacity and cycling performance. Generally, the improvement is due to the disruption of the Jahn-Teller effect that occurs when 50% or more of the metal ions are Jahn-Teller active.

Exploitation of the cubic spinel solid solution between  $\text{LiMn}_2\text{O}_4$  and  $\text{Li}_4\text{Mn}_5\text{O}_{12}$  has also been attempted.<sup>40,60,61</sup> Takada *et al.* showed improved cyclability in samples with composition  $0.04 \leq x \leq 0.125$  (Figure 1.18).

However, higher levels of doping with 3d transition metal cations has produced an altogether different effect, as will be described in section 1.2.2b.

### 1.2.2b Five-volt Materials

Cells with cathodes based on spinel structured compounds often show electrochemical responses at  $\sim 4$  V; however, some can show higher operating voltages: 4.8 V for  $\text{LiNiVO}_4$  (an inverse spinel)<sup>62-64</sup> and  $\text{LiCr}_x\text{Mn}_{2-x}\text{O}_4$ <sup>65-68</sup> and 4.7 V for  $\text{LiNi}_x\text{Mn}_{2-x}\text{O}_4$ .<sup>69-73</sup> In 1998 Kawai *et al.*<sup>74</sup> were the first to report a battery, with  $\text{Li}_2\text{CoMn}_3\text{O}_8$  as the active material, operating over 5 V (see Figure 1.19).

A similar performance was shown for  $\text{Li}_2\text{FeMn}_3\text{O}_8$ <sup>75</sup> shortly thereafter; this was the first Fe-containing cathode material to exhibit such a high operating voltage. The  $\text{Li}_2\text{Co}_{1+x}\text{Mn}_{3-x}\text{O}_8$  ( $-1 \leq x \leq 1$ ) solid solution of normal spinels (*i.e.* with Li on the tetrahedral site) was studied; for  $x \geq -0.6$ , reversible extraction of lithium was found to occur initially at a plateau centred at *ca.* 4 V, then at a second plateau centred on *ca.* 5.1 V. With increasing  $x$ , a smooth change was observed in the relative lengths of the two plateaux, *i.e.* the plateau centred on 5.1 V became longer as the plateau centred on 4 V became shorter.

The active redox couples were suggested to be:

- (i)  $\text{Mn}^{3+}_{\text{oct}} \rightleftharpoons \text{Mn}^{4+}_{\text{oct}}$   
(ii)  $\text{Co}^{3+}_{\text{oct}} \rightleftharpoons \text{Co}^{4+}_{\text{oct}}$

When  $x = 1$  ( $\text{LiCoMnO}_4$ ) there should only be  $\text{Mn}^{4+}$  and  $\text{Co}^{3+}$  present, *i.e.* only the 5 V plateau should be present since only the  $\text{Co}^{3+} \rightleftharpoons \text{Co}^{4+}$  redox reaction should be active. It is interesting to note that the same redox process in  $\text{LiCoO}_2$  results only in a 4 V plateau; the reason for this higher voltage in the ternary spinels (*e.g.*  $\text{LiCoMnO}_4$ ,  $\text{LiNiVO}_4$  *etc.*) has not yet been confirmed, but seems linked to structural differences. Theoretical and observed capacities for the solid solution are presented in Figure 1.20; the observed capacity for  $\text{LiCoMnO}_4$  was  $\sim 95 \text{ mAh.g}^{-1}$ , well below the theoretical limit.

The reasons for this shortfall were unknown; had the material performed to its theoretical maximum, a single plateau at  $\sim 5.1 \text{ V}$  would have had capacity  $\sim 145 \text{ mAh.g}^{-1}$  and thus an energy density ( $740 \text{ Wh.kg}^{-1}$ ) high enough for ZEV applications. Robertson *et al.*<sup>76</sup> reported problems with cation mixing in  $\text{LiCoMnO}_4$ , with Co occupying the 8a tetrahedral lithium site. Published work by this author<sup>77</sup> has indicated issues regarding oxygen stoichiometry; this is discussed in Chapter 5.

Copper and zinc<sup>78</sup> have also been substituted into  $\text{LiMn}_2\text{O}_4$  and shown to have active potentials at  $\sim 5 \text{ V}$  (Figure 1.21). However, as yet, none of the 5 V materials has shown high enough capacity and capacity retention on cycling to be of real commercial viability.

**Figure 1.19** – Potential profile for  $\text{Li}_2\text{CoMn}_3\text{O}_8$ .<sup>74</sup>

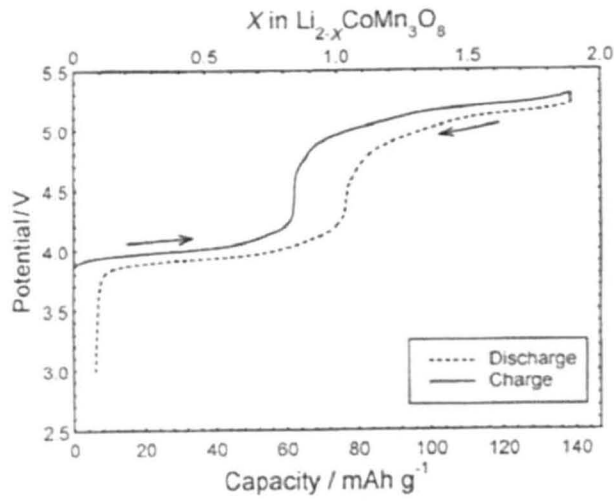


**Figure 1.20** – Variation with composition,  $x$ , in initial total charge/discharge ( $\square/\square$ ), capacity at 4.0 V ( $\bullet/\circ$ ) and capacity at 5.1 V ( $\blacksquare/\square$ ) for  $\text{Li}_2\text{Co}_{1+x}\text{Mn}_{3-x}\text{O}_8 \mid \text{LiPF}_6/\text{PC} \mid \text{Li}$  cell.

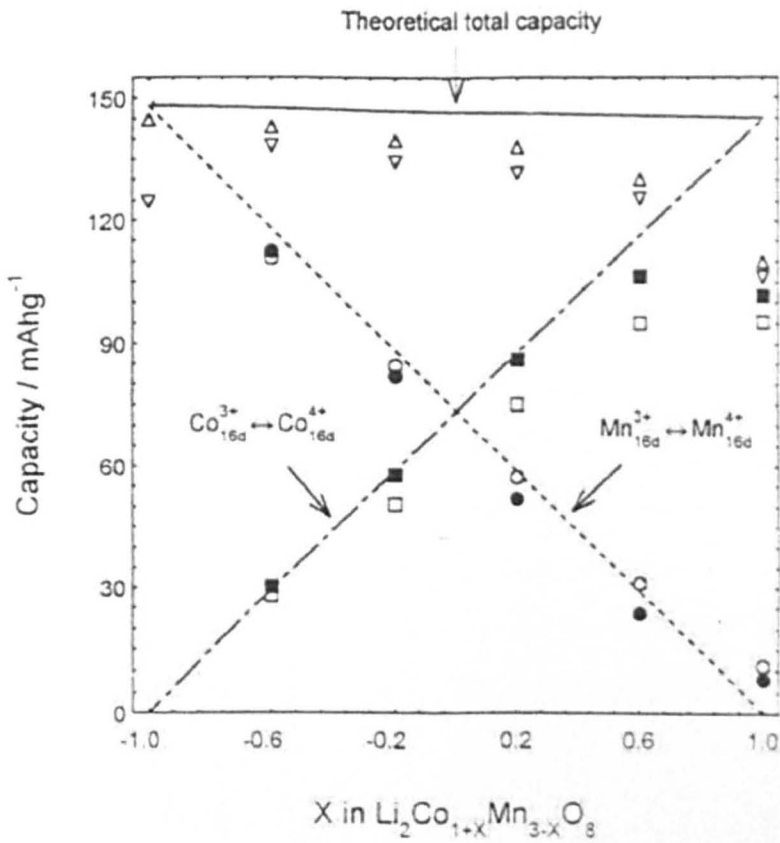
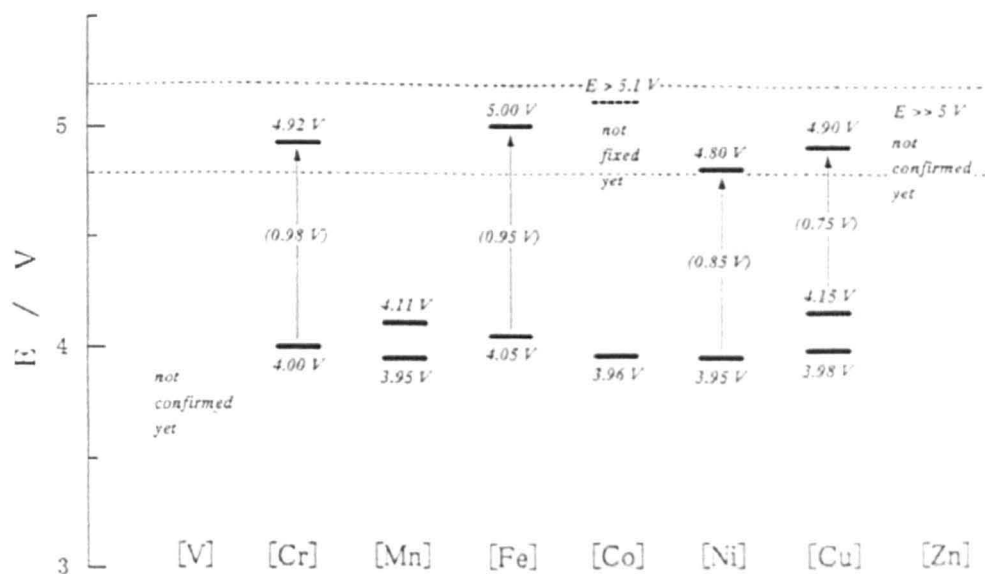


**Figure 1.21** – Levels of solid state redox potentials estimated from slow-scan voltammetry for  $\text{Li}[\text{Me}_{1/2}\text{Mn}_{3/2}]\text{O}_4$ <sup>78</sup>



### 1.2.3 Olivines

The olivine group of structures are analogous to spinels, and have the same cation coordination. They differ in the oxygen stacking sequence, however, since olivines have a hexagonally close-packed (h.c.p.) anion array.

$\text{LiMnPO}_4$ <sup>79</sup> and  $\text{LiFePO}_4$ <sup>80</sup> both have the olivine structure, with space group Pnmb. The two also form a complete solid solution.<sup>81</sup> Both show good electrochemical properties.

$\text{LiMnPO}_4$  exhibits a single plateau centred on  $\sim 3.9$  V, with quoted capacities of 140 to 160  $\text{mAh.g}^{-1}$ ,<sup>79,81</sup> comparing well with the theoretical maximum of 171  $\text{mAh.g}^{-1}$ . The cycling performance is also good.

$\text{LiFePO}_4$  exhibits a single plateau centred on  $\sim 3.4$  V, with capacity  $\sim 160$   $\text{mAh.g}^{-1}$ , comparing well with the theoretical maximum of 170  $\text{mAh.g}^{-1}$ . The cycling performance is excellent (Figure 1.22).

Samples of intermediate composition, in the  $\text{LiMn}_y\text{Fe}_{1-y}\text{PO}_4$  solid solution, exhibit plateaux at both 3.9 and 3.4 V (Figure 1.23), with the 3.9 V plateau becoming shorter (and the 3.4 V plateau becoming longer) as Fe content increases (*i.e.* as  $y$  decreases).

Figure 1.22 – Typical discharge curves of  $\text{LiMn}_y\text{Fe}_{1-y}\text{PO}_4$ .<sup>81</sup>

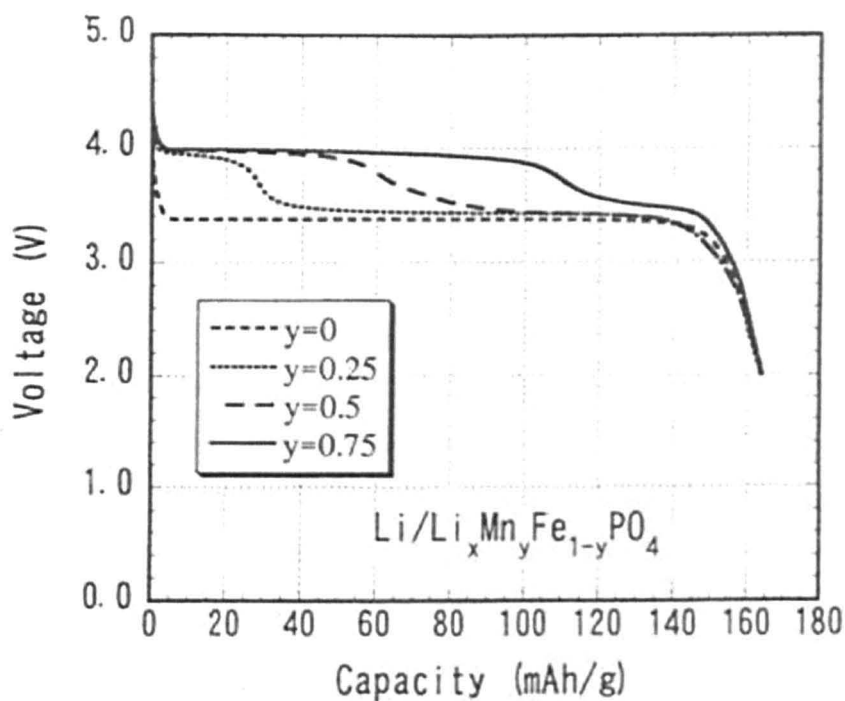
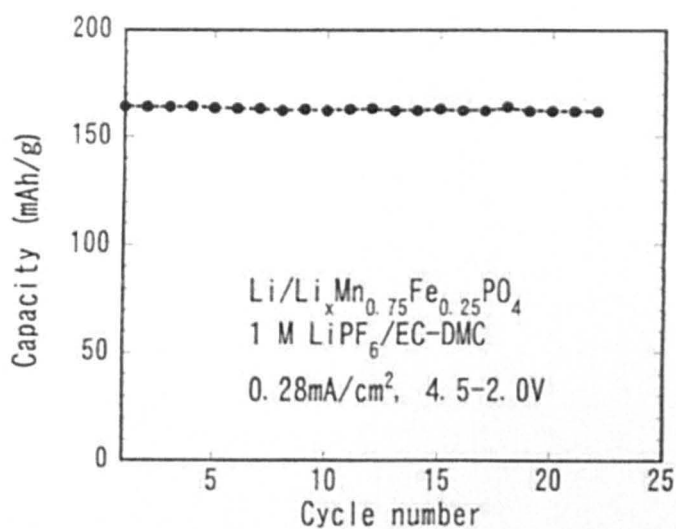


Figure 1.23 – Cycling performance of  $\text{LiMn}_{0.75}\text{Fe}_{0.25}\text{PO}_4$ .<sup>81</sup>



## 1.2.4 PLiON

The Li-ion cells currently commercially available almost exclusively have one feature in common – they all use a liquid electrolyte containing a Li-salt (*e.g.*  $\text{LiPF}_6$  or LiBOB – lithium bis(oxalato)borate). In 1996, Bellcore developed the first plastic rechargeable Li-ion – or ‘PLiON’ – battery.<sup>82</sup> This cell uses a plastic electrolyte, *i.e.* a ‘hybrid’ of a polymer electrolyte and liquid electrolyte (used as a plasticizer). Over a limited composition range, a plastic ‘tape’ is formed. The active materials (Li-based 3d-metal oxide cathode, and a carbonaceous anode) are then dispersed on either side of this. Performance is comparable with the analogous liquid electrolyte cell. The hunt is now definitely on for the next generation of electrolyte materials based on this sort of polymeric structure, aiming to meet the requirements of good ionic conductivity, reproducibility, low cost, high melting temperature and low creep.

## 1.2.5 Theoretical capacities for cathode materials

Table 1.2 lists theoretical capacities for all the cathode materials discussed, to allow comparison. These are calculated by:

$$Q_{To} = (e \cdot F) / 3.6 \times M$$

where,  $e$  = number of electrons involved in complete reaction

$$F = \text{Faraday's constant} / 9.469 \times 10^4 \text{ C.mol}^{-1}$$

$$M = \text{molar mass of active material} / \text{g.mol}^{-1}$$

It should also be noted that 3.6 Coulomb = 1 mA.h.

**Table 1.2 – Comparison of active potential and theoretical capacity for candidate cathode materials.**

Cathode material	Description	Voltage / V	Theoretical Capacity / mAh.g <sup>-1</sup>
LiCoO <sub>2</sub>	Layered rocksalt	3.90	268.75
LiNiO <sub>2</sub>	Layered rocksalt	3.95	269.40
LiMnO <sub>2</sub>	Various polymorphs	3.25 / 4.00	280.17
LiFeO <sub>2</sub>	Various polymorphs	4.05	277.48
LiMn <sub>2</sub> O <sub>4</sub>	Spinel	4.10	145.46
Li <sub>2</sub> CoMn <sub>3</sub> O <sub>8</sub>	Spinel	4.00 / 5.10	143.88
LiCoMnO <sub>4</sub>	Spinel	5.10	142.32
Li <sub>2</sub> FeMn <sub>3</sub> O <sub>8</sub>	Spinel	5.00	145.10
LiNiVO <sub>4</sub>	Inverse spinel	4.80	145.66
Li <sub>2</sub> CrMn <sub>3</sub> O <sub>8</sub>	Spinel	4.92	146.66
Li <sub>2</sub> NiMn <sub>3</sub> O <sub>8</sub>	Spinel	4.80	143.96
LiFePO <sub>4</sub>	Olivine	3.40	166.73
LiMnPO <sub>4</sub>	Olivine	3.90	167.69

### 1.3 Anode materials

Early rechargeable lithium batteries used lithium metal as the negative ‘anode’ electrode. There are severe safety problems associated with this, and large capacity losses also occurred when such electrodes were cycled using organic solvent liquid electrolytes. As a result, alternative materials were sought. The first commercial cell, released by Sony in 1991 instead used graphite as the active material in the anode. The search is underway for the materials to be used as anodes in the next generation of lithium-ion batteries and is discussed in this section.

Sawai *et al.*<sup>83</sup> considered the criteria that possible alternatives to metallic lithium must comply with to be:

- Operating voltage close to metallic lithium with low polarization, *e.g.*  $\leq 1$  V vs. Li.
- High energy density
- Dimensional and morphological stability – so material remains intact on use.
- No dendritic formation – cell cycling can be continued safely, even at high rate.

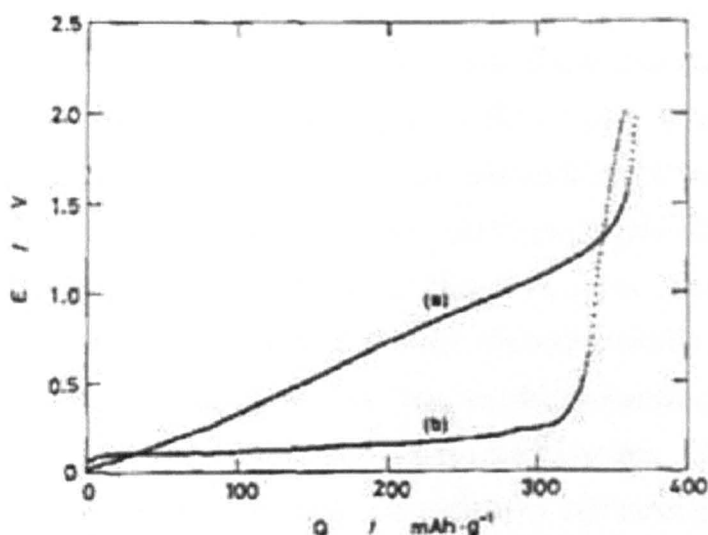
We can also add to these:

- No reaction with electrolyte.
- Easy fabrication of composite anode.
- Good capacity retention on cycling.
- Relatively flat voltage profile on charge/discharge.
- Good electrical conductivity.
- Low cost.
- Low mass material (to preserve the energy density of the cell).
- Low toxicity
- Material must be environmentally benign.

### 1.3.1 Graphite

Graphite has a layered structure, with the hexagonal space group  $P6_3/mmc$ , with all carbon atoms equivalently located on 4f sites. The bonding between the layers is much weaker than the carbon-carbon bonds in the plane. Graphite layers can slide over one another and can also be easily peeled off. Li ions can be intercalated into the structure, and sit between pairs of carbon 'hexagons'; *i.e.* if all these primary sites are used, a stoichiometry of  $LiC_6$  can be reached, giving a specific capacity of  $372 \text{ mAh}\cdot\text{g}^{-1}$ . If further lithium ions are intercalated, *e.g.* using pressure,  $LiC_3$  can be reached for a capacity of  $744 \text{ mAh}\cdot\text{g}^{-1}$ . Various carbon materials were studied by Sawai *et al.*<sup>83</sup> and Endo *et al.*<sup>11</sup>, with 'NG-7' (natural graphite, The Kansai Coke and Chemicals Co., Ltd., Japan) was found most ideal (Figure 1.24).

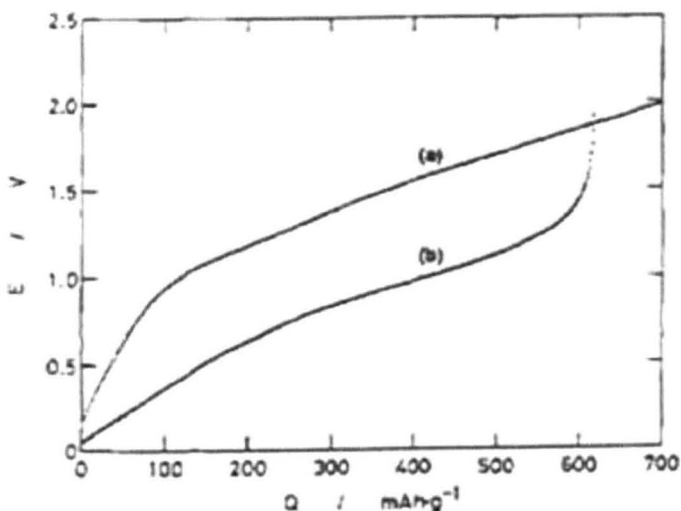
**Figure 1.24** – Change in voltage as a function of specific capacity for electrochemical oxidation of (a) lithiated petroleum coke, and (b) lithiated natural graphite (NG-7) in 1 M  $LiClO_4$  EC/DME (1/1 by volume) solution at rate  $0.17 \text{ mA}\cdot\text{cm}^{-2}$  at  $30^\circ\text{C}$ .<sup>83</sup>



Use of high surface area materials, such as carbon fibres (*e.g.* GF-8, Nihon Carbon Co., Ltd., Japan), allowed intercalation of more lithium, attaining a final stoichiometry approaching  $LiC_3$ . These materials exhibited specific capacities of  $\sim 600 \text{ mAh}\cdot\text{g}^{-1}$  (Figure 1.25), though the profiles are not flat enough to be of applicable use.

High area carbon materials seem to be characterized by wide linear operating voltages as shown in Figure 1.25. Graphitic electrodes are also prone to lithium plating if overcharged, with subsequent safety and cell life concerns.

**Figure 1.25** – Change in voltage as a function of specific capacity for electrochemical oxidation of (a) lithiated high-area carbon in 1 M LiClO<sub>4</sub> EC/DME (1/1 by volume) solution, and (b) lithiated carbon felt (GF-8) in 1 M LiClO<sub>4</sub> PC/DME (1/1 by volume) solution at rate 0.17 mA.cm<sup>-2</sup> at 30 °C.<sup>83</sup>

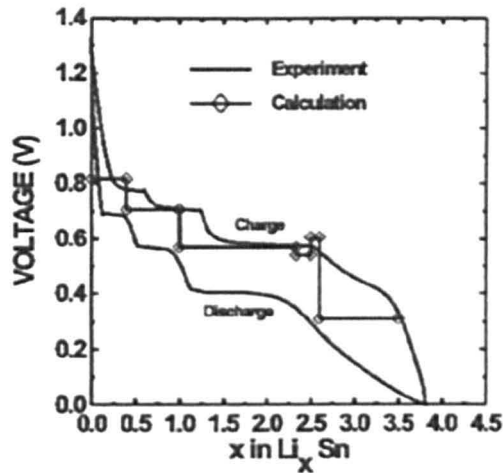


### 1.3.2 Tin-based amorphous oxides

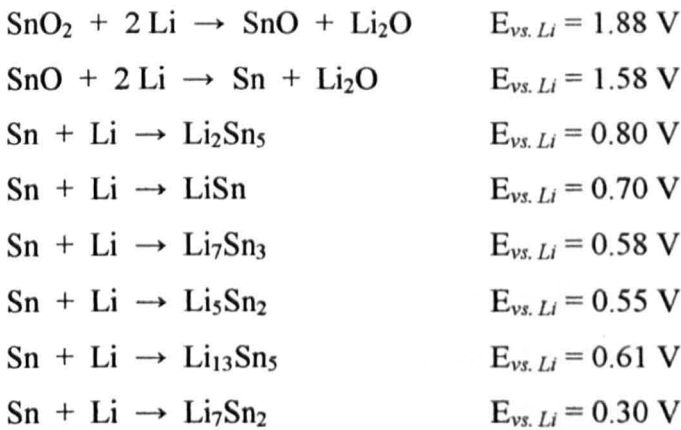
The first major breakthrough in the search for a new anode material was made in 1997 by Idota *et al.*<sup>84</sup> Tin-based composite oxides ('TCO') were found to be capable of intercalating 8 equivalent moles of Li ions per unit mole of TCO; 5 Li ions could be subsequently removed and cycled with almost 100 % coulombic efficiency. TCO has a basic formula represented by SnM<sub>x</sub>O<sub>y</sub>, where M was a number of glass-forming cations (B<sup>3+</sup>, P<sup>5+</sup> and Al<sup>3+</sup>) and  $x \geq 1$ . Sn(II) forms the electrochemically active centre for Li adsorption, while the other metal cations form an electrochemically inactive network structure of -(M-O)- bonding that delocalises the Sn(II) centre. Cells using this as the active anode material obtained reversible capacities of > 600 mAh.g<sup>-1</sup>, double that of the graphitic anodes.

These tin oxides have been shown to work via several steps (Figure 1.26). The lithium first reduces the tin oxide to the metallic state, forming lithia. This is followed by the formation of lithium-tin alloys; it is this alloy that is then cycled, *i.e.* this is not a true topotactic process.<sup>85,86</sup>

Figure 1.26 – Calculated and experimental electrochemical voltage profiles for the lithium-tin system.<sup>85</sup>



The processes involved are:



Numerous follow up studies have been made on tin oxide, crystalline tin phosphates ( $\text{SnP}_2\text{O}_7$ ,  $\text{Sn}_2\text{P}_2\text{O}_7$ ) and lithium tin phosphates ( $\text{LiSn}_2(\text{PO}_4)_3$ ), and amorphous tin borophosphates ( $\text{SnBPO}_6$ ).<sup>87-89</sup> None of these materials gave capacities comparable with the work of Idota *et al.*; the best performance was identified for cubic  $\text{SnP}_2\text{O}_7$  with a reversible specific charge capacity of  $> 360 \text{ mAh.g}^{-1}$ , with capacity retention of 96 % over 50 cycles, when cycled between 0.02 and 1.20 V vs. Li metal.

### 1.3.3 Transition metal oxides

Another approach to obtaining high capacity anode materials has been to do away with the glass forming elements altogether, thereby reducing the mass of the active material. Work in the early 1980's by Thackeray *et al.* studied the intercalation of Li ions into  $\text{Fe}_3\text{O}_4$ ,  $\text{Fe}_2\text{O}_3$  and  $\text{Mn}_3\text{O}_4$ .<sup>14,90</sup> Open-circuit voltages for these materials were in the

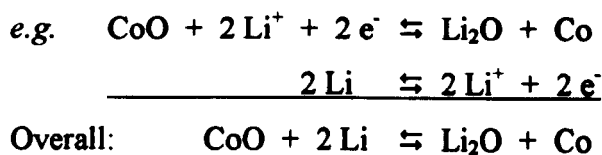
range 1.0 – 2.0 V, with lithiation ranges of  $0 < x < 2$  identified for  $\text{Li}_x\text{Fe}_3\text{O}_4$ ,  $\text{Li}_x\text{Fe}_2\text{O}_3$  and  $\text{Li}_x\text{Mn}_3\text{O}_4$ .

The possible applicability of transition metal oxides as anodes in Li-ion batteries was first identified by Poizot *et al.*<sup>91</sup> in 2000. This group studied a range of nanosized transition metal monoxides (MO, where M = Co, Ni, Cu or Fe),  $\text{Cu}_2\text{O}$  and  $\text{Co}_3\text{O}_4$  spinel; the cobalt oxides were found to have the best performance, with  $\text{Co}_3\text{O}_4$  having a reversible capacity of  $\sim 1000 \text{ mAh.g}^{-1}$ , and excellent capacity retention. This represents almost a tripling of the capacity of the graphitic compounds. Numerous studies have since been conducted on  $\text{CoO}$  and  $\text{Co}_3\text{O}_4$ ,<sup>92-95</sup> and have identified that small (*i.e.* nanometre-sized) particle size is of huge benefit to both the capacity obtained and cycling performance.

Investigation of other metal oxides has also been reported recently.  $\text{NiFe}_2\text{O}_4$  spinel showed good first cycle charge capacities of  $\sim 900 \text{ mAh.g}^{-1}$ , but capacity retention on cycling was poor.<sup>96</sup> The effect of particle size on the ability of  $\text{Fe}_2\text{O}_3$  (hematite) to intercalate Li was studied,<sup>97</sup> with samples in the micrometer range giving flatter charging profiles at  $\sim 0.9 \text{ V vs. Li metal}$ . A small plateau at 1.6 V was also identified, which was longer for nanosized materials, due to the preservation of the original corundum structure for a limited amount of intercalation. Overall,  $\sim 8$  Li ions were intercalated into the electrode material.

The preparation and use of NiO film electrodes has also been recently studied; charge capacity was limited to  $\sim 650 \text{ mAh.g}^{-1}$ . Capacity retention was reasonable.<sup>98</sup>

These transition metal oxides generally work by full electrochemical reduction of the active material to the metallic state; this leads to the formation of composite materials made up of nanometric metallic clusters suspended in an amorphous  $\text{Li}_2\text{O}$  matrix.<sup>97</sup>



This is highly reversible. When the metal is present in the oxide in its lowest oxidation state (*i.e.* in  $\text{CoO}$ ,  $\text{NiO}$ ,  $\text{Cu}_2\text{O}$ ), the formation of metal clusters starts with the onset of reduction. Intermediate processes are involved in the reduction of the oxides of higher

valence metal cations (*i.e.*  $\text{Co}_3\text{O}_4$ ), and these evidence themselves in the form of short plateaux at higher potentials in the voltammetry experiments.

### 1.3.4 Lithium-containing metal oxides

Several other lithium-containing crystal compounds have also been proposed for use as anode materials.  $\text{Li}_4\text{Ti}_5\text{O}_{12}$  operates as an anode at  $\sim 1.5$  V vs. Li metal, but is an insulator, *i.e.* carbon black would have to be used to boost conductivity in the electrode, thereby increasing its weight considerably and reducing specific charge capacity. Small amounts of doping with  $\text{Mg}^{2+}$  and  $\text{Al}^{3+}$  has been reported to result in improvements in conductivity by several orders of magnitude.<sup>99</sup>

Recently, an alternative doped lithium titanate has been proposed<sup>100</sup> as a candidate anode material, with formula  $\text{Li}_2\text{MTi}_6\text{O}_{14}$  ( $\text{M} = \text{Sr}$  or  $\text{Ba}$ ). These materials also cycle at  $\sim 1.5$  V vs. Li, with the strontium-containing compound showing slightly better charge capacity at  $\sim 160$   $\text{mAh.g}^{-1}$ . While capacity retention is good, the capacity is too low to compete with the candidate materials mentioned elsewhere, *e.g.* the cobalt oxides, and even the graphites.

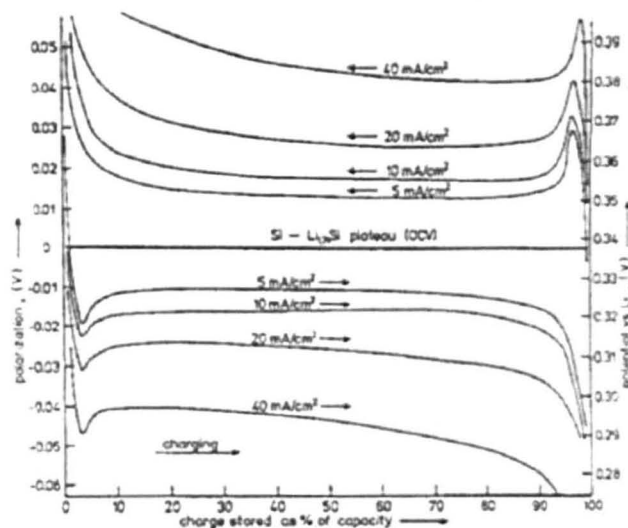
The amorphous thin films of  $\text{LiNiVO}_4$  reported by Lee *et al.* show more promise.<sup>101</sup> Though not single phase, charge capacities of  $\sim 787$   $\text{mAh.g}^{-1}$  were obtained, and capacity retention was reasonable. The charge plateau was not flat, however, and varied approximately linearly from 0 V to 2 V.

### 1.3.5 Intermetallic alloys

It was observed for the tin oxides that ‘intercalation’ of lithium proceeded via an alloying reaction between lithium and tin in their metallic state; a number of groups sought to do away with both the glass forming elements and oxygen from TCO, and attempt lithiation of metals and intermetallic alloys.

The Li-Sn phase diagram and ternary systems with Si or Cd have been studied extensively by Huggins,<sup>102</sup> in an attempt to better understand how the electrochemical reactions proceed. The charge/discharge profile plateaux have a small dependence on the applied (dis)charge rate (Figure 1.27).

Figure 1.27 – Charge-discharge curves in the Li-Sn-Si system at different current densities at 415 °C.<sup>102</sup>



Li-Si alloys, due to their low mass, were shown to have very high gravimetric capacities, of  $4211 \text{ mAh.g}^{-1}$ .<sup>103</sup> Electrode cracking and cell failure were major issues. Lithiated amorphous silicon also gave high capacities on first cycle,  $\sim 1023 \text{ mAh.g}^{-1}$ , with a relatively flat charge plateau centred at  $\sim 0.3 \text{ V}$ . The capacity retention on cycling is very poor however, with capacity of only  $\sim 246 \text{ mAh.g}^{-1}$  on third cycle.

Tin and tin-based intermetallics were studied by Wachtler *et al.*<sup>104</sup> Sn/SnSb electrodes were cycled galvanostatically, with charge capacities of  $\sim 600 \text{ mAh.g}^{-1}$  observed. Capacity retention on cycling was good in the data shown, though many problems with electrode degradation were encountered. The authors proposed that this would be a large issue for all intermetallic alloy electrodes to overcome.

Cobalt triantimonide,  $\text{CoSb}_3$ , belongs to the skutterudite family, a group of cubic solids derived from the general  $\text{Pm-3m ABX}_3$  perovskite structure. High initial charge capacities of  $\sim 800 \text{ mAh.g}^{-1}$  were not retained on cycling, and cycling ability was poor.

Alloys with the zinc-blende structure (InSb, GaSb, AlSb) were studied by Vaughey *et al.*<sup>105,106</sup> The rocksalt structured  $\text{SnSb}^{91}$  was also studied. Cells containing these alloys as the active material were cycled between  $1.2 - 0.5 \text{ V}$  vs. Li metal, with rechargeable capacities of  $\sim 300 \text{ mAh.g}^{-1}$  obtained for InSb. Between  $1.2$  and  $0.7 \text{ V}$  lithium insertion proceeds into an open framework structure, followed by indium extrusion. Between  $0.7$  and  $0.5 \text{ V}$ , a more complex mechanism occurs with indium extrusion from a stable f.c.c. Sb anion array and subsequent lithiation of the indium. Capacity retention is good; note

that there is only a 4.4 % volume difference between  $\text{Li}_3\text{Sb}$  and  $\text{InSb}$ ; however, when the extruded indium is taken into account, the volume difference rises to 46.5 %. By comparison, the volume difference on lithium insertion into  $\text{SnSb}$  is 40 %; for insertion into  $\text{Sb}$ , to give  $\text{Li}_3\text{Sb}$ , the volume change is more significant – 137 %.

Many of these metals and intermetallic alloys are plagued by very poor capacity retention on cycling. This is due to massive volume expansion on inserting lithium resulting in cracking of the particles of active material and loss of structural integrity. This results in loss of electronic contact to the current collector. This is likely to be an issue for the vast majority of metals and alloys; further work is needed to improve the capacity of those materials that can cycle well.

### 1.3 References

- (1) Dell, R. M.; Rand, D. A. J. *Understanding Batteries*; The Royal Society of Chemistry: Cambridge, 2001.
- (2) West, A. R. *Basic Solid State Chemistry*; John Wiley & Sons: Chichester, 1997.
- (3) Shannon, R. D.; Prewitt, C. T. *Acta Crystallographica* **1969**, *B25*, 925.
- (4) Rao, C. N. R.; Gopalakrishnan, J. *New Directions in Solid State Chemistry*, 2 ed.; Cambridge University Press, 1997.
- (5) Shriver, D. F.; Atkins, P. W.; Langford, C. H. *Inorganic Chemistry*, 2 ed.; Oxford University Press, 1995.
- (6) Whittingham, M. S. *Solid State Ionics* **2000**, *134*, 169.
- (7) Whittingham, M. S. *Science* **1976**, *192*, 1226.
- (8) Noréus, D. "Substitution of rechargeable NiCd batteries," European Commission, 2000.
- (9) Armstrong, A. R.; Robertson, A. D. *Chemistry in Britain* **2002**, *38*, 38.
- (10) Bruce, P. G.; Armstrong, A. R.; Gitzendanner, R. *Journal of Materials Chemistry* **1999**, *9*, 193.
- (11) Endo, M.; Kim, C.; Nishimura, K.; Fujino, T.; Miyashita, K. *Carbon* **2000**, *38*, 183.
- (12) Tarascon, J. M.; Armand, M. *Nature* **2001**, *414*, 359.
- (13) Mizushima, K.; Jones, P. C.; Wiseman, P. J.; Goodenough, J. B. *Materials Research Bulletin* **1980**, *15*, 783.
- (14) Thackeray, M. M.; David, W. I. F.; Bruce, P. G.; Goodenough, J. B. *Materials Research Bulletin* **1983**, *18*, 461.
- (15) Nagaura, T.; Tozawa, K. *Prog. Batteries Solar Cells* **1990**, *9*, 209.
- (16) Mizushima, K.; Jones, P. C.; Wiseman, P. J.; Goodenough, J. B. *Materials Research Bulletin* **1980**, *15*, 783.

- (17) Reimers, J. N. "Li-ion technology for transportation applications"; International meeting on lithium batteries 11, 2002, Monterey, CA, USA.
- (18) Lee, C. K.; Rhee, K. I. *Journal of Power Sources* **2002**, *109*, 17.
- (19) Wang, G. X.; Horvat, J.; Bradhurst, D. H.; Liu, H. K.; Dou, S. X. *Journal of Power Sources* **2000**, *85*, 279.
- (20) Kanno, R. "Structure, phase relationship and electrochemical properties of cathode materials - nickel, manganese and iron systems"; International Open Seminar - High Energy Density Lithium Batteries for the Coming Generation, 1998, Italian Institute of Culture, Tokyo.
- (21) Sheu, S. P.; Shih, I. C.; Yao, C. Y.; Chen, J. M.; Hurng, W. M. *Journal of Power Sources* **1997**, *68*, 558.
- (22) Jang, Y. I.; Chiang, Y.-M. *Solid State Ionics* **2000**, *130*, 53.
- (23) Ammundsen, B.; Paulsen, J. *Advanced Materials* **2001**, *13*, 943.
- (24) Shirane, T.; Kanno, R.; Kawamoto, Y.; Takeda, Y.; Takano, M.; Kamiyama, T.; Izumi, F. *Solid State Ionics* **1995**, *79*, 227.
- (25) Kanno, R.; Shirane, T.; Kawamoto, Y.; Takeda, Y.; Takano, M.; Ohashi, M.; Yamaguchi, Y. *Journal of the Electrochemical Society* **1996**, *146*, 2435.
- (26) Lee, Y. S.; Yoon, C. S.; Sun, Y. K.; Kobayakawa, K.; Sato, Y. *Electrochemistry communications* **2002**, *4*, 727.
- (27) Tabuchi, M.; Ado, K.; Sakaebe, H.; Masquelier, C.; Kageyama, H.; Nakamura, O. *Solid State Ionics* **1995**, *79*, 220.
- (28) Ado, K.; Tabuchi, M.; Kobayashi, H.; Kageyama, H.; Nakamura, O.; Inaba, Y.; Kanno, R.; Tsutsui, S.; Nasu, S.; Sakaebe, H. *Journal of the Electrochemical Society* **1997**, *144*, L177.
- (29) Tabuchi, M.; Tsutsui, S.; Masquelier, C.; Kanno, R.; Ado, K.; Matsubara, I.; Nasu, S.; Kageyama, H. *Journal of Solid State Chemistry* **1998**, *140*, 159.

- (30) Tabuchi, M.; Ado, K.; Kobayashi, H.; Matsubara, I.; Kageyama, H.; Wakita, M.; Tsutsui, S.; Nasu, S.; Takeda, Y.; Masquelier, C.; Hirano, A.; Kanno, R. *Journal of Solid State Chemistry* **1998**, *141*, 554.
- (31) Sakurai, Y.; Arai, H.; Okada, S.; Yamaki, J. *Journal of Power Sources* **1997**, *68*, 711.
- (32) Lee, Y. S.; Sato, S.; Sun, Y. K.; Kobayakawa, K.; Sato, Y. *Electrochemistry communications* **2003**, *5*, 359.
- (33) Bragg, W. H. *Philosophical Magazine* **1915**, *30*, 305.
- (34) Nishikawa, S. *Proc. Math. Phys. Soc. Tokyo* **1915**, *8*, 199.
- (35) Sickafus, K. E.; Wills, J. M.; Grimes, N. W. *Journal of the American Ceramic Society* **1999**, *82*, 3279.
- (36) Navrotsky, A.; Kleppa, O. J. *J. Inorg. Nucl. Chem.* **1967**, *29*, 2701.
- (37) Berg, H.; Göransson, K.; Noläng, B.; Thomas, J. O. *Journal of Materials Chemistry* **1999**, *9*, 2813.
- (38) Rouse, G.; Masquelier, C.; Rodriguez-Carvajal, J.; Elkaim, E.; Lauriat, J.-P.; Martinez, J. L. *Chemistry of Materials* **1999**, *11*, 3629.
- (39) Paolone, A.; Roy, P.; Rouse, G.; Masquelier, C.; Rodriguez-Carvajal, J. *Solid State Communications* **1999**, *111*, 453.
- (40) Takada, T.; Hayakawa, H.; Enoki, H.; Akiba, E.; Slegel, H.; Davidson, I.; Murray, J. *Journal of Power Sources* **1999**, *81-82*, 505.
- (41) Tomeno, I.; Kasuya, Y.; Tsunoda, Y. *Physical Review B* **2001**, *64*, 1.
- (42) Wills, A. S.; Raju, N. P.; Greedan, J. E. *Chemistry of Materials* **1999**, *11*, 1510.
- (43) Yamada, A.; Tanaka, M.; Tanaka, K.; Sekai, K. *Journal of Power Sources* **1999**, *81-82*, 73.
- (44) Hayakawa, H.; Takada, T.; Enoki, H.; Akiba, E. *Powder Diffraction* **2000**, *15*, 19.

- (45) Tabuchi, M.; Masquelier, C.; Kobayashi, H.; Kanno, R.; Kobayashi, Y.; Akai, T.; Maki, Y.; Kageyama, H.; Nakamura, O. *Journal of Power Sources* **1997**, *68*, 623.
- (46) Thackeray, M. M.; Mansuetto, M. F.; Dees, D. W.; Vissers, D. R. *Materials Research Bulletin* **1996**, *31*, 133.
- (47) Mandal, S.; Rojas, R. M.; Amarilla, J. M.; Calle, P.; Kosova, N. V.; Anufrienko, V. F.; Rojo, J. M. *Chemistry of Materials* **2002**, *14*, 1598.
- (48) Tarascon, J. M.; McKinnon, W. R.; Coowar, F.; Bowmer, T. N.; Amatucci, G.; Guyomard, D. *Journal of the Electrochemical Society* **1994**, *141*, 1421.
- (49) Yamada, A.; Miura, K.; Hinokuma, K.; Tanaka, M. *Journal of the Electrochemical Society* **1995**, *142*, 2149.
- (50) Strobel, P.; Le Cras, F.; Seguin, L.; Anne, M.; Tarascon, J. M. *Journal of Solid State Chemistry* **1998**, *135*, 132.
- (51) Sugiyama, J.; Atsumi, T.; Hioki, T.; Noda, S.; Kamegashira, N. *Journal of Alloys and Compounds* **1996**, *235*, 163.
- (52) Gummer, R. J.; Thackeray, M. M. *Journal of the Electrochemical Society* **1994**, *141*, 1178.
- (53) Zhang, S. S.; Jow, T. R. *Journal of Power Sources* **2002**, *109*, 172.
- (54) Kang, S.-H.; Goodenough, J. B. *Journal of the Electrochemical Society* **2000**, *147*, 3621.
- (55) Youn, S. G.; Lee, I. H.; Yoon, C. S.; Kim, C. K.; Sun, Y.-K.; Lee, Y. S.; Yoshio, M. *Journal of Power Sources* **2002**, *108*, 97.
- (56) Shen, C. H.; Liu, R. S.; Gundakaram, R.; Chen, J. M.; Huang, S. M.; Chen, J. S.; Wang, C. M. *Journal of Power Sources* **2001**, *102*, 21.
- (57) Banov, B.; Todorov, Y.; Trifonova, A.; Momchilov, A.; Manev, V. *Journal of Power Sources* **1997**, *68*, 578.

- (58) Morita, M.; Nakagawa, T.; Yamada, O.; Yoshimoto, N.; Ishikawa, M. *Journal of Power Sources* **2001**, *97-98*, 354.
- (59) Jeong, I. S.; Kim, J. U.; Gu, H. B. *Journal of Power Sources* **2001**, *102*, 55.
- (60) Dziembaj, R.; Molenda, J.; Majda, D.; Walas, S. *Solid State Ionics* **2003**, *157*, 81.
- (61) Takada, T.; Hayakawa, H.; Kumagai, T.; Akiba, E. *Journal of Solid State Chemistry* **1996**, *121*, 79.
- (62) Fey, G. T.-K.; Li, W.; Dahn, J. R. *Journal of the Electrochemical Society* **1994**, *141*, 2279.
- (63) Liu, J. R.; Wang, M.; Lin, X.; Yin, D. C.; Huang, W. D. *Journal of Power Sources* **2002**, *108*, 113.
- (64) Prabakaran, S. R. S.; Michael, M. S.; Radhakrishna, S.; Julien, C. *Journal of Materials Chemistry* **1997**, *7*, 1791.
- (65) Sigala, C.; Guyomard, D.; Verbaere, A.; Piffard, Y.; Tournoux, M. *Solid State Ionics* **1995**, *81*, 167.
- (66) Sigala, C.; Le Gal Le Salle, A.; Piffard, Y.; Guyomard, D. *Journal of the Electrochemical Society* **2001**, *148*, A812.
- (67) Sigala, C.; Verbaere, A.; Mansot, J. L.; Guyomard, D.; Piffard, Y.; Tournoux, M. *Journal of Solid State Chemistry* **1997**, *132*, 372.
- (68) Terada, Y.; Yasaka, K.; Nishikawa, F.; Konishi, T.; Yoshio, M.; Nakai, I. *Journal of Solid State Chemistry* **2001**, *156*, 286.
- (69) Amine, K.; Tukamoto, H.; Yasuda, H.; Fujita, Y. *Journal of the Electrochemical Society* **1996**, *143*, 1607.
- (70) Kanamura, K.; Hoshikawa, W.; Umegaki, T. *Journal of the Electrochemical Society* **2002**, *149*, A339.

- (71) Sun, Y. K.; Lee, Y. S.; Yoshio, M.; Amine, K. *Electrochemical and Solid-State Letters* **2002**, *5*, A99.
- (72) Zhong, Q.; Bonakdarpour, A.; Zhang, M.; Gao, Y.; Dahn, J. R. *Journal of the Electrochemical Society* **1997**, *144*, 205.
- (73) Gao, Y.; Myrtle, K.; Zhang, M.; Reimers, J. N.; Dahn, J. R. *Physical Review B* **1996**, *54*, 16670.
- (74) Kawai, H.; Nagata, M.; Tukamoto, H.; West, A. R. *Journal of Materials Chemistry* **1998**, *8*, 837.
- (75) Kawai, H.; Nagata, M.; Tabuchi, M.; Tukamoto, H.; West, A. R. *Chemistry of Materials* **1998**, *10*, 3266.
- (76) Robertson, A. D.; Armstrong, A. R.; Bruce, P. G. *Journal of Power Sources* **2001**, *97-98*, 332.
- (77) Reeves, N.; Kirk, C. A.; West, A. R. *Journal of Materials Chemistry* **2001**, *11*, 249.
- (78) Ohzuku, T.; Takeda, S.; Iwanaga, M. *Journal of Power Sources* **1999**, *81-82*, 90.
- (79) Li, G.; Azuma, H.; Tohda, M. *Electrochemical and Solid-State Letters* **2002**, *5*, A135.
- (80) Prosini, P. P.; Carewska, M.; Scaccia, S.; Wisniewski, P.; Passerini, S.; Pasquali, M. *Journal of the Electrochemical Society* **2002**, *149*, A886.
- (81) Li, G.; Azuma, H.; Tohda, M. *Journal of the Electrochemical Society* **2002**, *149*, A743.
- (82) Tarascon, J. M.; Gozdz, A. S.; Schmutz, C.; Shokoohi, F.; Warren, P. C. *Solid State Ionics* **1996**, *86-88*, 49.
- (83) Sawai, K.; Iwakoshi, Y.; Ohzuku, T. *Solid State Ionics* **1994**, *69*, 273.
- (84) Idota, Y.; Kubota, T.; Matsufuji, A.; Maekawa, Y.; Miyasaka, T. *Science* **1997**, *276*, 1395.

- (85) Courtney, I. A.; Tse, J. S.; Mao, O.; Hafner, J.; Dahn, J. R. *Physical Review B* **1998**, *58*, 15583.
- (86) Machill, S.; Shodai, T.; Sakurai, Y.; Yamaki, J. *Journal of Power Sources* **1998**, *73*, 216.
- (87) Courtney, I. A.; Dunlap, R. A.; Dahn, J. R. *Electrochimica Acta* **1999**, *45*, 51.
- (88) Behm, M.; Irvine, J. T. S. *Electrochimica Acta* **2002**, *47*, 1727.
- (89) Belliard, F.; Connor, P. A.; Irvine, J. T. S. *Solid State Ionics* **2000**, *135*, 163.
- (90) Thackeray, M. M.; David, W. I. F.; Goodenough, J. B. *Materials Research Bulletin* **1982**, *17*, 785.
- (91) Poizot, P.; Laruelle, S.; Grugeon, S.; Dupont, L.; Tarascon, J. M. *Nature* **2000**, *407*, 496.
- (92) Wang, G. X.; Chen, Y.; Konstantinov, K.; Lindsay, M.; Liu, H. K.; Dou, S. X. *Journal of Power Sources* **2002**, *109*, 142.
- (93) Wang, G. X.; Chen, Y.; Konstantinov, K.; Yao, J.; Ahn, J. H.; Liu, H. K.; Dou, S. X. *Journal of Alloys and Compounds* **2002**, *340*, L5.
- (94) Badway, F.; Plitz, I.; Grugeon, S.; Laruelle, S.; Dolle, M.; Gozdz, A. S.; Tarascon, J. M. *Electrochemical and Solid-State Letters* **2002**, *5*, A115.
- (95) Choi, H. C.; Lee, S. Y.; Kim, S. B.; Kim, G. M.; Lee, M. K.; Shin, H. J.; Lee, J. S. *The Journal of Physical Chemistry B* **2002**, *106*, 9252.
- (96) Alcantara, R.; Jaraba, M.; Lavela, P.; Tirado, J. L.; Jumas, J. C.; Olivier-Fourcade, J. *Electrochemistry communications* **2003**, *5*, 16.
- (97) Larcher, D.; Sudant, G.; Leriche, J.-B.; Chabre, Y.; Tarascon, J. M. *Journal of the Electrochemical Society* **2002**, *149*, A234.
- (98) Nuli, Y. N.; Zhao, S. L.; Qin, Q. Z. *Journal of Power Sources* **2003**, *114*, 113.

- (99) Chen, C. H.; Vaughey, J. T.; Jansen, A. N.; Dees, D. W.; Kahaian, A. J.; Goacher, T.; Thackeray, M. M. *Journal of the Electrochemical Society* **2001**, *148*, A102.
- (100) Belharouak, I.; Amine, K. *Electrochemistry communications* **2003**, *5*, 435.
- (101) Lee, S. J.; Lee, H. Y.; Ha, T. S.; Baik, H. K.; Lee, S. M. *Electrochemical and Solid-State Letters* **2002**, *5*, A138.
- (102) Huggins, R. A. *Journal of Power Sources* **1999**, *81-82*, 13.
- (103) Netz, A.; Huggins, R. A.; Weppner, W. *Ionics* **2001**, *7*, 433.
- (104) Wachtler, M.; Besenhard, J. O.; Winter, M. *Journal of Power Sources* **2001**, *94*, 189.
- (105) Vaughey, J. T.; Johnson, C. S.; Kropf, A. J.; Benedek, R.; Thackeray, M. M.; Tostmann, H.; Sarakonsri, T.; Hackney, S.; Fransson, L.; Edstrom, K.; Thomas, J. O. *Journal of Power Sources* **2001**, *97-98*, 194.
- (106) Thackeray, M. M.; Vaughey, J. T.; Johnson, C. S.; Kropf, A. J.; Benedek, R.; Fransson, L. M. L.; Edstrom, K. *Journal of Power Sources* **2003**, *113*, 124.

## Chapter 2

### Experimental Techniques

#### 2.1 Sample Preparation

Attempts were made to prepare samples with compositions in the Li-Co-Mn-O system using oxide (Co and Mn) and carbonate (Li) reagents, following on from the work of Kawai *et al.*<sup>1-3</sup> These attempts were largely unsuccessful, leading to poor quality samples, with poor crystallinity and second phases present. The presence of Li<sub>2</sub>MnO<sub>3</sub> as a second phase in the Li-Mn-O system has long been considered a problem.<sup>4</sup>

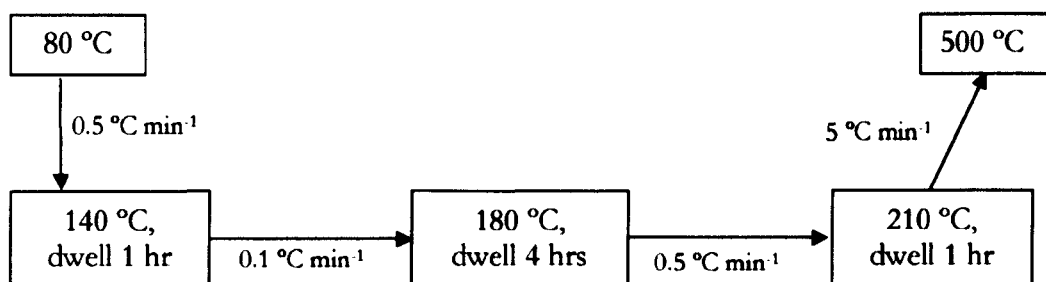
Instead, a new synthesis route was designed to produce samples of better homogeneity and phase purity by using a combination of nitrate and acetate reagents; those used are listed in Table 2. TG analysis showed that both the cobalt nitrate hexahydrate (6 H<sub>2</sub>O) and the anhydrous manganese acetate lost slightly more weight on heating than was expected; it is suggested that these powders were more hydrated than reported by the supplier. The formula and mass for each reagent was corrected from the TG data to allow for this excess hydration; the corrected values (presented in Table 2.1) were used in sample preparation.

*Table 2.1 - Starting reagents used for synthesis of samples in Li-Co-Mn-O phase diagram using mixed acetate/nitrate route. Formulae from TG analysis.*

Reagent	Formula weight / g mol <sup>-1</sup>	Source	Purity
Co(NO <sub>3</sub> ) <sub>2</sub> · 6.23H <sub>2</sub> O	295.33	Aldrich	> 98 %
LiNO <sub>3</sub>	68.95	Fisher Chemicals	> 98 %
(CH <sub>3</sub> CO <sub>2</sub> ) <sub>2</sub> Mn · 0.23H <sub>2</sub> O	177.198	Aldrich	> 98 %

These materials were not treated (*e.g.* dried) in any way before use, since they melt at temperatures close to ambient conditions; indeed, manganese nitrate was going to be used in place of manganese acetate as one of the reagents, but melted at < 30 °C, making general laboratory use impractical.

These powders were weighed accurately using a 5 decimal place balance (Precisa), ground intimately with a mortar and pestle, placed into gold boats, and moved into a furnace at 80 °C. The samples were slowly heated to 500 °C using the following heating regime:



This process was found to be necessary since the nitrate/acetate mix melted on heating, and more rapid heating could result in spitting and overpouring of the sample mixture, which raised concerns over furnace contamination. The composition of the samples produced also had a tendency to differ from the desired composition; loss was not necessarily ‘homogeneous’. The regime detailed above was found to be the most reliable for the wide range of Li-Co-Mn-O compositions studied, with the dwell temperatures corresponding approximately to temperature regions where reagent decomposition was reasonably rapid.

After heating to 500 °C, samples were removed and reground, then heated at 800 °C for 3 days, with intermittent regrinding by mortar and pestle for twenty minutes daily. A subsequent post-reaction annealing step at 500 °C was used to optimise oxygen contents. This last step is a significant departure from the literature; Kawai *et al.* annealed samples of  $\text{LiCoMnO}_4$  at 600 °C. Oxygen loss has been reported<sup>5</sup> for some compositions in the Li-Co-Mn-O phase diagram; for example, for  $\text{LiCoMnO}_4$  oxygen loss begins at  $\sim 570$  °C. Therefore, use of the lower annealing temperature was designed to ensure maximised oxygen contents.

The same conditions were used for all compositions studied, even when no evidence of oxygen loss was noted, to ensure that all parameters (*e.g.* unit cell dimensions) were examined from the same viewpoint.

The high temperature structures of the materials prepared were also studied. This was carried out using two vertical tube quench furnaces – one for ‘low’ temperature ranges

(< 1100 °C) and one for quenches from 1100 – 1500 °C. Samples of ~ 0.1 g were wrapped in gold (when quenching from < 1000 °C) or platinum envelopes, and suspended from a jig using 0.1 mm diameter Pt wire. The jig used a four-bore recrystallised alumina tube fitted with a Pt/Pt13%Rh thermocouple; this allowed accurate measurement of the temperature from which samples were being quenched. The samples were dropped into mercury at room temperature, by using a capacitor discharge to melt the suspending wire instantaneously. Using this technique, the samples were cooled rapidly from a known temperature, and, where possible, any high temperature structure was 'frozen in'.

## 2.2 X-ray powder diffraction

### 2.2.1 Background theory

This technique relies on the fact that x-rays can have a wavelength of  $\sim 1 \text{ \AA}$ , *i.e.* a wavelength similar to the interplanar spacing in a crystalline material. The x-rays can therefore be diffracted by the atoms or ions residing in these planes, in a manner analogous to the diffraction of light by an optical grating.

Braggs' Law arises from considering crystals as being made up from semi-transparent layers or planes. Bragg's Law is given in Equation 2.1:

$$2d \sin \vartheta = n \lambda \quad (\text{Equation 2.1})$$

Where:  $d$  = interplanar spacing, or 'd-spacing',  
 $\vartheta$  = reflection, or Bragg, angle,  
 $n$  = order of reflection, and  
 $\lambda$  = wavelength of incident radiation.

The order of reflection,  $n$ , is always taken as unity in x-ray diffraction experiments. Any higher order reflections can be treated as 1<sup>st</sup> order reflections with the indices multiplied by  $n$ , *e.g.* a (222) reflection can be considered to be a second order (111) reflection.

X-rays are generated when high-energy electrons are fired through 40,000 volts at a metal source. This results in the emission of two kinds of radiation. *White* radiation arises when the electrons are slowed by the source and their kinetic energy converted to x-rays. A broad 'hump' in radiation wavelengths is observed. The minimum wavelength, known as the 'Duane-Hunt limit', of this hump can be found by Equation 2.2.

$$\lambda_{min} = h.c / V.e \quad (\text{Equation 2.2})$$

Where:  $\lambda$  = Duane-Hunt limit of minimum wavelength for an applied voltage,  
 $h$  = Planck's constant,  
 $c$  = speed of light,

$V$  = applied voltage

$e$  = charge on an electron.

This simplifies to the form presented in Equation 2.3:

$$\lambda_{min} = 12,399 / V \quad \text{(Equation 2.3)}$$

An x-ray tube operating at 40 kV will therefore emit white radiation with a minimum wavelength of  $(12,399 / 40,000 = )$  0.31 Å.

*Monochromatic* x-rays are produced when the electron strikes the metal 'target' with sufficient energy to cause ionisation of a core electron. An outer shell electron immediately drops down to fill the empty energy level, with the emission of radiation whose energy, and therefore wavelength, is characteristic of the transition. This emission is superimposed on top of the white radiation. Generally the transition is either 3p to 1s (resulting in 'K $\beta$ ' radiation) or 2p to 1s (resulting in K $\alpha_1$  and K $\alpha_2$  radiation, due to the two spin states that 2p electrons can adopt).

## 2.2.2 Instrumentation

The equipment used for the diffraction experiments reported in this work was a Philips PW1710 diffractometer, with a cobalt source.

The beam of x-rays is not truly monochromatic in this instrument. K $\beta$  radiation is stripped by passing the radiation through a Ni filter. The sample, applied to an aluminium 'boat', then reflects the x-rays according to Bragg's Law (Equation 2.1). The instrument scans through  $2\theta$  and the reflection data are collected by a position sensitive detector.

Most instruments use a monochromator, *e.g.* to 'filter' the x-rays and allow only a single wavelength of x-rays to pass. However, the Philips PW1710 has no monochromator, so the sample is exposed to both Co K $\alpha_1$  (wavelength = 1.78897 Å) and Co K $\alpha_2$  (wavelength = 1.79285 Å)<sup>6</sup> radiation. This essentially adds a second term to the Bragg Law, with diffraction peaks from both of these slightly different wavelengths being observed. Therefore, using a non-monochromatized x-ray beam

from a cobalt source two reflections are observed, one from the  $K_{\alpha 1}$  radiation, and one from the  $K_{\alpha 2}$  radiation. A rearrangement of Bragg's Law, as in Equation 2.4, shows that the separation of the two sets of peaks will increase with theta, due to the nature of the  $\sin \theta$  vs.  $\theta$  curve.

$$\sin \theta = \lambda / 2d \quad \text{(Equation 2.4)}$$

Hence, care had to be taken not to index  $K_{\alpha 2}$  peaks during data analysis. There were numerous diffractometers available that did have monochromators fitted as standard, which would have avoided this problem. However, these were not used since they all used Cu radiation sources, which gave rise to high background levels in the XRD patterns with the samples being studied.

### **2.2.3 Fluorescence problems**

When x-rays strike an atom whose atomic number is a little lower than that of the source, the wavelength of the incident x-rays most likely fall close to the atom's absorption edge. The result is high levels of absorption of the radiation and a large amount of diffusely scattered radiation re-emitted at wavelengths characteristic of the absorbing atom. This produces higher levels of background radiation than would be observed otherwise. As an example of this phenomenon, Co and Mn have  $Z = 27$  and  $25$  respectively. When Cu ( $Z = 29$ )  $K_{\alpha}$  radiation is used in the XRD study of materials containing these atoms, high levels of background radiation are noted. This often obscures any peaks of low intensity, making characterisation more difficult. Often, any secondary phases are harder to detect. Hence, Co  $K_{\alpha}$  radiation was used for the XRD experiments conducted here.

### **2.2.4 Scanning conditions used**

Patterns were recorded using a scan rate of  $0.25 \text{ }^{\circ} \text{ min}^{-1}$ , over a  $2\theta$  range of  $15 - 80^{\circ}$ . The step size used was  $0.02 \text{ }^{\circ}$ . This was found to give good quality data, with least squares refinements from the collected data found most acceptable. All data were collected under ambient conditions.

## **2.3 Thermogravimetry (TG), Differential Thermal Analysis (DTA) and Differential Scanning Calorimetry (DSC)**

Thermal behaviour was studied using a combined TG-DTA (Stanton-Redcroft). This equipment enabled experiments to be run using temperatures of up to ~ 1475 °C. A variety of gases were available; those principally used here were air, oxygen and nitrogen. The majority of experiments were run under a flowing air atmosphere, with heating/cooling rates programmed at 10 °C min<sup>-1</sup>. Generally, the samples used weighed ~ 40 – 50 mg. Data analysis was conducted using Microsoft Excel, with data exported to OriginLabs' Origin 6.1 software for better presentation.

### **2.3.1 Thermogravimetry (TG)**

This technique can be used to measure the change in sample mass as a function of temperature, or time. The difference in weight,  $\Delta W$ , can be used to help identify the nature of the process causing the weight loss.

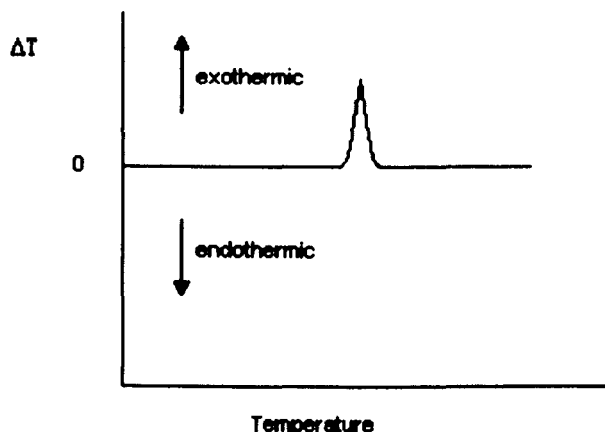
The weight output from the TG was calibrated regularly using 10 mg and 100 mg calibration weights.

It is important to remember the effect of atmosphere on decomposition processes. Decomposition reactions often happen at lower temperatures under a vacuum, or an inert atmosphere, *e.g.* N<sub>2</sub>.

### **2.3.2 Differential Thermal Analysis (DTA)**

Thermal events – exothermic and endothermic reactions – cause a sample to give out or absorb heat from its surroundings. Therefore, should any thermal event occur in the sample during heating or cooling, comparing the sample temperature with that of an inert reference material (Al<sub>2</sub>O<sub>3</sub>) results in a difference in temperature between the sample and reference. This  $\Delta T$  value can then be plotted against temperature, as shown in Figure 2.1.

**Figure 2.1 - Schematic of a typical exothermic DTA peak**



If no thermal event occurs, zero output is recorded. An exothermic event causes the sample response to lead that of the reference, and vice versa. DTA data can then be used to help identify what thermal processes occur in a sample.

### **2.3.2 Differential Scanning Calorimetry**

Differential scanning calorimetry is very similar to the DTA technique. The equipment used was a TA Instruments DSC-910, running with TA2000 control software. This type of DSC works by measuring the difference in temperature between the sample and a reference material; this is essentially the same as a DTA. However, the cell is designed in such a way as to give a more accurate calorimetric response.

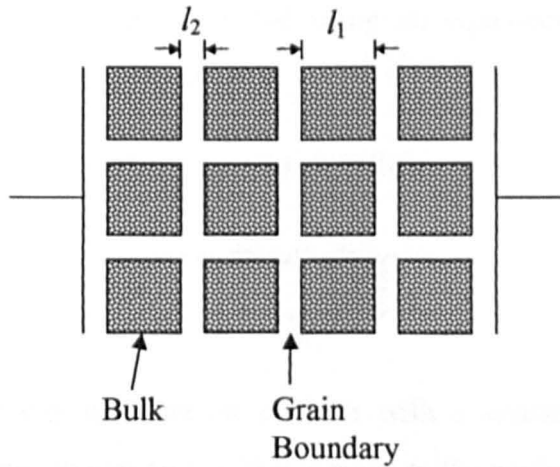
Heating rates for the experiments were set to  $10\text{ }^{\circ}\text{C min}^{-1}$ . It was not possible to record cooling data on the equipment used. All samples were weighed into pans, which were then crimped shut, and run in a flowing Ar atmosphere, with a flow rate of  $\sim 100\text{ ml min}^{-1}$ . The inert reference was simply an empty crimped pan. Data analysis had to be performed on the PC supplied with the equipment.

## 2.4 Impedance Spectroscopy

Impedance spectroscopy is an ideal technique for measuring the electrical properties of ceramic materials and any inhomogeneities that they may contain, *e.g.* bulk, grain boundary, surface effects. It can also be applied to look for evidence of ionic conductivity. The aim in this work was to study the bulk electronic conductivity of various spinel materials, to determine the nature and extent of any variation with composition, and to look for any grain boundary effects.

The impedance technique<sup>7,8</sup> works by the application of an alternating potential difference across a sample over a range of frequencies, and measuring the current output. Ceramic samples are usually polycrystalline, where the structure may be described by the brickwork model (Figure 2.2).

*Figure 2.2 – Brickwork model of grain and grain boundary regions in a polycrystalline ceramic material placed between two metal electrodes. Adapted from West et al.<sup>7</sup>*



As the current passes through the material it usually passes through the various different elements of the structure (*i.e.* grains, grain boundaries *etc.*). The model in Figure 2.2 can be viewed as a parallel plate capacitor, and as such the capacitance for the various components can be worked out using Equation 2.5. Here,  $l$ , the separation between the plates, is the dominant factor. Generally, each structural element has a characteristic ‘thickness’ (*e.g.*  $l_1$  for bulk in Figure 2.2), and subsequently we can expect the ‘thicker’ bulk elements to have a lower capacitance than ‘thinner’ grain boundary regions and even thinner surface layer regions.

$$C = \epsilon' \cdot \epsilon_0 \cdot (A / l) \quad \text{(Equation 2.5)}$$

Where:  $C$  = capacitance of the element  
 $e'$  = sample permittivity  
 $e_0$  = permittivity of free space,  $8.854 \times 10^{-14}$  F cm<sup>-1</sup>  
 $A$  = area of parallel plate capacitor  
 $l$  = plate separation

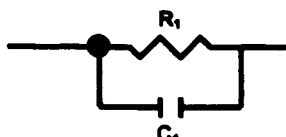
Example capacitance values for different structural elements are presented in Table 2.2.

*Table 2.2 – General capacitance values for various structural elements.*

Element	Capacitance / F.cm <sup>-1</sup>
Bulk	$10^{-11} - 10^{-12}$
Grain boundary	$10^{-8} - 10^{-11}$
Surface layer	$10^{-7} - 10^{-9}$
Sample-electrode interface	$10^{-5} - 10^{-7}$
Electrochemical reaction	$10^{-4}$

The different regions of the sample also have their own characteristic resistances, and so their electrical response can be modelled using an equivalent circuit, such as the ‘parallel RC element’ shown in Figure 2.3.

*Figure 2.3 – Parallel RC element*



From a.c. theory we can say that an element with a characteristic resistance and capacitance has a relaxation constant,  $\tau$ , that is equal to the product of the two:

$$\tau = RC \quad \text{(Equation 2.6)}$$

The time constant has the units as seconds. From the relationship:

$$\omega_{max}RC = 1 \quad \text{(Equation 2.7)}$$

We can define  $\omega_{max}$ , the frequency of maximum loss, as in Equation 2.8 where  $f$  is the frequency in Hz.

$$\omega_{max} = 2\pi f \quad \text{(Equation 2.8)}$$

Therefore if measurements are made over a wide range of frequencies it is possible to separate the different elements.

The equations for the admittance ( $Y^*$ ) and complex impedance ( $Z^*$ ) can be derived:

$$Y^* = 1/Z^* = 1/R + j\omega C \quad (\text{Equation 2.9})$$

$$Z^* = \frac{R}{1 + [\omega RC]^2} - \frac{j\omega R^2 C}{1 + [\omega RC]^2} \quad (\text{Equation 2.10})$$

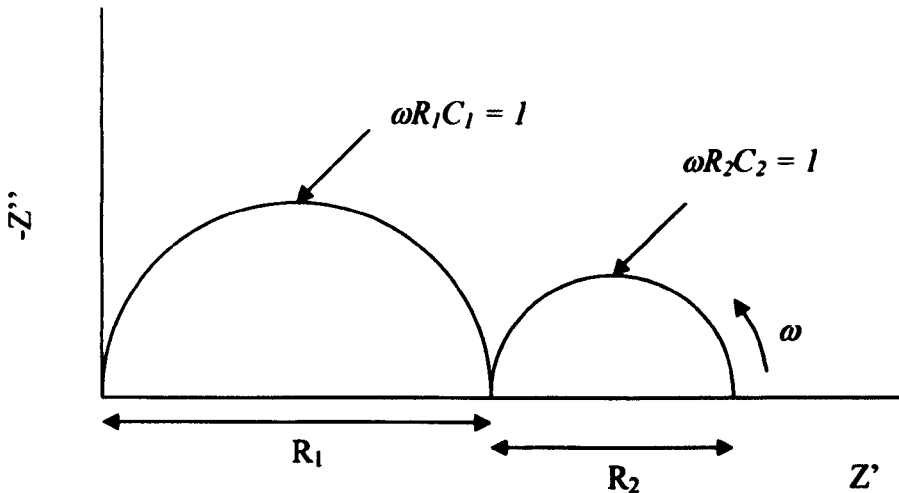
Where  $j = \sqrt{-1}$ . Since  $Z^* = Z' - jZ''$ , equation 2.10 breaks down into:

$$Z' = \frac{R}{1 + [\omega RC]^2} \quad (\text{Equation 2.11})$$

$$Z'' = \frac{j\omega R^2 C}{1 + [\omega RC]^2} \quad (\text{Equation 2.12})$$

A plot of  $Z''$  vs.  $Z'$  is known as the impedance complex plane plot, and gives a semi-circle for a parallel RC element. The resistance and capacitance values,  $R_{\text{element}}$  and  $C_{\text{element}}$ , can be worked out from the intercept on the  $Z'$  axis and the maximum value of the arc (since  $\omega RC = 1$ ) respectively, as shown in Figure 2.4.

*Figure 2.4 – Schematic impedance complex plane plot for a ceramic modelled on two R-C elements*



The electric modulus formalism,  $M^*$ , can also be of use in determining capacitance data, especially when the elements are not cleanly resolved in the  $Z^*$  presentation. A plot of  $M''$  vs. log frequency can be used to find the capacitance for each element since:

$$M^* = j\omega C_0 Z^* \quad (\text{Equation 2.13})$$

$$= j\omega C_0 Z' - j^2 \omega C_0 Z'' \quad (\text{Equation 2.14})$$

$$\therefore M'' = \omega C_0 Z' = C_0 / C \cdot [(\omega R C) / (1 + [\omega r C]^2)] \quad (\text{Equation 2.15})$$

The second term in equation 2.15 is that for a Debye peak. The peak maximum equals  $C_0 / 2C$ . From  $M''$  data, which are already corrected both for the permittivity of free space and the geometry of the pellet, equation 2.16 can be used to find the capacitance for an element:

$$C_{element} = 1 / (2 \times M''_{max}) \quad (\text{Equation 2.16})$$

From this, the resistivity,  $\rho$ , (and conductivity,  $\sigma$ ) of the element can be calculated:

$$\rho_{element} = 2 \cdot \pi \cdot f \cdot C_{element} \quad (\text{units } \Omega \text{ cm}) \quad (\text{Equation 2.17})$$

$$\sigma_{element} = 1 / \rho_{element} \quad (\text{units } S \text{ cm}^{-1}) \quad (\text{Equation 2.18})$$

Resistivity and conductivity are now used since the data is corrected for geometry. Conductivity data plotted against temperature usually fit a straight line, assuming only one conduction process contributes to the data. The Arrhenius equation (equations 2.19 and 2.20) can then be used to calculate the activation energy for the conduction process.

$$\sigma = A \cdot \exp(-E_a / kT) \quad (\text{Equation 2.19})$$

$$\ln \sigma = \ln A - (E_a / kT) \quad (\text{Equation 2.20})$$

Where:  $A$  = pre-exponential factor  
 $k$  = Boltzmann constant,

The activation energy can be calculated from the gradient  $-E_a / k$ , since:

$$\ln \sigma \text{ vs. } 1/T \Rightarrow m = E_a / k$$

To convert into the log scale and  $1000/T$  commonly used in graphs, and then to convert into electron-volts rather than joules:

$$m = -E_a \times e^- / 2.303 \times 1000 \times k \quad (\text{Equation 2.21})$$

$$E_a (eV) = [(2.303 \times 1000 \times k) / e^-] \times m \quad (\text{Equation 2.22})$$

$$= 0.1986 \times m \quad (\text{Equation 2.23})$$

The simplification in equation 2.23 only holds for graphs where the temperature scale is  $1000/T$ .

### 2.4.1 Sample preparation for ac Impedance measurements

For impedance measurements the powders were pressed, uniaxially under  $\sim 1/2$  tonne of pressure, into pellets using a 3mm die, and sintered on Pt foil at 850 – 1100 °C, depending on composition, then slow-cooled to room temperature. The aim was to produce pellets with greater than 70 % of the theoretical density. Density measurements were made directly from the dimensions and mass of the pellet, and compared with the theoretical maximum.

$$D_{theoretical} = (FW \times Z \times 1.66) / V \quad (\text{Equation 2.24})$$

$$D_{sample} = \text{pellet mass} / \text{pellet volume} \quad (\text{Equation 2.25})$$

where:  $FW$  = Formula weight for the sample / g  
 $Z$  = unit cell contents  
 $V$  = unit cell volume / Å

The sample density can then be displayed as a percentage of the theoretical density.

For impedance measurements it was necessary to apply metal electrodes to each face of the pellet. In all cases, the first aim of the experiment was to produce an Arrhenius plot to show how conductivity varied with temperature. To this end, an organo-platinum paste was applied to one face of the pellet, and dried at 200 °C for 15 minutes. Small strips of platinum foil were attached using a small bead of paste, and the drying step repeated. This was repeated for the other face. The paste was then decomposed to leave the Pt metal electrodes by heating to 800 °C, and dwelling for 2 hours. Heating/cooling rates were set at 10 °C min<sup>-1</sup>. Note that pellets of Li-containing compositions were subsequently annealed at 500 °C for 3 days to ensure the oxygen contents were optimised. The pellet was then fixed to a conductivity ‘spaghetti’ jig and placed into a tube furnace for measurement at different temperatures.

Impedance measurements were recorded using an HP 4192A impedance analyser, in the frequency range of  $\sim 5$  Hz – 13 MHz. Data analysis was performed using the ZView software, with resistivity and capacitance values extracted from the plots of  $-Z''$  vs.  $Z'$  and  $M''$  vs. log frequency.

## **2.5 Electrochemical measurements**

There were two major steps in this process, which will be discussed in turn:

- (a) Battery construction, including:**
  - (i) Active electrode film preparation**
  - (ii) Electrolyte preparation**
  - (iii) Coin cell construction**
- (b) Battery Testing**

### **2.5.1 Battery Construction**

#### **2.5.1a Electrode film preparation**

All of the chemicals and materials used in the battery construction process are listed in Table 2.3.

In this study, an 80:10:10 wt% mix of active cathode material, carbon black (to improve conductivity) and PVdF (to act as a binder) was used. The materials were transferred to a small bottle, and a small amount (*ca.* 5 ml) of THF added to dissolve the PVdF binder and create a slurry of more consistency than water, but not too thick. This was stirred by a magnetic stirrer overnight to make a well-mixed suspension.

High purity aluminium foil was taped onto a very flat surface, scratched with an ordinary kitchen scouring pad (to roughen the surface and help adhesion of the cathode material), and then cleaned thoroughly with acetone. Thin films of cathode slurry were then deposited using a doctor blade (RK Print-Coat Instruments Ltd) technique; the height of the blade was set to 0.5 mm. Thick films tend to crack, thinner films tend to be patchy.

The deposited film was allowed to dry overnight, and then placed into a furnace to dry fully at 120 °C.

The dried film was pressed uniaxially under 1 tonne of pressure between two pieces of clean, smooth steel. A punching tool (designed in-house) was then used to punch cathode disks of ~ 13 mm diameter. The disks were then weighed and transferred to an

argon-filled glove box. It is necessary to know the mass of active material (typically 2 – 5 mg) to later calculate the performance, in particular the capacity, of the battery.

*Table 2.3 - Chemicals used in the various stages of battery construction*

<b>Chemical / Material</b>	<b>Supplier</b>	<b>Purity</b>
Carbon Super S (carbon black)	MMM	-
Poly(vinylidene fluoride) 'KYNAR' – PVdF (-CH <sub>2</sub> CF <sub>2</sub> ) <sub>n</sub> Average M <sub>w</sub> ~ 534,000	Aldrich	-
Tetrahydrofuran, anhydrous, C <sub>4</sub> H <sub>8</sub> O (THF)	Aldrich	99.9 %
Lithium hexafluorophosphate, LiPF <sub>6</sub>	Aldrich	99.99 + %
Propylene carbonate, C <sub>4</sub> H <sub>6</sub> O <sub>3</sub> (PC)	Aldrich	99.7 %
Lithium metal ribbon, 0.38 mm thick	Aldrich	99.9 %
Aluminium foil, 0.05 mm thick	Aldrich	99.8 %
Lithium manganate (III,IV) spinel (LiMn <sub>2</sub> O <sub>4</sub> )	Aldrich	“Electrochemical Grade”

### **2.5.1b Electrolyte preparation**

The electrolyte used in the battery testing was 1 M LiPF<sub>6</sub> dissolved in propylene carbonate. This preparation was conducted in the glove box under a dry argon atmosphere, to prevent water contamination.

### **2.5.1c Coin cell construction**

The various coin cell components, listed in Table 2.4, were stored in the glove box, under argon, at all times. These parts were obtained from the National Research Council, Canada, with the constructed coin cell designation 2325, *i.e.* the dimensions of the constructed cell were 23 mm in diameter and 2.5 mm thick.

All parts were laid out in advance. The plastic grommet was fitted around the anode cap, for use later.

*Table 2.4 - Coin cell components and their uses.*

<b>Component</b>	<b>Notes</b>
High purity chromium steel 'caps' (anode) and 'cases' (cathodes)	'External' parts
Spacers and springs	For internal pressure maintenance.
Li metal	Counter-electrode
Whatman glass fibre separators	Used to separate cathode and anode, and for 'storing' the liquid electrolyte.
Electrolyte	1 M LiPF <sub>6</sub> in PC
Plastic grommets	Ring to fit around anode cap, to prevent short circuit.

The electrode disk was placed in the centre of the cathode 'base' piece. The separator was then placed on top of this disk. Using a pipette, 7 – 8 drops of electrolyte were soaked into the separator, which was left moist but not over-wet. A 1.69 cm<sup>2</sup> disk of lithium metal was cut from the ribbon using a hand tool (made in-house), and placed on top of the separator with tweezers. Any metallic contact between the Li metal (or parts placed on subsequently) and the lower parts would cause a short circuit and cell failure. A spacer and a conical spring were placed on top of the pile, and then the anode cap slotted into place with a little pressure, ensuring that the cap was sitting level. After this point, the cell was only handled with plastic tweezers (to avoid short-circuiting). The cell was crimped shut with a pneumatic closing tool (also supplied by the National Research Council, Canada), operating under high pressure (3000 lbs) argon gas. The cell could then be removed from the glove box for testing in a normal atmosphere.

A schematic diagram showing the order of construction of the 2325 coin cells is presented in Figure 2.5.

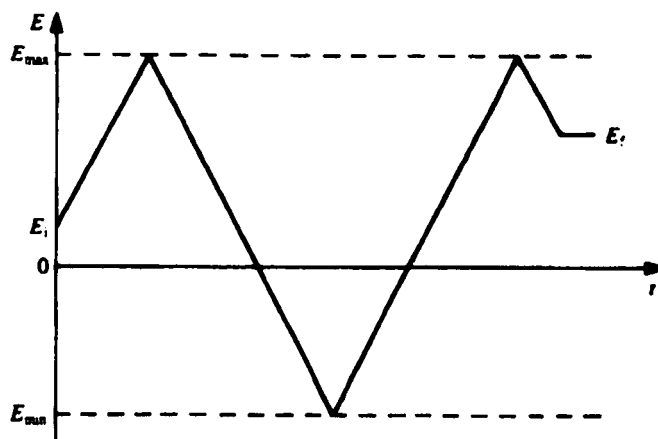
## 2.5.2 Battery testing

Battery testing was conducted on a Bio-Logic VMP (Variable Multichannel Potentiostat) distributed by Perkin-Elmer. This instrument allowed for the separate testing of up to 8 cells at any given time.

### 2.5.2a Cyclic Voltammetry

Cyclic voltammetry (CV) is a potentiodynamic technique often used for studying electrode processes<sup>9</sup> in lithium-ion battery systems. This involves recording how current intensity in a cell changes as the potential changes, within a chosen potential 'window' (Figure 2.6), at a fixed scan rate. Upon reaching the chosen potential limit the sweep direction is reversed (hence 'cyclic' voltammetry). Typical scan rates used are in the order of  $0.1 - 0.25 \text{ mV.s}^{-1}$ . Slow scans are necessary to allow for the diffusion of ionic species in the active materials and the kinetics of the electrochemical reactions taking place.

*Figure 2.6 – Schematic diagram showing variation of applied potential with time.  $E_{max}$  and  $E_{min}$  denote the upper/lower limits of the potential 'window'.  $E_i$  and  $E_f$  mark the initial and final potential. The scan rate can be calculated from  $|dE/dt| = v$ . From Brent and Brent.<sup>9</sup>*



A number of sequential cycled sweeps can be performed to study the reversibility of the electrode process(es) of interest.

The main use of cyclic voltammetry in Li-ion battery research is to identify whether a material is electrochemically active. If a material is found to be active, the potential of

## 2.5.2b Galvanostatic Cycling with Potentiostatic Limitation (GCPL)

In the GCPL technique, a constant current is applied across the cell while the variation in cell potential is recorded. To know what current rate a cell is being (dis)charged at, it is necessary first to know the theoretical capacity for the cell.

$$Q_{To} = (e \cdot F) / 3.6 \times M \quad (\text{Equation 2.27})$$

This can be extended for a practical cell if the sample mass is known:

$$Q_{To} = (e \cdot F \cdot m) / 3.6 \times M \quad (\text{Equation 2.28})$$

where,  $e$  = number of electrons involved in complete reaction

$$F = \text{Faraday's constant} / 9.469 \times 10^4 \text{ C.mol}^{-1}$$

$$M = \text{molar mass of active material} / \text{g.mol}^{-1}$$

$$m = \text{sample mass} / \text{g}$$

It should also be noted that 3.6 Coulomb = 1 mA.h, hence the correction factor in equations 2.27 and 2.28.

So  $Q_{To}$ , the maximum theoretical capacity that would be observed upon full lithium deintercalation, has the units mA.h.g<sup>-1</sup>. Using equation 2.27, we can calculate the theoretical capacity for LiMn<sub>2</sub>O<sub>4</sub> to be ~ 148 mA.h.g<sup>-1</sup>. The theoretical reaction time can then be worked out simply from Equation 2.29. Note that  $t$  is time, in hours.

$$Q_T = I \times t \quad (\text{Equation 2.29})$$

The system used to measure charge/discharge is denoted by different multiples of C, where 1C is designated as the rate required to intercalate or deintercalate one lithium ion in one hour, i.e.  $Q_T = I$ . If a battery was constructed containing 10mg of LiMn<sub>2</sub>O<sub>4</sub> as the active material, for example, then we could calculate that to discharge the battery at the C-rate a current of 1.48 mA would have to be applied. A rate of 1C is very fast – it should be noted a more typical rate for studies would be C/10, i.e. (de)intercalation of 1 lithium ion in 10 hours.

To run the experiment, this constant current (hence 'galvanostatic') is applied over a chosen potential window (hence 'potential limitation'). This range is typically somewhere between 0 and 5.5 V, and can be chosen after performing cyclic

voltammetry to help identify regions of electrochemical activity. For example, if the active material under study was  $\text{LiMn}_2\text{O}_4$  and the region of interest was centred around the electrochemical processes occurring at  $\sim 4$  V, then a potential window of 3.5 – 4.5 V could be chosen. This flexibility can be very useful since some charge/discharge processes can be very time-consuming. There are also further concerns currently with regards to charging cells to high voltages. The current generation of polymer electrolytes, like propylene carbonate, are widely used but begin to suffer under the highly oxidative conditions at high voltage. This can cause a large loss of capacity and can contribute to capacity fading. This is a problem that is hindering the study of high voltage materials such as the Co- and Fe-doped  $\text{LiMn}_2\text{O}_4$ , where electrochemical activity happens at *ca.* 5 V.

The software charged with the running of the VMP equipment outputs the data in the form of graphs of potential against time (as in Figure 2.8). These data are exported to a spreadsheet package, such as Microsoft Excel, where the capacity related to any plateaux can easily be worked out from the  $Q = I \times t$  relationship. The capacity data can then be presented for both charging and discharging processes.

It is then possible to plot the data for numerous cycles performed in succession to study the cyclability of the electrode materials. This can be presented in plots of capacity against cycle number (as in Figure 2.9), where any issues regarding capacity fading are immediately obvious.

The data presented in Figures 2.8 and 2.9 show the cycling performance for a cell made using commercially-supplied  $\text{LiMn}_2\text{O}_4$  as the active cathode material. The raw data in Figure 2.8 show that the cell is cycling well in the 3.5 – 4.4 V window, with closely-separated plateaux indicating electrochemical activity on charging at  $\sim 4.1$  V. The data show that this activity is reversible on discharge at a slightly lower voltage,  $\sim 3.9$  V, and that the reversibility over a number of cycles is reasonably good. By extracting the capacity data for the charging plateaux, we can see how the capacity changes on cycling; a noticeable drop occurs after the first cycle, but then there is only an 11 % drop in charging capacity over the next 8 cycles.

## 2.6 References

- (1) Kawai, H.; Nagata, M.; Kageyama, H.; Tukamoto, H.; West, A. R. *Electrochimica Acta* **1999**, *45*, 315.
- (2) Kawai, H.; Nagata, M.; Tukamoto, H.; West, A. R. *Journal of Materials Chemistry* **1998**, *8*, 837.
- (3) Kawai, H.; Nagata, M.; Tukamoto, H.; West, A. R. *Electrochemical and Solid-State Letters* **1998**, *1*, 212.
- (4) Mandal, S.; Rojas, R. M.; Amarilla, J. M.; Calle, P.; Kosova, N. V.; Anufrienko, V. F.; Rojo, J. M. *Chemistry of Materials* **2002**, *14*, 1598.
- (5) Reeves, N.; Kirk, C. A.; West, A. R. *Journal of Materials Chemistry* **2001**, *11*, 249.
- (6) Klug, H. P.; Alexander, L. E. *X-ray diffraction procedures*, 2nd ed.; John Wiley & Sons: London, 1974.
- (7) Irvine, J. T. S.; Sinclair, D. C.; West, A. R. *Advanced Materials* **1990**, *2*, 132.
- (8) West, A. R.; Sinclair, D. C.; Hirose, N. *Journal of Electroceramics* **1997**, *1*, 65.
- (9) Brett, C. M. A.; Brett, A. M. O. *Electrochemistry: Principles, Methods and Applications*; Oxford University Press: Oxford, UK, 1996.
- (10) Gummer, R. J.; Thackeray, M. M. *Journal of the Electrochemical Society* **1994**, *141*, 1178.
- (11) Zhang, S. S.; Jow, T. R. *Journal of Power Sources* **2002**, *109*, 172.

## Chapter 3

### Phase relations in the cobalt oxide – manganese oxide system

#### 3.1 Literature review

The phase diagram for the cobalt oxide – manganese oxide system in air (Figure 3.1a) was reported by Aukrust and Muan.<sup>1</sup> Thermogravimetry and XRD on quenched samples were applied to study the extent and stability of  $(\text{Co,Mn})_3\text{O}_4$  solid solutions with the spinel structure,<sup>2</sup> and  $(\text{Co,Mn})\text{O}$  rock salt solid solutions at high temperature. The authors reported a complete solid solution of compositions with the cubic (space group  $\text{Fd}\bar{3}\text{m}$ ) spinel structure; however, this could not be preserved in quenched samples containing more than  $\sim 33\%$   $\text{Mn}_3\text{O}_4$  since quenched phases in this compositional range were found to have a tetragonal  $\text{Mn}_3\text{O}_4$  spinel type structure (space group  $\text{I4}_1/\text{amd}$ ).

Irani *et al.*<sup>3</sup> (and to a lesser extent Dorris & Mason<sup>4</sup>), conducted high temperature XRD on various manganates, including  $\text{Mn}_3\text{O}_4$  and  $\text{CoMn}_2\text{O}_4$ . These spinel phases exhibited a tetragonal to cubic transition at elevated temperatures; for  $\text{CoMn}_2\text{O}_4$  (Figure 3.1b), this transition was shown by DTA to occur at  $900\text{ }^\circ\text{C}$ .

Naka *et al.*<sup>5</sup> and de Vidales *et al.*<sup>6</sup> studied the phases obtained for  $\text{Co}_{3-x}\text{Mn}_x\text{O}_4$  in air; in samples reacted at  $1000\text{ }^\circ\text{C}$ , both identified a cubic spinel single phase for the compositional range  $0.0 \leq x \leq 1.3$ , and a tetragonal spinel for  $1.9 \leq x \leq 3.0$ . When samples with  $1.4 \leq x \leq 2.0$  were cooled slowly to room temperature a mixture of cubic and tetragonal spinels was found; however, only the tetragonal spinel was observed in samples quenched from  $1000\text{ }^\circ\text{C}$ . Single phase cubic spinels were observed in this region by high temperature XRD (at temperatures  $> 750\text{ }^\circ\text{C}$ ). A rapid cubic  $\rightarrow$  tetragonal transition occurs on cooling. Quenching is too slow to prevent this rapid transition. A high temperature cubic ‘NaCl’-type phase was reported for  $0.0 \leq x \leq 0.9$  at  $1000\text{ }^\circ\text{C}$ .

Figure 3.1a – Phase relations in the  $\text{Co}_3\text{O}_4 - \text{Mn}_3\text{O}_4$  system in air.<sup>7</sup>

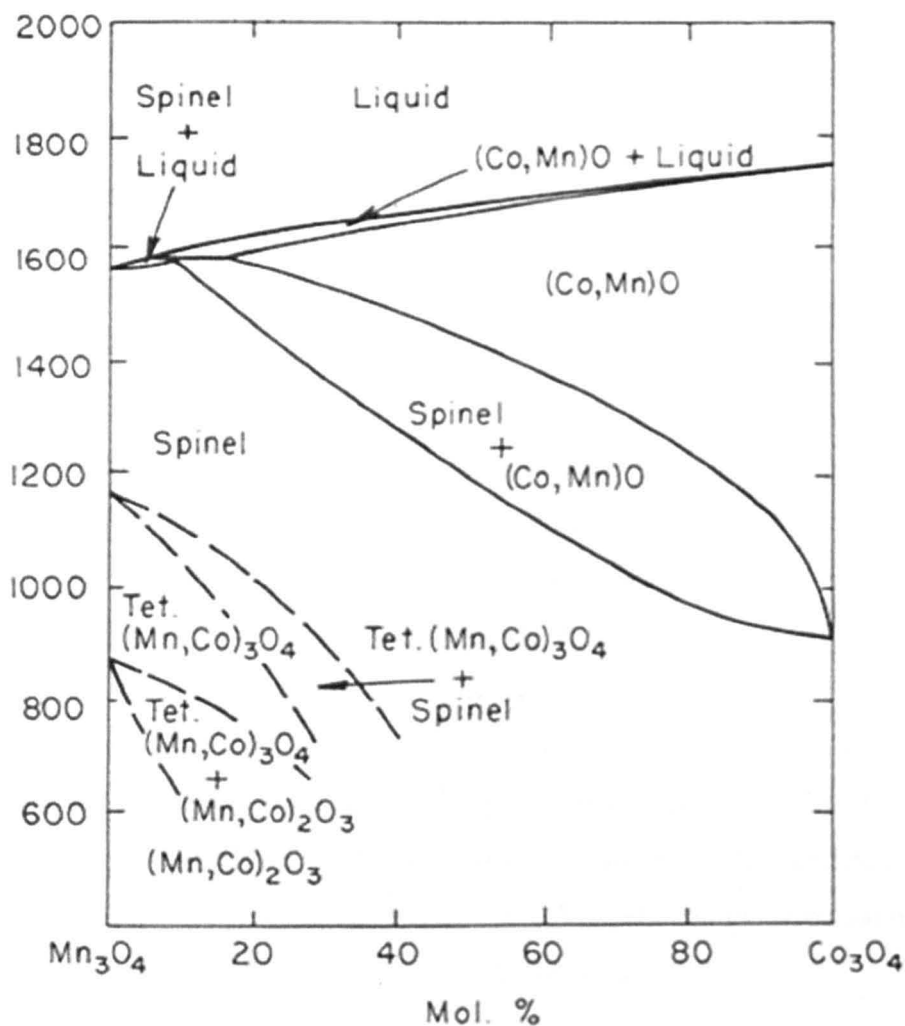
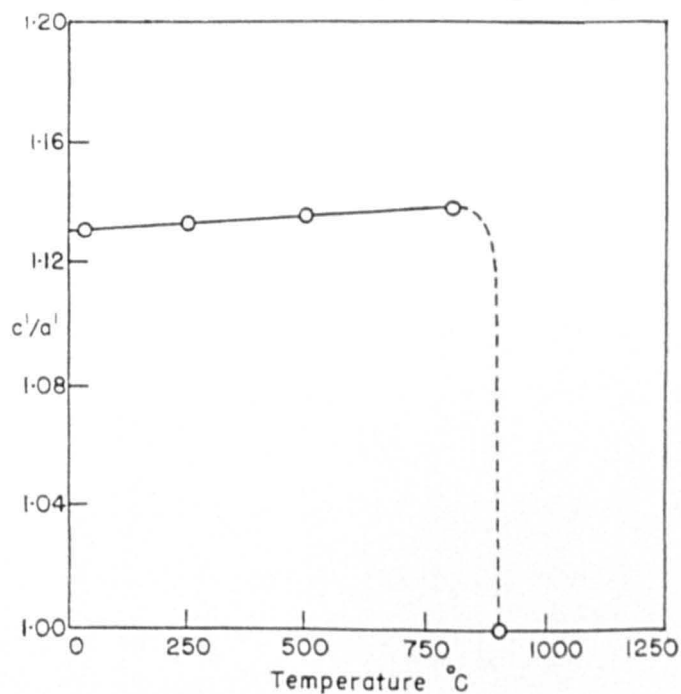


Figure 3.1b – Evolution of unit cell dimensions with temperature for  $\text{CoMn}_2\text{O}_4$ .<sup>3</sup>



The thermal behaviour of compositions with  $0.0 \leq x \leq 1.0$  was studied by de Vidales *et al.*,<sup>8</sup> who report that single phase Co-Mn oxides with rock salt structure are formed in air between 1100 and 1300 °C, in agreement with Aukrust & Muan. Reported TG work on these phases is limited. Most authors do not discuss the possibility of oxygen non-stoichiometry. Aukrust & Muan comment solely on the existence and stability limits of the various phases. Irani *et al.*<sup>3</sup> studied tetragonal – cubic phase transitions in a range of  $MMn_2O_4$  compounds (M = Mn, Mg, Zn and Co) by DTA, but did not study the rock salt phase or any oxygen non-stoichiometry.

Manganese cobaltites are noted<sup>8,9</sup> to be of possible interest as oxide ion conductors, catalysts and NTC thermistors. They also exhibit a CMR effect at low temperatures.<sup>10</sup> Recent work has attempted to improve these properties by reducing particle size or doping with lithium. Low temperature techniques reported by de Vidales *et al.*<sup>11</sup> have produced cobalt manganate powders with mean particle size as low as 11 nm, yielding high surface area (44 m<sup>2</sup>/g) materials. The preparation of  $LiCo_yMn_{2-y}O_4$  ( $0 \leq y \leq 0.66$ ) spinel phases, with small particle size (250 – 400 Å), from reaction of  $Co_xMn_{3-x}O_4$  ( $0.00 \leq x \leq 0.99$ ) precursors<sup>12</sup> with  $LiOH \cdot H_2O$  was also reported. Electrochemical studies were limited to a maximum charging voltage of 4.5 V; the composition range studied includes the 5 V cathode materials reported by Kawai *et al.*<sup>13</sup>

The objective of the work presented here has been to study the Co-Mn-O phase diagram and determine more clearly the extent of spinel and rock salt solid solutions at various temperatures.

## 3.2 Experimental

Samples on the binary join  $\text{Co}_{3-x}\text{Mn}_x\text{O}_4$ , with  $0.00 \leq x \leq 3.00$ , were prepared by the solid state route. The reagents used were cobalt nitrate hexahydrate and manganese acetate. Samples were heated slowly from 80 to 800 °C, as described in Chapter 2, and reacted at 800 °C for 3 days, with intermittent regrinding, followed by annealing at 500 °C for 3 days (to ensure parity in samples studied across the ternary phase diagram,  $\text{Li}_2\text{O}-\text{CoO}_x-\text{MnO}_y$ ). This annealing step made little or no difference to the XRD data.

Both as-prepared samples and samples quenched from elevated temperatures (up to ~ 1450 °C) were characterised by XRD. Lattice parameter data were obtained using least squares refinement of XRD peaks corrected by Si internal standards.

Combined TG and DTA were conducted on samples of composition  $\text{Co}_{3-x}\text{Mn}_x\text{O}_4$ , using Stanton-Redcroft TG-DTA equipment, in flowing air, with programmed heating/cooling rates of 10 °C min<sup>-1</sup>.

## 3.3 Results

### 3.3.1 X-ray diffraction

A range of compositions with  $0.00 \leq x \leq 3.00$  was prepared. XRD patterns were obtained for each sample, and three distinct compositional regions were identified:

- A single cubic spinel (space group Fd3m) phase for  $0.00 \leq x \leq 1.30$ .
- A mixture of cubic and tetragonal (space group I4<sub>1</sub>/amd) spinels for  $1.30 \leq x \leq 2.16$ .
- A mixture of bixbyite (M<sub>2</sub>O<sub>3</sub> phase, space group Ia-3) and tetragonal spinel for  $x \geq 2.30$ .

Lattice parameters were refined for each phase, where possible, and are presented in Table 3.1. Comparison of the unit cell volumes of cubic and tetragonal spinels can be achieved by doubling the tetragonal unit cell volume; the variation of lattice parameters for the cubic and tetragonal spinel phases with composition,  $x$ , is shown in Figures 3.2(a) and (b).

An expansion of the lattice occurs with the replacement of Co by Mn. However, there is a clear inflexion in the lattice parameter data (Figure 3.2(b)) at *ca.*  $x = 0.30$ , *i.e.*  $a$  values for samples with compositions  $\leq 0.30$  were higher than expected.

When  $x > 1.30$ , the cubic spinel lattice parameter became constant, within errors. A tetragonal spinel phase was also observed, indicating that the cubic spinel solid solution limit in samples prepared at 800 °C with subsequent annealing at 500 °C was at  $x = 1.30$  (Co<sub>1.70</sub>Mn<sub>1.30</sub>O<sub>4</sub>).

The lattice parameter for the tetragonal spinel is also relatively unchanged over the compositional range  $1.30 < x < 2.16$ . The cubic spinel phase was observed to  $x = 2.16$ , but data were not of sufficient intensity / quality to allow refinement of lattice parameters.

**Table 3.2** – Lattice parameters for observed phases. \* indicates that the phase was present, but lattice parameters could not be refined.

x in Co <sub>3-x</sub> Mn <sub>x</sub> O <sub>4</sub>	Cubic Spinel		Tetragonal spinel			Bixbyite	
	<i>a</i> / Å	Cell volume / Å <sup>3</sup>	<i>a</i> / Å	<i>c</i> / Å	Cell volume / Å <sup>3</sup>	<i>a</i> / Å	Cell volume / Å <sup>3</sup>
0.00	8.0838 (19)	528.26 (21)	-	-	-	-	-
0.10	8.0956 (13)	530.58 (15)					
0.20	8.1140 (11)	534.20 (12)					
0.30	8.1265 (10)	536.67 (12)	-	-	-	-	-
0.60	8.1808 (10)	547.50 (12)	-	-	-	-	-
0.90	8.2386 (9)	559.18 (11)	-	-	-	-	-
1.00	8.2582 (10)	563.20 (12)	-	-	-	-	-
1.30	8.3127 (6)	574.41 (7)	-	-	-	-	-
1.33	8.3125 (21)	574.4 (3)	*	*	*	-	-
1.40	8.3110 (5)	574.0 (6)	*	*	*	-	-
1.50	8.3103 (17)	573.91 (20)	5.7195 (12)	9.254 (4)	302.72 (13)	-	-
1.75	8.3115 (11)	574.17 (13)	5.7183 (8)	9.2621 (21)	302.86 (7)	-	-
2.00	8.307 (6)	573.1 (7)	5.719 (7)	9.265 (2)	303.03 (6)	-	-
2.16	*	*	5.7243 (21)	9.322 (3)	305.46 (7)	-	-
2.30	-	-	5.7308 (5)	9.3314 (12)	306.46 (4)	*	*
2.46	-	-	5.7221 (13)	9.318 (4)	305.09 (11)	9.4008 (9)	830.80 (14)
2.60	-	-	5.7336 (8)	9.3552 (24)	307.54 (7)	9.3992 (19)	830.37 (21)
3.00	-	-	-	-	-	9.4071 (11)	832.46 (17)

When samples of two compositions, with  $x = 0.00$  and  $0.30$ , were heated to  $\sim 900$  °C the low temperature cubic spinel structure was maintained. On heating  $x = 0.00$  above  $1000$  °C, only a primitive rock salt pattern was observed in XRD traces. At intermediate temperatures, a mixture of cubic spinel and rock salt patterns was observed. Refined lattice parameters for  $\text{Co}_3\text{O}_4$  ( $x = 0.00$ ) are presented in Table 3.2; neither the spinel nor the rock salt lattice parameter changes with increasing temperature, suggesting that the stoichiometry of the phases does not change upon heating.

For  $x = 0.30$ , the cubic spinel was maintained to  $\sim 964$  °C. A simple rock salt pattern was observed only for the sample quenched from  $1387$  °C; a mixture of spinel and rock salt phases was observed at intermediate temperatures. Lattice parameter data for all quenched samples are presented in Table 3.3. The cubic spinel lattice parameter remains unchanged on heating to at least  $965$  °C, and only changes once the two-phase region is entered. In the sample quenched from  $1192$  °C the spinel had tetragonal symmetry.

Assuming that upon heating the composition is passing through a two phase region in the phase diagram, and that no oxygen non-stoichiometry can occur for either the spinel or rock salt phases at this composition, the lattice parameter data can be used to estimate the compositions of phases observed in quenched samples using Figure 3.2(b) as a calibration. A crude estimate of the rock salt composition can be made knowing the lattice parameters of the high temperature rock salts  $\text{CoO}$  and  $\text{Co}_{2.70}\text{Mn}_{0.30}\text{O}_3$ .

*Table 3.2 – Lattice parameter data for  $\text{Co}_3\text{O}_4$  quenched from a series of temperatures. Estimated standard deviations given in parentheses.*

Treatment temperature / °C	$a_{\text{spinel}}$ / Å	$a_{\text{rock salt}}$ / Å	Cell volume / Å <sup>3</sup>	
			Spinel	Rock salt
500	8.0838 (19)	-	528.26 (21)	-
853	8.0848 (7)	-	528.45 (6)	-
977	8.0826 (2)	4.2602 (4)	528.02 (21)	77.319 (12)
1003	-	4.2611 (5)	-	77.368 (17)
1095	-	4.2611 (4)	-	77.366 (13)

**Table 3.3** – Lattice parameter data for  $\text{Co}_{2.70}\text{Mn}_{0.30}\text{O}_4$  quenched from various temperatures, and suggested formulae for observed phases assuming no oxygen non-stoichiometry occurs.

Treatment temperature / °C	$a_{\text{spinel}}$ / Å	$a_{\text{rock salt}}$ / Å	Suggested composition, $x$	
			Spinel	Rock salt
500	8.1265 (10)	-	0.30	-
965	8.1267 (14)	-	0.30	-
1023	8.2292 (10)	4.2609 (4)	0.83	0.00
1093	8.2671 (11)	4.263 (4)	1.04	0.10
1387	-	4.2691 (16)	-	0.30

Samples of composition  $0.60 \leq x \leq 1.30$  were single phase cubic spinels when annealed at 500 °C. On heating above ~ 1000 °C a two phase mixture was identified for all compositions; XRD traces indicated the presence of a spinel phase and a rock salt phase. The spinel phase had cubic symmetry at lower temperatures (*i.e.* as the sample entered the two-phase region), and tetragonal symmetry at higher temperatures. No single phase rock salt was obtained for any composition in this range. It should also be noted that as the quench temperature was increased, the intensity of the XRD peaks attributed to the spinel phase decreased, while those indexed on the rock salt phase increased.

At  $x = 1.33$ , a mixture of cubic and tetragonal spinel phases was observed in samples annealed at 500 °C; the cubic spinel has stoichiometry ~  $\text{Co}_{1.70}\text{Mn}_{1.30}\text{O}_4$ . In samples quenched from ~ 800 to 1000 °C only a single cubic spinel phase was observed. The refined lattice parameters for this phase are presented in Table 3.4; a small increase, in excess of the errors, is observed on heating to 800 °C. The lattice parameter then becomes constant, within errors, to 986 °C.

**Table 3.4** – Variation in cubic spinel lattice parameter for annealed (500 °C) and quenched  $\text{Co}_{1.62}\text{Mn}_{1.33}\text{O}_4$

Treatment temperature / °C	$a_{\text{spinel}}$ / Å
500	8.3125 (21)
800	8.3191 (18)
864	8.3193 (21)
986	8.3164 (14)

The tetragonal lattice parameters change with starting composition;  $a$  decreases and  $c$  increases as Mn content,  $x$ , increases.

Cell volume data for  $Mn_2O_3$  and  $Mn_3O_4$  are presented in Table 3.6. The unit cell of body-centred  $Mn_2O_3$  contains 16 formula units, *i.e.*  $Z = 16$ . Comparison with the tetragonal structure, where  $Z = 4$ , can be achieved by dividing cell volume data for  $Mn_2O_3$  by 4. This gives an equivalent unit cell<sup>Volume</sup> for  $Mn_2O_3$  of  $\sim 208 \text{ \AA}^3$ , *i.e.* smaller than tetragonal  $Mn_3O_4$  ( $\sim 314 \text{ \AA}^3$ ), despite the loss of oxygen ions from the structure in transforming to the spinel.

XRD data for samples quenched from 995 – 1246 °C all showed a tetragonal spinel pattern, and were indexed on the  $I4_1/amd$  space group. Both cell volume and the degree of tetragonal distortion remained constant, within errors, as temperature increased to 1135 °C. A small drop in cell volume was observed on heating to 1246 °C.

**Table 3.6 - Lattice parameter data for  $Mn_3O_4$  quenched from a series of temperatures. Estimated standard deviations given in parentheses. Note  $a' = a\sqrt{2}$ .**

Temperature / °C	$a_{\text{bixbyite}}$ / Å	$a_{\text{tetragonal}}$ / Å	$c_{\text{tetragonal}}$ / Å	$c/a'$ ratio	Cell volume / Å <sup>3</sup>
500	9.4071 (11)	-	-	-	832.47 (17)
586	9.4094 (20)	-	-	-	833.1 (3)
745	9.4087 (15)	-	-	-	832.9 (3)
904	9.4088 (19)	-	-	-	832.9 (3)
995	-	5.7616 (3)	9.4705 (8)	1.162	314.37 (3)
1056	-	5.7620 (11)	9.4710 (30)	1.162	314.46 (10)
1135	-	5.7620 (4)	9.4681 (9)	1.162	314.35 (3)
1246	-	5.7622 (6)	9.4651 (16)	1.162	314.27 (5)

Single phase spinel (with either cubic or tetragonal symmetry) can be prepared for any composition in the range  $0.00 \leq x \leq 3.00$ . Figure 3.5 shows the variation in spinel unit cell volume with composition for  $0.00 \leq x \leq 3.00$ . The data appear to deviate from linearity, with possible inflexions observed at  $x = 1.30$  and  $2.30$ . Figure 3.6 shows the variation with composition of the  $c/a'$  tetragonal distortion parameter for the single phase tetragonal spinels. There is a possible inflexion at  $\sim x = 2.30$ .

atoms) was observed on further heating to  $\sim 1470$  °C; this was fully reversible on cooling to 1200 °C.

In samples with compositions  $x = 0.00$  and 0.30, a weight loss approaching 1 oxygen atom was observed in the TG data on heating.  $\text{Co}_3\text{O}_4$  (*i.e.*  $x = 0.00$ ) shows a rapid single-stage weight loss (Figure 3.7), over a 40 °C period, between  $\sim 917$  °C and  $\sim 957$  °C. This large weight loss ( $\sim 6.36$  % of sample mass) approximates to  $\sim 0.95$  oxygen atoms. The weight loss was fairly reversible on cooling ( $\Delta W = 0.43$  %).

$\text{Co}_{2.70}\text{Mn}_{0.30}\text{O}_4$  ( $x = 0.30$ ) also shows a one-stage weight loss on heating, of  $\sim 6.30$  % ( $\sim 0.97$  O atoms), starting at  $\sim 920$  °C. A plateau in the TG data is observed at  $\geq 1200$  °C. The  $\Delta W$  (degree of weight loss on heating that was not regained on subsequent cooling) observed in the TG data between heating and cooling was 2.71 %, much more than was observed for  $\text{Co}_3\text{O}_4$ . XRD on the sample after thermal analysis indicated a three-phase mixture: two cubic spinel phases and a rock salt phase were present. Comparison of the lattice parameters for the two spinels with Figure 3.4 gives compositions of  $\sim \text{Co}_3\text{O}_4$  (8.0820 (9) Å) and  $\text{Co}_{2.04}\text{Mn}_{0.96}\text{O}_4$  (8.2526 (13) Å). The lattice parameter of the rock salt phase (4.2599 (1) Å) matches that of CoO. After subsequent annealing at 800 °C, single phase cubic spinel was re-obtained.

For the range of compositions with  $0.60 \leq x \leq 2.46$ , TG data indicated a weight loss starting at temperatures  $> 1000$  °C. The temperature at which this loss started increased with Mn content. In all cases weight loss was equivalent to less than 1 oxygen atom. However, no plateaux were observed in the TG data at high temperatures ( $> 1000$  °C) within experimental limits ( $\sim 1473$  °C). Instead, weight loss was still continuing at this temperature, with an inflexion in the TG data for samples with  $x < 1.75$  after loss of  $\sim 0.75$  oxygen atoms. A mixture of spinel and rock salt phases was observed in XRD patterns of samples in this compositional range quenched from up to  $\sim 1400$  °C, as discussed in section 3.3.2.

### 3.3.4 DTA data

DTA data were recorded for a range of compositions, where  $0.00 < x < 3.00$ . These data are presented, along with the TG data discussed in section 3.3.3, in the appendix to this chapter (Figures 3.7 – 3.22).

DTA traces for all compositions studied showed at least one DTA peak; the temperatures of all DTA features are listed in Table 3.7, and plotted in Figure 3.23.

Samples with composition,  $x, \leq 0.30$  showed a single sharp DTA peak. As Mn content increased to  $x = 1.30$  this peak was still observed but with significant broadening. Peak onset/end temperatures are listed under ‘Peak 1’ in Table 3.7.

This broadened ‘Peak 1’ was observed in samples with composition increasing up to  $x = 2.46$ . However for compositions with  $x \geq 1.33$ , a second DTA peak, ‘Peak 2’ emerges at low temperatures. Peak maximum temperatures are listed in Table 3.7 since onset/end temperatures were not clearly defined.

For samples with composition  $2.46 \leq x \leq 3.00$ , another DTA peak emerges at temperatures intermediate to Peaks 1 and 2; peak maximum temperatures for this ‘Peak 3’ are given in Table 3.7.

The data in Figure 3.24 show that all DTA peaks move to higher temperatures as Mn content increases.

## 3.4 Discussion

### 3.4.1 Phase diagram construction

The completed phase diagram for the cobalt oxide – manganese oxide binary join is presented in Figure 3.25. After reaction at 800 °C, samples were annealed at 500 °C; therefore this temperature is taken as the thermal minimum in the presentation of the phase diagram.

A combination of the XRD, TG and DTA data confirms that  $\text{Co}_3\text{O}_4$  undergoes a spinel to rock salt transition at  $\sim 937$  °C, with the associated loss of 1 oxygen atom. An increase in equivalent volume occurs in moving from  $\text{Co}_3\text{O}_4$  (*ca.*  $528.2 \text{ \AA}^3$ ) to  $\text{CoO}$  (*ca.*  $618.9 \text{ \AA}^3$ ). This can be explained by the reduction of  $\text{Co}^{3+}$  (ionic radius =  $0.610 \text{ \AA}$ ) in the spinel to the larger  $\text{Co}^{2+}$  cation ( $0.735 \text{ \AA}$ )<sup>16</sup> in the rock salt.

A transition from  $\text{Mn}_2\text{O}_3$  to  $\text{Mn}_3\text{O}_4$  is also clearly observed in XRD, TG and DTA data. The TG data indicate a weight loss ( $\sim 3.28 \%$ ), with an associated DTA feature at  $\sim 950$  °C, that is in good agreement with the expected value ( $3.38 \%$ ). Only the single  $\text{Mn}_2\text{O}_3$  ‘bixbyite’ phase is observed in samples quenched from below 950 °C; in quenches from higher temperatures, however, the tetragonal spinel pattern is observed. A DTA peak at 1198 °C infers a transition to the cubic spinel phase; on cooling the reverse transition must occur rapidly, and the cubic phase cannot be stabilised to room temperature by quenching.

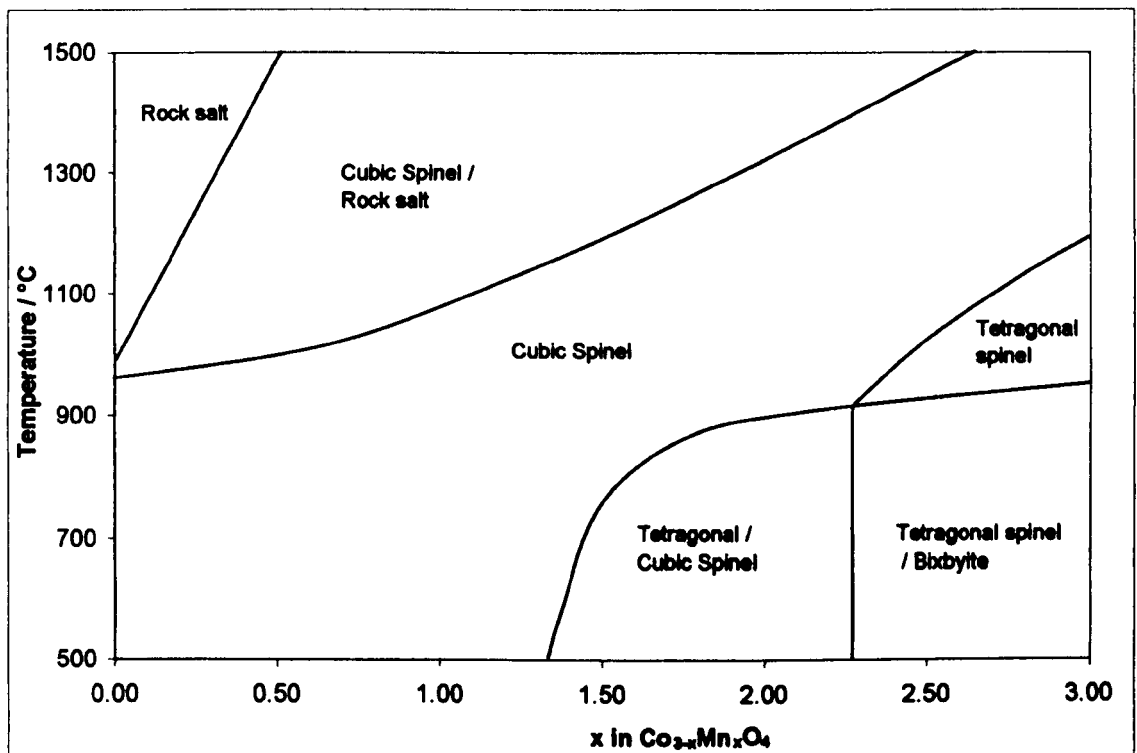
A two phase region, with tetragonal spinel and bixbyite phases present, was identified for  $x \geq 2.30$  at 500 °C. The transition from this region to single phase tetragonal spinel on heating involves a weight loss; zero weight loss should occur when the bixbyite concentration is zero. Extrapolation of the data in Figure 3.22 gives the compositional limit of this two-phase region to be  $x = 2.28 (\pm 0.01)$ , in agreement with XRD data.

The consumption of the bixbyite phase at  $\sim 930$  °C in cobalt-doped samples (*i.e.* with  $x \geq 2.30$ ) leads to the formation of single phase tetragonal spinels, as observed in XRD traces of samples quenched from  $\sim 1000$  °C. The DTA data for ‘Peak 3’ show these compositions exhibiting a transition to the cubic spinel at higher temperatures, forming a clear pattern (see Figure 3.23) with the end member  $\text{Mn}_3\text{O}_4$ .

In samples annealed at 500 °C, a range of compositions with  $x \leq 1.30$  formed a spinel solid solution, with lattice parameter,  $a$ , increasing as Mn content increased. A two phase region, with cubic and tetragonal spinels present, was identified for samples with composition  $1.33 \geq x \geq 2.16$ . The DTA data show, in agreement with XRD on quenched samples, that a transition occurs on heating to give single phase spinels for the whole of this compositional range,  $1.33 \geq x \geq 2.16$ . It is proposed that this spinel actually has the cubic structure, but reverts to the tetragonal spinel on cooling. A cubic spinel solid solution forms for the entire compositional range studied.

A limited rock salt solid solution area was also found at high temperatures. TG and XRD data on quenched samples were used to identify the compositional limits of this region. DTA data were insensitive to the end of the spinel  $\rightarrow$  rock salt transition and suggested a much greater rock salt compositional range, *i.e.* the peak end temperatures presented in Figure 3.24 would denote the lower solvus of this solid solution area and rock salt phases would have been easily stabilised to room temperature by quenching. However, no single phase rock salts were identified at any temperature for  $x \geq 0.60$ .

Figure 3.25 – The  $\text{Co}_{3-x}\text{Mn}_x\text{O}_4$  pseudo-binary phase diagram.



The tetragonal spinel / bixbyite  $\rightarrow$  tetragonal spinel reaction was found to be irreversible on cooling, under the conditions used here. All other reactions encountered

were found to be fully reversible after an annealing step at low temperature (*e.g.* 3 days at 700 °C).

### 3.4.2 Deviations from Vegard's Law in $\text{Co}_{3-x}\text{Mn}_x\text{O}_4$ spinels ( $x \leq 1.30$ )

The lattice parameter (Figure 3.2(a)) and cell volume (Figure 3.2(b)) data for Co-rich spinels, with composition  $0.00 \leq x \leq 1.30$ , show a slight downward deviation from linear Vegard's law behaviour which indicates that intermediate compositions have a slightly smaller unit cell than expected. This may be attributed to an extra stability of these intermediate compositions. Since there are two sets of cation sites available, two different cations and mixed oxidation states, it is difficult to quantify the reasons for this extra stability.

This non-linear behaviour has not been reported elsewhere; only Naka<sup>5</sup> *et al.* discuss lattice parameter data for cubic  $\text{Co}_{3-x}\text{Mn}_x\text{O}_4$  spinels, but only at 1000 °C in different atmospheres; these data were calculated from (511) or (400) reflections and showed an approximately linear dependence on composition.

### 3.4.3 Substitution mechanisms in $\text{Co}_{3-x}\text{Mn}_x\text{O}_4$ spinels

The spinel lattice parameter data in Figure 3.5 do not fit a straight line well. Small inflexions were observed at  $\sim x = 1.40, 1.75$  and  $2.30$  – either side of which the data curve slightly – suggesting deviations from Vegard's Law behaviour.

The lattice expansion observed for the cubic spinel phase is to be expected since the cationic radii of  $\text{Mn}^{2+}$  and  $\text{Mn}^{3+}$  are larger than  $\text{Co}^{2+}$  and  $\text{Co}^{3+}$  respectively. The cubic spinel undergoes a rapid transition on cooling to give the tetragonal spinel for  $x \geq 1.40$ . Since the cooperative Jahn-Teller effect requires roughly half of the transition metal ions to be of the active species for a distortion to occur, all of the Mn in  $\text{Co}_{1.4}\text{Mn}_{1.6}\text{O}_4$  must be Jahn-Teller active  $\text{Mn}^{3+}$ . If this was not the case, no tetragonal distortion would occur. For the tetragonal spinel, the increase in the  $c/a$  ratio (Figure 3.5) with Mn content indicates an increase in the concentration of Jahn-Teller active cations (*i.e.*  $\text{Mn}^{3+}$ ), relative to the concentration of non-active cations (*i.e.*  $\text{Co}^{2+/3+}$ ).

It is concluded that Mn-doping of  $\text{Co}_3\text{O}_4$  proceeds initially with  $\text{Mn}^{3+}$  replacing  $\text{Co}^{3+}$ , at least to  $x \approx 1.40$ . Further doping of Co with Mn then results in the replacement of  $\text{Co}^{2+}$  by  $\text{Mn}^{2+}$  at some composition where  $x > 1.40$ , e.g. at  $x = 2$  if  $\text{M}^{3+}$  substitution is completed before  $\text{M}^{2+}$  substitution occurs.

There is also a clear inflexion in the  $c/a'$  ratio (Figure 3.6) at  $x \sim 2.30$ , further suggesting a change in the doping mechanism at this composition. This is in reasonable agreement with the work of de Vidales *et al.*,<sup>17</sup> who witness an inflexion in the distortion parameter at  $x = 2.00$ , attributed to a change in doping mechanism from replacing  $\text{Co}^{3+}$  with  $\text{Mn}^{3+}$  on the octahedral site at  $x \leq 2.00$ , to replacing  $\text{Co}^{2+}$  with  $\text{Mn}^{2+}$  on the tetrahedral site at  $x > 2.00$ .

It may be that these deviations suggest changes in the doping mechanism in the spinel solid solution, e.g.:

- $\text{Mn}^{3+}$  replaces  $\text{Co}^{3+}$  for  $0.00 \leq x \leq 1.40$ ,
- Primarily  $\text{Mn}^{3+}$  replaces  $\text{Co}^{3+}$  for  $1.40 \leq x \leq 2.30$ ; some  $\text{Mn}^{2+}$  substitutes for  $\text{Co}^{2+}$  from  $\sim x = 1.75$ , and

$\text{Co}^{2+}$  is replaced solely by  $\text{Mn}^{2+}$  for compositions with  $x > 2.30$ .

#### 3.4.4 Oxygen non-stoichiometry in $\text{Co}_{3-x}\text{Mn}_x\text{O}_4$ spinels

The variation of the lattice parameters of the tetragonal spinel phase observed in samples quenched from 1215 °C is presented in Figures 3.4(a) and (b). The DTA data suggest that three compositional ranges exist at 1215 °C:

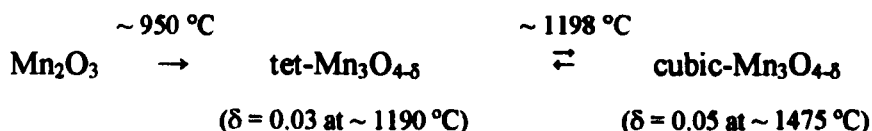
- (i) For  $x < \sim 0.30$ , the rock salt exists as a single phase,
- (ii) For  $0.30 < x < 1.60$ , a mixture of spinel and rock salt phases exist,
- (iii) For  $x > 1.60$ , only single phase cubic spinels exist, forming from the tetragonal phase on cooling.

It is clear that the composition of the tetragonal spinel is changing in the single phase region, though the variation from linearity in Figure 3.4(a) at  $x > \sim 2.40$  is not understood. One possible reason could be that the compositions of these quenches has

moved into the single phase tetragonal spinel region of the phase diagram; the lattice parameters match well.

For most of the mixed phase region, the composition of the tetragonal spinel remains unchanged, as indicated by the relatively constant lattice parameters. However, changes in the lattice parameters are observed (*i.e.*  $a$  decreases and  $c$  increases as Mn content increases) at significantly *lower* Mn contents than the DTA data suggest the composition should be changing. This suggests that there may be some degree of non-stoichiometry in the spinel compositions with  $x \sim 1.50$  on heating, and is supported by the TG data showing that a small weight loss ( $\sim 0.35$  % of original sample mass) has occurred by 1215 °C.

TG data for  $Mn_2O_3/Mn_3O_4$  indicated a continuous weight loss occurring for  $Mn_3O_4$ . This suggests that the reaction on heating  $Mn_2O_3$  can be summarised:



Dorris & Mason<sup>4</sup> found  $Mn_3O_4$  to be a normal spinel; the constant  $c/a$  ratio indicates that it remains normal on heating. Oxygen non-stoichiometry in manganese oxides has not been discussed in detail in the literature; Keller and Dieckmann<sup>18</sup> suggested that changes in stoichiometry on heating  $Mn_3O_4$  were negligible, though Metselaar *et al.*<sup>19</sup> showed some conductivity dependence on oxygen partial pressure on heating above 1200 °C. This would support the possibility of limited oxygen non-stoichiometry in  $Mn_3O_4$  suggested by the TG data presented here.

### 3.5 Conclusion

A study of the phase relations in the cobalt oxide – manganese oxide system in air has been undertaken. The results are largely in agreement with the literature. A cubic spinel solid solution was found at 500 °C for compositions in the range of  $0.00 < x < 1.30$ . This extended across the whole compositional range of the phase diagram at temperatures increasing with Mn content. Single phase spinel materials could be prepared with any Co:Mn ratio by heat treatment, *e.g.* by quenching from high temperature. In samples with  $\geq 50$  %  $\text{Mn}_3\text{O}_4$  content, *i.e.* with  $x \geq 1.50$ , the spinel reverted to tetragonal symmetry on cooling due to the high concentration of Jahn-Teller active  $\text{Mn}^{3+}$  cations.

A high temperature rock salt solid solution was also identified, as reported in the literature. However, the compositional range of this solid solution area was much more limited than was previously reported. DTA data were found to be inconsistent with TG data and XRD on quenched samples, and with high temperature XRD work reported by other authors.

Oxygen non-stoichiometry was found to be a problem at high temperatures in the single phase spinels in Mn-rich compositions, where  $x > \sim 1.50$ . For manganese oxide spinel, TG data suggested a stoichiometry of  $\sim \text{Mn}_3\text{O}_{3.95}$  at  $\sim 1475$  °C. It is possible that oxygen non-stoichiometry may be an issue for all compositions.

The effects of treatment to high temperatures (*e.g.* 1500 °C) were not fully reversible when fast cooling rates ( $\sim 10$  °C  $\text{min}^{-1}$ ) were used. However, post-treatment annealing at 800 °C was found to restore the original structure.

The completed phase diagram is presented in Figure 3.25.

### 3.6 References

- (1) Aukrust, E.; Muan, A. *Journal of the American Ceramic Society* **1963**, *46*, 511.
- (2) Sickafus, K. E.; Wills, J. M.; Grimes, N. W. *Journal of the American Ceramic Society* **1999**, *82*, 3279.
- (3) Irani, K. S.; Sinha, A. P. B.; Biswas, A. B. *Journal of Physics and Chemistry of Solids* **1962**, *23*, 711.
- (4) Dorris, S. E.; Mason, T. O. *Journal of the American Ceramic Society* **1988**, *71*, 379.
- (5) Naka, S.; Inagaki, M.; Tanaka, T. *Journal of Materials Science* **1972**, *7*, 441.
- (6) de Vidales, J. L. M.; Vila, E.; Rojas, R. M.; Garcia-Martinez, O. *Chemistry of Materials* **1995**, *7*, 1716.
- (7) Aukrust, E.; Muan, A. Phase Diagrams for Ceramists - 1969 Supplement; Levin, E. M., Robbins, C. R., McMurdie, H. F., Eds.; The American Ceramic Society: Columbus, Ohio, 1969; pp 22.
- (8) Rojas, R. M.; Vila, E.; Garcia, O.; de Vidales, J. L. M. *Journal of Materials Chemistry* **1994**, *4*, 1635.
- (9) Yamamoto, N.; Higashi, S.; Kawano, S.; Achiwa, N. *Journal of Materials Science Letters* **1983**, *2*, 525.
- (10) Philip, J.; Kutty, T. R. N. *Materials Letters* **1999**, *39*, 311.
- (11) de Vidales, J. L. M.; Garcia-Martinez, O.; Vila, E.; Rojas, R. M.; Torralvo, M. J. *Materials Research Bulletin* **1993**, *28*, 1135.
- (12) Amarilla, J. M.; de Vidales, J. L. M.; Rojas, R. M. *Solid State Ionics* **2000**, *127*, 73.
- (13) Kawai, H.; Nagata, M.; Kageyama, H.; Tukamoto, H.; West, A. R. *Electrochimica Acta* **1999**, *45*, 315.
- (14) Geller, S. *Acta Crystallographica, Sec. B* **1971**, *27*, 821.
- (15) *Powder Diffraction File, Card No. 24-508.*
- (16) Shannon, R. D.; Prewitt, C. T. *Acta Crystallographica* **1969**, *B25*, 925.
- (17) Vila, E.; Rojas, R. M.; de Vidales, J. L. M.; Garcia-Martinez, O. *Chemistry of Materials* **1996**, *8*, 1078.
- (18) Keller, M.; Dieckmann, R. *Ber. Bunsenges Phys. Chem.* **1985**, *89*, 1095.
- (19) Metselaar, R.; Van Tol, R. E. J.; Peircy, P. *Journal of Solid State Chemistry* **1981**, *38*, 335.

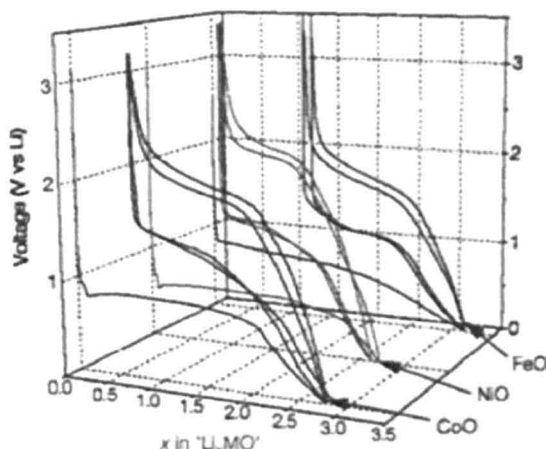
## Chapter 4

### Electrochemical properties of 'Co<sub>3-x</sub>Mn<sub>x</sub>O<sub>4</sub>' spinels

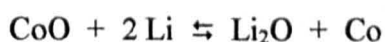
#### 4.1 Literature review

The possible application of transition metal oxides as anode materials for Li-ion batteries has received much attention in recent years.<sup>1,2</sup> Studies by Tarascon *et al.*<sup>3,4</sup> have highlighted cobalt oxides to be of notable interest. Long plateaux were observed in the discharge profiles of CoO (Figure 4.1) and Co<sub>3</sub>O<sub>4</sub> at ~ 0.8 V, with the potential then sloping down to the cut-off voltage.

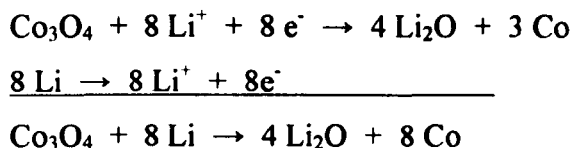
**Figure 4.1** – Charge/discharge profiles for MO/Li cells (M = Co, Ni, Fe).<sup>3</sup>



Very high capacities for CoO (~ 700 mAh.g<sup>-1</sup>) and Co<sub>3</sub>O<sub>4</sub> (~ 1000 mAh.g<sup>-1</sup>) were noted. A significant drop in capacity is observed after the first discharge; thereafter cells cycle very well with ~ 100 % capacity retention to 100 cycles. Other metal oxides, such as NiO, FeO and Cu<sub>2</sub>O showed similar behaviour but with much poorer cycling performance. Tarascon also indicated that particle size was a factor in capacity retention. The mechanism for the electrochemical behaviour has been proposed as a displacive redox reaction. For CoO:



And for  $\text{Co}_3\text{O}_4$ :



It is proposed that  $\text{Co}_3\text{O}_4$  then forms  $\text{CoO}$  on 1<sup>st</sup> charge, and the active material cycles as  $\text{CoO} \rightleftharpoons \text{Co}$  thereafter. The amount of Li that can be ‘inserted’ into the anode material on first charge is essentially limited by the number of oxygen atoms present; the specific capacity, however, is directly related to the formula weight of the active material and hence the interest in  $\text{CoO}$ .

The impressive cycling performance noted for  $\text{Co}_3\text{O}_4$  and  $\text{CoO}$  by Tarascon *et al.*<sup>3,4</sup> has not been reproduced elsewhere; the cycling profiles obtained by Tarascon and Wang are presented in Figures 4.2 and 4.3.

As cells were cycled, in situ XRD was performed by Tarascon *et al.*,<sup>3</sup> Choi *et al.*<sup>5</sup> and Wang *et al.*<sup>6</sup> and it was noted that for  $\text{CoO}$  the rock salt pattern was lost on discharge (*i.e.* as Li was inserted), with only a flat featureless trace obtained. No XRD peaks were observed on subsequent charging. This suggested that the 0.8 V plateau involved the decomposition/amorphization of  $\text{CoO}$ . TEM confirmed the formation of Co metal nano-sized amorphous particles during the first discharge. SAED showed a  $\text{Co} \rightarrow \text{CoO}$  transition on charging. Choi *et al.*<sup>5</sup> used XANES to show that 1.32 Li were inserted before Co metal began to form; the addition of Li caused local distortions around the Co atoms, and Co metal clusters began to evolve gradually on further lithiation.

The large initial capacity loss on discharge for metal oxides, such as  $\text{Co}_3\text{O}_4$ , is problematic as it involves consuming much of the Li from the cathode during the first cycle, which is lost to the cell thereafter. One potential solution, suggested by Tarascon *et al.*<sup>4</sup> was to use a cathode with excess Li, *e.g.*  $\text{Li}_{1+x}\text{Mn}_2\text{O}_4$ , where  $x = 0.33$ . Here, the excess Li ‘reservoir’, responsible for the 3 V plateau in cycling  $\text{Li}_{1+x}\text{Mn}_2\text{O}_4$  vs. Li, is used up on the first charge and accounts for the irreversible loss in the  $\text{Co}_3\text{O}_4$  anode; thereafter the material is cycled with  $\text{LiMn}_2\text{O}_4$  as the cathode.

The  $\text{Co}_{3-x}\text{Mn}_x\text{O}_4$  phase diagram has been extensively studied,<sup>7,8</sup> and was discussed in Chapter 3. These materials have attracted interest for their electrical properties; however, with the exception of the end-members ( $\text{Co}_3\text{O}_4$  and  $\text{Mn}_3\text{O}_4$ ), no reports have been made on their possible electrochemical properties. Cobalt is generally perceived as expensive and toxic, and doping with manganese would alleviate these problems; this work will study the intercalation of Li into single phase spinels with stoichiometry  $0.00 \leq x \leq 3.00$ .

**Figure 4.2** – Capacity retention for Li/CoO and Li/Co<sub>3</sub>O<sub>4</sub> cells at room temperature, cycled at C/2 rate over 0.01 to 3.0 V. Electrode area was 1 cm<sup>2</sup>; the mass of electroactive material was 4 mg.<sup>4</sup>

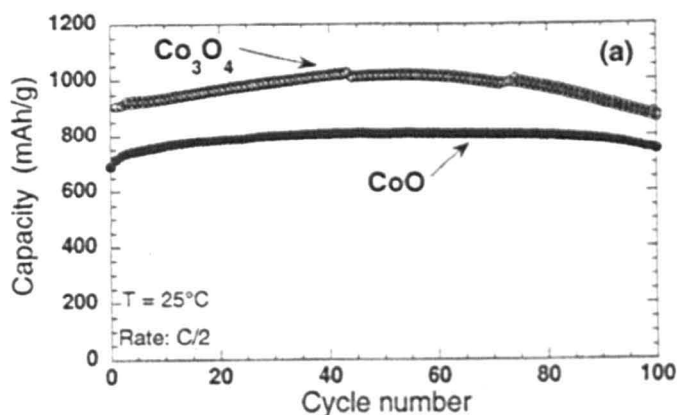
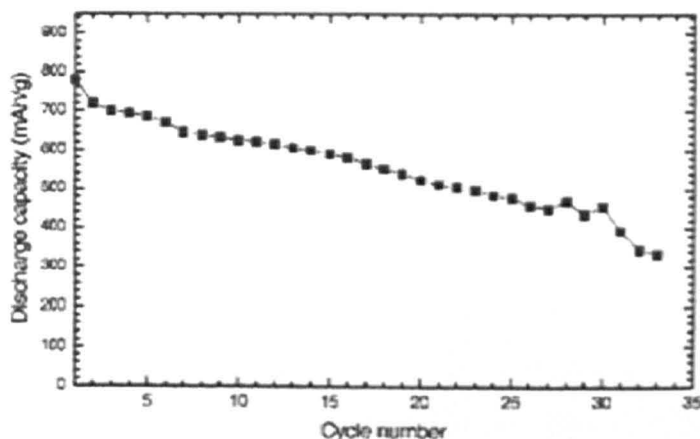


**Figure 4.3** – Capacity retention for Li/Co<sub>3</sub>O<sub>4</sub> cells at room temperature, cycled at 20 mA/g over 0.01 to 3.0 V. The mass of electroactive material was 1 - 2 mg.<sup>6</sup>



## 4.2 Experimental

The method for preparing single phase spinels was discussed in Chapter 3; single phase spinels with cubic symmetry and composition  $0.00 \leq x \leq 1.30$  were prepared for study by the GCPL technique by treatment at 800 °C, with subsequent annealing at 500 °C to ensure the correct oxygen content. Single phase spinels with tetragonal symmetry and composition  $1.50 \leq x \leq 2.60$  were also prepared for study by the GCPL technique, by the same method, and then subsequently heating overnight at 1150 °C.

Cells for study by GCPL were constructed and tested with the assistance of Dr Denis Pasero, a post-doctoral researcher. Test electrodes were composite materials containing 5-10 mg of the active material, *i.e.*  $\text{Co}_{3-x}\text{Mn}_x\text{O}_4$  ( $x = 0.0 - 3.0$ ), carbon black and PVdF binder in a ratio of 80/10/10 wt%. A 1.69 cm<sup>2</sup> Li metal disk acted as a counter-electrode. The electrolyte used was 1 M LiPF<sub>6</sub> in propylene carbonate. All cells were constructed in an argon-filled glove box, with care taken to eliminate water from the atmosphere. Cells were cycled at C/5 rate (*i.e.* 1 Li per formula unit every 5 hours) using a potential window of 0.25 – 3.5 V. ‘Discharging’ of the transition metal oxides is to be considered the ‘lithiation’ process, where Li is inserted, in whatever form this occurs; this is the terminology commonly used in the literature.

where:  $e$  = number of electrons involved in complete reaction  
 $F$  = Faraday's constant /  $9.469 \times 10^4 \text{ C.mol}^{-1}$   
 $M$  = molar mass of active material /  $\text{g.mol}^{-1}$

Note that 3.6 Coulomb = 1 mA.h, hence the correction factor in Equation 4.1.

Therefore, the theoretical capacity for adding 1 Li to 1  $\text{Co}_3\text{O}_4$  unit is  $109.24 \text{ mAh.g}^{-1}$ . This gives a first charge capacity of  $1191.90 \text{ mAh.g}^{-1}$  for adding 10.91 Li to  $\text{Co}_3\text{O}_4$ .

Subsequent discharge/charge profiles follow a similar pattern; however, on each successive discharge the length of the 1.1 V plateau decreases, with less Li inserted each time as shown in the discharge profiles for the first six cycles in Figure 4.5. The plateau has also moved to a slightly lower voltage, centred on  $\sim 1 \text{ V}$ . Charge profiles have been omitted for clarity.

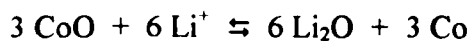
By the sixth cycle, 7.38 Li are being inserted during discharge, corresponding to a specific capacity of  $805.70 \text{ mAh.g}^{-1}$ . The cycling performance of the  $\text{Co}_3\text{O}_4$  anode is more clearly demonstrated in Figure 4.6.

These data show a large drop in capacity from the 1<sup>st</sup> to the 3<sup>rd</sup> cycle, after which the loss per cycle becomes smaller. However,  $\sim 32 \%$  of the first cycle capacity is lost after only 6 cycles, and capacity is dropping steadily by  $\sim 3 \%$  per cycle. If this linear drop in capacity per cycle were maintained, no capacity would remain after only 33 cycles.

The reaction mechanism for cobalt oxides is believed<sup>3-6,9</sup> to be a displacive redox reaction, producing lithia ( $\text{Li}_2\text{O}$ ) in a cobalt metal matrix. The capacity, therefore, is determined by the amount of oxygen atoms in the active material, *i.e.* for  $\text{Co}_3\text{O}_4$ , 8 lithium atoms would be needed to form four  $\text{Li}_2\text{O}$  molecules. On first charge, 10.91 Li were inserted, suggesting that cobalt oxide is reduced to the metal. It is likely that  $\sim 3$  Li are then used up in forming a Solid-Electrolyte Interface (SEI). The reaction at the active electrode can be summarised as:



A loss in capacity of 2 Li from 1<sup>st</sup> to 2<sup>nd</sup> cycle, in agreement with the literature, would suggest that CoO is formed after the first discharge, since:



It is CoO acting as the active material on subsequent cycles. The cycling performance is comparable with that of Wang, but still unsatisfactory. The reason for the poor cyclability observed is not understood.

All samples show similar (dis)charging behaviour. On first discharge at least eight Li ions are added into the host structure; subsequently, up to six Li can be removed and cycled (Figure 4.23). Further lithium, in excess of the initial eight atoms, is used up in the formation of SEI phenomena. A cell using  $\text{Mn}_3\text{O}_4$  as the active material was also constructed, but no capacity was observed in the electrochemical window used.

Figure 4.21 shows the variation of operating voltage with composition,  $x$ ; these data show that on first discharge, there is a linear decrease in operating voltage as  $x$  increases, *i.e.* as Mn content increases.

It can be noted that samples with composition  $0.60 \leq x \leq 2.00$  show a small hump corresponding to  $\sim 1.25$  Li atom on first discharge. The maximum voltage of this hump drops with composition,  $x$ , from  $\sim 1.2$  V for  $x = 0.60$  to  $\sim 0.66$  V for  $x = 2.60$  (Figure 4.22); the nature of the hump is also clearly different for  $x = 2.60$ , accounting for much less Li than  $x = 0.60$  and 1.50.

The specific discharge capacity obtained for cells of composition  $0.00 \leq x \leq 2.60$  on sixth cycle is presented in Figure 4.23. With the exception of  $\text{Co}_3\text{O}_4$  ( $x = 0.00$ ), all cells show a specific capacity of  $\sim 4.5$  Li atoms ( $\pm 0.5$  Li). This is equivalent to an approximate specific capacity of  $\sim 475$   $\text{mAh.g}^{-1}$  ( $\pm 75$   $\text{mAh.g}^{-1}$ ); this is significantly higher than the capacities obtained from the current commercially used graphite anodes.

The effect of doping on capacity retention can also be considered. Figure 4.24 shows the percentage of (a) first discharge, and (b) second discharge specific capacity remaining on sixth discharge. In a normal battery configuration, with a stoichiometric compound used as the active material, the amount of first discharge capacity retained on cycling would be most important. Following the work of Tarascon *et al.*, however, an excessively-lithiated compound, such as  $\text{Li}_{1+x}\text{Mn}_2\text{O}_4$  (where  $x = 0.33$ ) may be used as the active cathode material, providing the excess Li to account for the drop in capacity after the first discharge. In this case, the percentage of the second discharge capacity (b) retained on cycling is of more relevance.

Doping with Mn causes a clear drop in the amount of first cycle discharge capacity retained on cycling. For  $x = 2.60$  ( $\text{Co}_{0.4}\text{Mn}_{2.6}\text{O}_4$ ),  $\sim 44$  % of the first discharge capacity was obtained on the sixth discharge.

However, the percentage of second discharge capacity retained on cycling increases with composition,  $x$ . For  $\text{Co}_3\text{O}_4$ ,  $\sim 80\%$  of the second cycle discharge capacity is retained on the sixth cycle. This figure rises to  $\sim 94\%$  for  $x = 2.60$ .

### 4.3.3 Differential potentiometry.

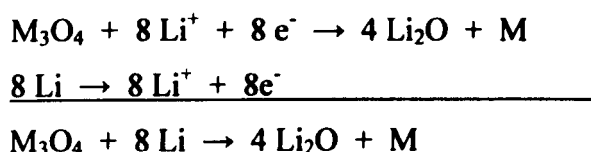
Rather than running separate cyclic voltammetry experiments, it is possible to obtain information on the processes that are occurring, and at what voltage, by taking the differential of the GCPL data, and plotting  $dV/dx$  vs.  $E$ . Differential potentiograms from the data collected on the second discharge/charge cycle for samples with composition  $x = 0.00 - 2.60$  are presented in Figures 4.25 – 4.32.

The differential potentiogram for  $\text{Co}_3\text{O}_4$  shows two pairs of peaks on charge and discharge. One pair is observed at 2.185 V on charge and 1.15 V on discharge; the peaks are centred on 1.668 V. The other pair is observed at 1.512 V on charge and 0.957 V on discharge; these peaks are centred at 1.235 V.

As Mn-doping proceeds, the intensity of the peaks centred at  $\sim 1.6$  V and  $\sim 1.24$  V decreases, while at the same time a new pair of peaks emerges on charging/discharging centred at  $\sim 1$  V. The intensity of this second pair of peaks increases with Mn-doping; for the sample with composition  $x = 2.60$ , only this new set of peaks is observed; on charge a peak at 1.229 V is observed, and on discharge a peak at 0.585 V is observed, *i.e.* the peaks are centred at 0.91 V. The peaks centred at higher voltages are not observed at all.

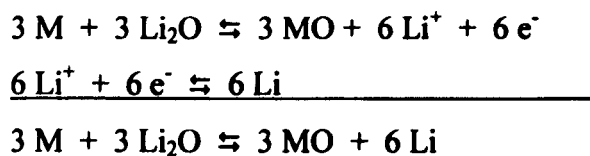
#### 4.3.4 Discussion of GCPL Results

The ability for hosting lithium reported for  $\text{Co}_3\text{O}_4$  is retained on doping with Mn. Compositions with  $0.00 \leq x \leq 2.60$  all showed the ability to accept lithium insertion and extraction reversibly, and therefore have potential as possible anode materials. While  $\text{Co}_3\text{O}_4$  showed an approximately linear decrease in specific discharge capacity on cycling, the materials with  $x \geq 0.30$  all showed a single drop after first discharge of  $\sim 2$  Li, followed by good capacity retention on further cycling. This is actually in better agreement with the proposed Li-uptake mechanism for  $\text{Co}_3\text{O}_4$ ; *i.e.* on first discharge, 8 Li ions are intercalated according to:



Where M = Mn/Co. Hence, the result of the first discharge is to produce Co and Mn metal particles (either separately or together in an alloy) in a lithia matrix. This is in agreement with Tarascon *et al.*, who proposes that the particle size of Co metal produced on cycling  $\text{Co}_3\text{O}_4$  is in the nanometre range. Discharging is observed to continue to  $> 8$  Li, consistent with the formation of solid-electrolyte interface (SEI) phenomena.

On charge, however, oxidation of the metal proceeds only to the monoxide(s), accompanied by the release of  $\sim 6$  Li ions:



The cell then cycles with good reversibility using MO as the intercalation host. In practice, these theoretical values are not obtained, and cells showed practical Li uptakes of  $\sim 4 - 5$  Li ions per  $\text{Co}_3\text{O}_4$  starting unit.

It is not clear why lithium could not be inserted into  $\text{Mn}_3\text{O}_4$ . Further work on this is required; extrapolation of the operating voltage data presented in Figure 4.21 gives a

very low operating voltage of  $\sim 0.30$  V vs. Li for  $\text{Mn}_3\text{O}_4$ , which would be impractical for use as cells would have to be operated to below 0.25 V to make full use of any possible potential. Below 0.25 V, the carbon black added to improve conductivity can react with Li, which would be problematic.

It is also interesting to note that, almost exclusively, the amount of Li that could be intercalated into the anode on discharge was equal to the amount that had been removed on the previous charge. This may have implications about the rate at which experiments were performed; cells may cycle better and show higher specific capacities if cycled at a slower rate. This may be either a thermodynamic or a kinetic effect. However, at the rate used (C/5) the experiments took over 24 hours per cycle for a battery; *i.e.* six cycles took a week to run. Time constraints did not allow for repeat experiments at slower cycle rates.

Samples with composition,  $x \geq 0.60$  exhibit a hump in capacity equivalent to  $\sim 1.25$  Li at  $\sim 1.1 - 0.8$  V on first discharge. This suggests the formation of an intermediate species in the reduction of  $\text{Co}_3\text{O}_4$ , and that discharging proceeded via the same route for all compositions. The composition of any intermediate formed appears to change with the starting composition of the active material, since the maximum voltage of the hump drops with Mn content. This may be linked to the findings of Choi *et al.*, who showed that during the first discharge, formation of Co metal began after intercalation of an initial 1.32 Li ions; further addition caused Co metal clusters to form.

If discrete Co and Mn particles were forming on first discharge, then lithiation of these would most likely proceed at different energies; *i.e.* two discharge/charge plateaux would be observed. Raw GCPL data for the whole compositional range studied indicate only a single process occurring in the operating range of 2.0 – 0.5 V; however, the differential potentiograms clearly show the existence of two processes for the Mn-doped materials. It appears that (de)lithiation of Co occurs at  $\sim 1.6$  V and  $\sim 1.2$  V, while (de)lithiation of Mn occurs at a lower operating voltage,  $\sim 1.0$  V; *i.e.* there are two discrete processes, indicating that a Co-Mn alloy is not forming during discharge.

The drop in operating voltage on doping with Mn is also favourable due to the greater potential difference vs. a cathode material. For example, a cell incorporating an anode operating at 1 V, and a cathode operating at 4 V, will actually operate at 3V. Replacing

the anode with one operating at 0.5 V will raise the operating voltage of the cell to 3.5 V. The energy density of the cell is the product of the voltage and the specific capacity; such an increase in operating voltage will bring a significant improvement in battery energy density.

The retention of first discharge capacity appears to worsen on Mn-doping. However, the linear drop in specific capacity observed on cycling  $\text{Co}_3\text{O}_4$ , if continued, would lead to zero capacity by the 33<sup>rd</sup> discharge. This would be completely unacceptable for any battery applications, where cells are ideally designed to be capable of hundreds, if not thousands, of cycles. However, the cell with composition  $x = 2.60$  cycles steadily with intercalation of  $\sim 3.7$  Li per discharge. While the cell has not undergone enough cycles to draw serious conclusions about cycling performance, the data do suggest that the cell will be capable of cycling for far more than 33 cycles.

The retention of second discharge capacity is of interest if lithium-excess cathodes, such as  $\text{Li}_{1+x}\text{Mn}_2\text{O}_4$ , are to be used to allow for the drop in capacity after the first cycle. There is a clear improvement in the retention of second discharge capacity upon doping with Mn. The reasons for this improvement are unclear; this may be linked to easier (de)lithiation of Co-Mn rock salts/alloys. One possible reason for this is the increase in unit cell size brought about by replacement of Co by Mn. This may allow more room for access by Li ions.

The most suitable composition for use as an anode material was found to be  $x = 2.60$ , since samples with this composition had (of the  $\text{Co}_{3-x}\text{Mn}_x\text{O}_4$  solid solution studied here):

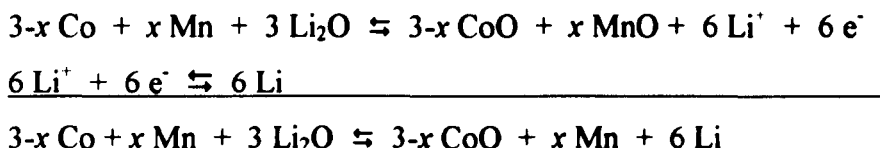
- acceptable capacity, offering a significant improvement over graphite anodes.
- the best capacity retention.
- the lowest operating voltage.
- flat discharging profile.
- $\sim 87$  % of the Co replaced by Mn, offering significant health and economic benefits over  $\text{Co}_3\text{O}_4$ .

Further work is necessary to try to obtain  $\text{Co}_{0.4}\text{Mn}_{2.6}\text{O}_4$  with closer to the theoretical capacity of  $684.92 \text{ mAh.g}^{-1}$  for repeated (de)insertion of 6 Li with good capacity

retention on cycling, on a charge plateau centred at  $\sim 0.6$  V. In addition, the impressive cycling performance of the cells produced Tarascon *et al.* has not been reproduced here, and future work should aim to understand the cause for this good performance and reproduce it for these materials. Such a material would be extremely attractive as a replacement anode for graphite in the next generation of Li-ion batteries.

## 4.4 Conclusions

Lithiation of samples of composition  $\text{Co}_{3-x}\text{Mn}_x\text{O}_4$  has been successfully attempted and proceeds via formation of separate grains of Co and Mn, possibly at the nanometre-level, and not a Co-Mn metal alloy. These discrete Co and Mn grains then re-oxidise on discharge; it is CoO and MnO that cycle thereafter:



Observed practical discharge capacities for Mn-doped materials were significantly lower ( $\sim 475 \text{ mAh.g}^{-1}$ ) than for  $\text{Co}_3\text{O}_4$  ( $\sim 800 \text{ mAh.g}^{-1}$ ), but in good agreement with the proposed mechanism.

The cycling performance of the doped materials did improve upon Mn-doping, however, with the very real possibility of a significant increase in cell life.

The most ideal candidate as an anode material was found to be  $\text{Co}_{0.4}\text{Mn}_{2.6}\text{O}_4$ , since this showed good capacity retention after the initial drop on first cycle, better specific capacity than the graphite anode materials currently used, and the lowest potential vs. Li metal, while also replacing most of the expensive and toxic Co with a more attractive metal, Mn.

Further work to improve the processing of the active materials and the quality of composite anode films may offer improvements in cell performance for these doped materials.

## 4.5 References

- (1) Thackeray, M. M.; David, W. I. F.; Bruce, P. G.; Goodenough, J. B. *Materials Research Bulletin* **1983**, *18*, 461.
- (2) Thackeray, M. M.; David, W. I. F.; Goodenough, J. B. *Materials Research Bulletin* **1982**, *17*, 785.
- (3) Poizot, P.; Laruelle, S.; Grugeon, S.; Dupont, L.; Tarascon, J. M. *Nature* **2000**, *407*, 496.
- (4) Badway, F.; Plitz, I.; Grugeon, S.; Laruelle, S.; Dolle, M.; Gozdz, A. S.; Tarascon, J. M. *Electrochemical and Solid-State Letters* **2002**, *5*, A115.
- (5) Choi, H. C.; Lee, S. Y.; Kim, S. B.; Kim, G. M.; Lee, M. K.; Shin, H. J.; Lee, J. S. *The Journal of Physical Chemistry B* **2002**, *106*, 9252.
- (6) Wang, G. X.; Chen, Y.; Konstantinov, K.; Yao, J.; Ahn, J. H.; Liu, H. K.; Dou, S. X. *Journal of Alloys and Compounds* **2002**, *340*, L5.
- (7) Aukrust, E.; Muan, A. *Journal of the American Ceramic Society* **1963**, *46*, 511.
- (8) de Vidales, J. L. M.; Garcia-Martinez, O.; Vila, E.; Rojas, R. M.; Torralvo, M. J. *Materials Research Bulletin* **1993**, *28*, 1135.
- (9) Wang, G. X.; Chen, Y.; Konstantinov, K.; Lindsay, M.; Liu, H. K.; Dou, S. X. *Journal of Power Sources* **2002**, *109*, 142.

## Chapter 5

### Cubic spinel and rock salt materials in the $\text{Li}_2\text{O-CoO}_x\text{-MnO}_y$ phase diagram

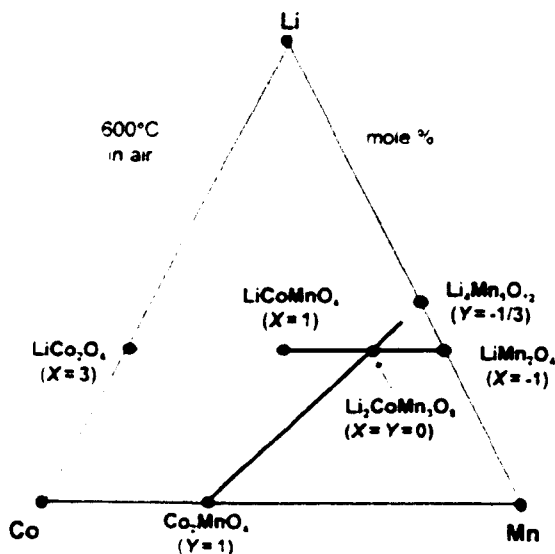
#### 5.1 Introduction

$\text{LiMn}_2\text{O}_4$  is of great potential as a 4 V cathode material. However, the high concentration of Jahn-Teller active  $\text{Mn}^{3+}$  cations causes structural distortions, and ultimately poor cycling performance, when the material is used as a cathode material in Li-ion batteries. A considerable amount of work has focussed on methods of improving the properties of  $\text{LiMn}_2\text{O}_4$ ; one approach has been to dope with cobalt, according to the formula  $\text{LiCo}_x\text{Mn}_{2-x}\text{O}_4$  (Kawai's  $\text{LiCo}_{1/2+x/2}\text{Mn}_{3/2-x/2}\text{O}_4$ ). This has also led to the study of the  $\text{Li}_2\text{O-CoO}_x\text{-MnO}_y$  phase diagram in general as a possible source of cathode materials for the next generation of Li-ion battery materials.

In 1998, Kawai *et al.* reported a complete solid solution along the join between  $\text{LiMn}_2\text{O}_4$  and  $\text{LiCoMnO}_4$  (Figure 5.1). While lithium deintercalation from  $\text{LiMn}_2\text{O}_4$  proceeds solely at  $\sim 4.0$  V, it was demonstrated that the addition of Co to the structure causes a decrease in capacity at  $\sim 4.0$  V, and the emergence of electrochemical activity at  $\sim 5.0$  V. These plateaux are linked to two separate redox reactions: (i)  $\text{Mn}^{3+} \rightleftharpoons \text{Mn}^{4+}$ , at 4.0 V, and (ii)  $\text{Co}^{3+} \rightleftharpoons \text{Co}^{4+}$  at 5.0 V. It was anticipated that  $\text{LiCoMnO}_4$ , with Li in 8a tetrahedral sites and  $\text{Co}^{3+}$  and  $\text{Mn}^{4+}$  occupying 16d octahedral sites, would only show activity at 5.0 V, since no  $\text{Mn}^{3+}$  would be available. However, some residual capacity at  $\sim 4.0$  V was observed; the reasons for this were unclear.

Kawai *et al.* also reported another spinel solid solution in the  $\text{Li}_2\text{O-CoO}_x\text{-MnO}_y$  phase diagram (Figure 5.1), with formula  $\text{Li}_{1-y}\text{Co}_{1/2+3y/2}\text{Mn}_{3/2-y/2}\text{O}_4$ , existing over a partial range ( $-0.17 \leq y \leq 0.84$ ) of the join between  $\text{Li}_4\text{Mn}_5\text{O}_{12}$  ( $y = -1/3$ ) and  $\text{Co}_2\text{MnO}_4$  ( $y = 1$ ). The best electrochemical performance was found for  $y = 0$  ( $\text{Li}_2\text{CoMn}_3\text{O}_8$ ); for  $y > 0$ , the solid solutions lost their electrochemical behaviour, possibly due to the blocking of the Li-ion diffusion pathway by Co ions.

**Figure 5.1** – Formation of ' $\text{Li}_{1-y}\text{Co}_{1/2+3y/2}\text{Mn}_{3/2-y/2}\text{O}_4$ ' and ' $\text{LiCo}_{1/2+x/2}\text{Mn}_{3/2-x/2}\text{O}_4$ ' spinel solid solutions in the system Li-Co-Mn-O. Oxygen contents are not specified.



The effect of heating on  $\text{LiMn}_2\text{O}_4$  has been studied, with oxygen loss shown to occur above  $\sim 800^\circ\text{C}$ . The spinel retains cubic symmetry until the stoichiometry reaches  $\text{LiMn}_2\text{O}_{3.86}$ , at  $\sim 880^\circ\text{C}$ ,<sup>1,2</sup> where a tetragonal symmetry is observed. Further structural transformations occur as oxygen loss proceeds on heating to higher temperatures, but little conclusive can be deduced about the nature of these changes. Thackeray proposed the segregation of the monoclinic rock salt phase  $\text{Li}_2\text{MnO}_3$  between  $\sim 880^\circ\text{C}$  and  $915^\circ\text{C}$ , with this phase then reacting with the remaining Mn-rich spinel phase to form the orthorhombic rock salt  $\text{LiMnO}_2$ . A single phase cubic spinel above  $1100^\circ\text{C}$ , with nominal stoichiometry ' $\text{Li}_{0.6}\text{Mn}_{2.4}\text{O}_4$ ' then forms, though this requires lithia loss. Sugiyama,<sup>3</sup> however, reports a straight reaction of:



Little evidence is presented for extensive lithia loss; a small degree of irreversible weight loss could easily be attributed to less than complete re-oxidation of the transition metal back to the average oxidation state of  $3.5^+$ .

The aim of the work presented in this chapter was to study the  $\text{Li}_2\text{O}-\text{CoO}_x-\text{MnO}_y$  phase diagram further. In particular, three possible solid solutions have been studied:

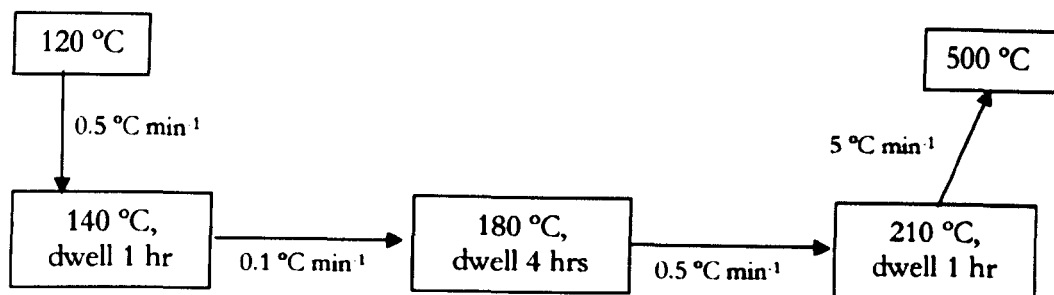
- (i) The reported cubic spinel solid solution between  $\text{LiMn}_2\text{O}_4$  and  $\text{LiCoMnO}_4$ . (i.e.  $\text{LiCo}_x\text{Mn}_{2-x}\text{O}_4$ ).

- (ii) An unreported join between  $\text{LiCoMnO}_4$  and  $\text{Co}_3\text{O}_4$ .  
(i.e.  $\text{Li}_{1-x}\text{Co}_{1+2x}\text{Mn}_{1-x}\text{O}_4$ ).
- (iii) An unreported join between  $\text{Li}_2\text{CoMn}_3\text{O}_8$  and  $\text{Co}_{1.7}\text{Mn}_{1.3}\text{O}_4$   
(i.e.  $\text{Li}_{1-x}\text{Co}_{1/2+6x/5}\text{Mn}_{1.5-x/5}\text{O}_4$ ).

Note that the compositional ranges for all three solid solutions are  $0.00 \leq x \leq 1.00$ . In join (iii),  $\text{Co}_{1.7}\text{Mn}_{1.3}\text{O}_4$  has been chosen as the end-member, since this composition forms the Mn-rich limit of the  $\text{Co}_{3-x}\text{Mn}_x\text{O}_4$  cubic spinel solid solution in samples prepared at 800 °C, as discussed in Chapter 3.

## 5.2 Experimental

Samples were prepared by mixing accurately weighed starting reagents ( $\text{LiNO}_3$ ,  $\text{Co}(\text{NO}_3)_2 \cdot 6\text{H}_2\text{O}$  and  $\text{Mn}(\text{CH}_3\text{CO}_2)_2$ ) in a mortar and pestle. The powders were placed in Au boats and moved to a furnace at  $120\text{ }^\circ\text{C}$ , then slowly heated to  $500\text{ }^\circ\text{C}$ :



Samples were subsequently reacted at  $800\text{ }^\circ\text{C}$  for 3 days. Post-reaction annealing at  $500\text{ }^\circ\text{C}$  for 3 days gave a considerable improvement in XRD pattern quality, with significantly sharper peaks observed indicating an improvement in sample crystallinity.

To attempt to quench in any high temperature structure, samples wrapped in platinum foil were suspended in a vertical tube furnace and dropped into mercury after 10 minutes.

Samples were studied by thermogravimetry (TG) and differential thermal analysis (DTA), using Stanton-Redcroft TG-DTA equipment. Experiments were conducted in an air atmosphere, except where stated otherwise. Heating/cooling rates were programmed to  $10\text{ }^\circ\text{C min}^{-1}$ .

DSC experiments were performed using a TA Instruments DSC-910, with samples in crimped Al pans run in an argon atmosphere with heating rates set to  $10\text{ }^\circ\text{C min}^{-1}$ . Liquid nitrogen was used to cool the samples to  $-180\text{ }^\circ\text{C}$  before starting the experiments.

The lattice parameter data in Table 5.1 and Figure 5.2 show linear relationships in the variation of lattice parameter with composition,  $x$ , in the ranges  $x = 0.00$  ( $\text{LiMn}_2\text{O}_4$ ) to  $x = 0.50$  ( $\text{LiCo}_{0.5}\text{Mn}_{1.5}\text{O}_4$ ), and from  $x = 0.50$  ( $\text{LiCo}_{0.5}\text{Mn}_{1.5}\text{O}_4$ ) to  $x = 1.00$  ( $\text{LiCoMnO}_4$ ). There is a change in slope in the data at  $x \sim 0.50$ , indicating a possible change in the mechanism of solid solution. This is in agreement with the work of Kawai *et al.* The reason for this is unclear, but suggests that there is either some special stability for compositions with  $x \sim 0.50$ , or a change in substitution mechanism to either side of  $x = 0.50$ .

### 5.3.2 Thermal behaviour studies

Samples with compositions in the range  $0.00 \leq x \leq 1.00$  were studied by combined TG-DTA; the TG and DTA data are presented together in Figures 5.3 – 5.8.

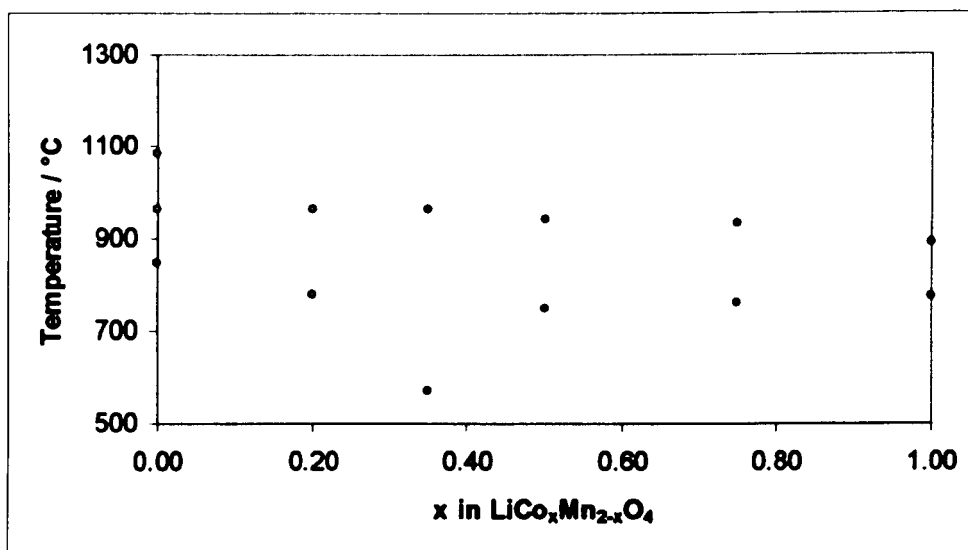
#### 5.3.2a Thermogravimetry results

The TG data for all samples show a weight loss on heating of *ca.* 7 – 8.5 % of the initial sample mass. Since weight loss is almost fully reversible, it is unlikely to be due to volatility of any of the metal species (*i.e.* Li, Co or Mn), and is most likely caused by oxygen loss; work by Mandal *et al.* has confirmed this.<sup>7</sup> For  $x \geq 0.35$ , a plateau was obtained above  $\sim 1250$  °C, indicating that weight loss was no longer occurring at these temperatures. The observed weight loss approached 1 oxygen atom for all samples.

In general, the temperature at which weight loss begins decreases with increasing Co content. For all samples, weight loss occurs in two stages, separated by a small inflexion in the data. The temperature at which this inflexion occurs decreases with increasing Co content (*i.e.* as  $x$  increases), as indicated in Figure 5.9.

Most of the weight lost during the heating profile was regained during the subsequent cooling cycle. However, all samples showed a small amount of irreversible weight loss ( $\Delta W$ ); it was observed that the size of the irreversible loss generally increases with Co content, though a direct comparison is not possible since samples were run to different temperatures in order to try and obtain a plateau in weight loss.

Figure 5.11 – Observed DTA peak maxima for samples with  $0.00 \leq x \leq 1.00$  in  $\text{LiCo}_x\text{Mn}_{2-x}\text{O}_4$



These DTA peaks fall roughly into three categories:

- (i) those below  $\sim 850$  °C; for  $x \leq 0.5$ , generally small, broad peaks were observed, while for  $x > 0.5$  sharper DTA peaks were observed,
- (ii)  $850$  °C  $\leq T$  / °C  $\leq 1000$  °C; sharp DTA peaks were observed for all samples, and
- (iii) above  $1000$  °C, a sharp DTA peak was observed for  $\text{LiMn}_2\text{O}_4$ .

### 5.3.2c DSC results

The sub-ambient DSC data for samples with composition  $0.00 \leq x \leq 1.00$  were recorded; for  $\text{LiMn}_2\text{O}_4$ , a single DSC peak was observed at  $\sim 23$  °C on heating, indicating that a transformation to another structure exists below room temperature. This is discussed in further detail in Chapter 7. However, for all cobalt-doped (*i.e.* for  $x > 0.00$ ) materials, no peaks or inflexions were observed in the DSC data.

### 5.3.3 Binary Phase Diagram for $\text{LiCo}_x\text{Mn}_{2-x}\text{O}_4$ join

The XRD data collected for samples with composition  $0.00 \leq x \leq 1.00$  quenched from a series of temperatures (roughly  $500 - 1300$  °C) were studied to determine the identity of the phases present. These data are presented in the form of a phase diagram in Figure 5.12. The temperatures of DTA data peak maxima, and at which the TG data indicate weight loss to be starting, are overlaid for comparison.

The observed transitions for the sample with composition  $x = 0.20$  are similar, with DTA data indicating the transition to tetragonal symmetry occurring at a lower temperature,  $\sim 778$  °C. There is no indication of a structural transformation at temperatures  $> 1000$  °C.

No single phase tetragonal spinel was observed for  $x = 0.35$ , with a cubic spinel  $\rightleftharpoons$   $\text{Li}_2\text{MnO}_3$  / spinel mixture transition occurring at  $\sim 571$  °C. This seems anomalously low in comparison to the neighbouring samples, suggesting that these data may be erroneous. However, all of the data for the sample are self-consistent.

For  $x = 0.50$  and  $0.75$ , the TG, DTA and quench data indicate three transitions occurring below  $\sim 1215$  °C. Oxygen loss begins at  $\sim 650$  °C, with the spinel structure retained on further heating until  $\sim 750$  °C. Between  $\sim 750$  °C and  $\sim 940$  °C, a two-phase mixture ( $\text{Li}_2\text{MnO}_3$  and a tetragonal spinel) exists. At  $\sim 940$  °C, the  $\text{Li}_2\text{MnO}_3$  decomposes, and instead a simple rock salt with a primitive unit cell coexists with the spinel. A single phase rock salt is obtained for  $x = 0.75$  on heating to  $1264$  °C.

Similar observations were made for  $x = 1.00$  ( $\text{LiCoMnO}_4$ ), with weight loss starting at  $\sim 559$  °C. The cubic spinel was retained on further heating, before decomposing at  $\sim 774$  °C to form the two-phase mixture of spinel and  $\text{Li}_2\text{MnO}_3$ . The  $\text{Li}_2\text{MnO}_3$ -type phase decomposed at  $\sim 891$  °C, with further heating yielding a mixture of cubic spinel and simple rock salt phases. Single phase rock salts were obtained upon further heating to  $\sim 1250$  °C. A rock salt solid solution, with probable stoichiometry ' $\text{LiCo}_x\text{Mn}_{2-x}\text{O}_3$ ', was obtained for  $0.50 \leq x \leq 1.00$  at  $\sim 1300$  °C. This will most likely extend further to compositions with lower Co content at higher temperatures.

It has been widely reported<sup>3,8,9</sup> that  $\text{LiMn}_2\text{O}_4$  can withstand a small amount of oxygen loss while retaining the cubic spinel structure, before a transition to an oxygen-deficient tetragonal spinel. This is reflected by a weight loss in TG data occurring at temperatures below those where a cubic spinel was still observed in quenched samples. This same trend is observed for compositions where  $x > 0.00$ ; it is therefore proposed that spinels in the  $\text{LiCo}_x\text{Mn}_{2-x}\text{O}_4$  solid solution can also withstand some oxygen loss before large structural transformations occur. Suggested minimum oxygen contents from TG data that heated cubic spinels can attain are listed in Table 3.2.

**Table 5.2** – Proposed minimum oxygen content for cubic spinel before transition to tetragonal symmetry (for  $x < 0.35$ ) or decomposition (for  $x > 0.35$ ).

$x$ in $\text{LiCo}_x\text{Mn}_{2-x}\text{O}_4$	Minimum oxygen content
0.00	$\text{O}_{3.97}$
0.20	$\text{O}_{3.96}$
0.35	$\text{O}_{4.00}$
0.50	$\text{O}_{3.90}$
0.75	$\text{O}_{3.89}$
1.00	$\text{O}_{3.79}$

It is interesting to note that the decomposition temperature of the  $\text{Li}_2\text{MnO}_3$ -type phase decreased with increasing amounts of Co in the starting spinel; this may suggest the formation of a  $\text{Li}_2\text{Mn}_{1-x}\text{Co}_x\text{O}_3$  solid solution. This, along with the possibility of oxygen non-stoichiometry, makes identification of the stoichiometries of the phases observed at intermediate temperatures impossible. Detailed structural refinement of the XRD data was also not possible due to the poor x-ray scattering of Li and O, and the similar x-ray scattering of Co and Mn.

Previous studies on this system used synthesis temperatures of  $\sim 800$  °C, followed by annealing at 600 °C. This work clearly shows that oxygen loss can begin in this solid solution at temperatures as low as 559 °C, and hence samples annealed at 600 °C are likely to be oxygen-deficient.

It can be concluded that a range of cubic spinel solid solutions forms at  $\sim 550$  °C for  $\text{LiCo}_x\text{Mn}_{2-x}\text{O}_4$ , where  $0.00 \leq x \leq 1.00$ . The possibility of oxygen deficiency may offer an explanation for the 4 V plateau observed in the electrochemical data for  $\text{LiCoMnO}_4$ . Samples prepared in an oxygen-deficient form would likely contain small amounts of  $\text{Mn}^{3+}$ , resulting in the presence of an unexpected  $\text{Mn}^{3+}/\text{Mn}^{4+}$  redox couple, and an associated small amount of capacity at  $\sim 4.0$  V. It is important that future work on this system reflect this, and aim for alternative synthesis methods, possibly by soft chemical routes.

The absence of peaks or inflexions in the low temperature DSC data for  $x > 0.00$  indicate that there are no first or second order phase transitions occurring below room temperature for the Co-doped compositions. Phases observed at 500 °C are retained on

cooling to at least -180 °C. Doping  $\text{LiMn}_2\text{O}_4$  with cobalt must, therefore, cause a reduction in the concentration of the Jahn-Teller active species; *i.e.*  $\text{Co}^{3+}$  replaces  $\text{Mn}^{3+}$  in the solid solution.

### 5.3.4 Conclusions

At  $\sim 550$  °C, a range of cubic spinel solid solutions forms for  $\text{LiCo}_x\text{Mn}_{2-x}\text{O}_4$ , where  $0.00 \leq x \leq 1.00$ . The inflexion in lattice parameter data centred at  $x = 0.50$  may indicate some special stability at this composition.

The stoichiometries of the majority of the high temperature phases cannot be determined exactly, but lie away from the low temperature join. However, where single phase rock salt materials were obtained at temperatures  $> 1000$  °C, the rock salt phase will most likely be of the same cationic composition as the starting spinel phase, *e.g.* the overall reaction for  $x = 1.00$  will be  $\text{LiCoMnO}_4 \rightleftharpoons \text{'LiCoMnO}_3\text{'}$ .

This work may offer an explanation for the 4 V plateau observed in the previously reported electrochemical data for  $\text{LiCoMnO}_4$ . Since samples may have been prepared in an oxygen-deficient form, they would likely contain small amounts of  $\text{Mn}^{3+}$ ; this would give a  $\text{Mn}^{3+}/\text{Mn}^{4+}$  redox couple, and a residual capacity likely to be centred at  $\sim 4.0$  V.

Future work on this system should be conducted to find alternative low temperature synthesis methods, possibly by soft chemical routes; powders prepared by such routes may also have lower particle size, of possible benefit to electrochemical performance.

## 5.4 'Li<sub>1-x</sub>Co<sub>1+2x</sub>Mn<sub>1-x</sub>O<sub>4</sub>' – phase relations in the LiCoMnO<sub>4</sub> - Co<sub>3</sub>O<sub>4</sub> system

### 5.4.1 Solid solution studies

Samples with compositions  $-0.39 \leq x \leq 1.00$  in Li<sub>1-x</sub>Co<sub>1+2x</sub>Mn<sub>1-x</sub>O<sub>4</sub> were prepared. Single phase cubic spinels were obtained for samples with  $0.00 \leq x \leq 1.00$ , *i.e.* along the join between LiCoMnO<sub>4</sub> and Co<sub>3</sub>O<sub>4</sub>.

Indexing and refinement data are presented in Table 5.3. Patterns for samples in the compositional range  $-0.39 \leq x \leq -0.14$  were found to contain traces of a second phase, Li<sub>2</sub>MnO<sub>3</sub>, whose peaks are largely overlapped by those of the majority spinel phase.

The lattice parameter data given in Table 5.3, with estimated standard deviations in parentheses, were obtained using silicon internal standard. Figure 5.13 shows the variation of lattice parameter with composition,  $x$ .

From these data, a linear increase in lattice parameter with composition,  $x$ , can be observed over the whole range  $0.00 \leq x \leq 1.00$  in Li<sub>1-x</sub>Co<sub>1+2x</sub>Mn<sub>1-x</sub>O<sub>4</sub>. This complies with Vegard's Law and suggests that a cubic spinel solid solution is formed between LiCoMnO<sub>4</sub> and Co<sub>3</sub>O<sub>4</sub>. The increase in lattice parameter from LiCoMnO<sub>4</sub> ( $x = 0.00$ ) out to the proposed end-member phase "Li<sub>1.5</sub>Mn<sub>1.5</sub>O<sub>4</sub>" ( $x = -0.50$ ) also suggested the formation of a solid solution, but for these samples Li<sub>2</sub>MnO<sub>3</sub> was also present as a second phase. It seems likely, therefore, that the spinel compositions for  $x < 0.00$  do not have the formula Li<sub>1-x</sub>Co<sub>1+2x</sub>Mn<sub>1-x</sub>O<sub>4</sub> but instead occur elsewhere on the phase diagram.

Figure 5.13 – Variation of lattice parameter with composition,  $x$ , for  $\text{Li}_{1-x}\text{Co}_{1+2x}\text{Mn}_{1-x}\text{O}_4$

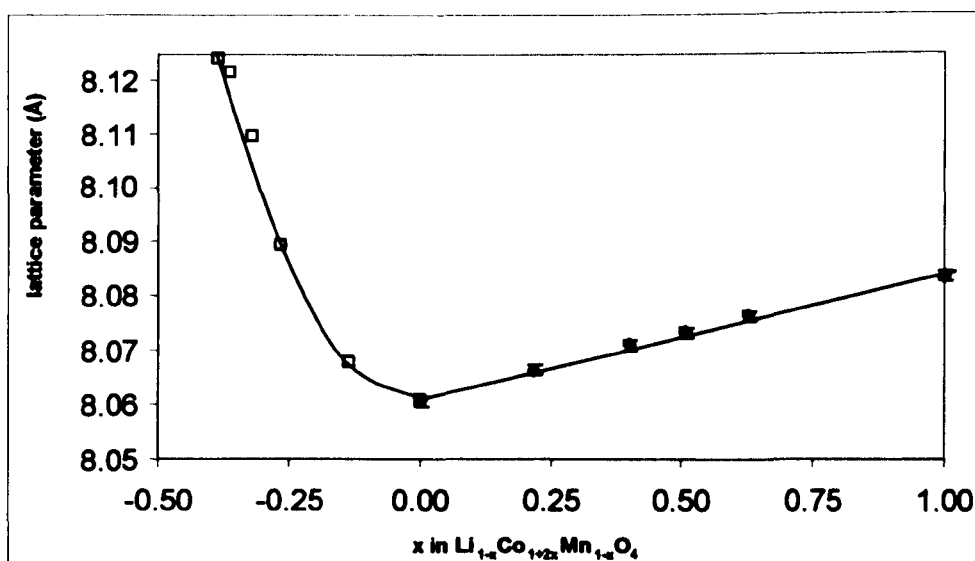


Table 5.3 – Lattice parameter data for  $x = -0.385 - 1$  in  $\text{Li}_{1-x}\text{Co}_{1+2x}\text{Mn}_{1-x}\text{O}_4$

\* - Samples contained traces of  $\text{Li}_2\text{MnO}_3$

$x$ in $\text{Li}_{1-x}\text{Co}_{1+2x}\text{Mn}_{1-x}\text{O}_4$	Stoichiometry	Lattice Parameter, $a$ (Å)
-0.39	" $\text{Li}_{1.38}\text{Co}_{0.22}\text{Mn}_{1.38}\text{O}_4$ "	8.1244 (10)*
-0.36	" $\text{Li}_{1.36}\text{Co}_{0.28}\text{Mn}_{1.36}\text{O}_4$ "	8.1215 (16)*
-0.32	" $\text{Li}_{1.32}\text{Co}_{0.36}\text{Mn}_{1.32}\text{O}_4$ "	8.1097 (17)*
-0.26	" $\text{Li}_{1.26}\text{Co}_{0.48}\text{Mn}_{1.26}\text{O}_4$ "	8.0892 (10)*
-0.14	" $\text{Li}_{1.14}\text{Co}_{0.72}\text{Mn}_{1.14}\text{O}_4$ "	8.0680 (3)*
0.00	$\text{LiCoMnO}_4$	8.0606 (14)
0.22	$\text{Li}_{0.78}\text{Co}_{1.44}\text{Mn}_{0.78}\text{O}_4$	8.0665 (7)
0.40	$\text{Li}_{0.60}\text{Co}_{1.80}\text{Mn}_{0.60}\text{O}_4$	8.0684 (4)
0.51	$\text{Li}_{0.49}\text{Co}_{2.02}\text{Mn}_{0.49}\text{O}_4$	8.0733 (6)
0.63	$\text{Li}_{0.37}\text{Co}_{2.26}\text{Mn}_{0.37}\text{O}_4$	8.07629 (17)
1.00	$\text{Co}_3\text{O}_4$	8.0838 (19)

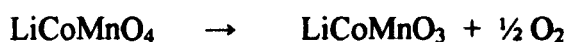
## 5.4.2 Thermal behaviour studies

Post-reaction annealing at 500 °C gave samples of improved crystallinity; Kawai<sup>4-6</sup> linked this stage to a small increase in the oxygen content of the LiCoMnO<sub>4</sub> spinel. To study this further, samples with  $0.00 \leq x \leq 1.00$  in Li<sub>1-x</sub>Co<sub>1+2x</sub>Mn<sub>1-x</sub>O<sub>4</sub> were studied using combined TG and DTA. The data for  $x = 0.00$  (LiCoMnO<sub>4</sub>) in air were discussed in section 5.3.2, with data presented in Figure 5.8. Studies on this composition were also conducted in nitrogen and oxygen atmospheres, with data presented here in Figure 5.14. The data obtained for  $x > 0.00$  are presented in Figures 5.15 – 5.19.

### 5.4.2a Thermogravimetry results

From these data it can be observed that all samples exhibit weight loss, on heating to 1000 – 1200 °C, corresponding to  $> 0.95$  oxygen atoms. This loss is assumed to be due to oxygen loss, a valid assumption due to the degree of reversibility (any cation volatility would almost certainly be irreversible), and verified by mass spectroscopy by Mandal *et al.*<sup>7</sup>

The effect of atmosphere is, therefore, of interest. Figure 5.14 demonstrates the effect of changing oxygen partial pressure on the reaction taking place:



By using an oxygen atmosphere (high  $p\text{O}_2$ ), the equilibrium in this reaction is shifted to the left-hand side, following Le Chatelier's principle, and oxygen loss subsequently occurs at a higher temperature. Correspondingly, running the experiment in a nitrogen atmosphere (low  $p\text{O}_2$ ) shifts the equilibrium to the right-hand side, with oxygen loss occurring at lower temperatures.

It can also be seen that for  $x = 1.00$  (Co<sub>3</sub>O<sub>4</sub>, Figure 5.19) a sharp weight loss occurs over a narrow range of temperatures ( $\sim 40$  °C). As  $x$  decreases (*i.e.* as Co content decreases), the weight loss occurs over a wider temperature range, starts at an earlier temperature and gradually shifts from being a definite one-step process to a clear two-step process.

The reasons behind this are unknown, but it appears as though the oxygen loss becomes increasingly irreversible with decreasing Co content (*i.e.* as  $x$  decreases).

### 5.4.3 Binary Phase Diagram for $\text{Li}_{1-x}\text{Co}_{1+2x}\text{Mn}_{1-x}\text{O}_4$ join

To study the thermal behaviour further, samples were quenched from 600 – 1250 °C (*i.e.* to attempt stabilisation of high temperature phase(s) to room temperature). The samples were then studied by XRD, with lattice parameters obtained using least squares refinement of XRD peaks from Si internal standards.

The results for all quenching experiments are presented in Figure 5.21 as a phase diagram. For the whole compositional range, the spinel structure was retained to at least 700 °C (for  $x = 0.00$ ); the stability range increased with cobalt content (*i.e.* for  $x = 1.00$ , the spinel was stable to > 900 °C). At high temperatures (> 1200 °C for  $x = 0.00$ , decreasing to > 1000 °C for  $x = 1.00$ ) a simple pattern was observed that could be indexed on a face centred cubic cell. Intensity calculations showed good agreement with a simple rock salt structure containing a disordered arrangement of octahedrally coordinated Li, Co and Mn, consistent with a 1:1 cation:oxygen ratio as in 'LiCoMnO<sub>3</sub>'.

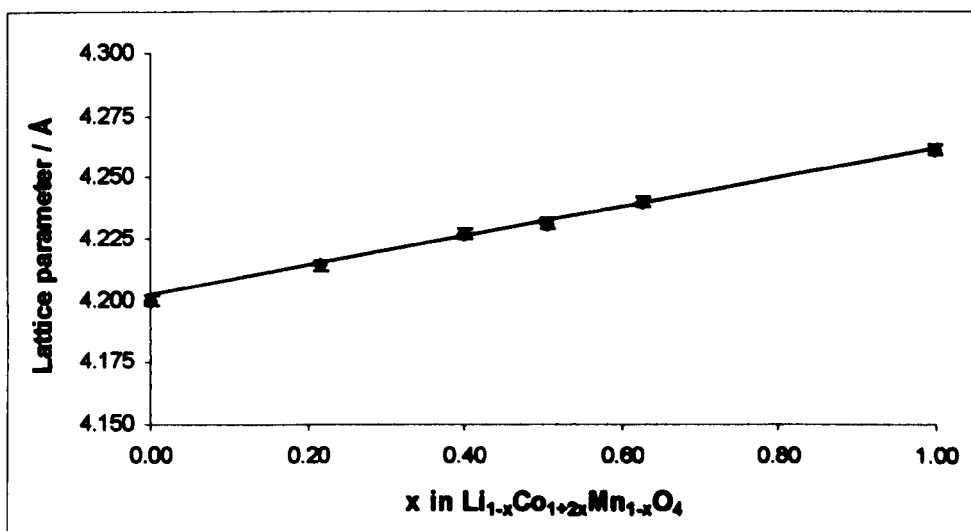
At intermediate temperatures, a pair of two phase regions was identified. For  $x < 0.51$ , samples quenched from temperatures inside the area enclosed by two sets of DTA peaks were found to give a mixture of spinel and  $\text{Li}_2\text{MnO}_3$ . At temperatures above the second DTA peak, and above the single DTA peak observed for  $x \geq 0.51$ , a mixture of cubic spinel and simple disordered cubic rock salt was observed.

The TG data show weight loss beginning at significantly lower temperatures than the DTA or quench experiments indicate structural transformations occur; this suggests that the spinel phase can withstand some oxygen loss before the rock salt phase starts to form, but that for the majority of the weight loss period, two phases (a cubic spinel and either  $\text{Li}_2\text{MnO}_3$  or a simple disordered rock salt) are present. At elevated temperatures – *i.e.* once the rock salt structure is attained – the rate at which weight is lost from the samples decreases dramatically. A high temperature plateau is observed only for the  $\text{Co}_3\text{O}_4$  sample. This may be present at higher temperatures for the other samples (corresponding to an oxygen content of 3.0), but these were not studied due to the risk

During the two-phase region where disordered rock salt and spinel mixtures occur, the composition of both phases is clearly changing, as evidenced by the change in lattice parameters. It is not currently known whether the compositional changes are due to changes in the cation stoichiometry of the two phases, or, more simply, due to changes in their oxygen contents. For both phases, the lattice parameters increase with increasing temperature, and with decreasing oxygen content. This would be consistent with a reduction in oxygen content of both phases, since the reduction in average cation valence should lead to an expansion in unit cell volume.

The lattice parameter for these high temperature rock salt phases decreases in a linear manner with decreasing Co content / increasing Li content along the rock salt solid solution (Figure 5.24). This decrease in lattice parameter with composition can be explained by the smaller ionic radii for Li than for Co and Mn.<sup>10</sup>

*Figure 5.24 – Rock salt lattice parameters for samples with compositions in the solid solution  $Li_{1-x}Co_{1+2x}Mn_{1-x}O_4$  quenched from ~ 1220 °C.*



#### 5.4.4 Conclusions

A single phase spinel solid solution forms for the compositional range  $\text{Li}_{1-x}\text{Co}_{1+2x}\text{Mn}_{1-x}\text{O}_4$ , with  $0.00 \leq x \leq 1.00$ . As reported for  $\text{LiCoMnO}_4$  previously,<sup>11</sup> this solid solution loses one oxygen atom per formula unit to form a single phase rock salt, of stoichiometry 'LiCoMnO<sub>3</sub>' (or  $\text{Li}_{1/3}\text{Co}_{2/3}\text{Mn}_{1/3}\text{O}$ ), at high temperatures. This reaction is fully reversible, although the spinel formed with faster cooling rates is oxygen deficient. Difficulties have had to be overcome in preparing single-phase materials with  $x < 0.51$ , due to oxygen loss occurring below the reaction temperature, and the segregation of  $\text{Li}_2\text{MnO}_3$  as a second phase. Future work should aim to research possible low temperature synthesis methods.

The stoichiometries of the intermediate phases are unknown. The changes in lattice parameter of the spinel and rock salt phases coexisting at intermediate temperatures suggest that either their cation stoichiometry or oxygen content (or both) are changing with temperature.

The lattice parameter,  $a$ , increases in a non-linear manner with composition,  $x$ ; *i.e.* this solid solution does not comply with Vegard's Law. No evidence of any second phases was observed in the samples annealed at 500 °C. The substitution mechanism for doping on this join is:



In Chapter 3 it was proposed that all Mn in  $\text{Co}_{1.7}\text{Mn}_{1.3}\text{O}_4$  (*i.e.*  $x = 1.00$ ) is  $\text{Mn}^{3+}$ . It was proposed by Kawai *et al.*<sup>5</sup> that the most likely stoichiometry for  $x = 0.00$  was  $\text{Li}^+(\text{Co}^{3+})_{0.5}(\text{Mn}^{3+})_{0.5}(\text{Mn}^{4+})_{1.0}\text{O}_4$ . Therefore, moving from  $x = 0.00$  to  $x = 1.00$  should result in a decrease in the average oxidation states of Co ( $\text{Co}^{3+}$  to  $\text{Co}^{2.41+}$ ) and Mn ( $\text{Mn}^{3.67+}$  to  $\text{Mn}^{3+}$ ) for charge balance. A reduction in the average oxidation states of the metal cations would be consistent with an increase in unit cell dimensions.

## 5.5.2 Thermal Behaviour studies

Samples with compositions in the range  $0.00 \leq x \leq 1.00$  were studied by combined TG-DTA. The TG-DTA data for the end-members of this join have already been discussed; for  $x = 0$  ( $\text{LiCo}_{0.5}\text{Mn}_{1.5}\text{O}_4$ ) in section 5.3 and for  $x = 1.00$  ( $\text{Co}_{1.7}\text{Mn}_{1.3}\text{O}_4$ ) in Chapter 3. TG and DTA data for  $0.24 \leq x \leq 0.80$  are presented here in Figures 5.26 – 5.28.

### 5.5.2a Thermogravimetry results

The TG data for  $x = 0.00$  (*i.e.*  $\text{LiCo}_{0.5}\text{Mn}_{1.5}\text{O}_4$ ) were discussed in section 5(i); a weight loss of ~ 8.5 % of the initial sample mass occurs upon heating to ~ 1300 °C. This was attributed to oxygen loss from the structure, resulting in the probable formation of a 'LiCo<sub>0.5</sub>Mn<sub>1.5</sub>O<sub>3</sub>' rock salt phase at high temperatures.

TG data for  $\text{Li}_{0.76}\text{Co}_{0.788}\text{Mn}_{1.452}\text{O}_4$  (Figure 5.26) also show a weight loss of  $\sim 8\%$ . As discussed in sections 5.3 and 5.4, the most likely cause for this is the loss of  $\sim 1$  oxygen atom from the spinel structure. This weight loss is largely reversible, with only  $\sim 1\%$  of the original sample mass not regained after cooling.

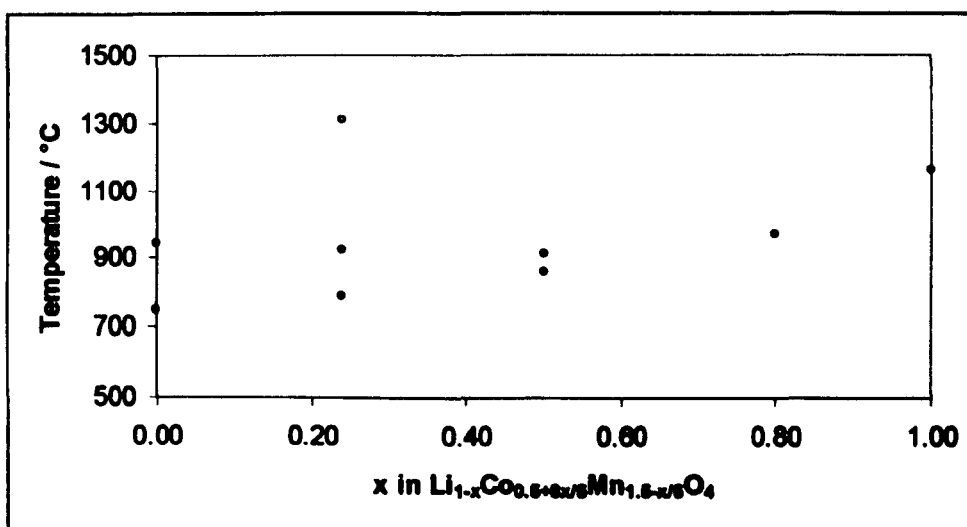
For  $x > 0.24$ , less oxygen is lost on heating, e.g. for  $x = 0.80$ , the weight lost on heating to  $1400\text{ }^\circ\text{C}$  is equivalent to only  $\sim 0.7$  oxygen atoms. There is no evidence of a plateau in the TG data at high temperatures ( $> 1200\text{ }^\circ\text{C}$ ); instead weight loss is still continuing at the maximum temperatures used.

In summary, the tendency to lose oxygen decreases with increasing  $x$ .

### 5.5.2b DTA results

The temperatures of DTA maxima were determined and are presented in Figure 5.29. Below  $1200\text{ }^\circ\text{C}$ , two peaks are observed for samples in the compositional range  $0.00 \leq x \leq 0.50$ ; only a single peak is observed in this temperature range for samples with  $x > 0.50$ . At higher temperatures, between  $1200\text{ }^\circ\text{C}$  and the maximum temperature used ( $\sim 1400\text{ }^\circ\text{C}$ ), a DTA peak is observed only for the sample with  $x = 0.24$ .

Figure 5.29 – DTA peak maxima for  $\text{Li}_{1-x}\text{Co}_{0.5+0.2x}\text{Mn}_{1.5-0.5x}\text{O}_4$



TG data showed that weight loss started at temperatures slightly lower than the two-phase regions indicated by the DTA data and the analysis of the XRD data collected from quenched samples. This suggests that a limited degree of oxygen non-stoichiometry may be possible for the cubic spinel compositions in this solid solution.

#### **5.5.4 Conclusions**

The join between  $\text{LiCo}_{0.5}\text{Mn}_{1.5}\text{O}_4$  and  $\text{Co}_{1.7}\text{Mn}_{1.3}\text{O}_4$  has been studied and a range of single phase materials prepared. These appear to form a solid solution, though the lattice parameters do not show a linear variation with composition. The proposed substitution formula for this join is  $\text{Li}_{1-x}\text{Co}_{1/2+6x/5}\text{Mn}_{1.5-x/5}\text{O}_4$ , where 5 Li and 1 Mn are replaced by 6 Co.

The thermal behaviour of samples with compositions on this join have been studied. Comparison of TG data with data from DTA and XRD on samples quenched from a range of temperatures indicate that the spinels on this join may be able to withstand a small degree of oxygen loss before decomposing to a mixture of phases. A single phase rock salt was isolated for  $x \leq 0.24$ , at temperatures in excess of 1300 °C.

## 5.6 Cubic spinel and rock salt solid solution areas in the $\text{Li}_2\text{O}-\text{CoO}_x-\text{MnO}_y$ phase diagram

### 5.6.1 Ternary $\text{Li}_2\text{O}-\text{CoO}_x-\text{MnO}_y$ phase diagram at 550 °C

In Chapter 5, the likely existence of three spinel solid solutions has been discussed, with all three stable to at least 550 °C:

- (i) The reported cubic spinel solid solution between  $\text{LiMn}_2\text{O}_4$  and  $\text{LiCoMnO}_4$ .  
(*i.e.*  $\text{LiCo}_x\text{Mn}_{2-x}\text{O}_4$ ).
- (ii) A previously unreported join between  $\text{LiCoMnO}_4$  and  $\text{Co}_3\text{O}_4$ .  
(*i.e.*  $\text{Li}_{1-x}\text{Co}_{1+2x}\text{Mn}_{1-x}\text{O}_4$ ).
- (iii) A previously unreported join between  $\text{Li}_2\text{CoMn}_3\text{O}_8$  and  $\text{Co}_{1.7}\text{Mn}_{1.3}\text{O}_4$ .  
(*i.e.*  $\text{Li}_{1-x}\text{Co}_{1/2+6x/5}\text{Mn}_{1.5-x/5}\text{O}_4$ ).

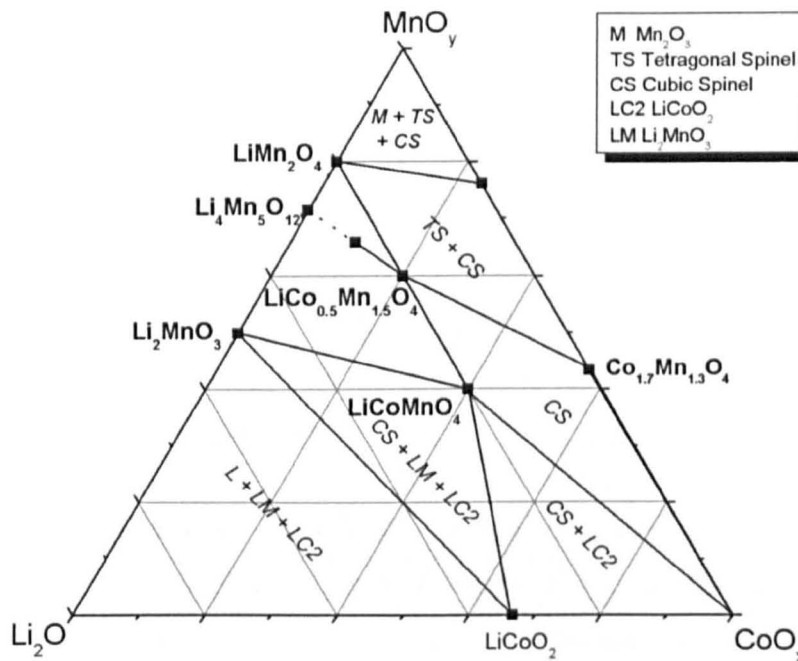
It can be seen that each of these solid solutions intersects with the other two joins, *i.e.* the  $\text{LiCo}_x\text{Mn}_{2-x}\text{O}_4$  solid solution touches both the  $\text{Li}_{1-x}\text{Co}_{1/2+6x/5}\text{Mn}_{1.5-x/5}\text{O}_4$  solid solution (at  $x = 0.50$ ) and the  $\text{Li}_{1-x}\text{Co}_{1+2x}\text{Mn}_{1-x}\text{O}_4$  solid solution (at  $x = 1.00$ ). A large portion of the  $\text{Li}_2\text{O}-\text{CoO}_x-\text{MnO}_y$  ternary phase diagram is, therefore, bounded by these three solid solutions. It is most likely that these joins are, in fact, three sections through a solid solution area, *i.e.* an area of compositions that forms single phase cubic spinels with variable lithium, cobalt and manganese ratios. Samples prepared with compositions lying within this solid solution area were single phase cubic spinels.

To these joins a further three spinel solid solutions can also be added. All have been previously reported in the literature, but two are also studied in this thesis, *viz*:

- (iv)  $\text{Co}_{3-x}\text{Mn}_x\text{O}_4$  (Chapter 3), where  $0.00 \leq x \leq 3.00$ ,
- (v)  $\text{Li}_{1+x}\text{Mn}_{2-x}\text{O}_4$  (Chapter 7), where  $0.00 \leq x \leq 0.33$ , and
- (vi) West's  $\text{Li}_{1-x}\text{Co}_{1/2+3x/2}\text{Mn}_{3/2-x/2}\text{O}_4$ , where  $-0.33 \leq x \leq 1.00$ .<sup>12</sup>

Compositions were also prepared on other possible joins and compatibility triangles in the  $\text{Li}_2\text{O}-\text{CoO}_x-\text{MnO}_y$  ternary system using the same reaction conditions. No other ternary phases or solid solutions were identified; the phase diagram obtained at ~ 550 °C in air is presented in Figure 5.30.

Figure 5.30 – The Li-Co-Mn-O phase diagram, at 500 °C in air.



### 5.6.2 Effect of temperature on spinel solid solution area

It is interesting to note that heating of any cubic spinel composition resulted in a weight loss being observed in TG data.

This weight loss was attributed to oxygen volatilization, after the work of Mandal *et al.*<sup>7</sup> A combination of TG, DTA and XRD performed on quenched samples has shown that cubic spinels in the  $\text{Li}_2\text{O}-\text{CoO}_x-\text{MnO}_y$  ternary system decompose via either of two processes:

- (i) Cubic spinel  $\rightarrow$  Spinel /  $\text{Li}_2\text{MnO}_3$  mixture
- (ii) Cubic spinel  $\rightarrow$  Spinel / disordered rock salt mixture

In general, samples with higher cobalt contents decomposed via the latter route; samples richer in Mn generally decomposed to give  $\text{Li}_2\text{MnO}_3$  as a second phase.

For all samples decomposing via route (i), an inflexion was observed in TG data after the loss of  $\sim 0.15 - 0.40$  oxygen atoms at  $\sim 900$  °C ( $\pm 30$  °C) (e.g. as observed for  $\text{LiMn}_2\text{O}_4$  (Figure 5.3) and  $\text{LiCoMnO}_4$  (Figure 5.8). This inflexion was absent in samples that decomposed to give spinel/disordered rock salt mixtures, with weight loss

#### **5.6.4 Variation of lattice parameter across spinel solid solution area**

The lattice parameters of the various single phase cubic spinel and rock salt phases were refined not only to further characterise the solid solutions, but also in an attempt to determine the stoichiometry of the intermediate compositions formed on heating. The lattice parameters for the cubic spinel and rock salt phases are overlaid onto the phase diagram in Figures 5.40 and 5.41, respectively.

The cubic spinel lattice parameter data show a minimum at  $\sim \text{LiCoMnO}_4$ , and a maximum at  $\sim \text{Co}_{1.7}\text{Mn}_{1.3}\text{O}_4$ ; the solid solution area appears to be crossed by lines of equal lattice parameter. The same trend is also witnessed for the rock salt compositions. The increase in unit cell dimensions in moving from  $\text{LiCoMnO}_4$  to  $\text{Co}_{1.7}\text{Mn}_{1.3}\text{O}_4$  is in agreement with expectations, due to the effect of the ionic radii in these compositions (*i.e.* large  $\text{Co}^{2+}/\text{Mn}^{3+}$  cations in  $\text{Co}_{1.7}\text{Mn}_{1.3}\text{O}_4$ , as opposed to the smaller  $\text{Co}^{3+}/\text{Mn}^{4+}$  cations in  $\text{LiCoMnO}_4$ ).

In every case studied the spinel lattice parameter remained unchanged on heating up until oxygen loss began. On further heating, the lattice parameter for the spinel phase (and the rock salt phase when formed) increased, until a weight loss equivalent to  $\sim 1$  oxygen atom had been completed. The rock salt lattice parameter then remained unchanged on further heating. There are a number of possible explanations for this behaviour:

- (i) Oxygen loss resulting in an oxygen deficient spinel would result in a decrease in transition metal oxidation state. The transition metals would have a larger effective cationic radii.
- (ii) A continuous compositional change in the spinel / rock salt phase on heating through the two-phase region, *e.g.* possibly involving the initial segregation of a rock salt phase with a cation content different from that of the initial spinel phase.
- (iii) A combination of both effects.

Due to the complexities of this system, it has been impossible to determine which, if any, of these possibilities is correct. The lattice parameter data suggest that both cubic spinel and rock salt solid solution areas are crossed by lines of equal lattice parameter; thus, any attempt to determine the stoichiometry of the phases observed at intermediate temperatures would be futile, since a range of compositions will share the same lattice parameter. This approach also assumed that all intermediate phases were oxygen-stoichiometric; this may not be appropriate. Determination of the precise stoichiometries of the 'intermediate' compositions observed on heating cubic spinels in the  $\text{Li}_2\text{O-CoO}_x\text{-MnO}_y$  ternary system would likely require structural analysis involving Rietveld refinement on neutron diffraction data collected over a range of temperatures.

- (1) Tarascon, J. M.; McKinnon, W. R.; Coowar, F.; Bowmer, T. N.; Amatucci, G.; Guyomard, D. *Journal of the Electrochemical Society* **1994**, *141*, 1421.
- (2) Yamada, A.; Miura, K.; Hinokuma, K.; Tanaka, M. *Journal of the Electrochemical Society* **1995**, *142*, 2149.
- (3) Sugiyama, J.; Atsumi, T.; Hioki, T.; Noda, S.; Kamegashira, N. *Journal of Alloys and Compounds* **1996**, *235*, 163.
- (4) Kawai, H.; Nagata, M.; Tukamoto, H.; West, A. R. *Electrochemical and Solid-State Letters* **1998**, *1*, 212.
- (5) Kawai, H.; Nagata, M.; Kageyama, H.; Tukamoto, H.; West, A. R. *Electrochimica Acta* **1999**, *45*, 315.
- (6) Kawai, H.; Nagata, M.; Tukamoto, H.; West, A. R. *Journal of Materials Chemistry* **1998**, *8*, 837.
- (7) Mandal, S.; Rojas, R. M.; Amarilla, J. M.; Calle, P.; Kosova, N. V.; Anufrienko, V. F.; Rojo, J. M. *Chemistry of Materials* **2002**, *14*, 1598.
- (8) Thackeray, M. M.; Mansuetto, M. F.; Dees, D. W.; Vissers, D. R. *Materials Research Bulletin* **1996**, *31*, 133.
- (9) Molenda, J.; Swierczek, K.; Kucza, W.; Marzec, J.; Stoklosa, A. *Solid State Ionics* **1999**, *123*, 155.
- (10) Shannon, R. D.; Prewitt, C. T. *Acta Crystallographica* **1969**, *B25*, 925.
- (11) Reeves, N.; Kirk, C. A.; West, A. R. *Journal of Materials Chemistry* **2001**, *11*, 249.
- (12) West, A. R.; Kawai, H.; Kageyama, H.; Tabuchi, M.; Nagata, M.; Tukamoto, H. *Journal of Materials Chemistry* **2001**, *11*, 1662.

## Chapter 6

### Electrical and Electrochemical Responses of $\text{Li}_{1-x}\text{Co}_{1+2x}\text{Mn}_{1-x}\text{O}_4$ ( $0.00 \leq x \leq 1.00$ ) and $\text{Li}_{1-x}\text{Co}_{1/2+6x/5}\text{Mn}_{1.5-x/5}\text{O}_4$ ( $0.00 \leq x \leq 1.00$ ) cubic spinels

#### 6.1 Experimental

Pellets (3mm diameter) for ac Impedance were pressed uniaxially with  $\sim 1$  tonne pressure, and sintered to produce pellets with greater than 70 % of the theoretical density. Pellets were sintered at 900 °C for 5 hours and annealed for 3 days at 500 °C to re-obtain the fully oxygenated single phase cubic spinel. Platinum electrodes were applied, and dried at 800 °C for 2 hours, with subsequent annealing at 500 °C. The pellets were removed from the furnace directly and studied by ac Impedance over the frequency range 5 Hz - 1.26 MHz.

Cells for study by GCPL were constructed and tested with the assistance of Dr Denis Pasero, a post-doctoral researcher. Test electrodes were composite materials containing 5-10 mg of the active material, *i.e.*  $\text{Li}_{1-x}\text{Co}_{1+2x}\text{Mn}_{1-x}\text{O}_4$  ( $0.00 \leq x \leq 1.00$ ) or  $\text{Li}_{1-x}\text{Co}_{1/2+6x/5}\text{Mn}_{1.5-x/5}\text{O}_4$  ( $0.00 \leq x \leq 1.00$ ), carbon black and PVdF binder in a ratio of 80/10/10 wt%. A 1.69 cm<sup>2</sup> Li metal disk acted as a counter-electrode. The electrolyte used was 1 M LiPF<sub>6</sub> in propylene carbonate. All cells were constructed in an argon-filled glove box, with care taken to eliminate water from the atmosphere.

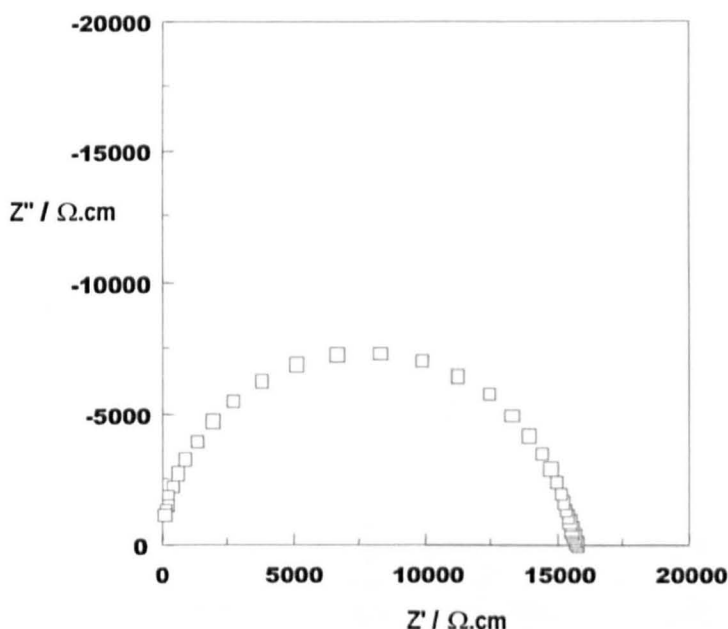
GCPL studies were undertaken in two ways: for anode studies, cells were cycled at C/5 rate (*i.e.* 1 Li per formula unit every 5 hours) using a potential window of 0.25 – 2.5 V; for cathode studies, cells were cycled at C/10 rate (*i.e.* 1 Li per formula unit every 10 hours) using a potential window of 2.5 – 5.1 V.

## 6.2 ac Impedance

### 6.2.1 $\text{Li}_{1-x}\text{Co}_{1+2x}\text{Mn}_{1-x}\text{O}_4$

Impedance data for  $0.00 \leq x \leq 1.00$  were recorded over a range of temperatures (25 – 133 °C); the complex plane plot for  $x = 0.00$  is presented in Figure 6.1. For all compositions studied, only a single arc was observed in the complex plane plots. This arc has an associated capacitance of  $\sim 2.3 \times 10^{-11} \text{ F cm}^{-1}$ , characteristic of a bulk response.

Figure 6.1 – Complex plane plot for  $\text{LiCoMnO}_4$  ( $x = 0.00$ ); data collected at room temperature.



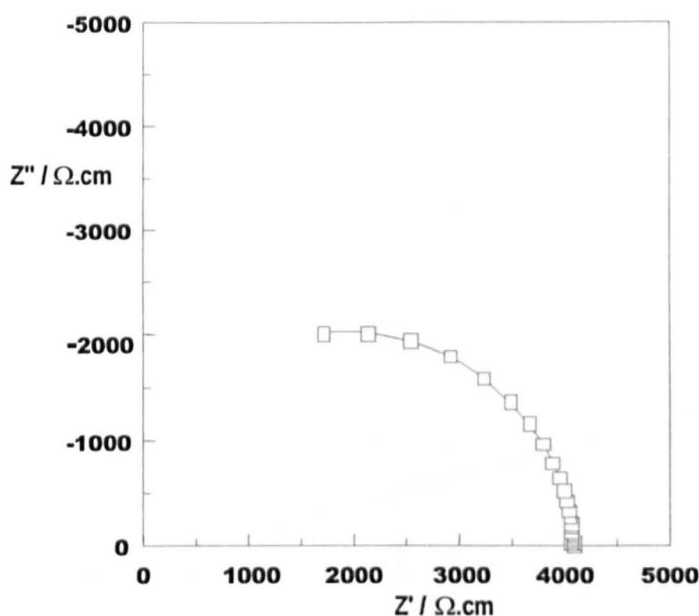
The modest level of semiconductivity observed for  $x = 0.00$  is in good agreement with data reported previously by Kawai *et al.*<sup>1</sup>

No lower frequency phenomena, such as grain boundary resistances or electrode spikes, were observed. The main charge carriers are likely to be electrons; this does not preclude the possibility of some  $\text{Li}^+$ -ion conductivity.

Bulk conductivities for samples of composition  $0.00 \leq x \leq 1.00$  are presented in the form of an Arrhenius plot in Figure 6.2. Activation energies are presented in Figure 6.3. The conductivity data have a maximum at  $x = 0.00$ , though the variation in conductivity with composition does not follow a clear pattern.

Impedance data for  $0.00 \leq x \leq 1.00$  were recorded over a range of temperatures (25 – ~ 70 °C); the complex plane plot for  $x = 0.50$  is presented in Figure 6.4. For all compositions studied, only part of a single arc was resolved in the complex plane plots. This arc has an associated capacitance of  $\sim 1.6 \times 10^{-11} \text{ F cm}^{-1}$ , characteristic of a bulk response.

Figure 6.4 – Complex plane plot for  $x = 0.50$ , recorded at 28 °C.



No low frequency phenomena, such as electrode spikes, were observed; therefore, the main charge carriers are likely to be electrons. However, it is possible that some  $\text{Li}^+$ -ion conductivity may still be occurring.

Bulk conductivities for samples of composition  $0.00 \leq x \leq 1.00$  are presented in the form of an Arrhenius plot in Figure 6.5. Activation energies are presented in Figure 6.6. The conductivity data have a maximum at  $x = 1.00$ . The conductivity data follow a clear pattern, decreasing from  $\text{Li}_2\text{CoMn}_3\text{O}_8$  ( $x = 0.00$ ), through a minimum between  $x = 0.24$  and  $x = 0.50$ . The activation energies also show an approximately linear increase with  $x$ .

## 6.3 Galvanostatic Cycling

### 6.3.1 Results for $\text{Li}_{1-x}\text{Co}_{1+2x}\text{Mn}_{1-x}\text{O}_4$

Cells containing samples with compositions on the  $\text{Li}_{1-x}\text{Co}_{1+2x}\text{Mn}_{1-x}\text{O}_4$  solid solution were cycled over two ranges of potential; *i.e.* (i) between 3.0 and 5.1 V, at C/10 rate, and (ii) between 0.25 and 2.5 V, at C/5 rate.

All samples showed at least some electrochemical activity in both potential 'windows'. The data for  $\text{LiCoMnO}_4$  (Figures 6.7, 6.8 and 6.11) and  $\text{Li}_{0.49}\text{Co}_{2.02}\text{Mn}_{0.49}\text{O}_4$  ( $x = 0.51$ , Figures 6.9, 6.10 and 6.12) are presented as examples; the electrochemical response of  $\text{Co}_3\text{O}_4$  (*i.e.*  $x = 1.00$  in this solid solution) was discussed in Chapter 4.

$\text{LiCoMnO}_4$  exhibits two plateaux on charging between 3.0 and 5.1 V; a short plateau centred on  $\sim 4.0$  V possesses capacity of  $\sim 10$  mAh  $\text{g}^{-1}$ , while at higher voltages a longer plateau, centred on  $\sim 5.0$  V, corresponds to a capacity of  $\sim 115$  mAh  $\text{g}^{-1}$ . This plateau, which has a small inflexion at  $\sim 5.0$  V, may extend to higher potentials, but electrolyte oxidation caused a significant false capacity reading at potentials over  $\sim 5.15$  V.

$\text{LiCoMnO}_4$  was also found to exhibit an electrochemical response (Figure 6.8) when cycled between 0.25 and 2.5 V, with  $\sim 7$  Li atoms inserted into the structure over a plateau centred on  $\sim 0.8$  V. On subsequent charging,  $\sim 4$  of the Li could be removed. Thereafter,  $\sim 4$  Li could be cycled in/out of the structure with good capacity retention. This level of reversible Li insertion corresponds to specific capacities of  $\sim 550$  mAh  $\text{g}^{-1}$ ; charge/discharge capacities for the first five cycles are presented in Figure 6.8.

Samples with composition,  $x > 0.00$  also exhibit a limited electrochemical response on a plateau centred at  $\sim 5.0$  V. For  $\text{Li}_{0.49}\text{Co}_{2.02}\text{Mn}_{0.49}\text{O}_4$  ( $x = 0.51$ ), a specific charge capacity of  $\sim 40$  mAh  $\text{g}^{-1}$  (Figure 6.9) was observed, though this is not reversible and therefore can only be attributed to electrolyte oxidation. On further cycling of cells with active materials in this compositional range, this '5 V' plateau moved to lower potentials, centred on  $\sim 4.5$  V. The capacity left for each composition after 10 cycles is presented in Figure 6.13. Only the cell with  $\text{LiCoMnO}_4$  as the active material showed a significant capacity.

Samples with composition,  $x > 0.00$  also exhibit an electrochemical response when cycled between 0.25 and 2.5 V; data for  $\text{Li}_{0.49}\text{Co}_{2.02}\text{Mn}_{0.49}\text{O}_4$  ( $x = 0.51$ ) are presented in Figure 6.10;  $\sim 9$  Li atoms can be inserted into the structure over a plateau centred on  $\sim 0.8$  V. On subsequent charging, almost 6 of the Li could be removed. Thereafter,  $\sim 5.5$  Li could be cycled in/out of the structure. This level of reversible Li insertion corresponds to specific capacities of  $\sim 700 \text{ mAh g}^{-1}$ ; discharge/charge capacities for the first five cycles are presented in Figure 6.12.

The variation of capacities, in terms of number of Li that can be inserted, with composition for 1<sup>st</sup> and 10<sup>th</sup> cycle are presented in Figure 6.14. In general, the capacity achieved (at any stage of cycling) increases as  $x$  increases, *i.e.* as the amount of Li in the original structure decreases.

The calculated specific capacity for the insertion of 1 Li atom into samples with compositions in the  $\text{Li}_{1-x}\text{Co}_{1+2x}\text{Mn}_{1-x}\text{O}_4$  solid solution is presented in Figure 6.15; the calculated specific capacity decreases as  $x$  increases; *i.e.* the samples of lowest formula weight have the greatest specific capacity for insertion of 1 Li. Insertion of 1 Li into  $\text{LiCoMnO}_4$  gives a 30 % increase in specific capacity relative to  $\text{Co}_3\text{O}_4$ .

**Figure 6.11** – Variation in discharge/charge specific capacity of plateau centred on  $\sim 0.8$  V upon cycling for  $\text{LiCoMnO}_4$  ( $x = 0.00$ ).

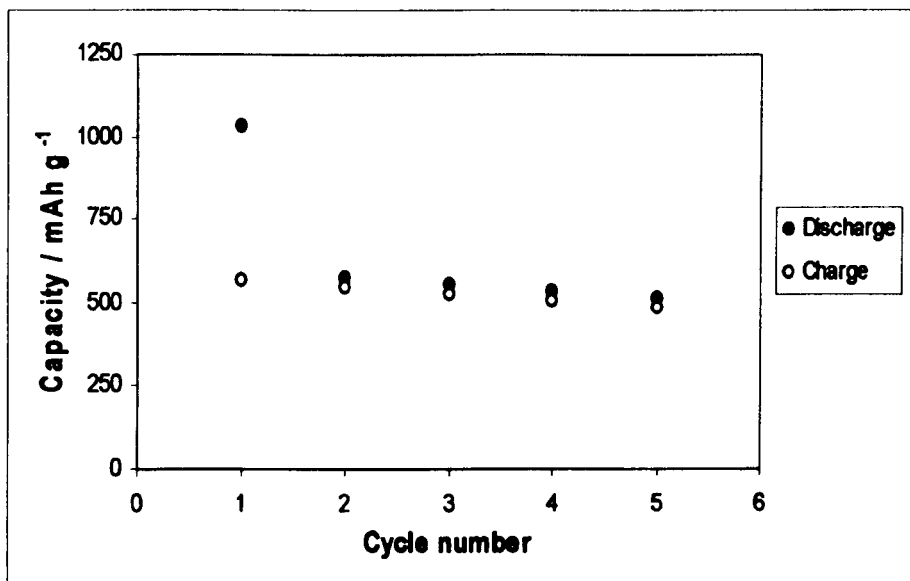
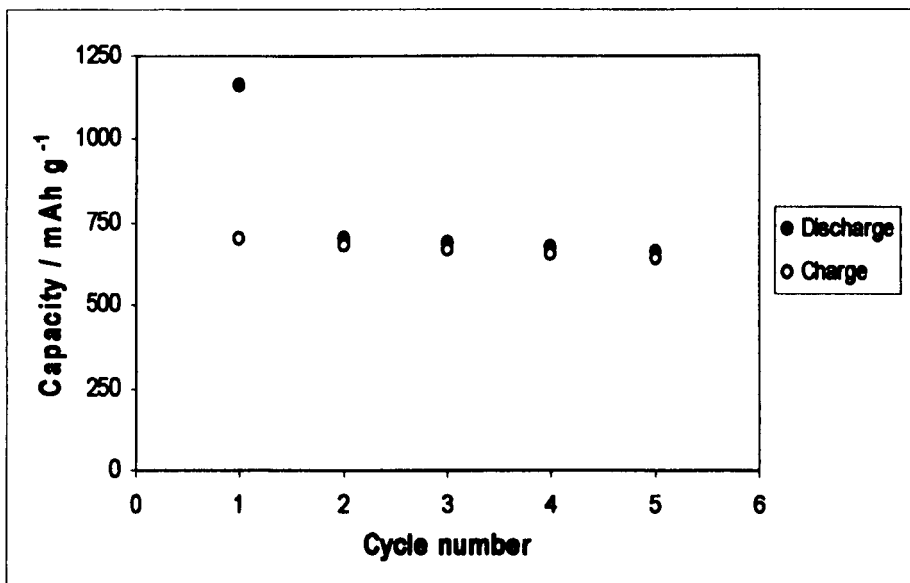


**Figure 6.12** – Variation in discharge/charge specific capacity of plateau centred on  $\sim 0.8$  V upon cycling for  $\text{Li}_{0.49}\text{Co}_{2.02}\text{Mn}_{0.49}\text{O}_4$  ( $x = 0.51$ ).



### 6.3.2. Discussion of results for $\text{Li}_{1-x}\text{Co}_{1+2x}\text{Mn}_{1-x}\text{O}_4$

The electrochemical response observed for  $\text{LiCoMnO}_4$  between 3.0 and 5.1 V is comparable with that observed in the literature. The presence of the small plateau centred on  $\sim 4.0$  V cannot be explained by these data; one possibility is that the post-reaction annealing step at 500 °C does not provide conditions energetic enough to produce a spinel that is either completely single phase (*i.e.* traces of  $\text{Li}_2\text{MnO}_3$  remain in the sample) and/or fully oxygenated (*i.e.* the reacted spinel has stoichiometry  $\text{LiCoMnO}_{4.8}$ ).

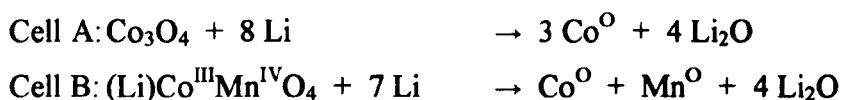
The long plateau at  $\sim 5.0$  V, with specific capacity of  $\sim 115$  mAh  $\text{g}^{-1}$ , gives an energy density of 575 W h  $\text{kg}^{-1}$  – comparable with that reported for  $\text{LiCoO}_2$ . The likely origin of this activity is the  $\text{Co}^{3+} \rightleftharpoons \text{Co}^{4+}$  redox couple. However, significant problems were encountered in cycling to the high potentials encountered, and improved electrolytes stable to high potentials ( $\geq 5.5$  V) are required to allow full study of this material.

This long plateau also shows evidence of an inflexion at  $\sim 5.0$  V, approximately at the middle of the charge plateau. A similar effect is observed for  $\text{LiMn}_2\text{O}_4$ , (see Figure 1.18 or Figure 2.7) and is attributed to the ordering of lithium ions over tetrahedral sites after 50 % of the lithium has been removed.

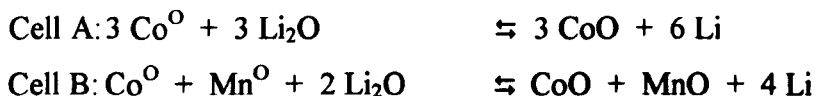
The cathodic performance of samples with  $x > 0.00$  was poor, with low irreversible capacities ( $< 50$  mAh  $\text{g}^{-1}$ ) observed. The observed practical capacities decreased rapidly with increasing Co dopant level, *i.e.* with  $x$ . This is likely to be partially due to the doping mechanism, where Co replaces both Li on the tetrahedral site and Mn on the octahedral site. The Co residing on the tetrahedral site will most likely block the  $\text{Li}^+$ -ion conduction pathway, thereby making it harder to remove Li. The amount of Li to remove also decreases with increasing Co dopant (following the doping mechanism of 1 Li and 1 Mn being replaced by 2 Co). The capacity observed here for  $x > 0.22$  is most likely due simply to electrolyte oxidation.

All of the compositions from the  $\text{Li}_{1-x}\text{Co}_{1+2x}\text{Mn}_{1-x}\text{O}_4$  solid solution showed significant capacity for Li insertion at  $\sim 0.8$  V. The data are consistent with the insertion reaction proposed in the literature<sup>2,3</sup> for  $\text{Co}_3\text{O}_4$ , *i.e.* on first discharge, the spinel is fully reduced to the metal, though any structural lithium forms lithia ( $\text{Li}_2\text{O}$ ). If we consider two

example test cells, where  $\text{Co}_3\text{O}_4$  ('cell A') or  $\text{LiCoMnO}_4$  ('cell B') are used as the active anode material:



Excess lithia is then consumed on further discharging to lower potentials due to the formation of solid-electrolyte interface (SEI) phenomena. On charge, the transition metals are only partially re-oxidised to form the rock salt, *e.g.*:



This reaction is then followed on subsequent discharge/charge cycles. The theoretical capacities presented in Figure 6.14 were calculated using this mechanism. The practical discharge capacities of cells with  $\text{Li}_{1-x}\text{Co}_{1+2x}\text{Mn}_{1-x}\text{O}_4$  as the active material, shown for cycles 1 and 10 in Figure 6.14 all agree well with this proposed mechanism, *i.e.* all show greater than theoretical capacity on first discharge (allowing for full reduction of the transition metals and formation of SEI phenomena) and then on subsequent cycling reach, or at least come close to, the theoretical capacity.

The theoretical and observed amount of lithium that can be inserted into the electrode material decreases as  $x$  decreases (*i.e.* as the amount of structural Li increases). However, the specific capacity associated with the insertion of a lithium ion is inversely proportional to the formula weight of the host structure, as shown in equation 2.28. The formula weight decreases with decreasing Li content, *i.e.* as  $x$  decreases; therefore, the specific capacity obtained for the insertion of a Li ion rises notably as  $x$  decreases. Large specific capacities can be obtained, as presented for  $x = 0.00$  (Figure 6.11) and  $x = 0.51$  (Figure 6.12), despite less Li being inserted; the observed specific capacity for  $x = 0.51$  of  $\sim 700 - 750 \text{ mAh g}^{-1}$  is comparable with the best reported capacities for other candidate anode materials (*e.g.*  $\text{Co}_3\text{O}_4$ ). The replacement of Co with Li and Mn also offers significant improvements in terms of cost and toxicity. These materials are of great interest for future study as possible anodes for the next generation of Li-ion batteries.

Studies on the capacity retention over a number of cycles were limited, due to the amount of time involved. However, the capacity retention for two cells, where  $x = 0.00$  and  $0.51$ , over the first five cycles is presented in Figures 6.11 and 6.12, respectively. After the large drop in capacity associated with the irreversible reduction of the spinel, both cells show excellent cycling performance; in particular, for  $x = 0.51$ , 57 % of first discharge capacity remains on 5<sup>th</sup> discharge. This rises to 94.3 % if we consider the amount of second charge capacity remaining; as discussed in Chapter 4, this becomes relevant if a 'lithium-rich' cathode (such as  $\text{Li}_{1+x}\text{Mn}_2\text{O}_4$ , where  $x > 0$ ) is used as the positive electrode.

The sample with composition  $x = 0.51$  has much potential as a possible anode material; the combination of high specific capacity and potentially good cycling performance, added to lower formula mass, cost and toxicity (compared to the much-reported candidate material,  $\text{Co}_3\text{O}_4$ ), make this composition very interesting for future study.

### 6.3.3 Results for $\text{Li}_{1-x}\text{Co}_{1/2+6x/5}\text{Mn}_{3/2-x/5}\text{O}_4$

Cells containing samples with compositions on the  $\text{Li}_{1-x}\text{Co}_{1/2+6x/5}\text{Mn}_{3/2-x/5}\text{O}_4$  solid solution were cycled over two ranges of potential; *i.e.* (i) between 3.0 and 5.1 V, at C/10 rate, and (ii) between 0.25 and 2.5 V, at C/5 rate.

All samples showed at least some electrochemical activity in both potential 'windows'. The data for  $\text{Li}_2\text{CoMn}_3\text{O}_8$  ( $x = 0.00$ , Figures 6.16, 6.17 and 6.20) and  $\text{Li}_{0.49}\text{Co}_{2.02}\text{Mn}_{0.49}\text{O}_4$  ( $x = 0.51$ , Figures 6.18, 6.19 and 6.21) are presented as examples; the electrochemical response of  $\text{Co}_{1.7}\text{Mn}_{1.3}\text{O}_4$  (*i.e.*  $x = 1.00$  in this solid solution) was discussed in Chapter 4.

The electrochemical extraction of lithium from  $\text{Li}_2\text{CoMn}_3\text{O}_8$  ( $x = 0.00$ , Figure 6.16) proceeds initially at a plateau centred on  $\sim 4.0$  V, then at a plateau centred on  $\sim 5.0$  V. The two plateaux are separated by a fairly sharp transition. The plateau at  $\sim 4.0$  V has a specific capacity of  $\sim 60$  mAh  $\text{g}^{-1}$ , while the plateau at  $\sim 5.0$  V had a lower observed specific capacity of  $\sim 50$  mAh  $\text{g}^{-1}$ . This plateau may continue to higher voltages; however, significant electrolyte oxidation occurred above 5.1 V, and so this could not be studied reliably.

The electrochemical insertion of  $\sim 8$  lithium ions into  $\text{Li}_2\text{CoMn}_3\text{O}_8$  ( $x = 0.00$ , Figure 6.17) was observed on first charge. Thereafter, only  $\sim 2$  Li ions could be extracted. The amount of lithium ions that could be inserted on subsequent discharges decreased notably with each cycle. Observed specific capacities were limited to  $\sim 250$  mAh  $\text{g}^{-1}$  (Figure 6.20).

Samples with composition,  $x > 0.00$  also exhibit a limited electrochemical response on charge plateaux centred at  $\sim 4.0$  V and  $\sim 5.0$  V. For  $\text{Li}_{0.5}\text{Co}_{1.1}\text{Mn}_{1.4}\text{O}_4$  ( $x = 0.50$ ), a specific charge capacity of  $\sim 40$  mAh  $\text{g}^{-1}$  (Figure 6.18) was observed. This capacity was not reversible on discharge. On further cycling of cells with active materials in this compositional range, the '4 V' and '5 V' plateaux moved to  $\sim 4.5$  V. The capacity remaining after 10 cycles for each composition is presented in Figure 6.22. Only the cells with compositions  $x \leq 0.24$  as the active material showed significant reversible capacity.

The electrochemical insertion of Li into cells with active electrodes containing samples with compositions  $x > 0.00$  also indicated that  $\sim 8$  lithium ions could be inserted on first discharge for each composition. However, on subsequent charge only  $\sim 3 - 4$  Li ions could be extracted from the lithium-doped materials. Almost 6 Li ions could be removed on first charge from the sample with  $x = 1.00$ , *i.e.*  $\text{Co}_{1.7}\text{Mn}_{1.3}\text{O}_4$ , which also showed the highest capacity; this is discussed in Chapter 4. From the lithium-containing materials,  $x = 0.50$  (Figure 6.21) showed the highest specific capacities ( $\sim 500 \text{ mAh g}^{-1}$ ).

The variation of capacities, in terms of number of Li that can be inserted, with composition for 1<sup>st</sup> and 10<sup>th</sup> cycle are presented in Figure 6.23. The capacity achieved on 10<sup>th</sup> cycle increases very approximately as  $x$  increases, *i.e.* as the amount of Li in the original structure decreases.

The calculated specific capacity for the insertion of 1 Li atom into samples with compositions in the  $\text{Li}_{1-x}\text{Co}_{1/2+6x/5}\text{Mn}_{3/2-x/5}\text{O}_4$  solid solution is presented in Figure 6.24; the calculated specific capacity decreases as  $x$  increases; *i.e.* samples of the lowest formula weight have the largest specific capacity for insertion of 1 Li. Insertion of 1 Li into  $\text{Li}_{2+y}\text{CoMn}_3\text{O}_8$  gives a  $\sim 29\%$  increase in specific capacity relative to  $\text{Co}_{1.7}\text{Mn}_{1.3}\text{O}_4$ .

#### 6.3.4 Discussion of results for $\text{Li}_{1-x}\text{Co}_{1/2+6x/5}\text{Mn}_{3/2-x/5}\text{O}_4$

The largest specific capacity in the 3.0 – 5.1 V potential window was observed for  $x = 0.00$ , *i.e.*  $\text{Li}_2\text{CoMn}_3\text{O}_8$ . The data obtained are comparable with those reported in the literature. The ‘4 V’ plateau is most likely due to the  $\text{Mn}^{3+} \rightleftharpoons \text{Mn}^{4+}$  redox couple; the ‘5 V’ plateau is most likely the result of the  $\text{Co}^{3+} \rightleftharpoons \text{Co}^{4+}$  redox couple.

Since full extraction of lithium proceeds at two separate potential steps, it is unlikely that this phase will be industrially applicable. For the phases in the  $\text{Li}_{1-x}\text{Co}_{1/2+6x/5}\text{Mn}_{3/2-x/5}\text{O}_4$  solid solution with  $x > 0.00$ , both high potential plateaux shorten. As  $x$  increases, the Li in the tetrahedral site is replaced by Co; therefore, there is less lithium to remove, and Co blocks the conduction pathway for the removal of what lithium remains, resulting in lower capacity. Again, the charge capacity for  $x \geq 0.50$  is most likely due entirely to electrolyte oxidation.

Insertion of lithium into phases with  $0.00 \leq x \leq 1.00$  proceeded at potentials below 1 V. On first discharge,  $\sim 8$  Li can be inserted for all compositions. The theoretical variation for the insertion of lithium causing full reduction of the transition metals is presented in Figure 6.23; *i.e.* for full reduction of the transition metals in  $\text{Co}_{1.7}\text{Mn}_{1.3}\text{O}_4$  ( $x = 1.00$ ), eight lithium ions will be required. Since all samples showed at least the theoretical minimum, this level of insertion is indicative of complete reduction of the transition metals and formation of solid-electrolyte interface phenomena.

The electrochemical response of  $\text{Co}_{1.7}\text{Mn}_{1.3}\text{O}_4$  has been discussed in Chapter 4; of the doped materials in the  $\text{Li}_{1-x}\text{Co}_{1/2+6x/5}\text{Mn}_{3/2-x/5}\text{O}_4$  solid solution, the sample with composition  $x = 0.50$  showed the best performance as an anode material. For cells containing this as the active material, around 4 Li could be extracted on first charge and then reversibly inserted and extracted with reasonable cyclability on further cycling. Specific discharge capacities (Figure 6.24) for the insertion of 1 Li into phases on this solid solution increase with Li content, since as  $x$  decreases the formula weight of the spinel also decreases. This helps to balance the relatively low amount of Li that can be inserted, and subsequently reasonable discharge capacities of  $\sim 500 \text{ mAh g}^{-1}$  were obtained for  $x = 0.50$  with reasonable capacity retention for the limited number of cycles performed.

## 6.4 Conclusions

A number of cubic spinel compositions were studied for possible cathode applications; of these,  $\text{LiCoMnO}_4$  exhibits the largest specific capacity, *ca.*  $115 \text{ mAh g}^{-1}$ , on a plateau centred at  $\sim 5.0 \text{ V}$  (most likely due to the  $\text{Co}^{3+} \rightleftharpoons \text{Co}^{4+}$  redox couple). A second plateau was also observed in the electrochemical data; at  $4.0 \text{ V}$  (the reason for this is unknown, but may be due to a  $\text{Mn}^{3+} \rightleftharpoons \text{Mn}^{4+}$  redox couple). The poor quality of ac Impedance results, combined with the presence of the  $4.0 \text{ V}$  plateau, suggests that some oxygen non-stoichiometry may persist in the spinel even after annealing at  $500 \text{ }^\circ\text{C}$ ; future work must be conducted to study this problem.

The  $\text{Li}_{1-x}\text{Co}_{1+2x}\text{Mn}_{1-x}\text{O}_4$  and  $\text{Li}_{1-x}\text{Co}_{1/2+6x/5}\text{Mn}_{3/2-x/5}\text{O}_4$  solid solutions have been studied for possible cathode and anode materials. No significant capacities were obtained in the  $2.5 - 5.1 \text{ V}$  potential window for materials with  $x > 0.00$  in either solid solution.

Compositions along the  $\text{Li}_{1-x}\text{Co}_{1+2x}\text{Mn}_{1-x}\text{O}_4$  solid solution show significant capacities for lithium insertion in the  $0.25 - 2.5 \text{ V}$  potential window. The mechanism for lithium insertion appears to involve full reduction of the metal cations in, and decomposition of, the spinel phase, giving the transition metals. Subsequent cycling involves the repeated reduction of, and re-oxidation to, the transition metal oxides. The best anode performance was observed for  $x = 0.51$ , where specific capacities of  $\sim 750 \text{ mAh g}^{-1}$  were obtained. This is acceptable for use as an anode material; future work must be conducted to study the cycling performance of these materials more rigorously.

The electrochemical activity observed for samples with compositions in both solid solutions studied here ( $\text{Li}_{1-x}\text{Co}_{1+2x}\text{Mn}_{1-x}\text{O}_4$  and  $\text{Li}_{1-x}\text{Co}_{1/2+6x/5}\text{Mn}_{3/2-x/5}\text{O}_4$ ) suggest that there may be a link between the ease of reduction of a spinel compound on heating and ease of reduction with Li. Many of the spinel compositions that perform well as anodes are also those that form rock salts on heating; an example of this is the  $\text{Li}_{1-x}\text{Co}_{1+2x}\text{Mn}_{1-x}\text{O}_4$  solid solution, where a rock salt solid solution was observed at high temperatures. Metal oxides with low thermal stability (*i.e.* that lose oxygen at relatively low temperatures when heated) should be investigated as possible anode materials for Li-ion batteries.

## 6.5 References

- (1) Kawai, H.; Nagata, M.; Kageyama, H.; Tukamoto, H.; West, A. R. *Electrochimica Acta* **1999**, *45*, 315.
- (2) Poizot, P.; Laruelle, S.; Grugeon, S.; Dupont, L.; Tarascon, J. M. *Nature* **2000**, *407*, 496.
- (3) Badway, F.; Plitz, I.; Grugeon, S.; Laruelle, S.; Dolle, M.; Gozdz, A. S.; Tarascon, J. M. *Electrochemical and Solid-State Letters* **2002**, *5*, A115.

## Chapter 7

### Low temperature polymorphism of $\text{Li}_{1+x}\text{Mn}_{2-x}\text{O}_4$

#### 7.1 Background

$\text{LiMn}_2\text{O}_4$  is of interest as a 4 V cathode material in Li-ion batteries, as a possible replacement for the toxic and expensive  $\text{LiCoO}_2$ . At room temperature,  $\text{LiMn}_2\text{O}_4$  has the cubic spinel structure, with the  $Fd-3m$  space group. A solid solution,  $\text{Li}_{1+x}\text{Mn}_{2-x}\text{O}_4$ , has also been reported,<sup>1-5</sup> in the range  $0.00 \leq x \leq 0.33$ . As  $x$  increases the structure becomes less stable, decomposing on heating to give  $\text{Li}_2\text{MnO}_3$  and manganese oxide. The temperature for this decomposition decreases markedly with  $x$ ;  $\text{LiMn}_2\text{O}_4$  ( $x = 0$ ) is stable to  $\sim 900$  °C, while  $\text{Li}_4\text{Mn}_3\text{O}_{12}$  (*i.e.*  $x = 0.33$ ) is stable only to  $\sim 400$  °C. Further decomposition occurs on heating beyond 1000 °C, though the mechanism for this is not clear; Thackeray *et al.* propose that segregation of  $\text{Li}_2\text{MnO}_3$ , and then  $\text{LiMnO}_2$  at higher temperatures, occurs, with recombination to a ' $\text{Li}_{0.6}\text{Mn}_{2.4}\text{O}_4$ ' spinel phase at  $\sim 1200$  °C. Sugiyama<sup>6</sup> reported a straight reaction to  $\text{LiMnO}_2$  and  $\text{Mn}_3\text{O}_4$ . Both authors attribute the decrease in weight on heating to oxygen loss; this was confirmed by Mandal *et al.*<sup>7</sup>

It has been widely reported that on cooling  $\text{LiMn}_2\text{O}_4$  below room temperature, a first-order phase transition occurs. This appears to be due to partial charge ordering of the Mn ions, resulting in a cooperative Jahn-Teller distortion to either orthorhombic or tetragonal symmetry at  $\sim 280$  K.

Intense superlattice reflections appear in the synchrotron x-ray diffraction patterns collected over a range of sub-ambient temperatures by Rouse *et al.*<sup>8</sup>, which can be indexed on a  $3a \times 3a \times a$  orthorhombic unit cell, where  $\underline{a} = 24.743$  Å,  $\underline{b} = 24.840$  Å,  $\underline{c} = 8.199$  Å. Other reports<sup>9-11</sup> have also suggested that the transition just below room temperature in  $\text{LiMn}_2\text{O}_4$  is to a phase whose structure has an orthorhombic unit cell.

Charge ordering may continue on further cooling to give a fully ordered state. Two separate papers<sup>10,12</sup> by members of the same group in Ibaraki, Japan, have indexed low temperature XRD patterns from  $\text{LiMn}_2\text{O}_4$  at  $\leq 70$  K on a tetragonal unit cell with the  $I4_1/amd$  space group. Similar patterns (recorded as low as 1.5 K) reported earlier by

Rousse *et al.*<sup>8</sup> were indexed on the orthorhombic space group, with the conclusion drawn that charge ordering never reached a fully ordered state. Similar findings were also reported by Tabuchi *et al.*<sup>13</sup>

However, on cooling  $\text{LiMn}_2\text{O}_4$  to 100 K Wills *et al.*<sup>14</sup> could index neutron diffraction patterns only on a large tetragonal unit cell, in the  $I4_1/amd$  space group, and found no evidence of a distortion to lower (*i.e.* orthorhombic) symmetry. Significant charge segregation still existed at 10 K. However, their samples also contained traces ( $\sim 4$  wt%) of a second phase,  $\lambda\text{-MnO}_2$ . Yamada *et al.*<sup>15</sup> suggested that below room temperature  $\text{LiMn}_2\text{O}_4$  underwent a gradual transition and that a tetragonal spinel coexisted with the high temperature cubic form.

As yet, the low temperature polymorphism of  $\text{LiMn}_2\text{O}_4$  is not sufficiently understood. In summary, one sub-ambient phase transition certainly exists for  $\text{LiMn}_2\text{O}_4$ ; the possibility of a second transition at lower temperatures has not been confirmed. DSC work reported in the literature<sup>16-18</sup> has been limited to  $\sim -40$  °C. Full charge ordering may be achieved at  $\sim 60$  K.

## 7.2 Experimental

Samples on the  $\text{Li}_{1+x}\text{Mn}_{2-x}\text{O}_4$  binary join with compositions  $0.00 \leq x \leq 0.16$  were prepared using  $\text{Li}_2\text{CO}_3$  and  $\text{MnO}_2$  as reagents. Both materials were of >99% purity and obtained from Aldrich.  $\text{MnO}_2$  was pre-milled using a planetary ball-mill at 400 rpm for 5 minutes to reduce the average particle size, and help with reaction.

The appropriate quantities of these reagents were accurately weighed, ground intimately and placed into gold boats. The powders were then fired at 650 °C, to decarbonate the lithium reagent, followed by reaction at 800 °C for 2 days, with intermittent regrinding by mortar and pestle for twenty minutes daily. A subsequent post-reaction annealing step – 500 °C for 3 days – was used to ensure optimised oxygen contents of the spinel materials.

Samples were characterised by XRD. Lattice parameter data were obtained using least squares refinement of XRD peaks corrected by Si internal standards.

Combined thermogravimetry (TG) and differential thermal analysis (DTA) were conducted, using Stanton-Redcroft TG-DTA equipment, in flowing air, with programmed heating/cooling rates of 10 °C min<sup>-1</sup>. Differential scanning calorimetry (DSC) was conducted using a TA Instruments DSC-910. Heating rates for the experiments were set to 10 °C min<sup>-1</sup>. Cooling to ~ -180 °C (93 K) was achieved using a cooling cap filled with liquid nitrogen; cooling data could not be recorded on the equipment used. All samples were run in crimped Al pans, in a flowing Ar atmosphere, with a flow rate of ~ 100 ml min<sup>-1</sup>. The inert reference was an empty crimped pan.

## 7.3 Results and Discussion

### 7.3.1 Solid solution formation in $\text{Li}_{1+x}\text{Mn}_{2-x}\text{O}_4$

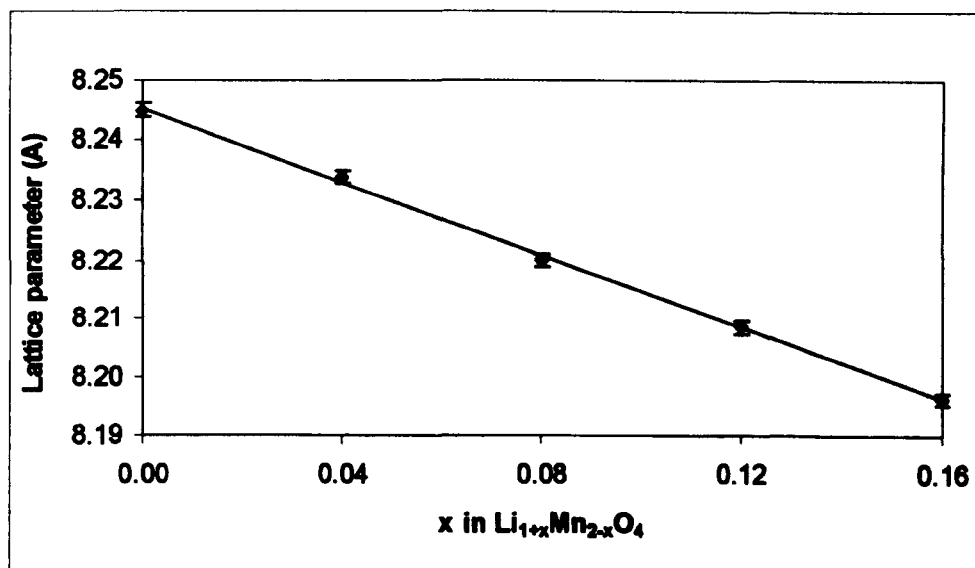
A range of samples were prepared on the binary join  $\text{Li}_{1+x}\text{Mn}_{2-x}\text{O}_4$ , with compositions  $0.00 \leq x \leq 0.16$ . All samples were indexed in the Fd-3m space group; refined lattice parameters are presented in Table 7.1.

*Table 7.1 – Refined lattice parameters for  $\text{Li}_{1+x}\text{Mn}_{2-x}\text{O}_4$  ( $0.00 \leq x \leq 0.16$ ; estimated standard deviations given in parentheses. Average Mn oxidation state calculated assuming  $\text{Li}_{1+x}\text{Mn}_{2-x}\text{O}_4$  stoichiometry.*

$x$ in $\text{Li}_{1+x}\text{Mn}_{2-x}\text{O}_4$	$a_{\text{spinel}} / \text{\AA}$	Calculated Mn oxidation state
0.00	8.2450 (13)	3.500
0.04	8.2338 (3)	3.551
0.08	8.2199 (7)	3.604
0.12	8.2084 (7)	3.660
0.16	8.1961 (12)	3.717

The variation in lattice parameter with composition,  $x$ , is presented in Figure 7.1. A clear linear dependence can be observed, in agreement with Vegard's Law for a solid solution. It is concluded that  $\text{Li}^+$  is replacing Mn on the octahedral sites; an increase in the overall Mn valency must occur for charge balance. Since  $\text{Mn}^{4+}$  has a smaller ionic radius than  $\text{Mn}^{3+}$ , an overall decrease in the cell dimensions occurs.

*Figure 7.1 – Lattice parameter vs. composition for  $\text{Li}_{1+x}\text{Mn}_{2-x}\text{O}_4$ .*



These results are in agreement with the literature<sup>1,2,5</sup>; a solid solution limit of  $x = 0.33$  (*i.e.* at  $\text{Li}_4\text{Mn}_5\text{O}_{12}$ ) has been identified, though this phase is unstable above  $\sim 400$  °C. The maximum temperature at which phases in this solid solution are stable has been shown to fall linearly with increasing Li content; from this work the solid solution limit in samples annealed at 500 °C occurs at  $x > 0.16$ .

### 7.3.2 High temperature behaviour

TG-DTA data were recorded for compositions with  $x = 0.00, 0.04, 0.08$  and  $0.12$  in  $\text{Li}_{1+x}\text{Mn}_{2-x}\text{O}_4$ ; data for  $\text{LiMn}_2\text{O}_4$  and  $\text{Li}_{1.08}\text{Mn}_{1.92}\text{O}_4$  are presented in Figures 7.2 and 7.3.

On heating  $\text{LiMn}_2\text{O}_4$  to  $\sim 1300$  °C a significant weight loss of  $\sim 7\%$  was noted, starting at  $\sim 800$  °C. This weight loss has been attributed to oxygen volatilization.<sup>7</sup> An inflexion incurred in the weight loss data at  $\sim 950$  °C, corresponding to a stoichiometry of  $\sim \text{LiMn}_2\text{O}_{3.84}$ . A sharp weight loss followed this inflexion, with a corresponding sharp DTA peak. When subsequently cooling to room temperature, the weight loss proved to be almost fully reversible; DTA peaks observed on heating were roughly reversible on cooling, with some hysteresis. XRD of the sample after this thermal cycling showed a single phase cubic spinel.

TG-DTA data for samples with composition  $0.04 \leq x \leq 0.12$  showed the same behaviour as  $\text{LiMn}_2\text{O}_4$ ; the only difference was that weight loss started at lower temperatures (*e.g.*  $\sim 709$  °C for  $x = 0.08$ ). Table 7.2 lists the temperatures at which weight loss is first observed in  $\text{Li}_{1+x}\text{Mn}_{2-x}\text{O}_4$  ( $0.00 \leq x \leq 0.12$ ).

*Table 7.2 – Temperatures at which weight loss started in TG-DTA for  $x = 0.00 - 0.12$  in  $\text{Li}_{1+x}\text{Mn}_{2-x}\text{O}_4$ .*

$x$ in $\text{Li}_{1+x}\text{Mn}_{2-x}\text{O}_4$	Temperature / °C
0.00	827
0.04	770
0.08	709
0.12	676

### 7.3.3 Low temperature Differential Scanning Calorimetry (DSC)

#### 7.3.3a Untreated, stoichiometric $\text{LiMn}_2\text{O}_4$

$\text{LiMn}_2\text{O}_4$  was cooled to  $\sim -30$  °C using liquid nitrogen; DSC data were then recorded on subsequent heating to 100 °C at  $10$  °C  $\text{min}^{-1}$ . The data (Figure 7.5) show a single sharp peak, indicating a phase transition occurring on heating at 23.54 °C. Such a transition has been widely reported, and has been attributed to the transition from the cubic phase to either a tetragonal or orthorhombic phase, due to Jahn-Teller distortions. Since the symmetry of the low temperature phase is not clearly identified, it is referred to here as  $\beta$ - $\text{LiMn}_2\text{O}_4$ ; the cubic spinel phase observed at room temperature and above will be described as  $\alpha$ - $\text{LiMn}_2\text{O}_4$ .

The DSC experiment was repeated, with initial cooling to lower temperatures (to as low as  $-180$  °C). It was noted that on cooling to  $\sim -135$  °C, and then recording data on heating, the same peak was observed at  $\sim 23.5$  °C. However, when samples had been cooled to temperatures of  $-180$  to  $-146$  °C, two extra peaks – at  $\sim 0$  °C ( $\pm 1$  °C) and  $\sim 15$  °C ( $\pm 2$  °C) – appeared in the DSC data (Figure 7.6) on heating. The original peak at  $\sim 23.5$  °C also remained, unchanged.

The lowest temperature peak, at  $\sim 0$  °C, was assigned to water condensing into the DSC cell when extreme temperatures were used. The second peak, at  $\sim 15$  °C, indicates a second phase transition occurring in  $\text{LiMn}_2\text{O}_4$ , but only in samples cooled to below  $-140$  °C. This new low temperature phase will be identified here as  $\gamma$ - $\text{LiMn}_2\text{O}_4$ . This  $\beta \rightleftharpoons \gamma$  transition shows a significant hysteresis of  $\sim 155$  °C on heating; a schematic demonstrating this large hysteresis effect is given in Figure 7.7.

Figure 7.5 – DSC data for untreated  $\text{LiMn}_2\text{O}_4$ , with initial cooling to  $\sim -40^\circ\text{C}$ .

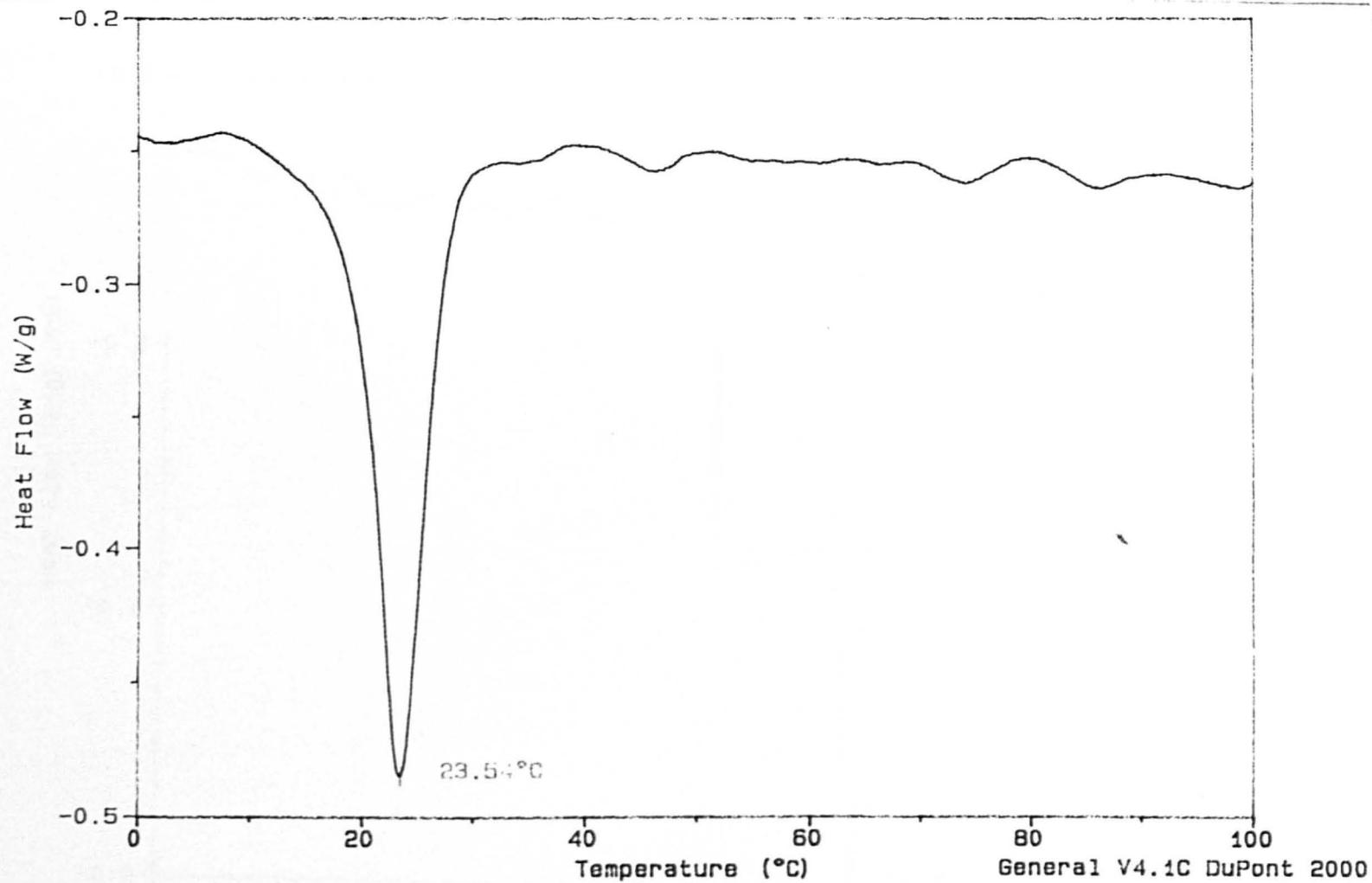
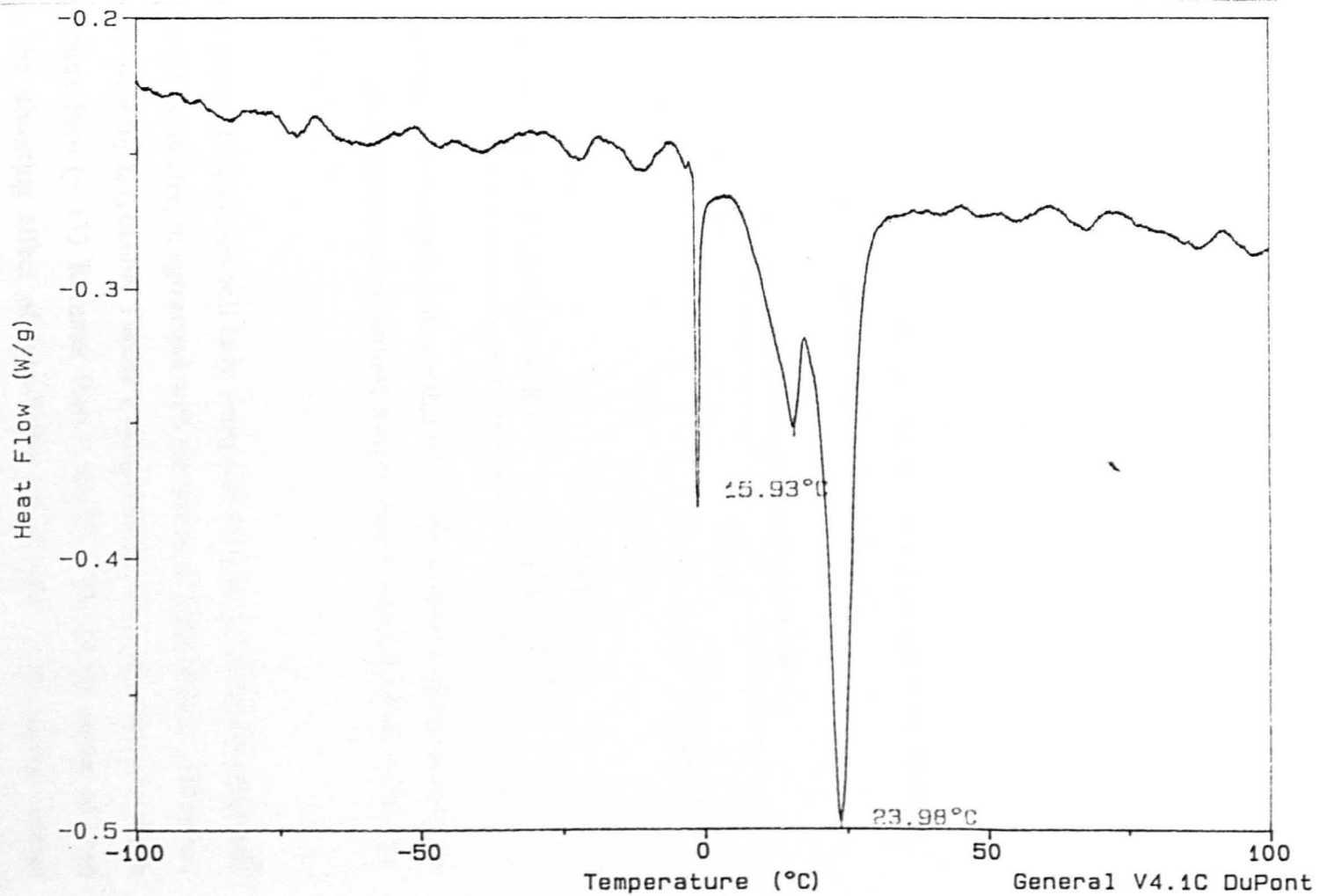


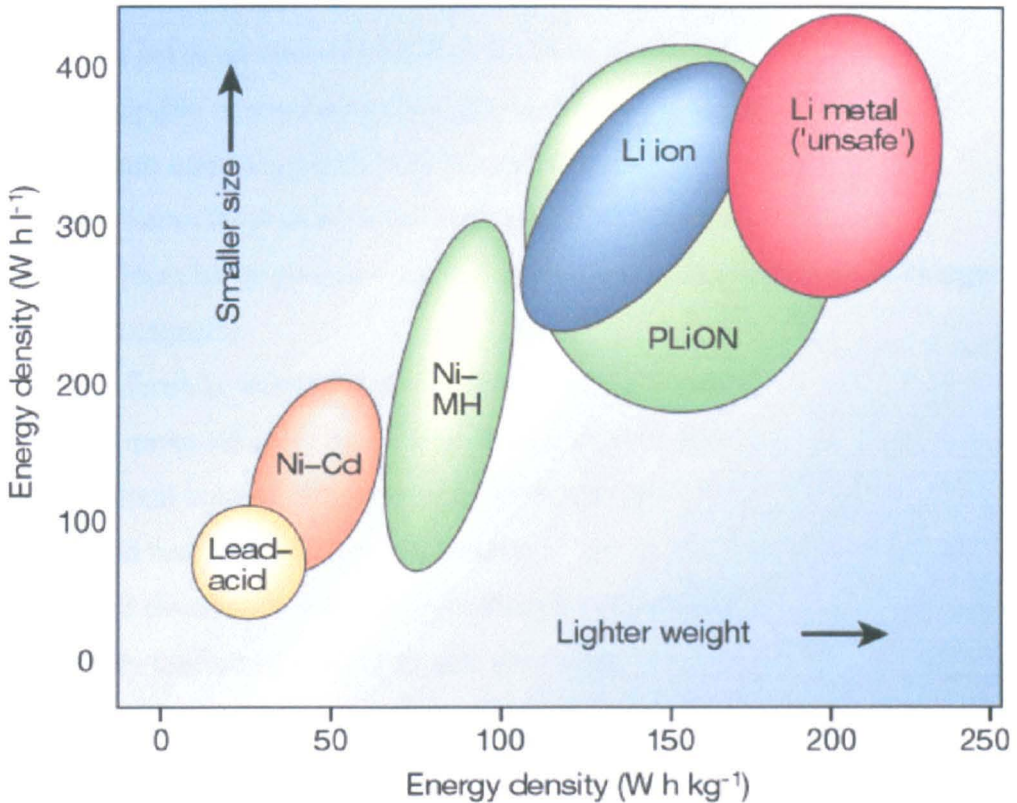
Figure 7.6 – DSC data for untreated  $\text{LiMn}_2\text{O}_4$ , with initial cooling to  $\sim -180^\circ\text{C}$ .



## 1.1.4 Why lithium?

Lithium is the lightest (at  $6.94 \text{ g mol}^{-1}$ ) and most electropositive metal ( $-3.04 \text{ V}$  vs. standard hydrogen electrode). This allows for production of cells with impressive energy densities, as indicated in Figure 1.5.

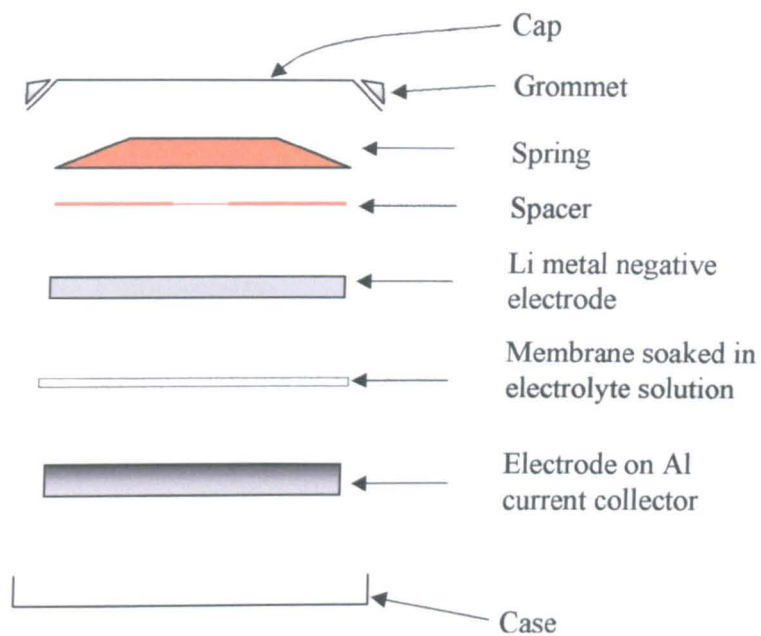
**Figure 1.5** – Comparison of the different battery technologies (Ni-Cd: Nickel Cadmium cell, Ni-MH: Nickel-Metal Hydride cell, PLiON: Plastic Lithium-Ion cell, Li-ion cell) in terms of volumetric and gravimetric energy density.<sup>12</sup>



As Figure 1.5 indicates, Li-ion cells offer potentially greater energy densities in both gravimetric and volumetric terms.

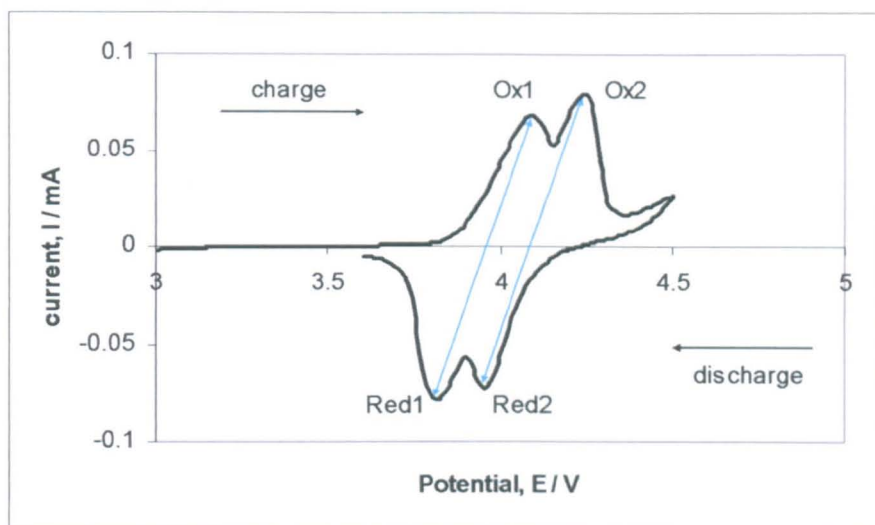
The significance of the development of modern Li-ion batteries can be seen through communications technology. An early 'mobile' phone, the Mobira Senator (Nokia, 1982), consisted of a small handset connected to a heavy brick-like battery pack, in total weighing 9.8kg. Modern mobile phones weigh *ca.* a hundredth of this ( $\sim 100$  grams) and have significantly lower volume, due largely to the more compact Li-ion battery used.

*Figure 2.5 – Coin cell construction.*



any redox couple can be identified. A typical CV plot is presented in Figure 2.7; the active material here is commercially supplied  $\text{LiMn}_2\text{O}_4$ .

**Figure 2.7** – Cyclic voltammogram for  $\text{LiMn}_2\text{O}_4$  | 1M  $\text{LiPF}_6$  in PC | Li metal cell cycled at C/10 rate.



Cyclic voltammograms are normally presented as in Figure 2.7 with applied voltage (x-axis) vs. current intensity (y-axis). It should be noted that if one plots the current intensity vs. time, then integrating the area below the curve yields the total capacity, due to the relationship:

$$dq = I(t) \cdot dt \quad \text{(Equation 2.26)}$$

From the voltammogram it can be seen that there are two separate electrochemical redox processes (labelled Ox1/Red1 and Ox2/Red2) occurring on charging in  $\text{LiMn}_2\text{O}_4$ , and that both are reversible on discharge. By taking the average of each pair of redox peaks we can state that we have two redox couples for  $\text{LiMn}_2\text{O}_4$ , occurring at *ca.* 4.10 and 3.955 V.

The data presented in Figure 2.7 for  $\text{LiMn}_2\text{O}_4$  are typical of those found in the literature. As discussed in Chapter 1, these processes are both linked to the removal of lithium from the spinel structure, and that extraction of lithium proceeds via a two-step process at  $\sim 4.1$  V, with  $\sim 0.1$  V separating the two processes.<sup>10,11</sup> This step is attributed to ordering of Li ions over half of the tetrahedral sites when  $x = \frac{1}{2}$  in  $\text{Li}_x\text{Mn}_2\text{O}_4$ . The peaks observed here in Figure 2.7 both then refer to the  $(\text{Mn}^{3+} \rightleftharpoons \text{Mn}^{4+} + e^-)$  redox couple.

**Figure 2.8** – Variation of voltage vs. time as a cell,  $\text{LiMn}_2\text{O}_4 \mid 1\text{ M LiPF}_6 \text{ in PC} \mid \text{Li metal anode}$ , is cycled at  $C/10$  rate.

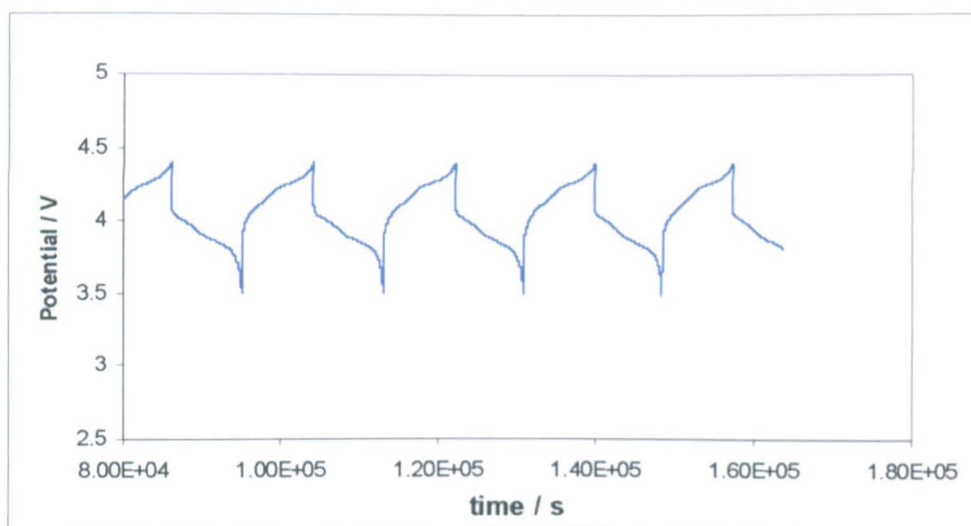


**Figure 2.9** – Cycling performance for a cell,  $\text{LiMn}_2\text{O}_4 \mid 1\text{ M LiPF}_6 \text{ in PC} \mid \text{Li metal anode}$ , cycled at  $C/10$  rate.

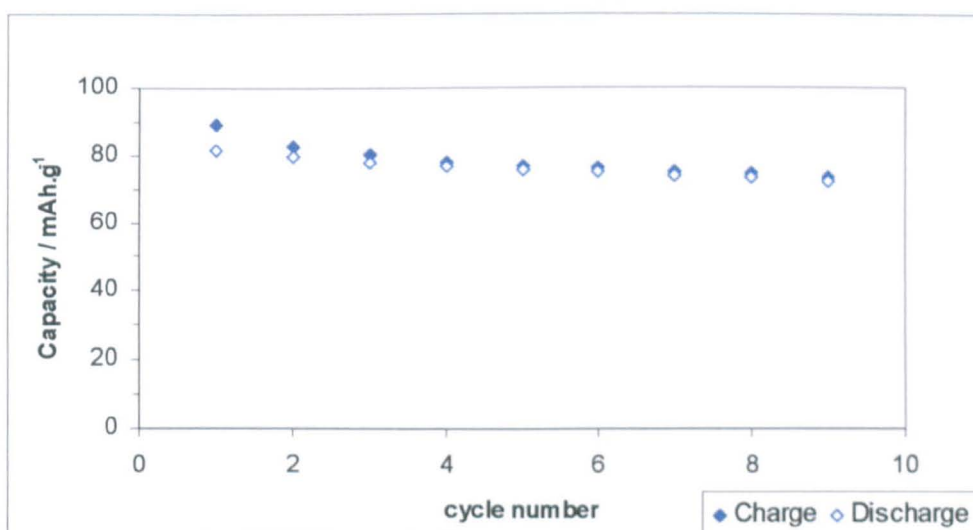


Figure 3.2(a) – Cubic spinel and equivalent tetragonal spinel unit cell volumes vs.  $x$  in  $Co_{3-x}Mn_xO_4$ .

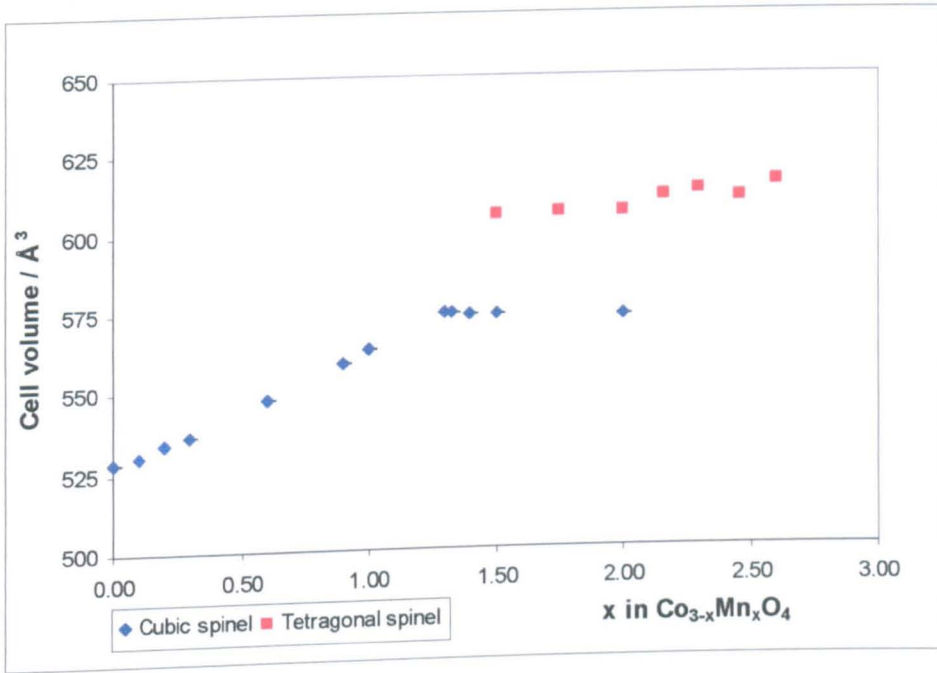
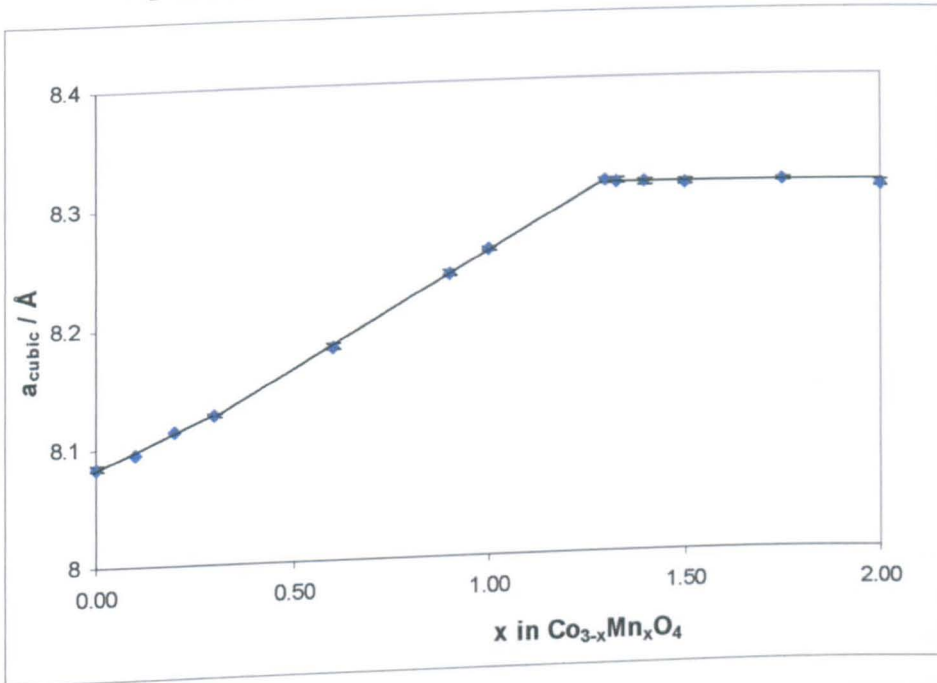


Figure 3.2(b) – Cubic spinel lattice parameter vs.  $x$  in  $Co_{3-x}Mn_xO_4$ .



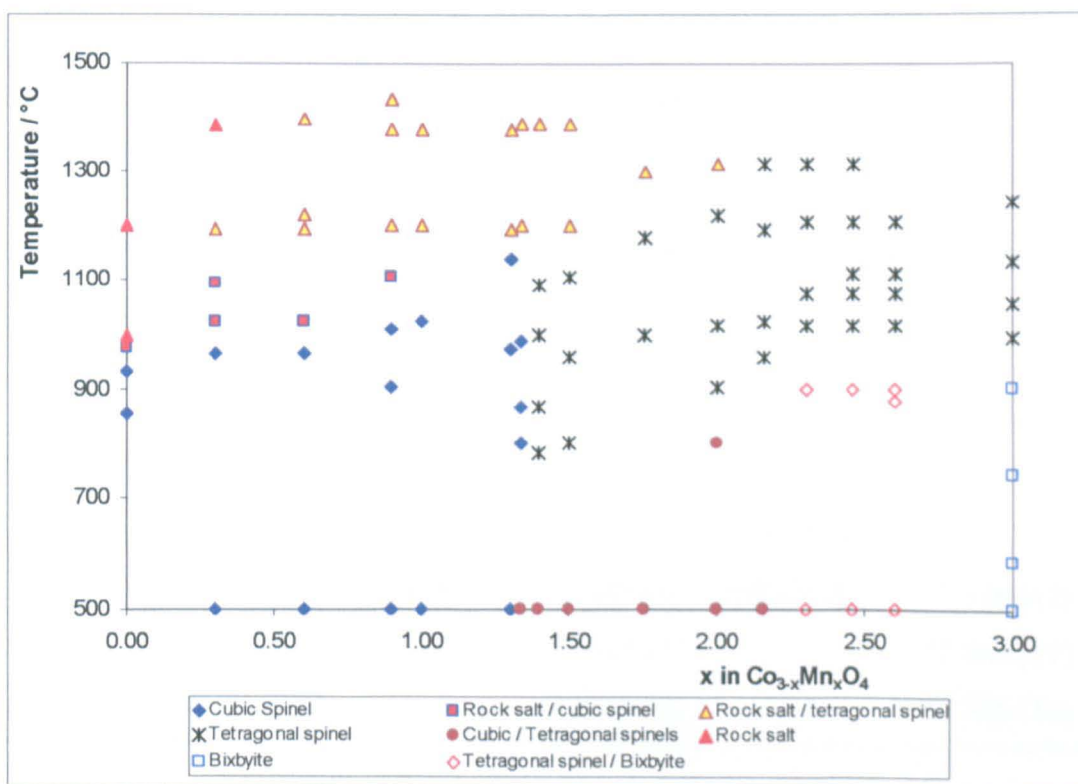
Single crystal studies by Geller *et al.*<sup>14</sup> show that  $\text{Mn}_2\text{O}_3$ , known as bixbyite, is body-centred cubic with space group Ia-3,  $a = 9.4091 \text{ \AA}$ .<sup>15</sup> XRD data collected here were indexed on a body-centred cubic unit cell, with lattice parameter  $a = 9.4088 (19) \text{ \AA}$ .

The lattice parameter for the bixbyite phase decreased from  $x = 3.00$  to  $x = 2.60$ , becoming constant thereafter, suggesting the formation of a limited bixbyite solid solution at  $x > 2.60$ . Both the  $a$  and  $c$  tetragonal spinel lattice parameters increase with Mn content, though barely in excess of the errors. A step occurs in the data at  $x \sim 2.16$ ; no single phase tetragonal spinels were identified at temperatures below 950 °C in any quenched composition.

### 3.3.2 High temperature structures in $\text{Co}_{3-x}\text{Mn}_x\text{O}_4$

A series of quenches were performed from a range of temperatures for all compositions. XRD data were collected for each sample and the patterns indexed where possible. Figure 3.3 shows the phase(s) identified at each quench temperature attempted.

Figure 3.3 – Phase analysis for all quenched samples.



Samples with composition  $1.40 \leq x \leq 2.16$  were quenched from temperatures of 1100 – 1200 °C; only a single tetragonal phase was observed. Refined lattice parameters are presented in Table 3.5. Refinement of lattice parameters for  $x = 1.40$  was not possible.

**Table 3.5** – Lattice parameters for tetragonal spinels obtained in single tetragonal spinel region.

$x$ in $\text{Co}_{3-x}\text{Mn}_x\text{O}_4$	$\underline{a}_{\text{tetragonal}}$ / Å	$\underline{c}_{\text{tetragonal}}$ / Å	Cell Volume / Å <sup>3</sup>	$\underline{c}/\underline{a}'$ ratio
1.50	5.8164 (14)	8.601 (4)	290.98 (13)	1.046
1.75	5.7789 (18)	8.857 (5)	295.77 (15)	1.084
2.00	5.7657 (11)	8.988 (3)	298.78 (9)	1.102
2.16	5.7400 (21)	9.143 (6)	301.23 (17)	1.126

For  $2.30 \leq x \leq 3.00$ , a mixture of tetragonal spinel and bixbyite phases was maintained in quenches made from up to  $\sim 900$  °C. Only the tetragonal spinel was observed at temperatures above 1000 °C in this compositional range. When a sample with composition  $x = 2.60$  was quenched from 1015 °C, the tetragonal spinel had lattice parameters  $\underline{a} = 5.7431$  (14) Å,  $\underline{c} = 9.377$  (3) Å. These lattice parameters are greater than those observed for the tetragonal spinel in the mixed phase region.

The variation of the lattice parameters of the tetragonal spinel phase observed in samples with  $x \geq 0.6$  quenched from  $\sim 1215$  °C is presented in Figures 3.4(a) and (b).

**Figure 3.4** – Variation in tetragonal spinel (a) lattice parameter and (b) cell volume with starting sample composition ( $x$ , in  $\text{Co}_{3-x}\text{Mn}_x\text{O}_4$ ). Samples quenched at  $\sim 1215$  °C ( $\pm 10$  °C).

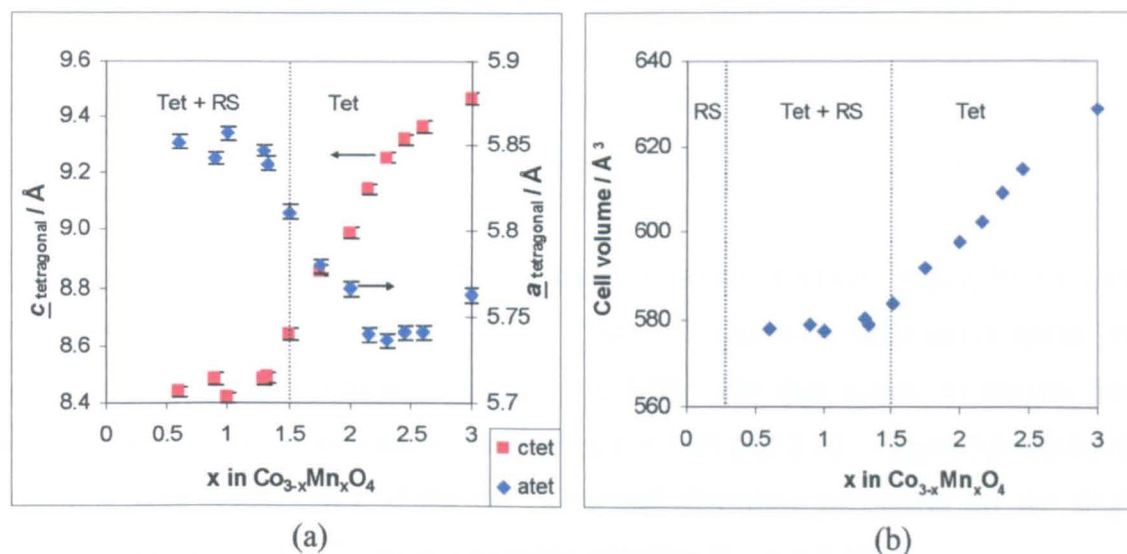


Figure 3.5 – Unit cell volume vs. single spinel phase composition, with linear guide.

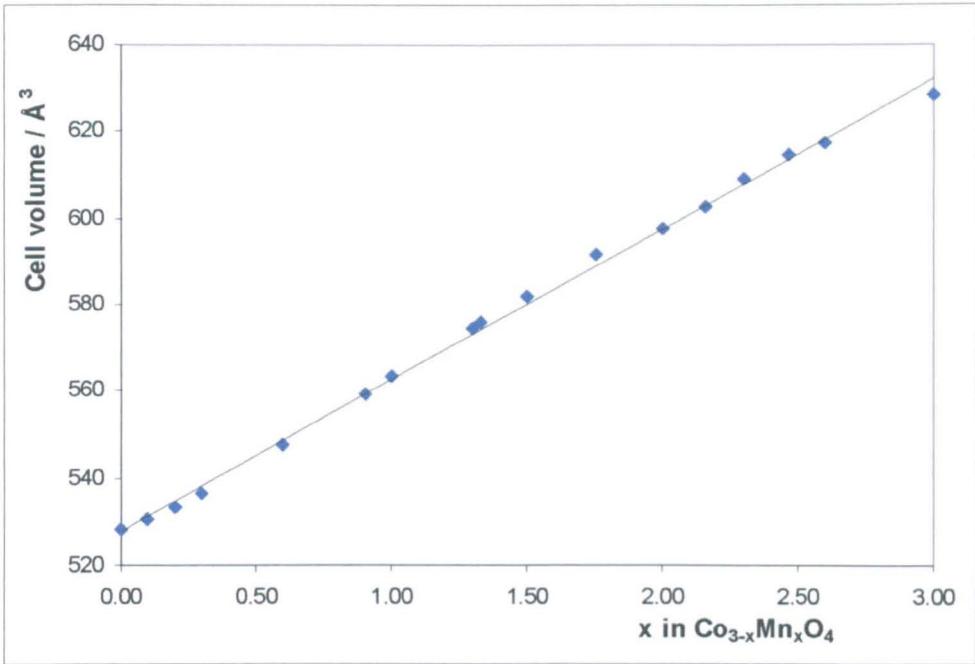
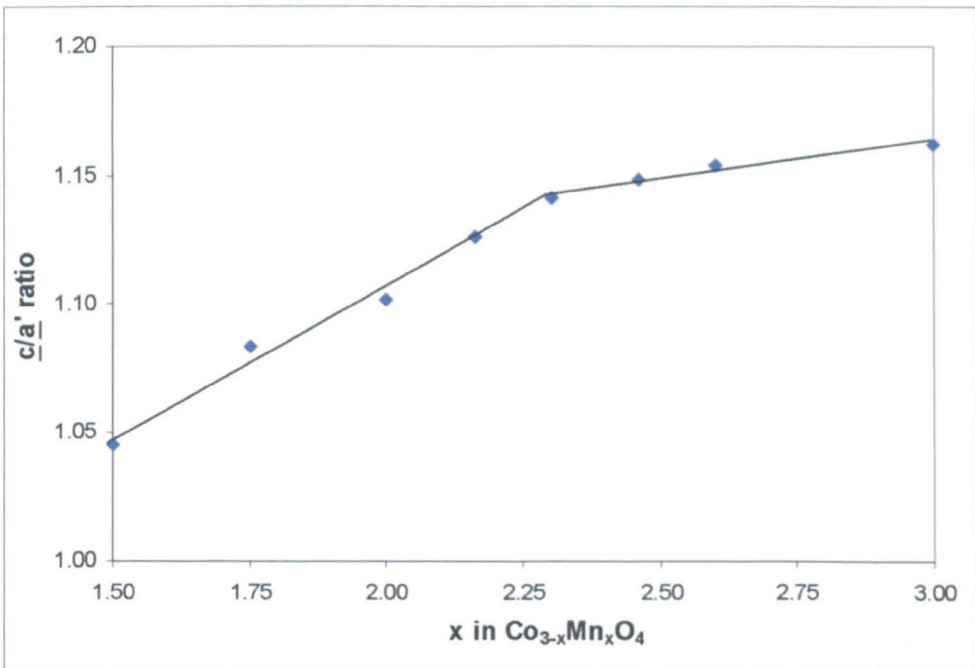


Figure 3.6 –  $\underline{c}/\underline{a}'$  ratio for tetragonal spinels in the compositional range  $1.50 \leq x \leq 3.00$ .



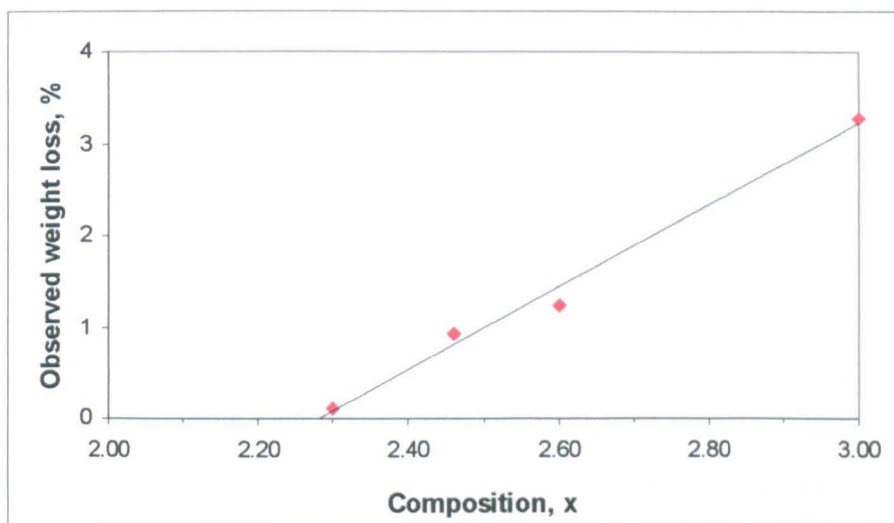
### 3.3.3 TG data

TG data were recorded for a range of compositions, where  $0.00 < x < 3.00$ . These data are presented, along with the DTA data to be discussed in section 3.3.4, in the appendix to this chapter (Figures 3.7 – 3.22).

For samples of compositions  $x \geq 2.3$ , a weight loss was observed at *ca.* 930 °C. The TG data for  $\text{Mn}_2\text{O}_3$  indicate a significant irreversible weight loss of  $\sim 3.28\%$  of the original sample mass ( $\sim 0.49$  O atoms), at 950 °C. No TG features were observed at this temperature on a second cycle of the same sample. The theoretical weight loss for an  $\text{Mn}_2\text{O}_3$  (or ' $\text{Mn}_3\text{O}_{4.5}$ ')  $\rightarrow$   $\text{Mn}_3\text{O}_4$  phase transition is 3.38 % (relative to  $\text{Mn}_2\text{O}_3$ ). This reaction is irreversible at the cooling rates used.

A weight loss at  $\sim 930$  °C was also observed for samples in the compositional range  $2.30 < x < 2.60$ ; this weight loss decreased in size with decreasing Mn content (Figure 3.23). Extrapolation of the data gives an intercept on the compositional axis at  $\sim x = 2.28$ .

**Figure 3.23** – Observed weight loss in TG data at  $\sim 930$  °C vs. composition,  $x$ , in  $\text{Co}_{3-x}\text{Mn}_x\text{O}_4$ .

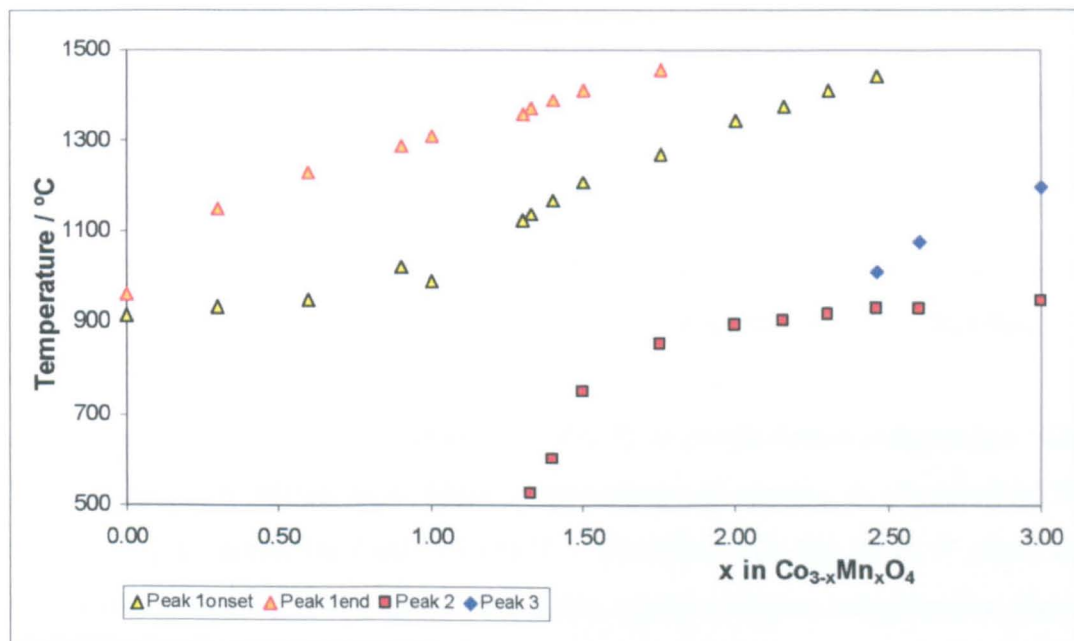


For  $x = 3.00$ , TG data indicated a small, continuous weight loss occurring at temperatures over 950 °C. An inflexion in the slope of the weight loss occurred on heating at  $\sim 1200$  °C. Weight loss of  $\sim 0.2\%$  ( $\sim 0.03$  O atoms) occurred between 950 and 1200 °C; this was irreversible on cooling. A weight loss of  $\sim 0.15\%$  ( $\sim 0.02$  O

**Table 3.7** – Temperatures of all observed DTA peaks. \* - peak end not observed within experimental limits.

Composition, x	Peak 1		Peak 2	Peak 3
	T <sub>onset</sub> / °C	T <sub>end</sub> / °C	T <sub>max</sub> / °C	T <sub>max</sub> / °C
0.00	917	962	-	-
0.30	935	1148	-	-
0.60	946	1229	-	-
0.90	1016	1287	-	-
1.00	987	1308	-	-
1.30	1119	1355	-	-
1.33	1136	1369	526	-
1.40	1166	1389	604	-
1.50	1207	1409	752	-
1.75	1267	1454	853	-
2.00	1345	*	891	-
2.16	1376	*	902	-
2.30	1409	*	913	-
2.46	1444	*	930	1008
2.60	-	-	928	1075
3.00	-	-	948	1198

**Figure 3.24** – Variation in observed DTA peak temperature with composition, x.



# Appendix to Chapter 3

## TG-DTA Data for $\text{Co}_{3-x}\text{Mn}_x\text{O}_4$

Figure 3.7 – TG data for  $\text{Co}_3\text{O}_4$  ( $x = 0.00$  in  $\text{Co}_{3-x}\text{Mn}_x\text{O}_4$ ).

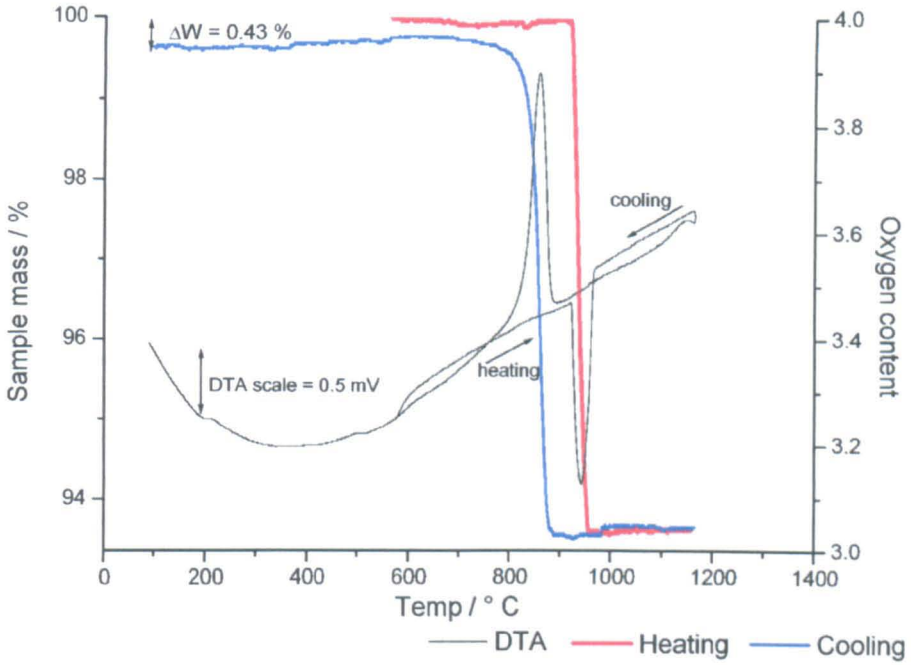


Figure 3.8 – TG data for  $\text{Co}_{2.7}\text{Mn}_{0.3}\text{O}_4$  ( $x = 0.30$  in  $\text{Co}_{3-x}\text{Mn}_x\text{O}_4$ ).

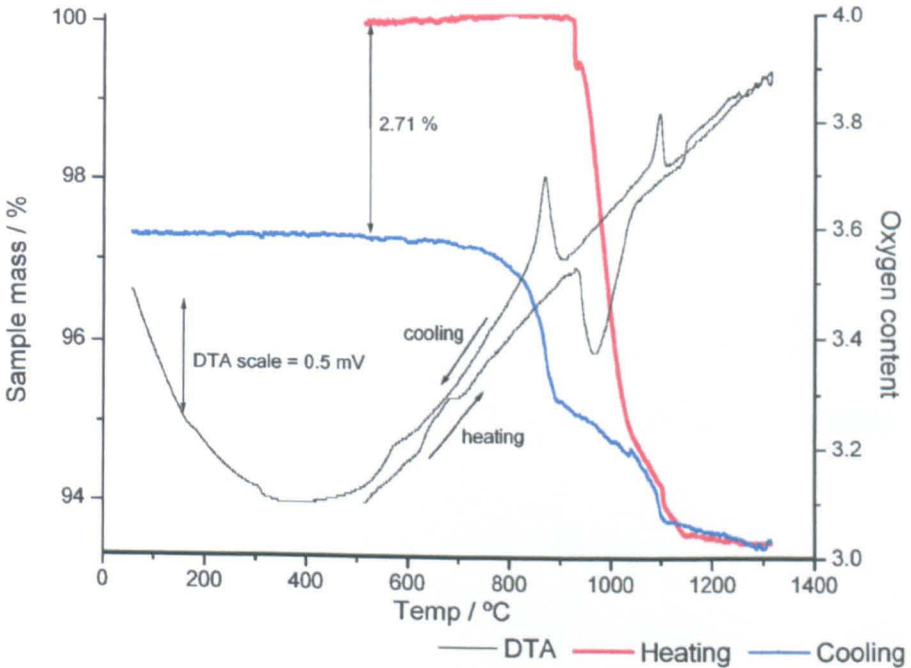


Figure 3.9 – TG data for  $Co_{2.4}Mn_{0.6}O_4$  ( $x = 0.60$  in  $Co_{3-x}Mn_xO_4$ ).

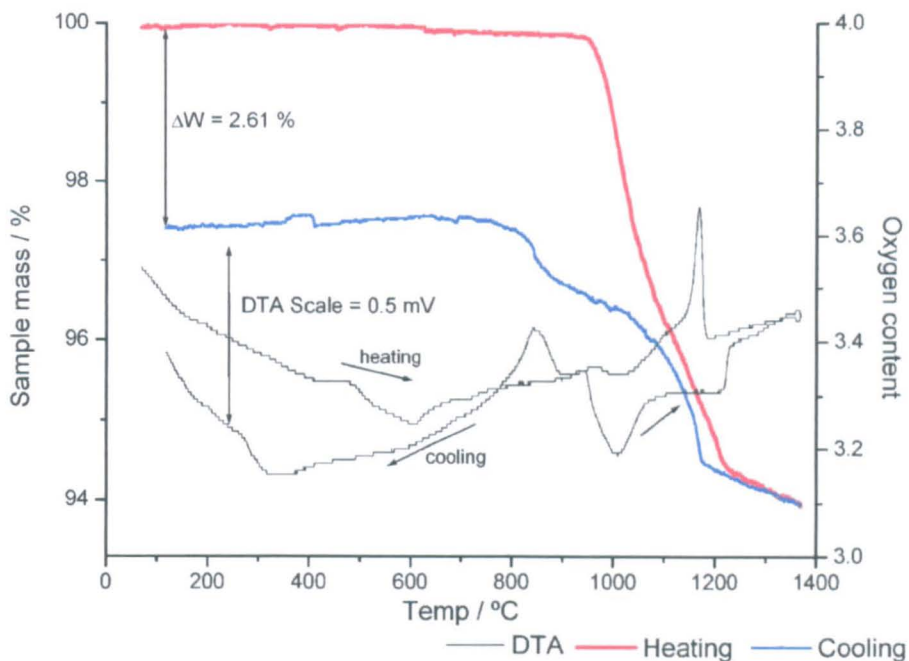


Figure 3.10 – TG data for  $Co_{2.1}Mn_{0.9}O_4$  ( $x = 0.90$  in  $Co_{3-x}Mn_xO_4$ ).

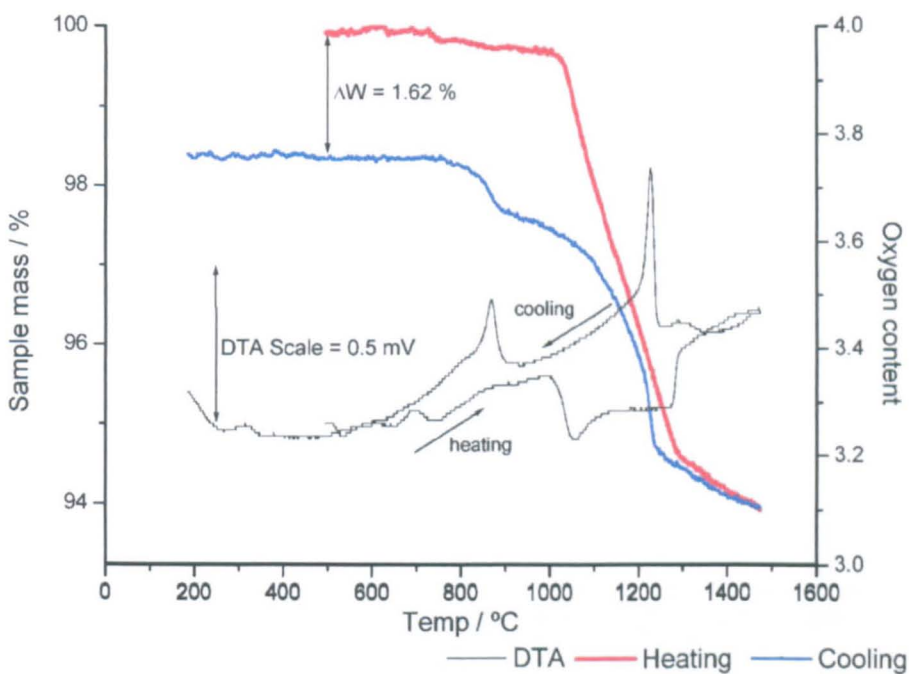


Figure 3.11 – TG data for  $\text{Co}_2\text{MnO}_4$  ( $x = 1.00$  in  $\text{Co}_{3-x}\text{Mn}_x\text{O}_4$ ).

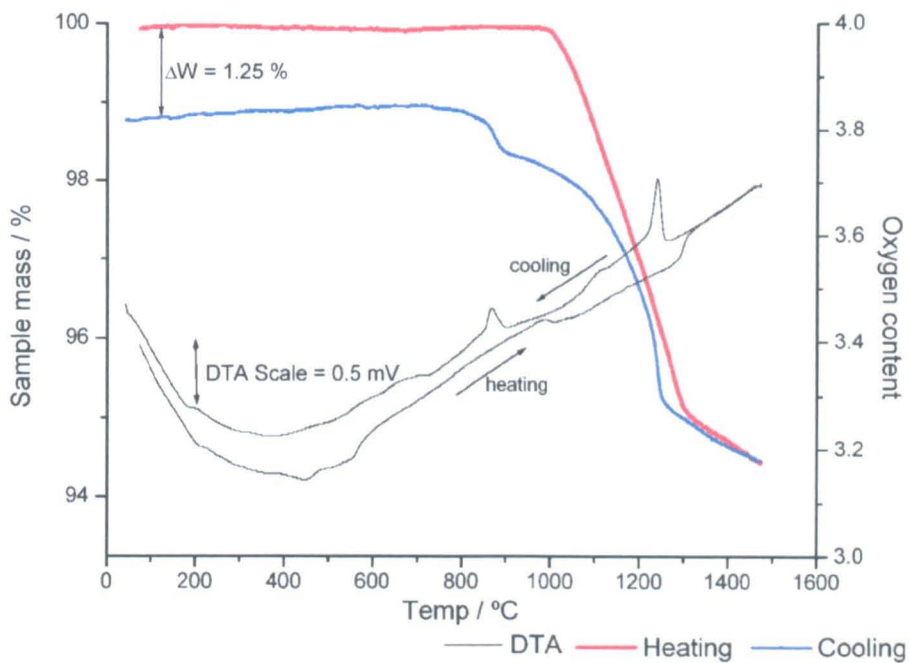
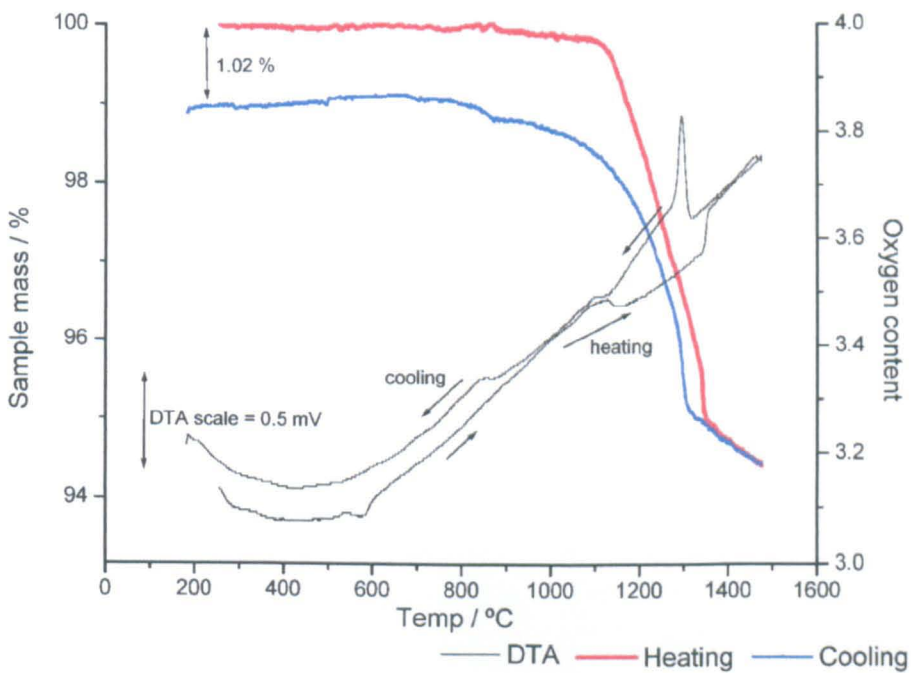
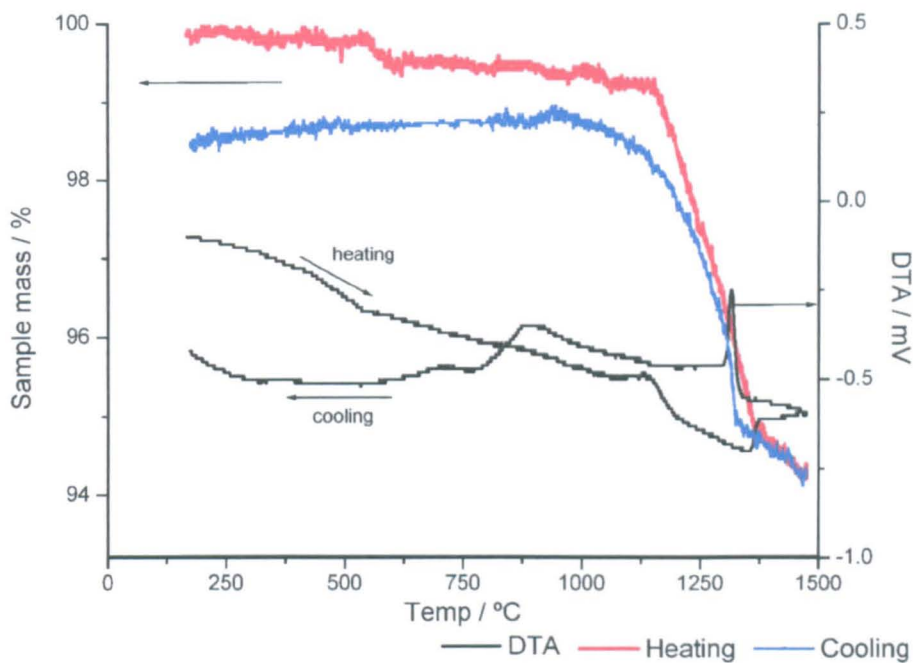


Figure 3.12 – TG data for  $\text{Co}_{1.7}\text{Mn}_{1.3}\text{O}_4$  ( $x = 1.30$  in  $\text{Co}_{3-x}\text{Mn}_x\text{O}_4$ ).



**Figure 3.13** – TG data for  $Co_{1.67}Mn_{1.33}O_4$  ( $x = 1.33$  in  $Co_{3-x}Mn_xO_4$ ).



**Figure 3.14** – TG data for  $Co_{1.6}Mn_{1.4}O_4$  ( $x = 1.40$  in  $Co_{3-x}Mn_xO_4$ ).

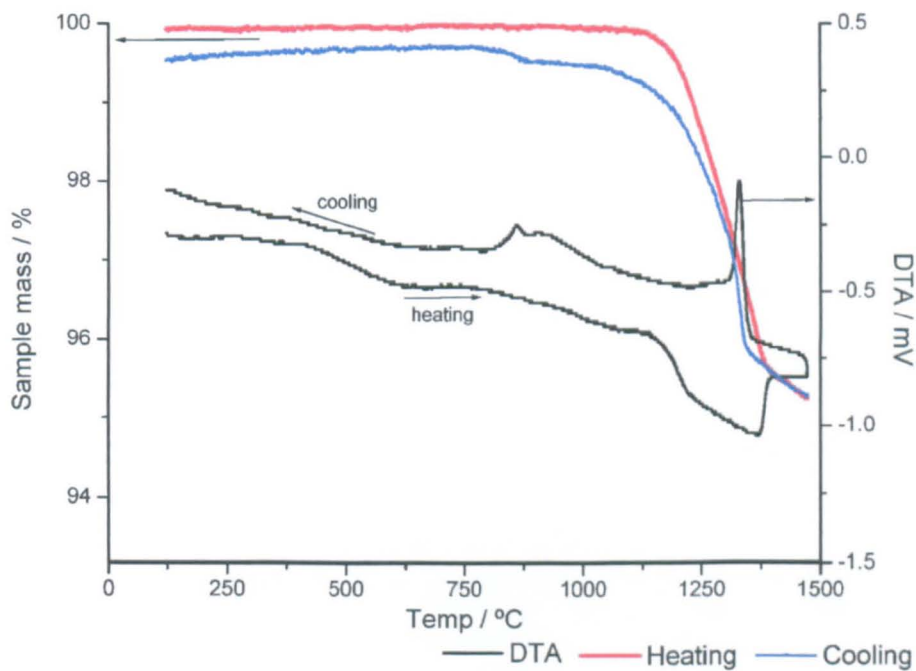


**Figure 3.15** – TG data for  $Co_{1.5}Mn_{1.5}O_4$  ( $x = 1.50$  in  $Co_{3-x}Mn_xO_4$ ).

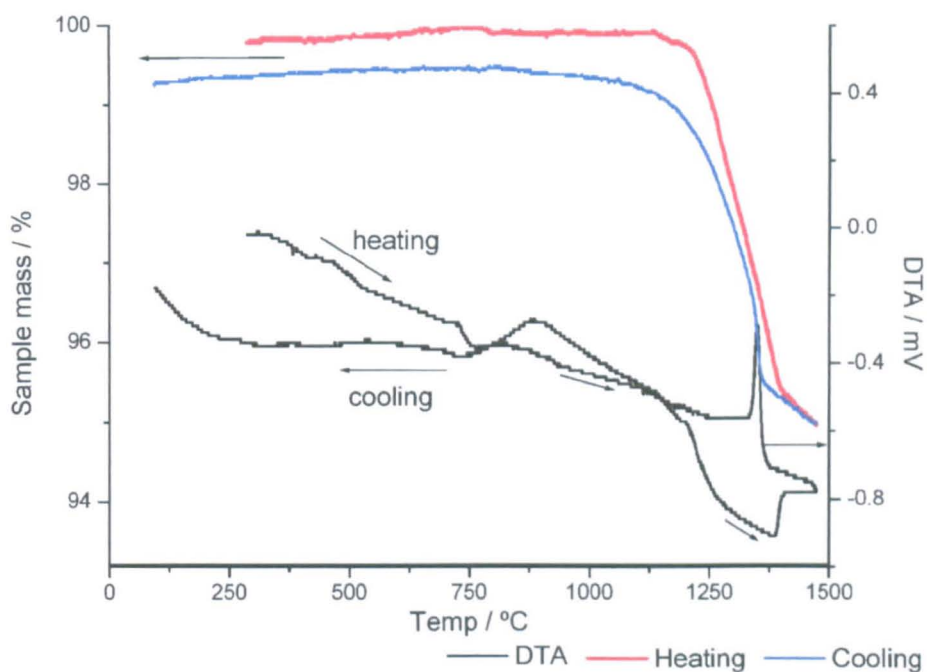


**Figure 3.16** – TG data for  $Co_{1.25}Mn_{1.75}O_4$  ( $x = 1.75$  in  $Co_{3-x}Mn_xO_4$ ).

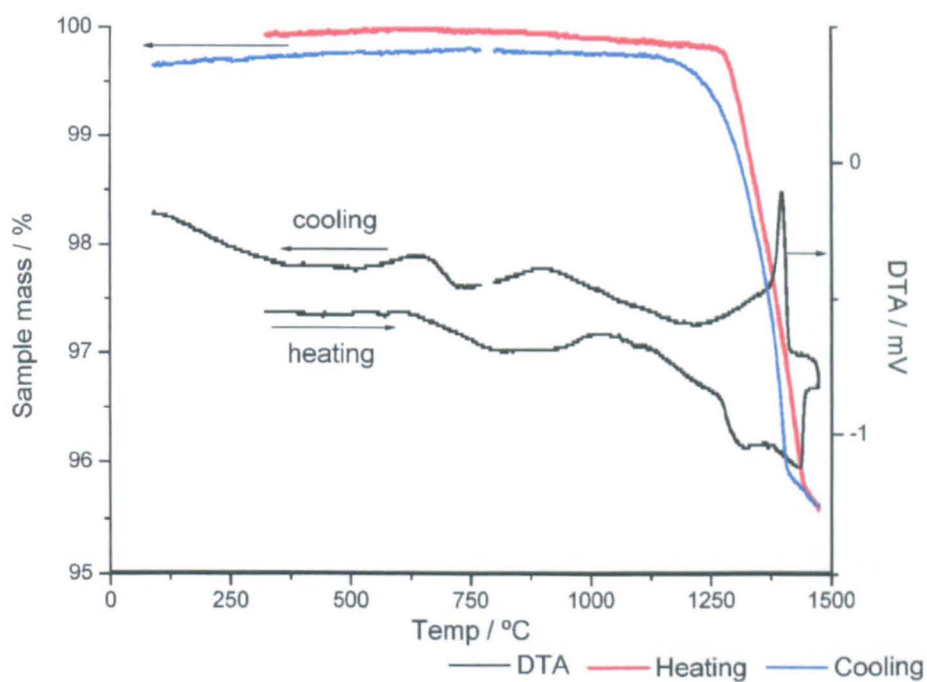


**Figure 3.17** – TG data for  $Co_{1.0}Mn_{2.0}O_4$  ( $x = 2.00$  in  $Co_{3-x}Mn_xO_4$ ).

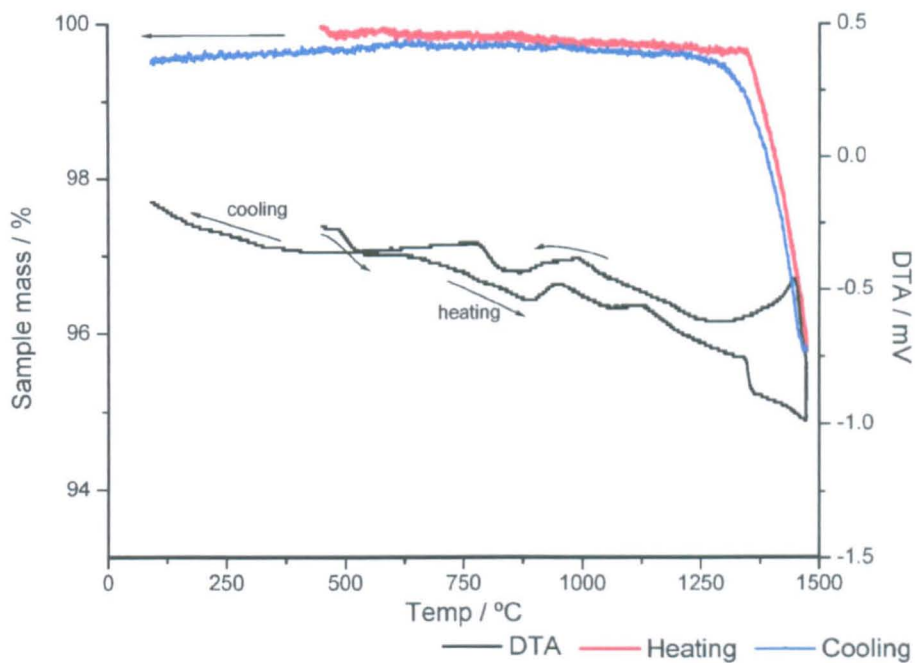


**Figure 3.18** – TG data for  $Co_{0.84}Mn_{2.16}O_4$  ( $x = 2.16$  in  $Co_{3-x}Mn_xO_4$ ).

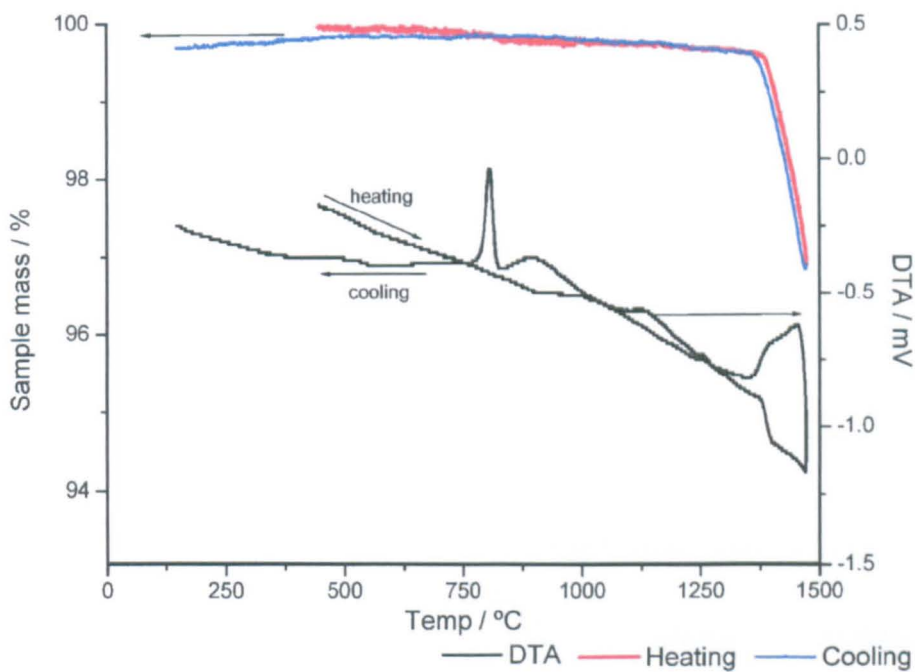


Figure 3.19 – TG data for  $\text{Co}_{0.7}\text{Mn}_{2.3}\text{O}_4$  ( $x = 2.30$  in  $\text{Co}_{3-x}\text{Mn}_x\text{O}_4$ ).

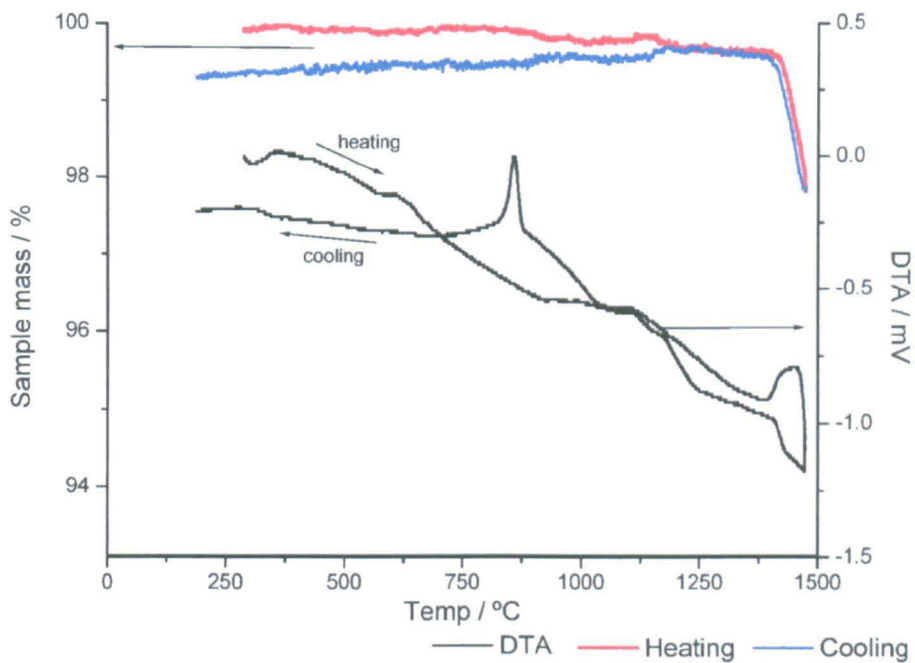


Figure 3.20 – TG data for  $\text{Co}_{0.54}\text{Mn}_{2.46}\text{O}_4$  ( $x = 2.46$  in  $\text{Co}_{3-x}\text{Mn}_x\text{O}_4$ ).

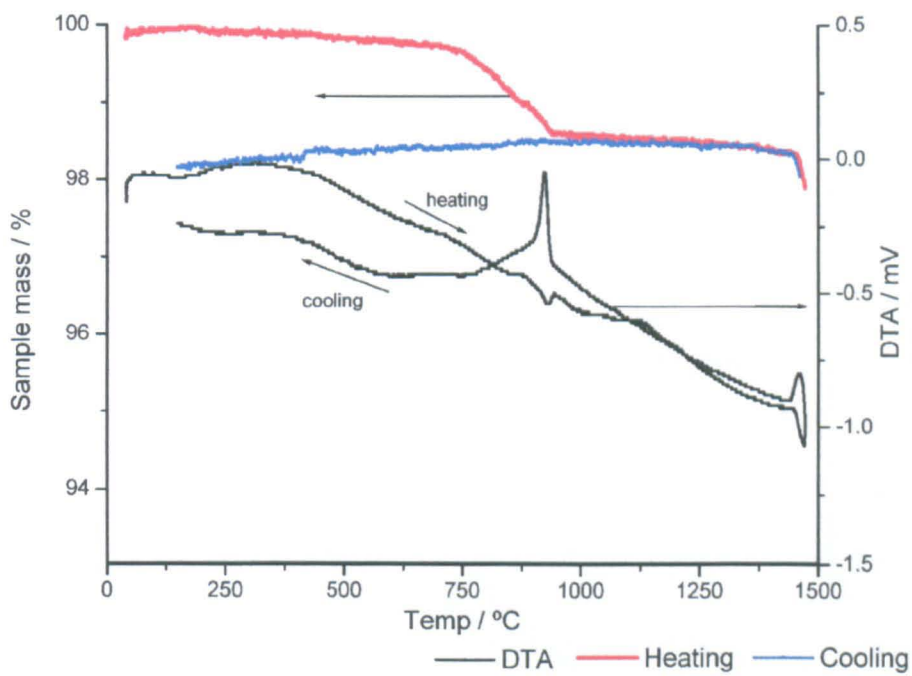


Figure 3.21 – TG data for  $Co_{0.4}Mn_{2.6}O_4$  ( $x = 2.60$  in  $Co_{3-x}Mn_xO_4$ ).

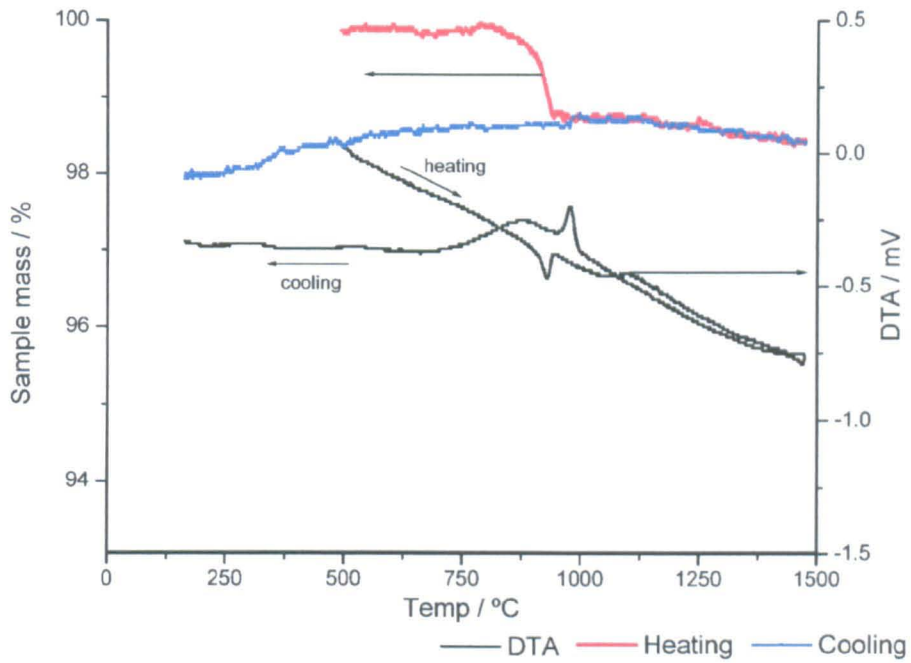
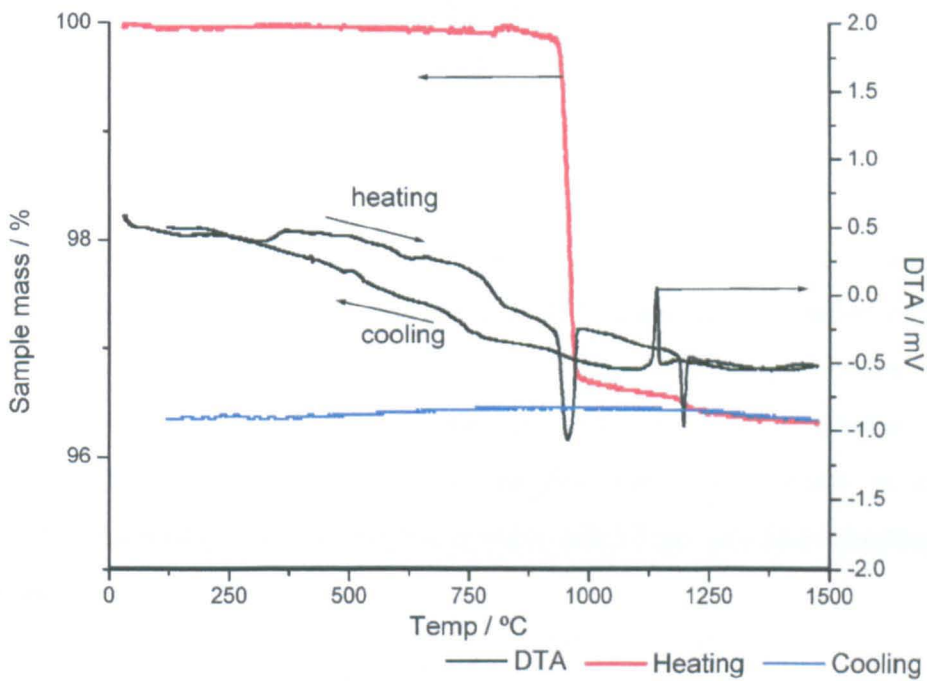


Figure 3.22 – TG data for  $Mn_2O_3$

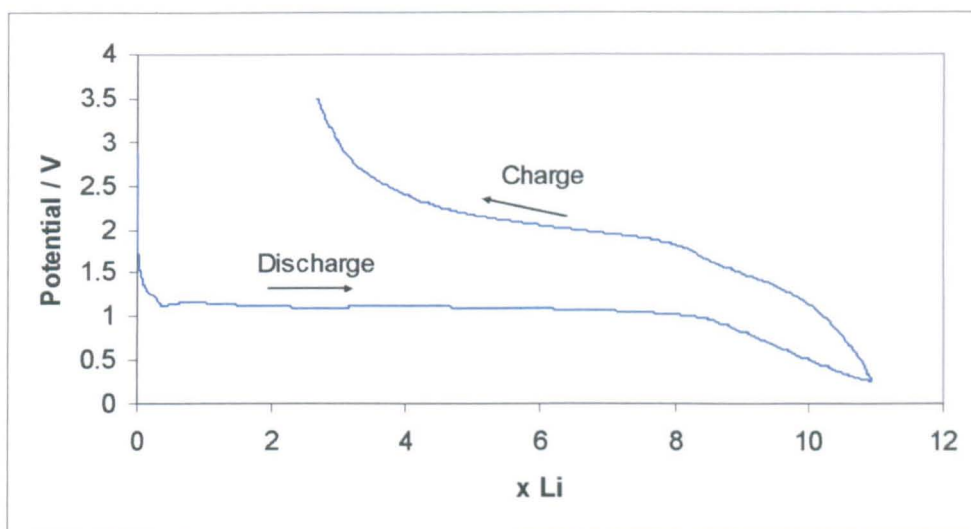


## 4.3 Galvanostatic Cycling with Potential Limitation

### 4.3.1 Charge / Discharge Profiles for $\text{Co}_3\text{O}_4$

Discharge ('adding Li') and charge ('removing Li') profiles for  $\text{Co}_3\text{O}_4$  are presented for the first cycle in Figure 4.4. On first charge, 10.91 Li atoms can be added to the anode per  $\text{Co}_3\text{O}_4$  formula unit; on subsequent discharge 8.23 Li atoms can be removed.

Figure 4.4 – First discharge/charge cycle for  $\text{Co}_3\text{O}_4$



The discharge profile shows a plateau centred at  $\sim 1.1$  V, where  $\sim 8$  Li atoms are added per  $\text{Co}_3\text{O}_4$  unit in the starting anode material. The data then slope down to the cut-off voltage at 0.25 V;  $\sim 3$  Li are added over this period. Two plateaux are observed on charge: roughly 3 Li are removed to  $\sim 1.6$  V, with further removal of  $\sim 5$  Li continuing at higher voltages to the cut-off at 3.5 V. An irreversible loss of  $\sim 3$  Li atoms is observed after first charge.

Gravimetric capacities are only applicable where the starting stoichiometry of the active material is considered; it should be remembered that this stoichiometry may be changed during this first discharge/charge cycle, and that the active material may no longer be  $\text{Co}_3\text{O}_4$  at the start of the second cycle. With this in mind, equation 4.1 gives the theoretical capacity ( $Q_{T0}$ ) for a material of known formula weight ( $M$ ):

$$Q_{T0} = (e \cdot F) / 3.6 \times M \quad (\text{Equation 4.1})$$

Figure 4.5 – Discharge profiles for  $\text{Co}_3\text{O}_4$  over the first six cycles. The legend indicates cycle number.

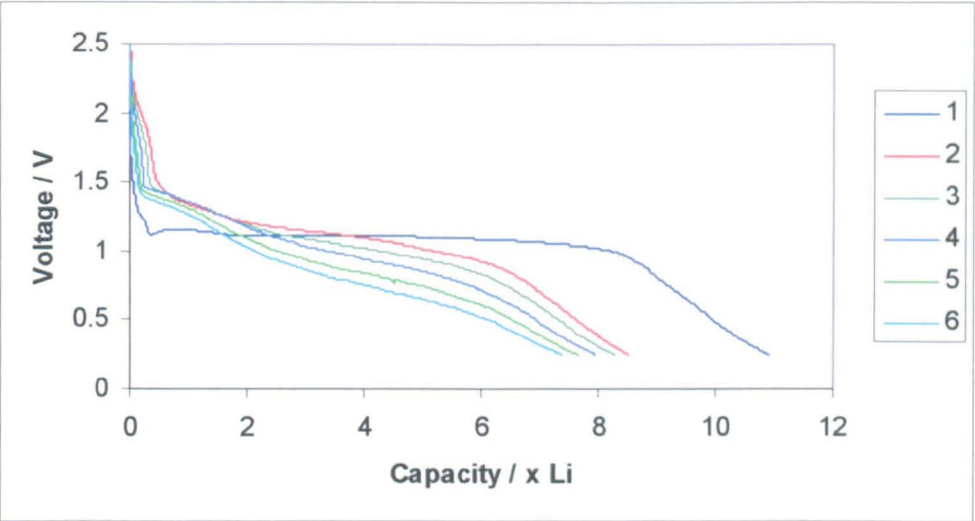
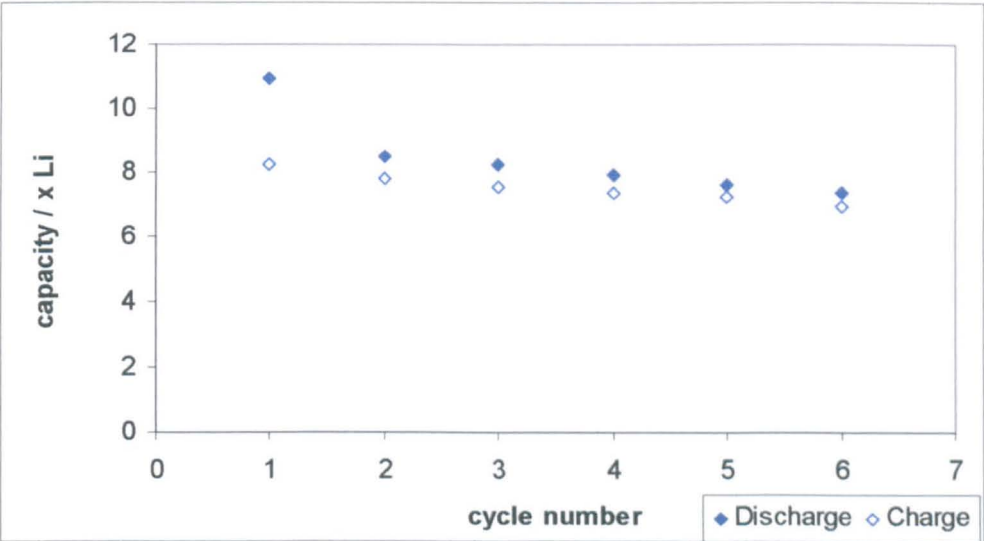
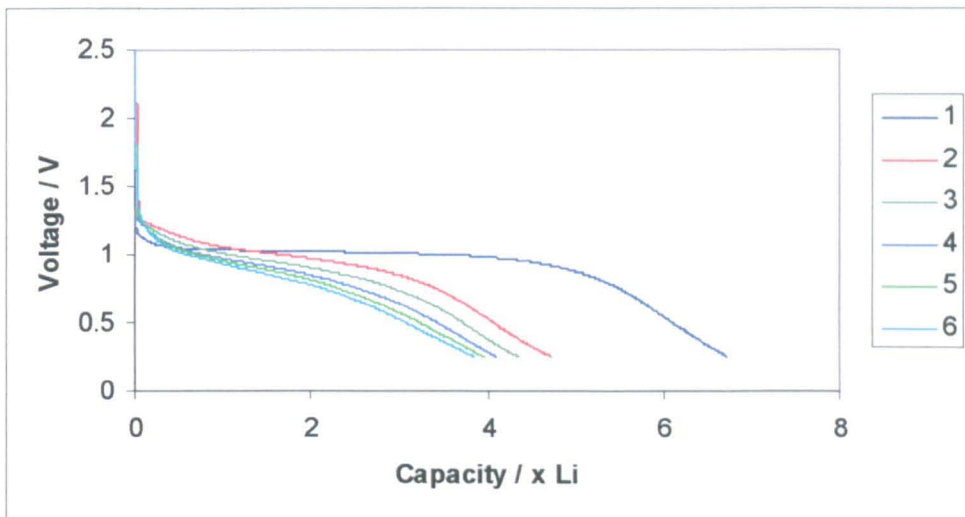


Figure 4.6 – Charge/discharge capacity vs. cycle number for  $\text{Co}_3\text{O}_4$ .



The charge/discharge behaviour of samples with compositions in the  $\text{Co}_{3-x}\text{Mn}_x\text{O}_4$  spinel solid solution ( $0.00 \leq x \leq 3.00$ ) were studied. Discharge profiles for all compositions are presented in Figures 4.7 – 4.20.

**Figure 4.7** – Discharge profiles for  $\text{Co}_{2.7}\text{Mn}_{0.3}\text{O}_4$  ( $x = 0.30$ ) for first 6 cycles.



**Figure 4.8** – Discharge/charge capacity vs. cycle number for  $\text{Co}_{2.7}\text{Mn}_{0.3}\text{O}_4$  ( $x = 0.30$ ).

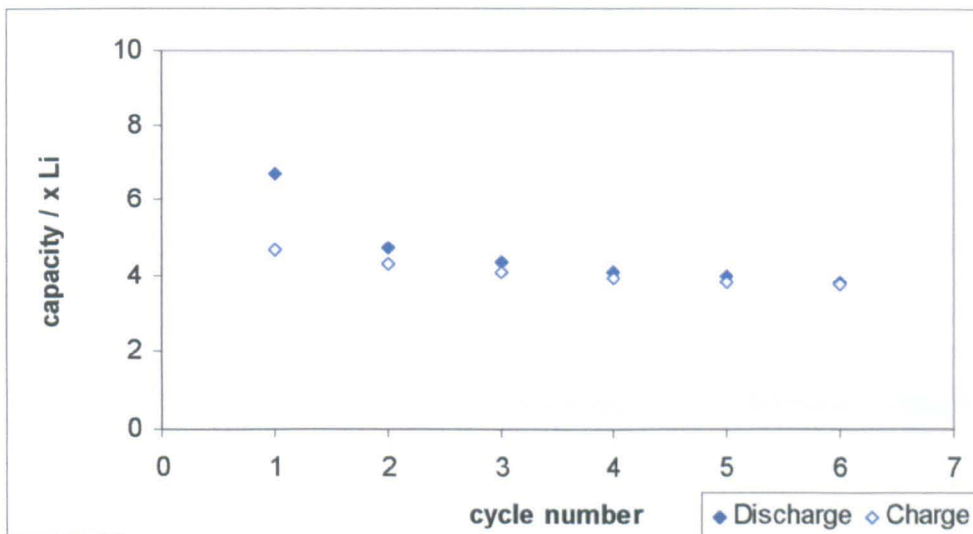


Figure 4.9 – Discharge profiles for  $\text{Co}_{2.4}\text{Mn}_{0.6}\text{O}_4$  ( $x = 0.60$ ) for first 6 cycles.

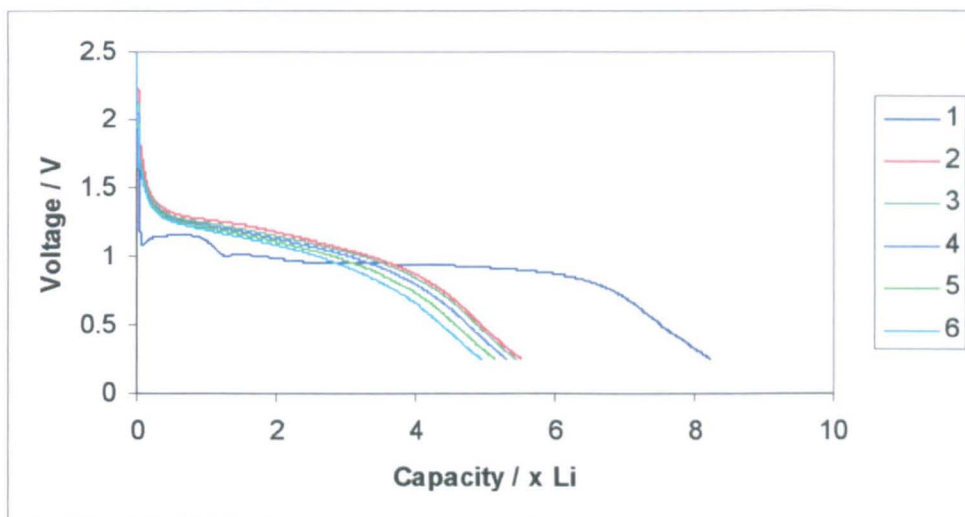


Figure 4.10 – Discharge/charge capacity vs. cycle number for  $\text{Co}_{2.4}\text{Mn}_{0.6}\text{O}_4$  ( $x = 0.60$ ).

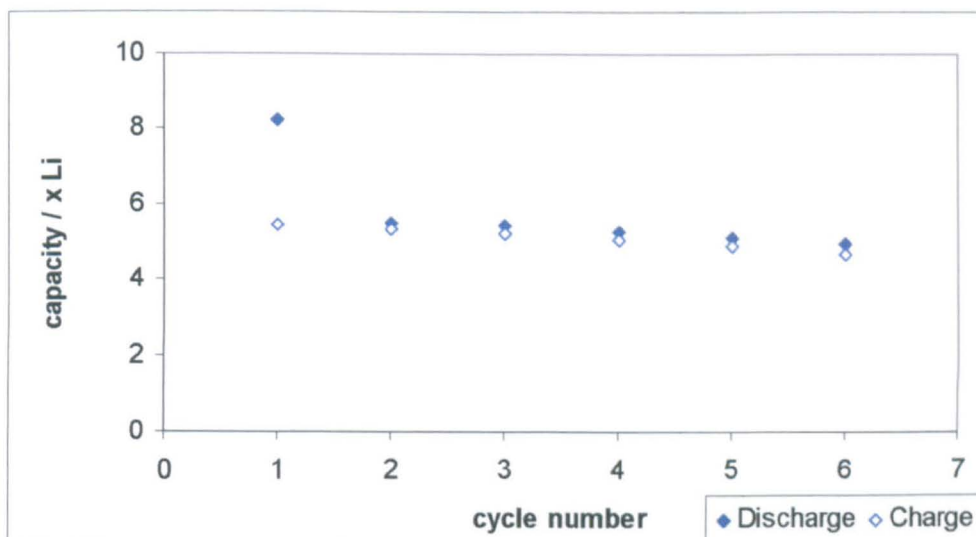


Figure 4.11 – Discharge profiles for  $\text{Co}_2\text{MnO}_4$  ( $x = 1.00$ ) for first 6 cycles.

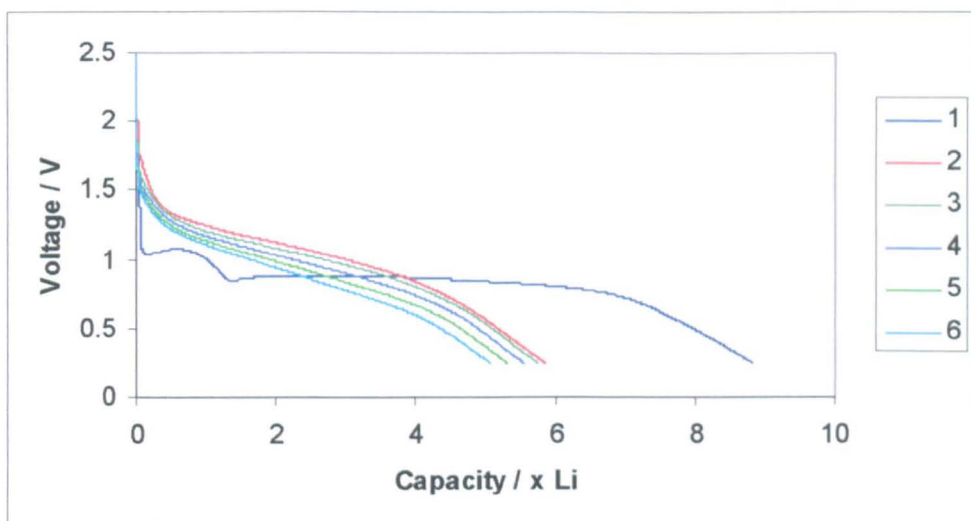


Figure 4.12 – Discharge/charge capacity vs. cycle number for  $\text{Co}_2\text{MnO}_4$  ( $x = 1.00$ ).

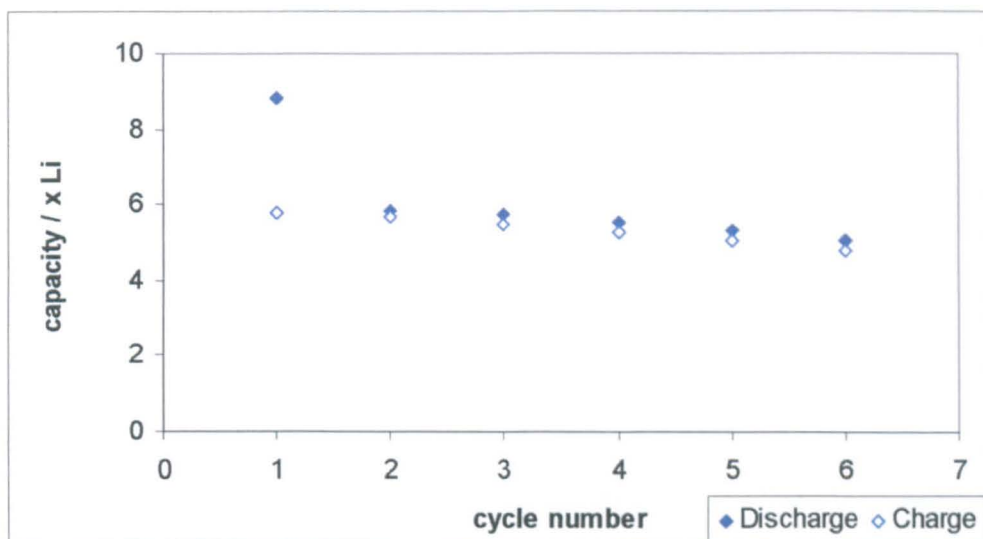


Figure 4.13 – Discharge profiles for  $\text{Co}_{1.7}\text{Mn}_{1.3}\text{O}_4$  ( $x = 1.30$ ) for first 6 cycles.

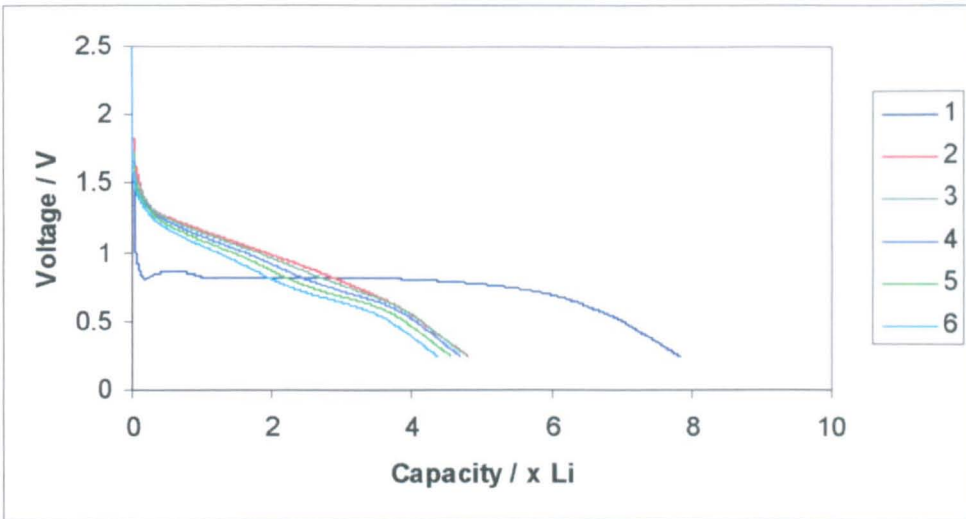


Figure 4.14 – Discharge/charge capacity vs. cycle number for  $\text{Co}_{1.7}\text{Mn}_{1.3}\text{O}_4$  ( $x = 1.30$ ).

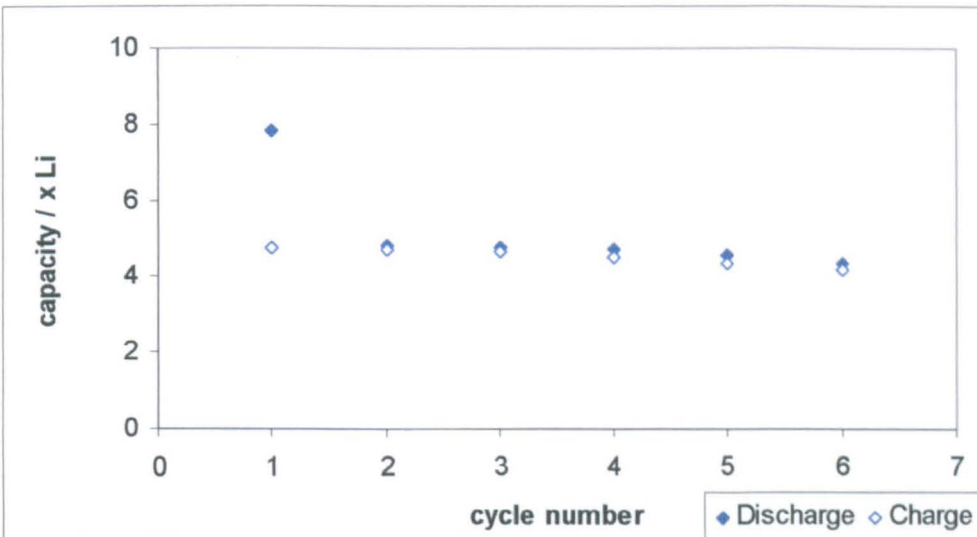


Figure 4.15 – Discharge profiles for  $\text{Co}_{1.5}\text{Mn}_{1.5}\text{O}_4$  ( $x = 1.50$ ) for first 6 cycles.

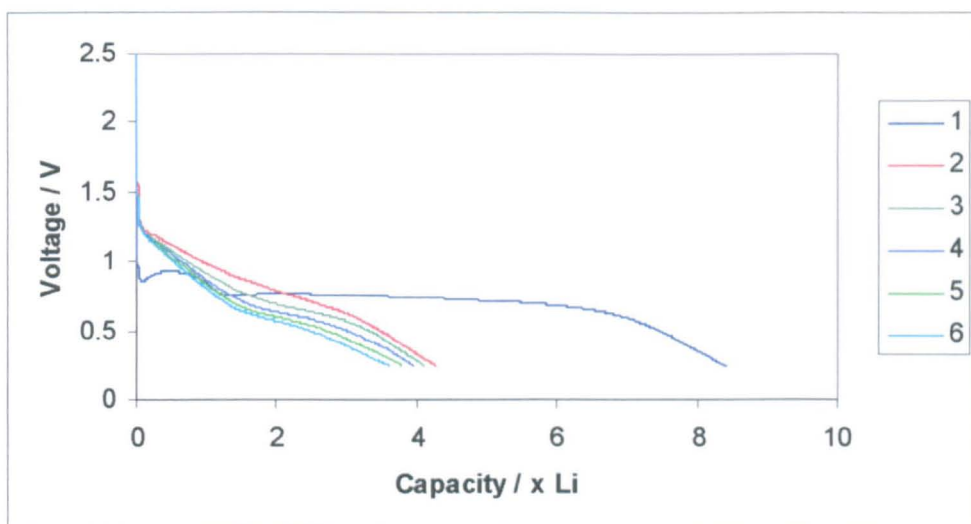


Figure 4.16 – Discharge/charge capacity vs. cycle number for  $\text{Co}_{1.5}\text{Mn}_{1.5}\text{O}_4$  ( $x = 1.50$ ).

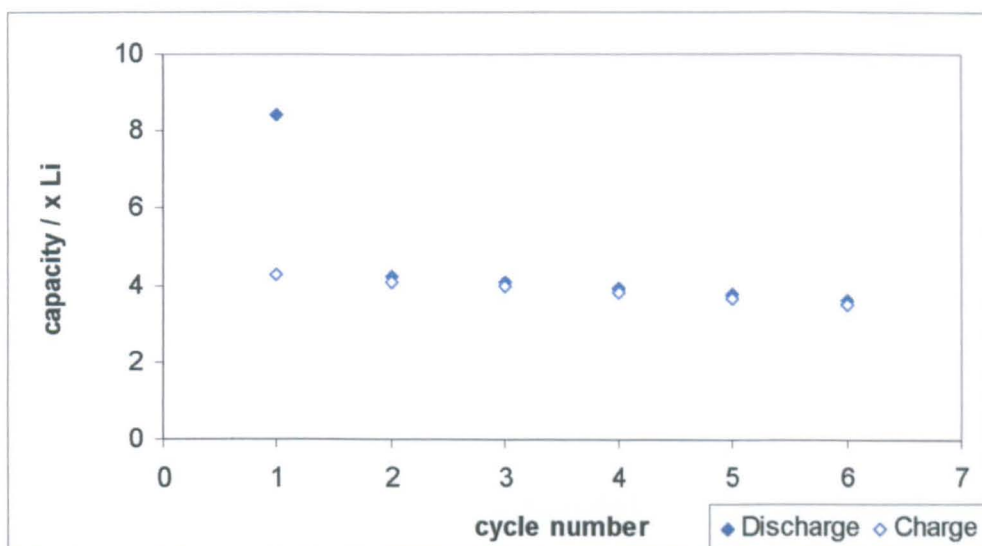


Figure 4.17 – Discharge profiles for  $\text{CoMn}_2\text{O}_4$  ( $x = 2.00$ ) for first 6 cycles.

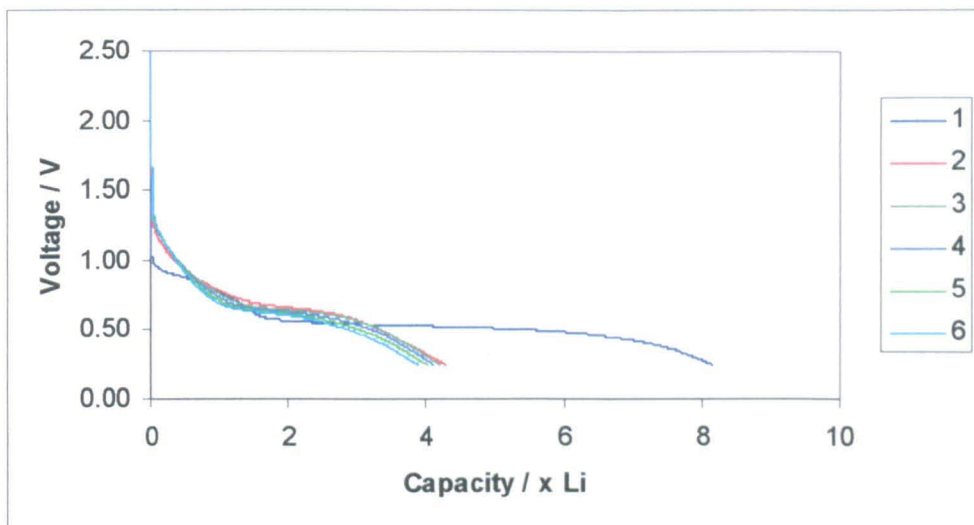


Figure 4.18 – Discharge/charge capacity vs. cycle number for  $\text{CoMn}_2\text{O}_4$  ( $x = 2.00$ ).

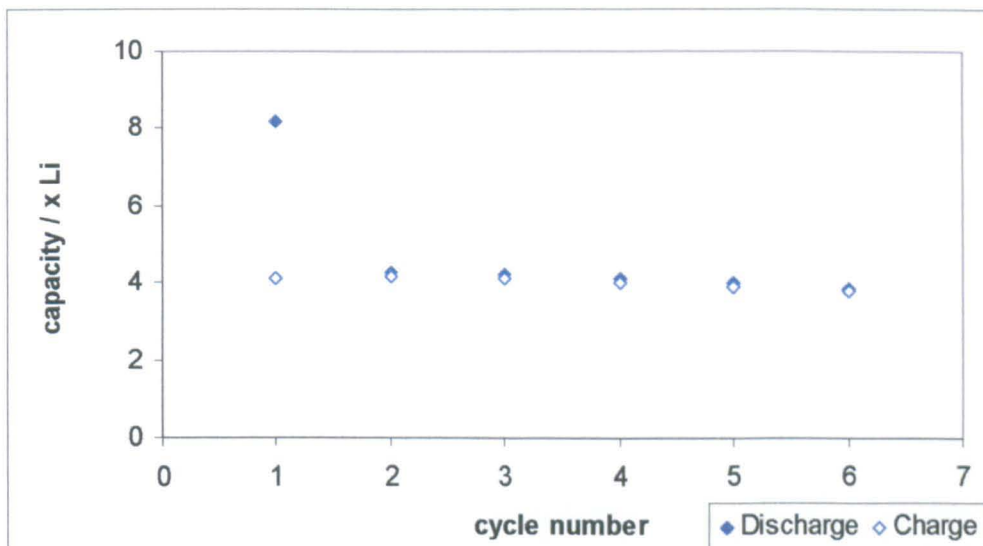


Figure 4.19 – Discharge profiles for  $Co_{0.4}Mn_{2.6}O_4$  ( $x = 2.60$ ) for first 6 cycles.

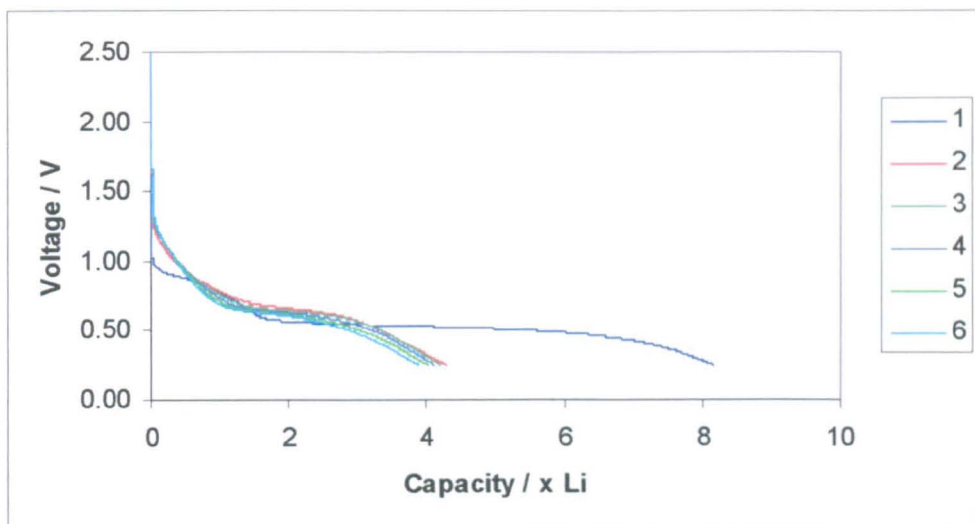


Figure 4.20 – Discharge/charge capacity vs. cycle number for  $Co_{0.4}Mn_{2.6}O_4$  ( $x = 2.60$ ).

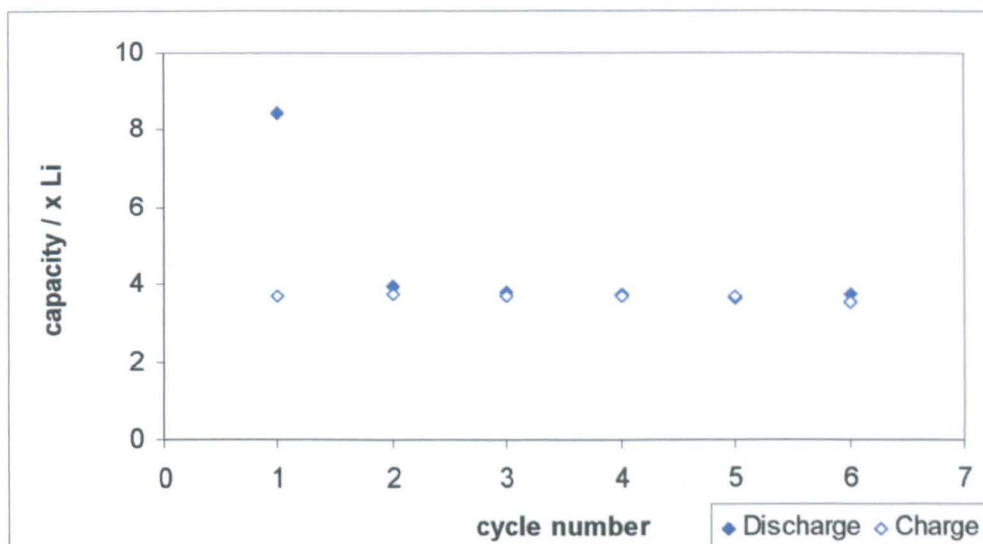


Figure 4.21 – Operating voltage vs. composition ( $x$ , in  $\text{Co}_{3-x}\text{Mn}_x\text{O}_4$ ) on first discharge.

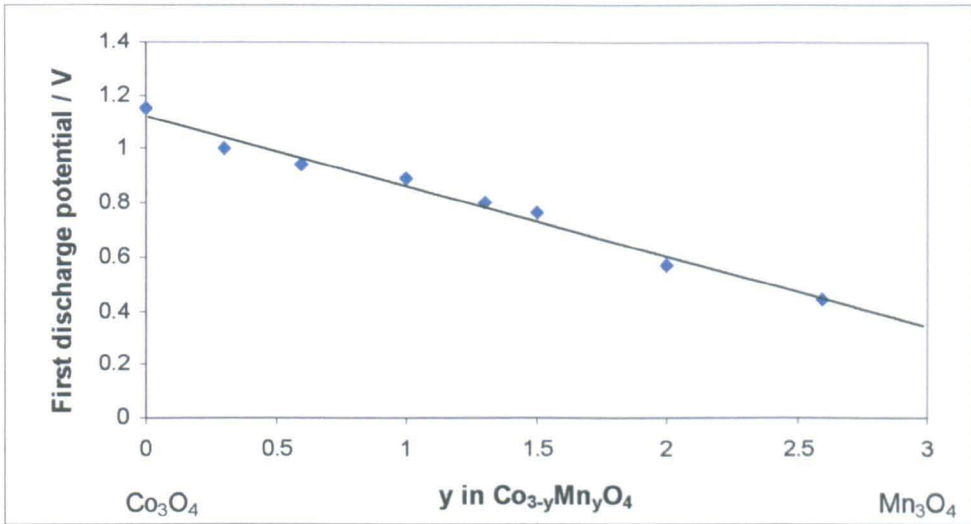
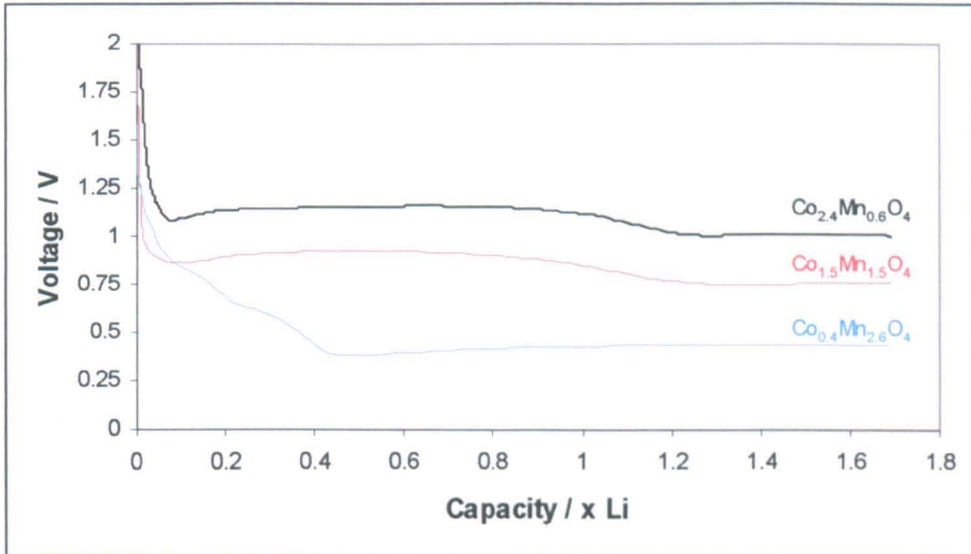
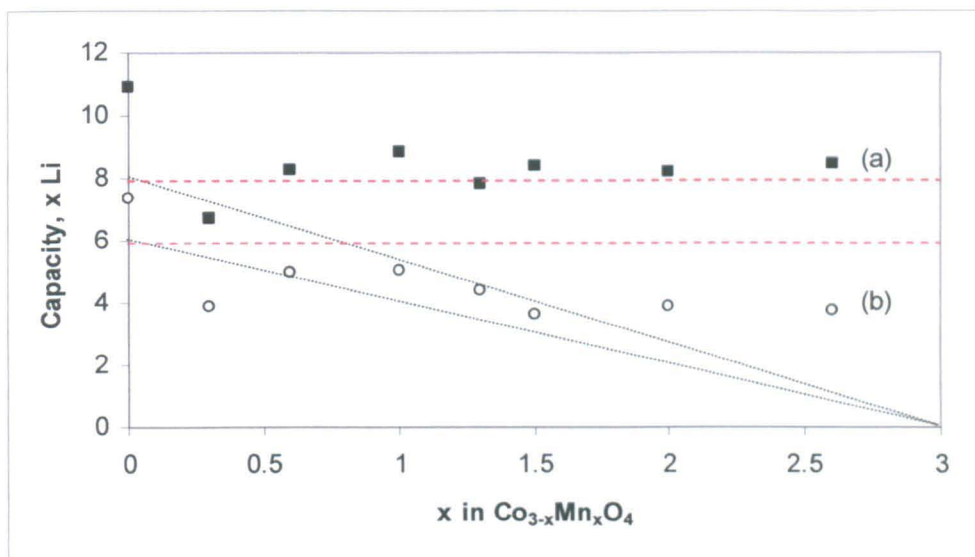


Figure 4.22 – ‘Hump’ in first discharge capacity data at low voltages for  $x = 0.60, 1.50$  and  $2.60$ .



**Figure 4.23** – Capacity,  $x$  Li, obtained on (a) 1<sup>st</sup> (■) and (b) 6<sup>th</sup> (○) discharge for cells with active material of composition  $x$ , where  $0.00 \leq x \leq 2.60$ . Predicted capacities on 1<sup>st</sup> (upper lines) and subsequent (lower lines) cycles are shown for Co as the lone active species (black dotted lines), or for both Co and Mn (red dashed lines) as the active material.



**Figure 4.24** – Specific discharge capacity ( $\text{mAh.g}^{-1}$ ) left after 6 cycles as a percentage of (a) first discharge capacity, ■, (b) second discharge capacity, ○, for cells with active material of composition  $0.00 \leq x \leq 2.60$ .

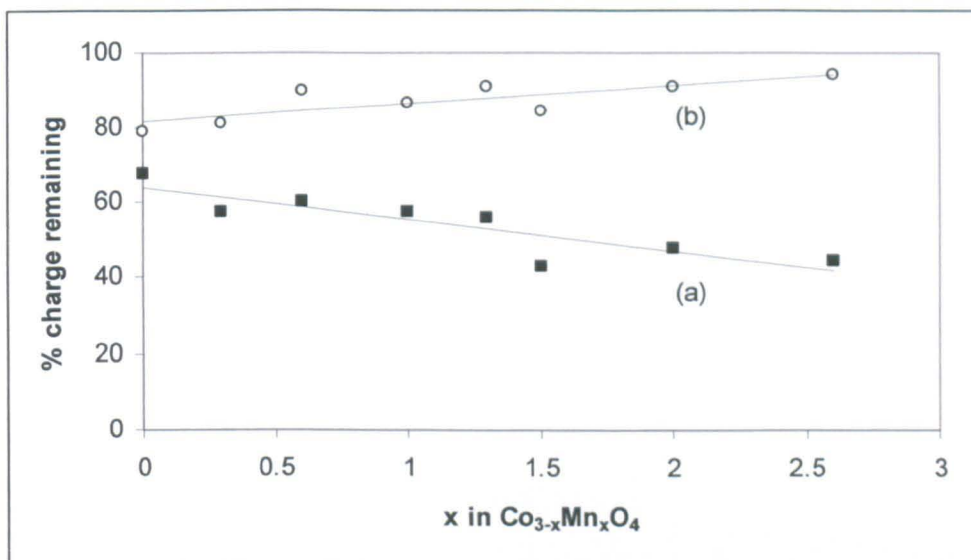


**Figure 4.25** – Differential potentiogram of GCPL data for  $x = 0.00$  ( $\text{Co}_3\text{O}_4$ ).

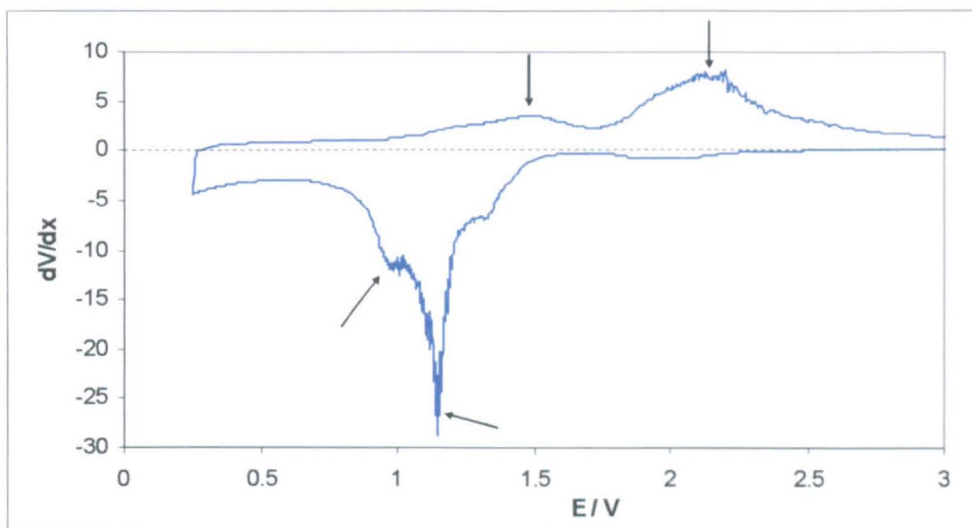


**Figure 4.26** – Differential potentiogram of GCPL data for  $x = 0.30$  ( $\text{Co}_{2.7}\text{Mn}_{0.3}\text{O}_4$ ).

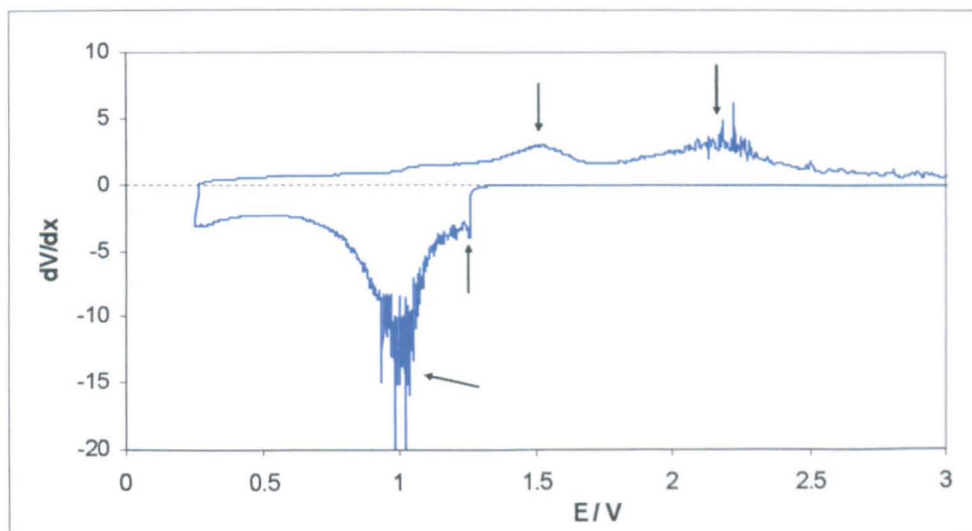


**Figure 4.27** – Differential potentiogram of GCPL data for  $x = 0.60$  ( $\text{Co}_{2.4}\text{Mn}_{0.6}\text{O}_4$ ).

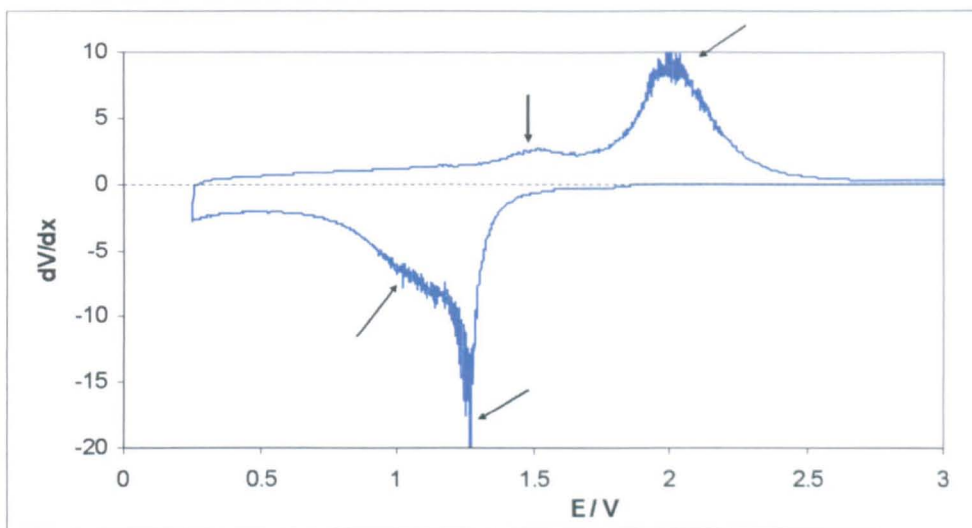


**Figure 4.28** – Differential potentiogram of GCPL data for  $x = 1.00$  ( $\text{Co}_2\text{MnO}_4$ ).

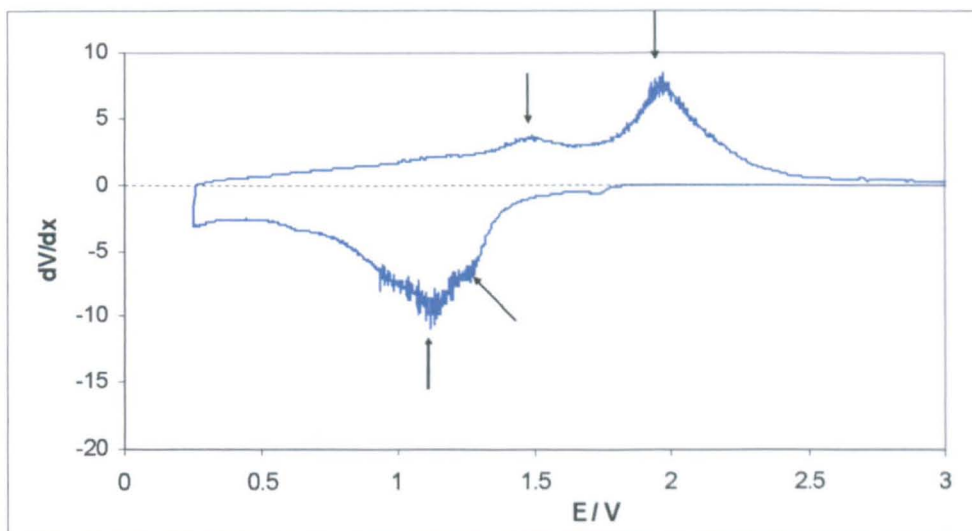


**Figure 4.29** – Differential potentiogram of GCPL data for  $x = 1.30$  ( $\text{Co}_{1.7}\text{Mn}_{1.3}\text{O}_4$ ).

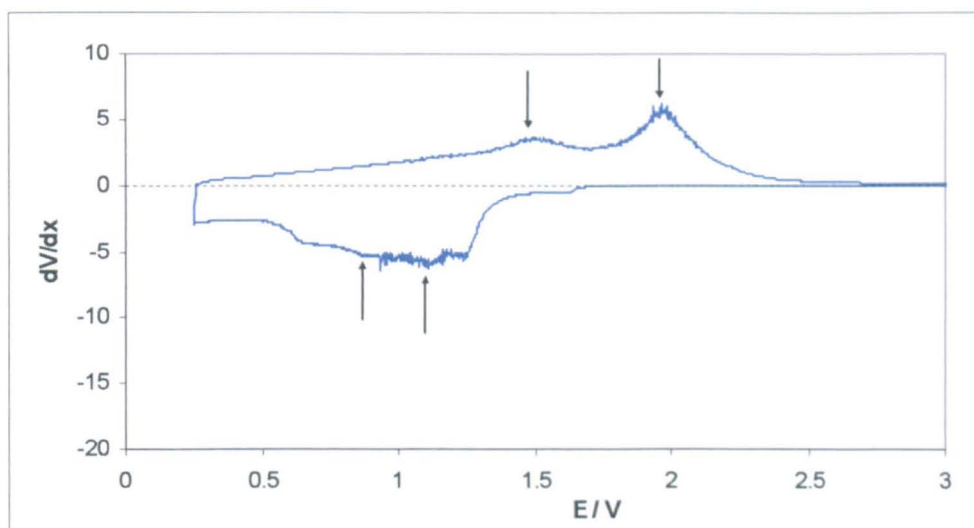


**Figure 4.30** – Differential potentiogram of GCPL data for  $x = 1.50$  ( $\text{Co}_{1.5}\text{Mn}_{1.5}\text{O}_4$ ).

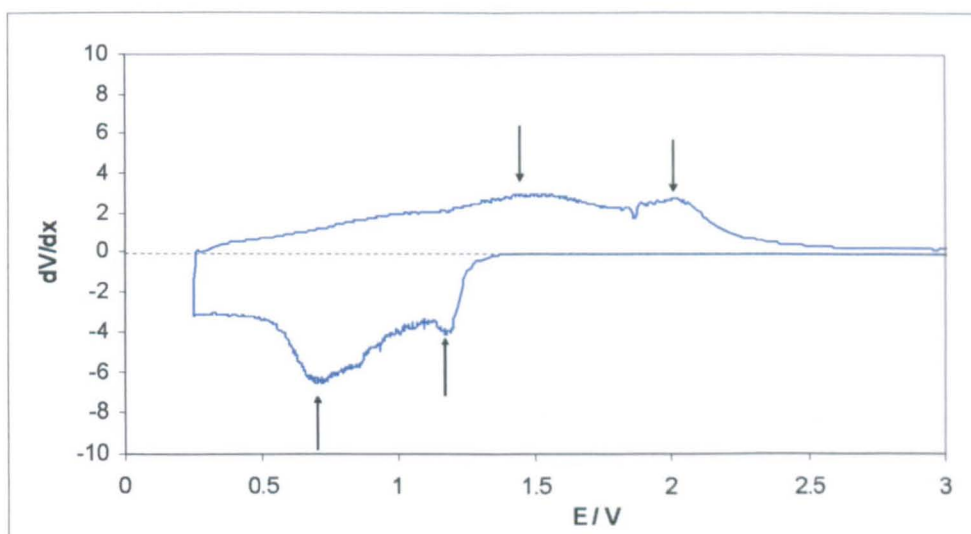


**Figure 4.31** – Differential potentiogram of GCPL data for  $x = 2.00$  ( $\text{CoMn}_2\text{O}_4$ ).

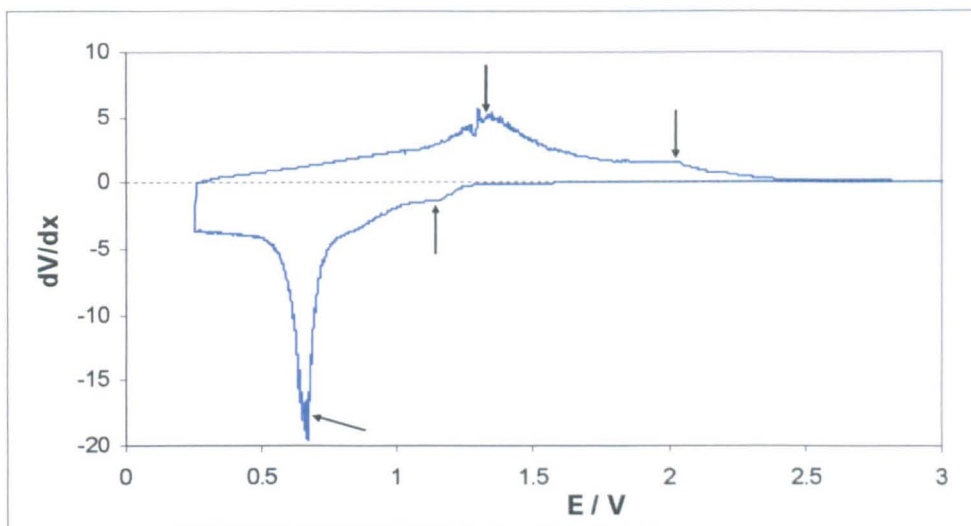
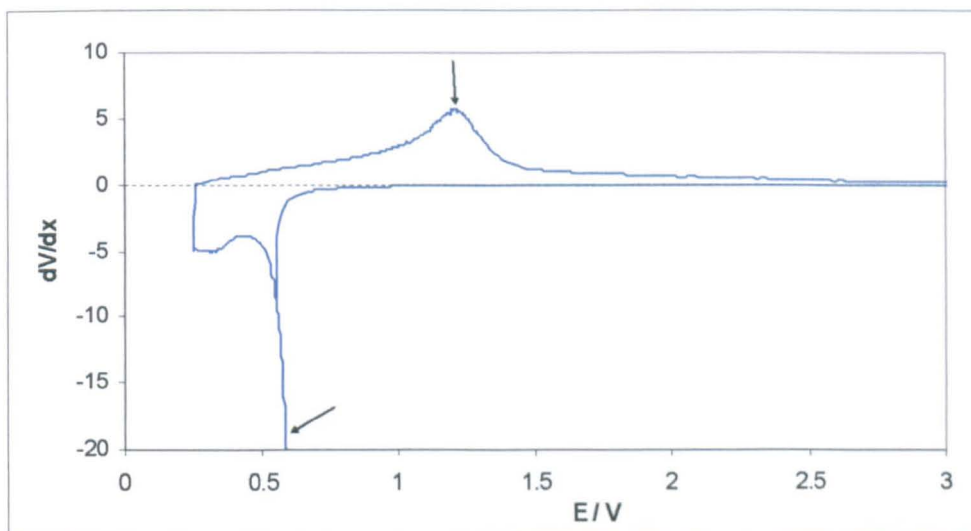


**Figure 4.32** – Differential potentiogram of GCPL data for  $x = 2.60$  ( $\text{Co}_{0.4}\text{Mn}_{2.6}\text{O}_4$ ).



## 5.3 'LiCo<sub>x</sub>Mn<sub>2-x</sub>O<sub>4</sub>' – Phase relations in the LiMn<sub>2</sub>O<sub>4</sub> - LiCoMnO<sub>4</sub> system

### 5.3.1 Solid solution studies

Samples with compositions  $0.00 \leq x \leq 1.00$  in LiCo<sub>x</sub>Mn<sub>2-x</sub>O<sub>4</sub> were prepared. This series has been reported by Kawai and West,<sup>4,6</sup> though little discussion was presented on the thermal behaviour of the materials.

A cubic spinel solid solution was found to extend over the compositional range  $0.00 \leq x \leq 1.00$  in LiCo<sub>x</sub>Mn<sub>2-x</sub>O<sub>4</sub>. Lattice parameter data, refined using silicon internal standards, are listed in Table 5.1, with the variation in lattice parameter with composition shown in Figure 5.2.

*Table 5.1 – Lattice parameter data for the compositional range  $0.00 \leq x \leq 1.00$  in LiCo<sub>x</sub>Mn<sub>2-x</sub>O<sub>4</sub>*

$x$ in LiCo <sub>x</sub> Mn <sub>2-x</sub> O <sub>4</sub>	Stoichiometry	$a_{\text{spinel}} / \text{Å}$
0.00	LiMn <sub>2</sub> O <sub>4</sub>	8.2450 (13)
0.20	LiCo <sub>0.2</sub> Mn <sub>1.8</sub> O <sub>4</sub>	8.2077 (6)
0.35	LiCo <sub>0.35</sub> Mn <sub>1.65</sub> O <sub>4</sub>	8.1752 (13)
0.50	LiCo <sub>0.5</sub> Mn <sub>1.5</sub> O <sub>4</sub>	8.1316 (8)
0.75	LiCo <sub>0.75</sub> Mn <sub>1.25</sub> O <sub>4</sub>	8.0975 (14)
1.00	LiCoMnO <sub>4</sub>	8.0606 (14)

*Figure 5.2 – Lattice parameter data for the compositional range  $0.00 \leq x \leq 1.00$  in LiCo<sub>x</sub>Mn<sub>2-x</sub>O<sub>4</sub>*

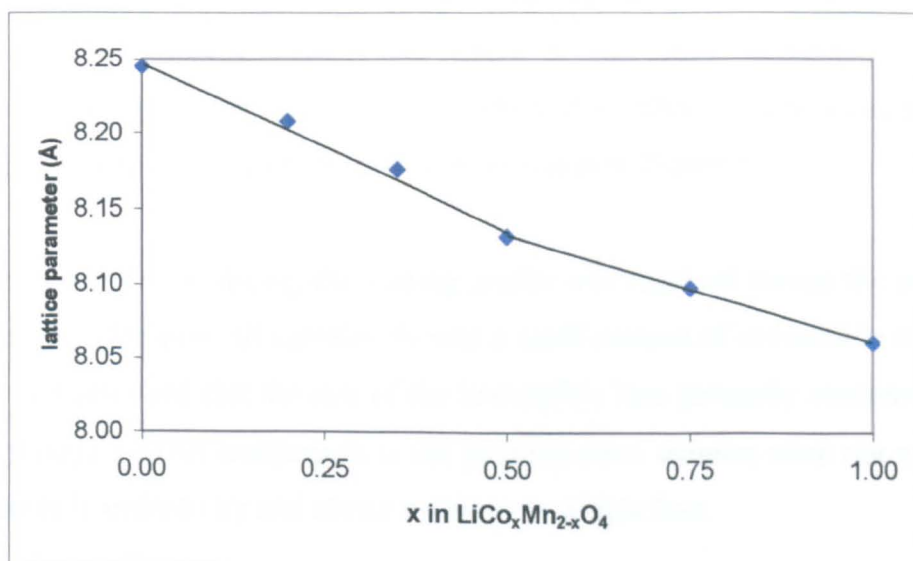


Figure 5.3 – TG and DTA data for  $\text{LiMn}_2\text{O}_4$ .

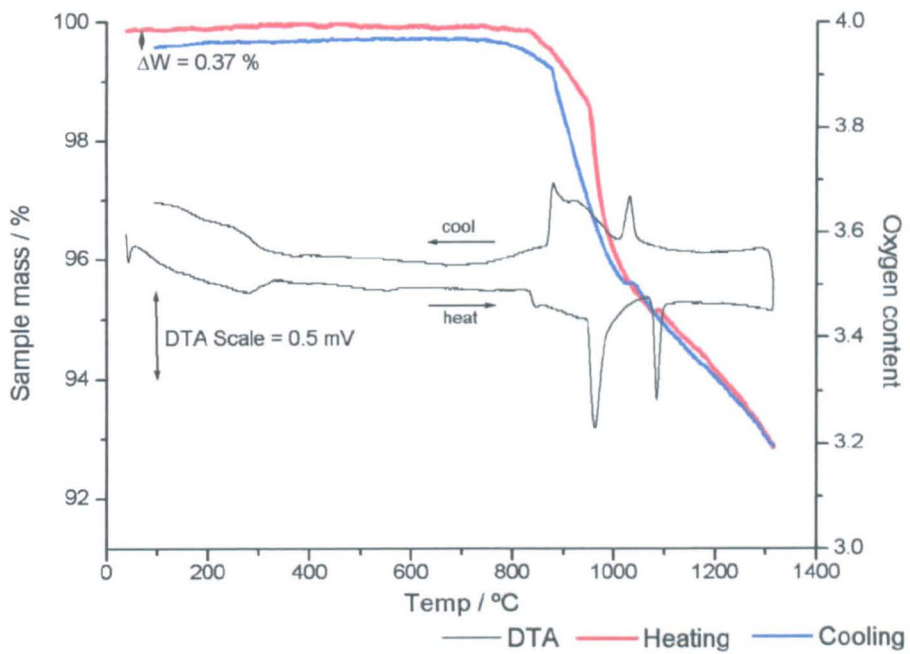


Figure 5.4 – TG and DTA data for  $\text{LiCo}_{0.2}\text{Mn}_{1.8}\text{O}_4$ .

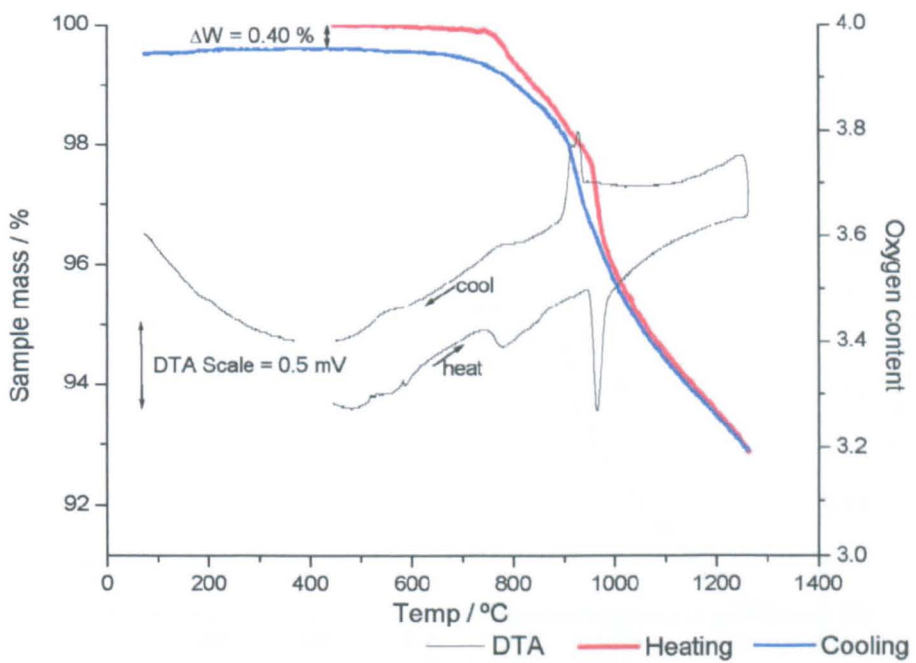


Figure 5.5 - TG-DTA data for  $\text{LiCo}_{0.33}\text{Mn}_{1.65}\text{O}_4$ .

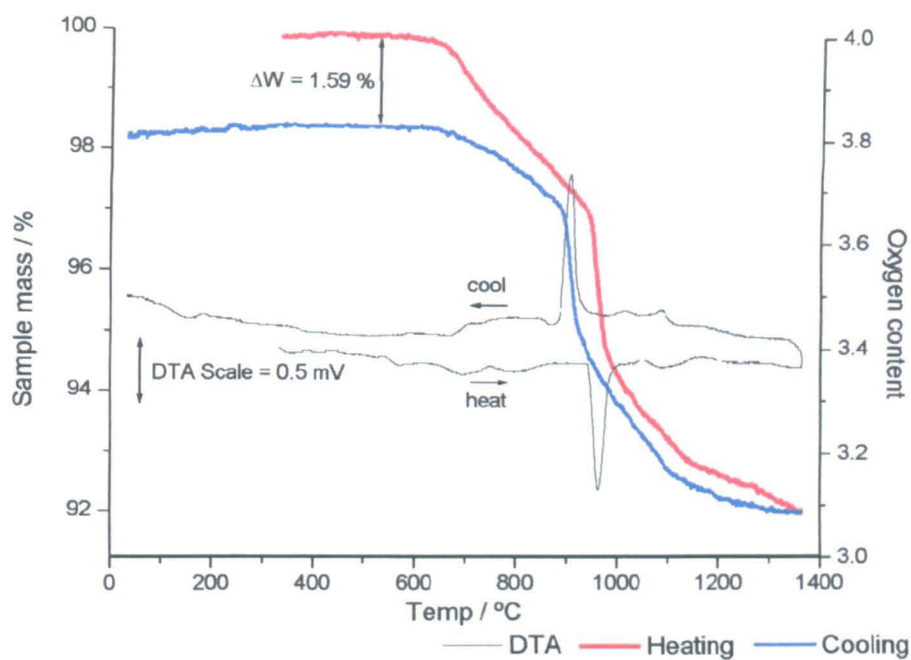
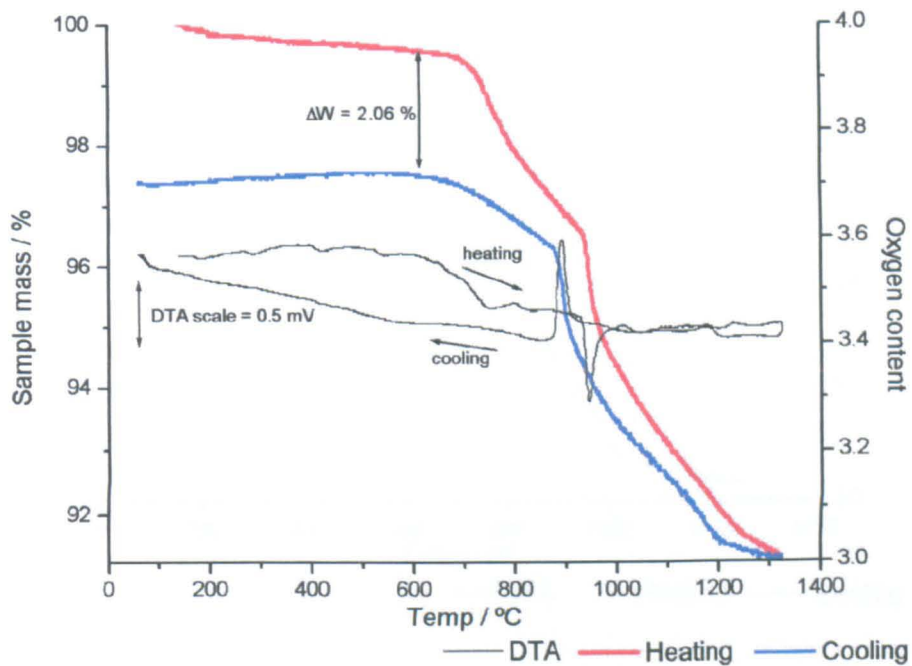
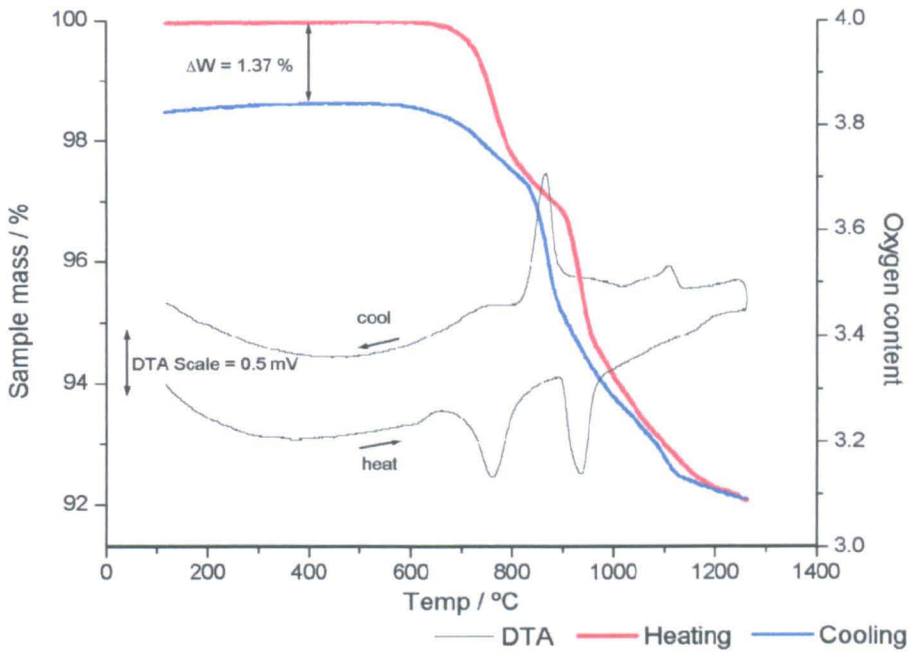


Figure 5.6 - TG and DTA data for  $\text{LiCo}_{0.5}\text{Mn}_{1.5}\text{O}_4$ .



**Figure 5.7** – TG and DTA data for  $\text{LiCo}_{0.75}\text{Mn}_{1.25}\text{O}_4$ .



**Figure 5.8** – TG and DTA data for  $\text{LiCoMnO}_4$ .

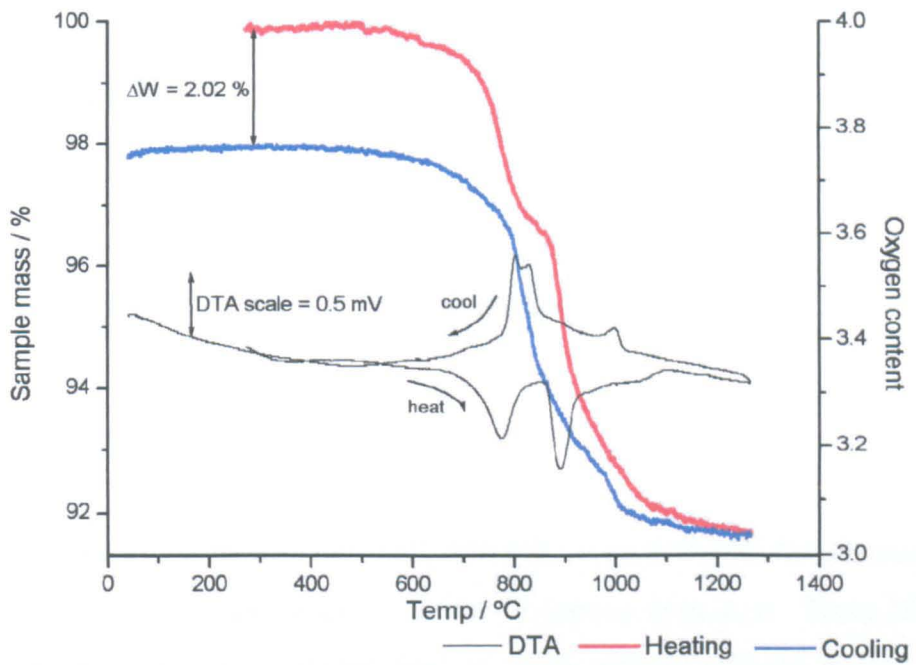


**Figure 5.9** – Temperature of observed inflexion in TG data for samples with composition  $0.00 \leq x \leq 1.00$  in  $\text{LiCo}_x\text{Mn}_{2-x}\text{O}_4$ .

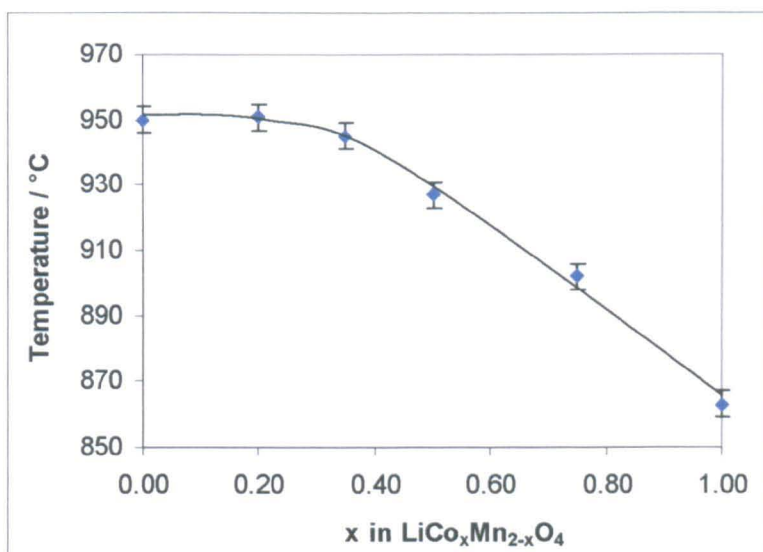
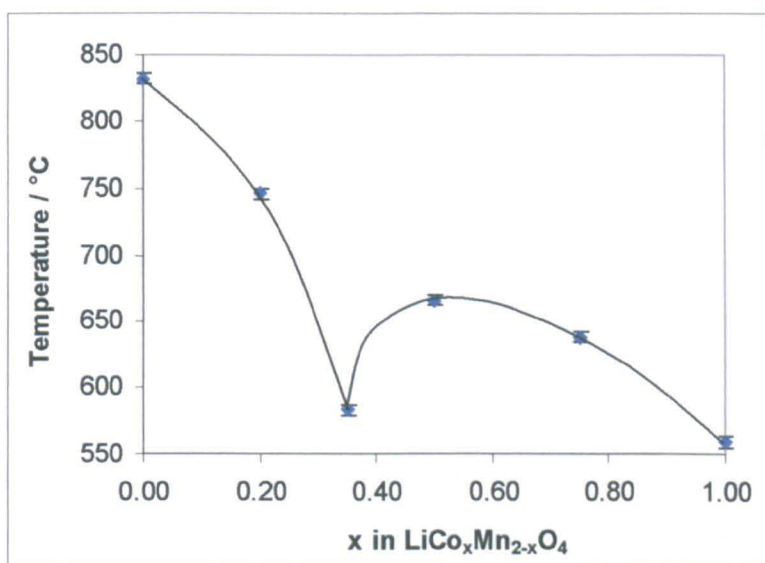


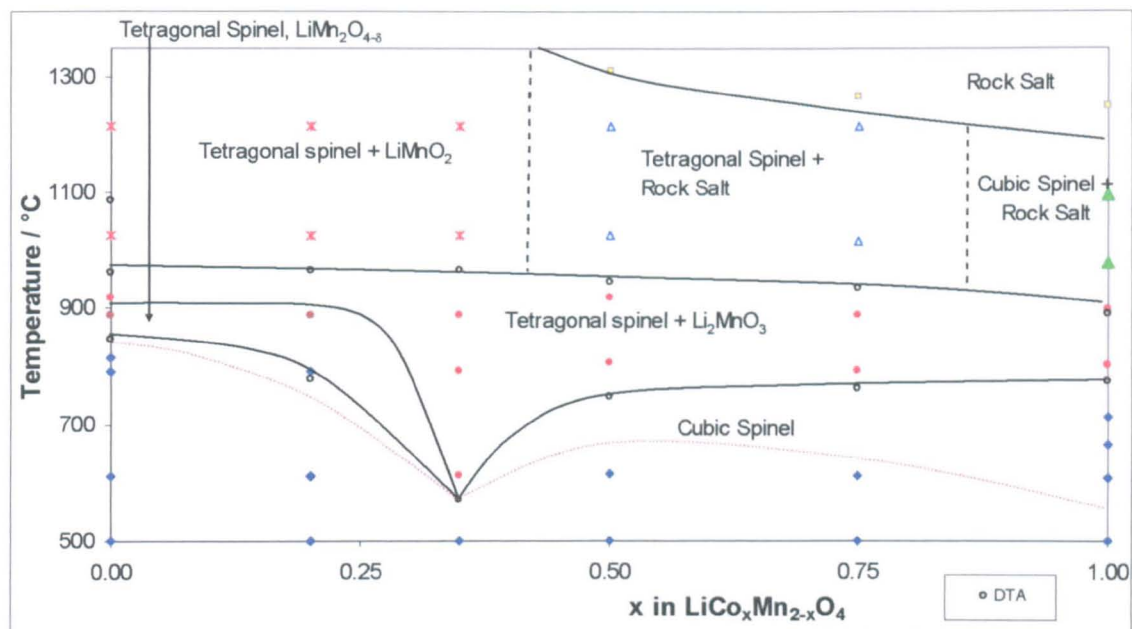
**Figure 5.10** – Initial temperature of observed weight loss in TG data for samples with composition  $0.00 \leq x \leq 1.00$  in  $\text{LiCo}_x\text{Mn}_{2-x}\text{O}_4$ .



### 5.3.2b DTA results

The peak maxima temperatures observed in the DTA data collected for all samples are presented in Figure 5.11; peak onsets could not always be identified. These DTA data indicate a number of peaks (either two or three clearly defined peaks) for all compositions studied. This suggests that more than one reaction occurs on heating the spinels to 1200 – 1300 °C.

**Figure 5.12** – The  $\text{LiCo}_x\text{Mn}_{2-x}\text{O}_4$  phase diagram. DTA peaks are indicated by empty circles, the temperature at which weight loss is first observed in TG data is indicated by the red dotted line.



For  $x = 0.00$  ( $\text{LiMn}_2\text{O}_4$ ), four distinct phase regions were identified in the quenched samples. The cubic spinel structure was retained in samples quenched from up to 814 °C. A tetragonal spinel was observed in the quench made from 886 °C. At 917 °C, a mixture of tetragonal spinel and  $\text{Li}_2\text{MnO}_3$  was observed. In samples quenched from 1024 and 1213 °C, a mixture of tetragonal spinel and  $\text{LiMnO}_2$  phases was observed.

The XRD data from quenched samples are largely consistent with the TG and DTA data. Though oxygen loss begins at  $\sim 830$  °C, the cubic spinel structure is initially retained. The DTA peak at 846 °C indicates a transition to tetragonal symmetry. The segregation of  $\text{Li}_2\text{MnO}_3$  then begins by 917 °C, though the broadened DTA peak suggests that the stoichiometries of the phases present continue to change. The sharp DTA peak at 962 °C indicates, in agreement with the quench data, that a transition to a mixture of  $\text{LiMnO}_2$  and a tetragonal spinel phase occurs around this temperature. A DTA peak at 1085 °C, which is reversible on cooling, suggests that a further structural change is occurring; however, quenches made from 1024 and 1213 °C showed mixtures of the same phases,  $\text{LiMnO}_2$  and a tetragonal spinel. Any change occurring must, therefore, be rapidly reversible on cooling since quenching into mercury was too slow to prevent it. One possibility may be, as suggested by Thackeray *et al.*,<sup>8</sup> that a tetragonal  $\rightleftharpoons$  cubic phase change in the high temperature spinel phase at 1085 °C, similar to that observed for  $\text{Mn}_3\text{O}_4$  at 1198 °C.

**Figure 5.14** – The effect of atmosphere on TG data for  $\text{LiCoMnO}_4$  ( $x = 0.00$  in  $\text{Li}_{1+x}\text{Co}_{1+2x}\text{Mn}_{1-x}\text{O}_4$ ).

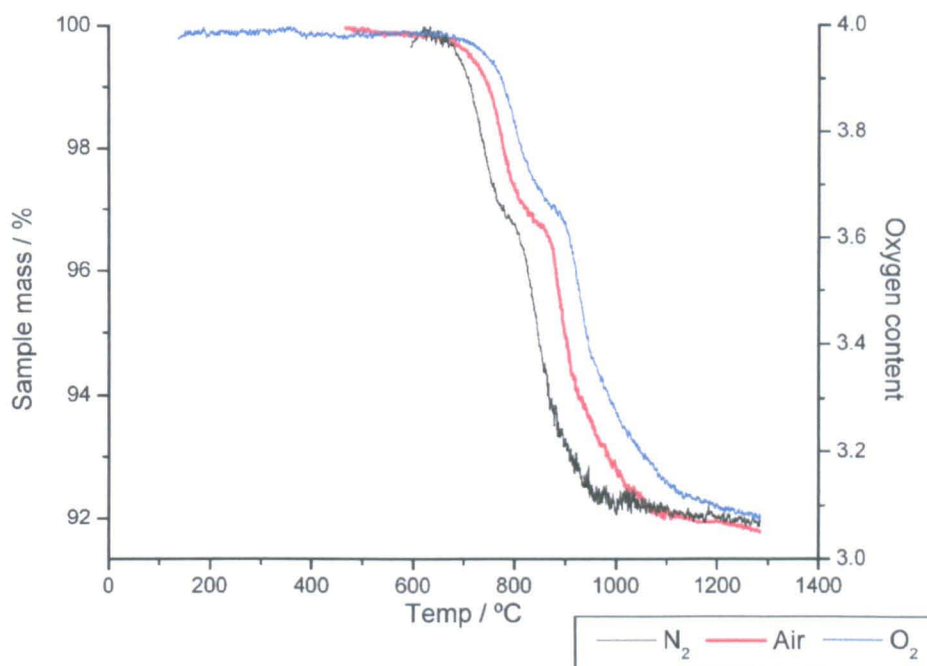


**Figure 5.15** – TG and DTA data for  $\text{Li}_{0.78}\text{Co}_{1.44}\text{Mn}_{0.78}\text{O}_4$  ( $x = 0.22$  in  $\text{Li}_{1+x}\text{Co}_{1+2x}\text{Mn}_{1-x}\text{O}_4$ ).

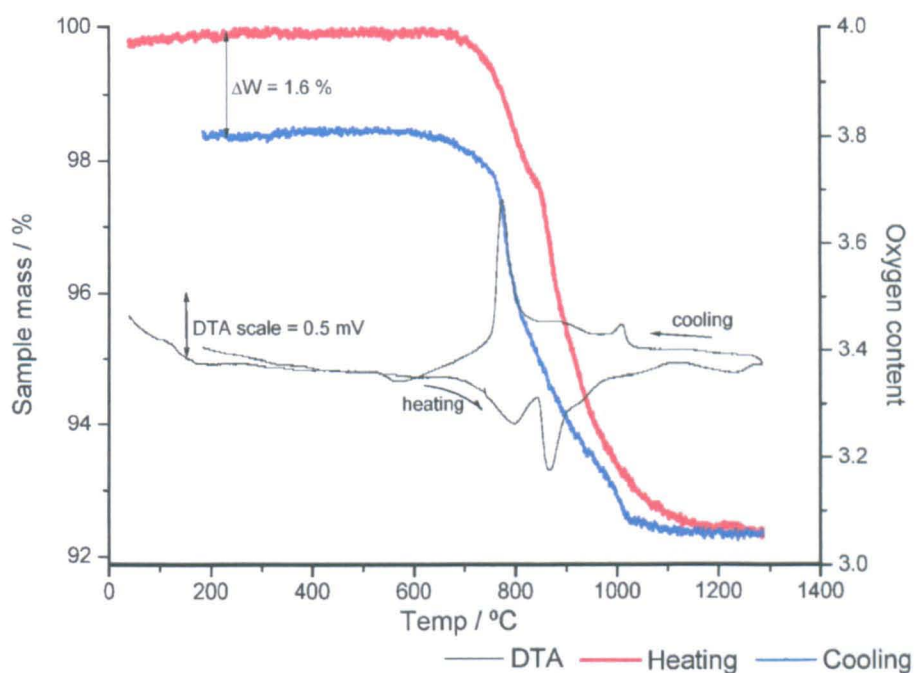


Figure 5.16 – TG and DTA data for  $\text{Li}_{0.6}\text{Co}_{1.8}\text{Mn}_{0.6}\text{O}_4$  ( $x = 0.40$  in  $\text{Li}_{1+x}\text{Co}_{1+2x}\text{Mn}_{1-x}\text{O}_4$ ).

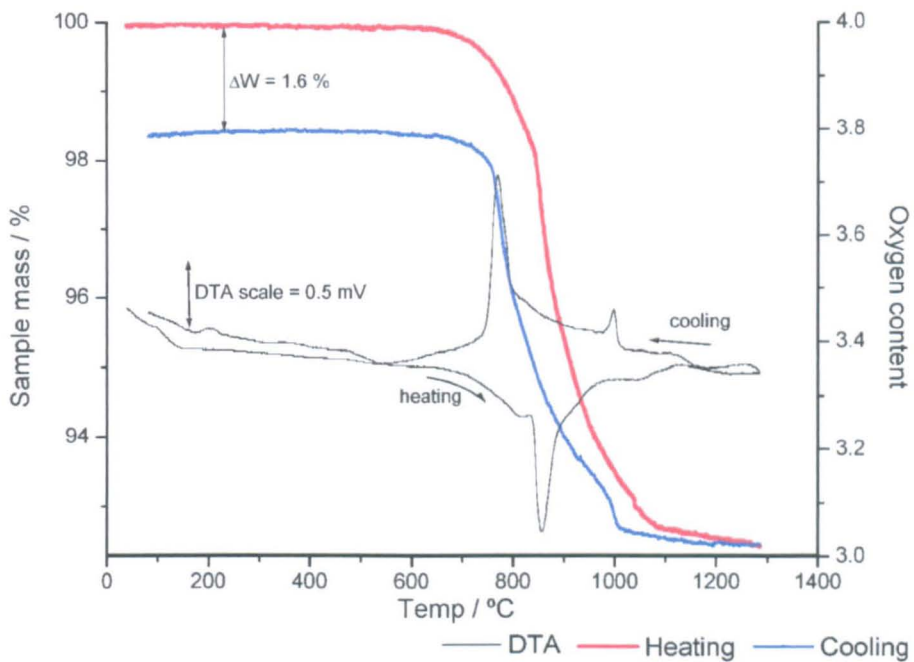


Figure 5.17 – TG and DTA data for  $\text{Li}_{0.49}\text{Co}_{2.02}\text{Mn}_{0.49}\text{O}_4$  ( $x = 0.51$  in  $\text{Li}_{1+x}\text{Co}_{1+2x}\text{Mn}_{1-x}\text{O}_4$ ).

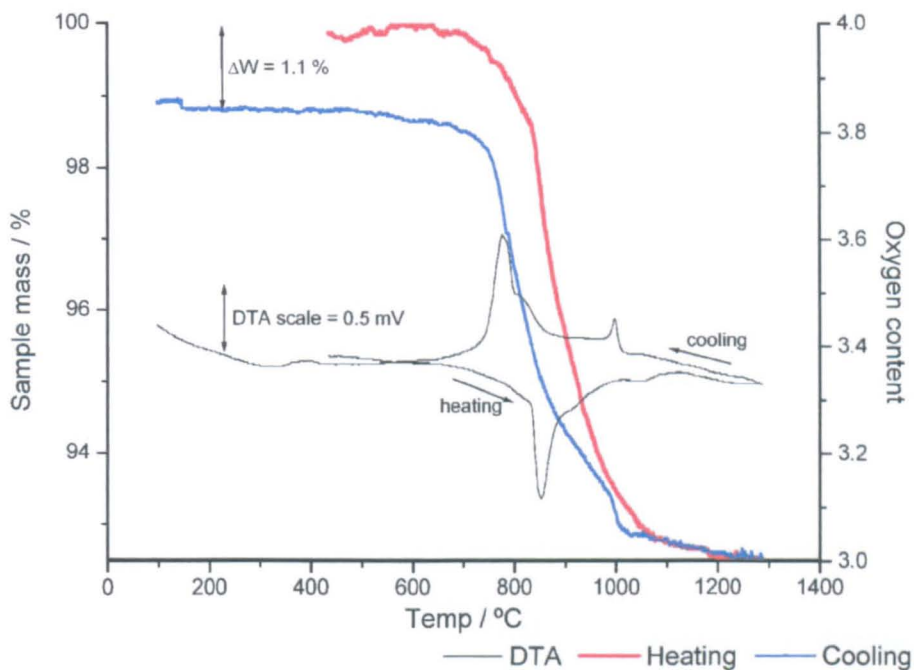


Figure 5.18 – TG and DTA data for  $\text{Li}_{0.37}\text{Co}_{2.26}\text{Mn}_{0.37}\text{O}_4$  ( $x = 0.63$  in  $\text{Li}_{1+x}\text{Co}_{1+2x}\text{Mn}_{1-x}\text{O}_4$ ).

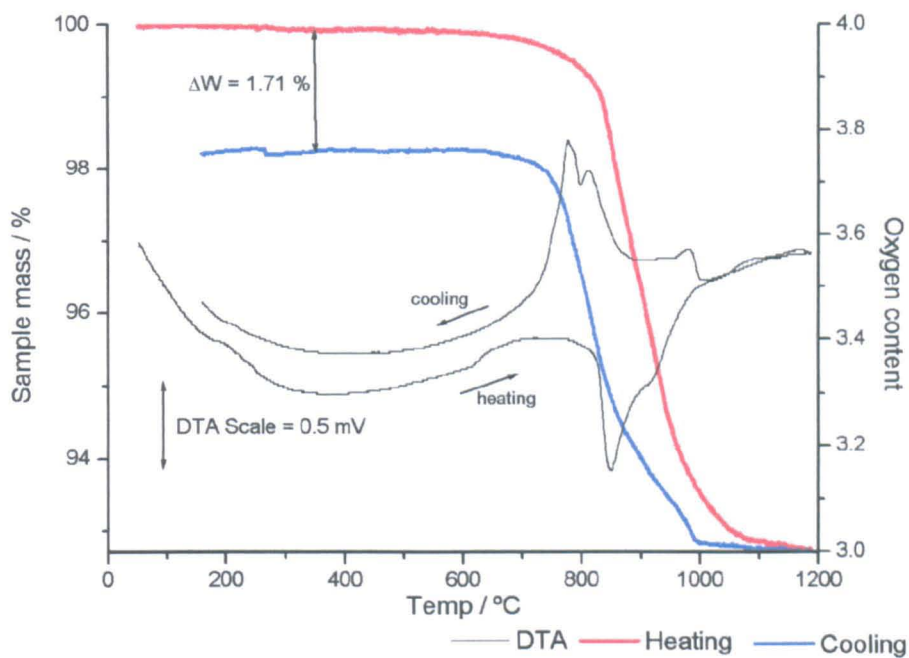
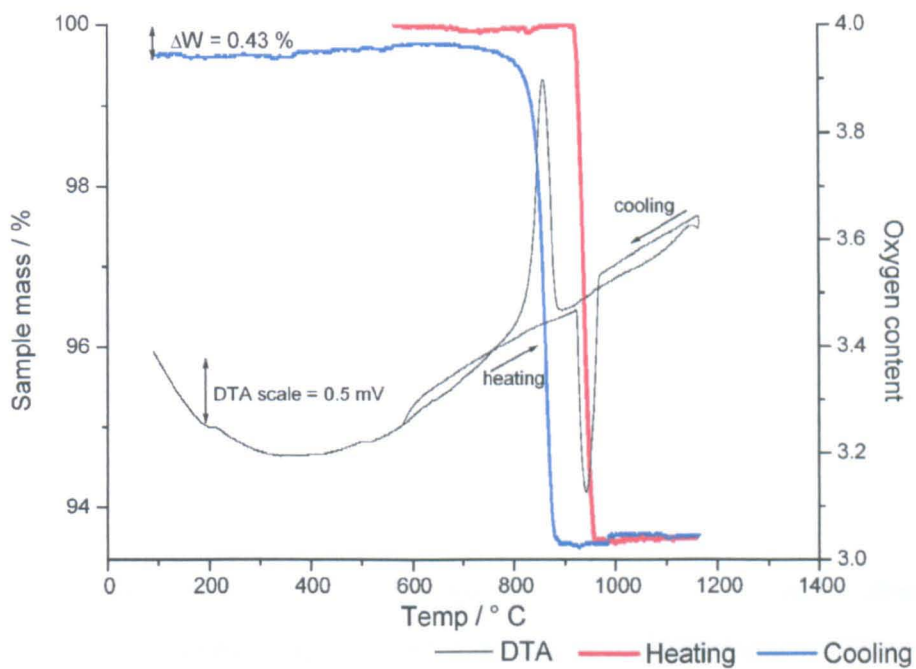


Figure 5.19 – TG and DTA data for  $\text{Co}_3\text{O}_4$  ( $x = 1.00$  in  $\text{Li}_{1+x}\text{Co}_{1+2x}\text{Mn}_{1-x}\text{O}_4$ ).

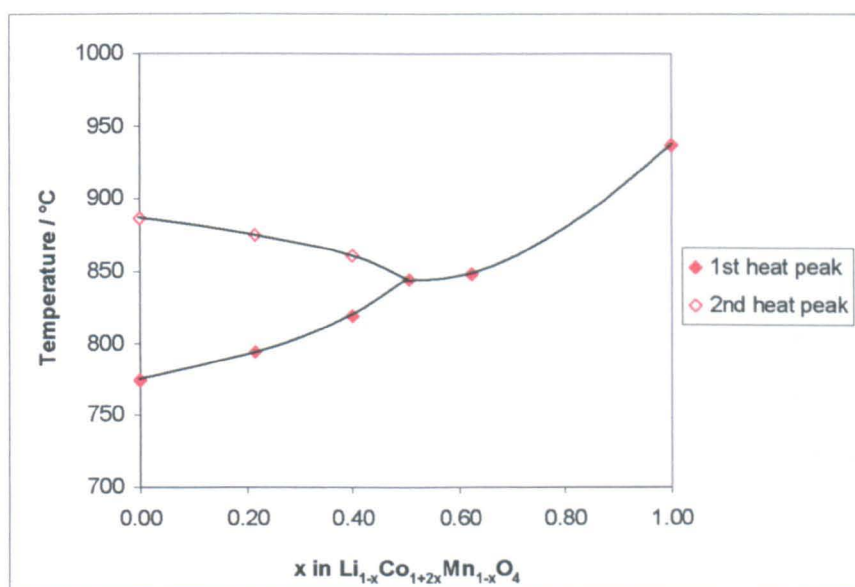


Upon cooling, all samples show a degree of irreversibility in the weight loss. Since this occurs for all samples, even  $\text{Co}_3\text{O}_4$ , it is assumed that this is due to the rate of re-oxygenation during cooling, *i.e.* the samples are relatively rapidly cooled, at  $10\text{ }^\circ\text{C min}^{-1}$  (*i.e.* cooled over  $\sim 2$  hours) as opposed to being annealed for 3 days at  $500\text{ }^\circ\text{C}$  to optimise the oxygen content.

#### 5.4.2b DTA results

A similar trend is observed in the DTA data, where a single DTA peak is observed on heating for  $x \geq 0.51$ , with this peak splitting into two distinct peaks for  $x \leq 0.40$ . The peak temperatures for this trend are presented in Figure 5.20. The high-temperature side of this peak shows significant broadening, with the peak not ending until much higher temperatures (*i.e.*  $\sim 1100\text{ }^\circ\text{C}$ ).

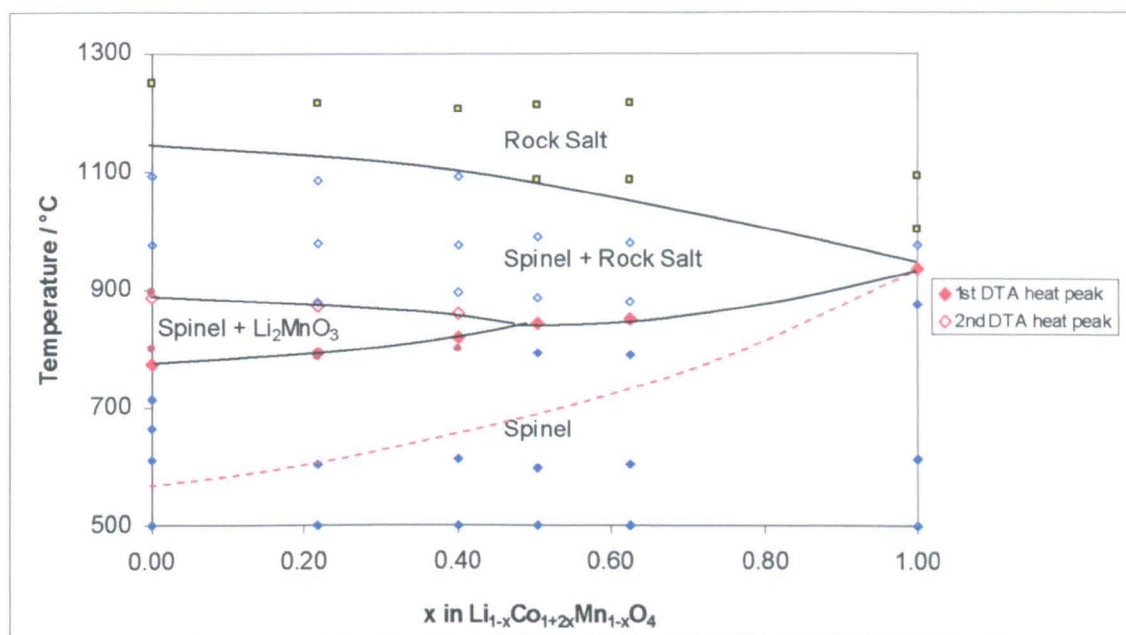
**Figure 5.20** - Variation in the temperature of DTA peaks in the heating profiles for  $\text{Li}_{1-x}\text{Co}_{1+2x}\text{Mn}_{1-x}\text{O}_4$ .  
The dotted lines are included as a guide for the eye.



The DTA data on cooling do not directly correlate with the DTA peaks observed on heating; however, it appears that all DTA peaks, on heating and cooling, can be associated approximately with either the onset or completion of oxygen loss. For  $x < 1.00$ , a DTA peak is observed on cooling at  $\sim 1010\text{ }^\circ\text{C}$ , as oxygen uptake begins. A second, large, DTA peak is observed at lower temperatures ( $\sim 800\text{ }^\circ\text{C}$ ), corresponding roughly to the end of oxygen uptake. This latter peak for  $\text{LiCoMnO}_4$  is seen to be splitting into two peaks, and occurs at an anomalously high temperature ( $\sim 850\text{ }^\circ\text{C}$ ).

of contaminating the TG-DTA instrument with Li, Co or Mn, all of which may be volatile at high temperatures. At this stage it is not known whether the gradual weight losses seen at high temperatures correspond to volatilisation of Li/Co/Mn or whether the rock salt phase is capable of being oxygen-rich and the excess oxygen is lost from heating to higher temperatures.

**Figure 5.21** –  $Li_{1-x}Co_{1+2x}Mn_{1-x}O_{4-\delta}$  phase diagram (in air). Red dotted line indicates temperature at which the onset of weight loss is observed in TG data.



The lattice parameters for the spinel and rock salt phases quenched from temperatures of  $\sim 600$  °C to  $\sim 1200$  °C for  $x = 0.22$  and  $0.40$  are presented in Tables 5.4 and 5.5. For both samples (Figures 5.22 and 5.23), an increase in spinel lattice parameter can be observed on increasing quench temperature. The rock salt phase appears at elevated temperatures ( $\sim 900$  °C), with the lattice parameter also increasing with quench temperature until the spinel phase has disappeared, where it reaches a plateau. The stoichiometry of these intermediate phases has yet to be determined.

**Table 5.4** - Spinel and rock salt lattice parameter data for  $x = 0.22$  in  $Li_{1-x}Co_{1+2x}Mn_{1-x}O_4$ .

Temperature / °C	$a_{\text{spinel}} / \text{Å}$	$a_{\text{rock salt}} / \text{Å}$
As annealed	8.0665 (7)	-
800	8.0791 (20)	-
880	8.217 (3)	4.1636 (22)
1088	8.318 (7)	4.2059 (12)
1216	-	4.2059 (18)

**Table 5.5** - Spinel and rock salt lattice parameter data for  $x = 0.40$  in  $Li_{1-x}Co_{1+2x}Mn_{1-x}O_4$ .

Temperature / °C	$a_{\text{spinel}} / \text{Å}$	$a_{\text{rock salt}} / \text{Å}$
As annealed	8.0684 (4)	-
614	8.0681 (8)	-
800	8.1026 (8)	-
897	8.174 (3)	4.1839 (9)
977	8.2374 (23)	4.2045 (11)
1095	8.305 (6)	4.226 (12)
1208	-	4.2268 (12)

**Figure 5.22** – Variation in lattice parameter of spinel and rock salt phases for  $x = 0.22$  in  $Li_{1-x}Co_{1+2x}Mn_{1-x}O_4$ .

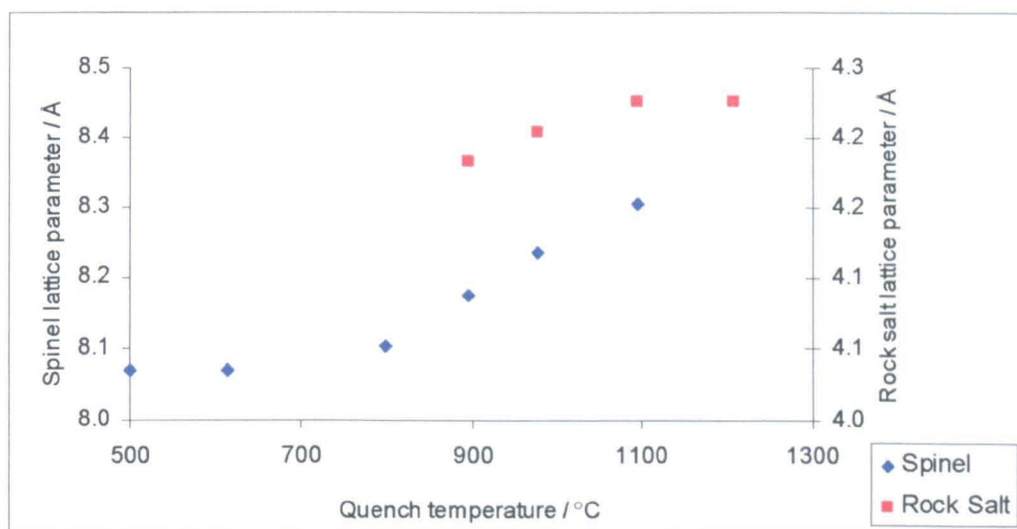
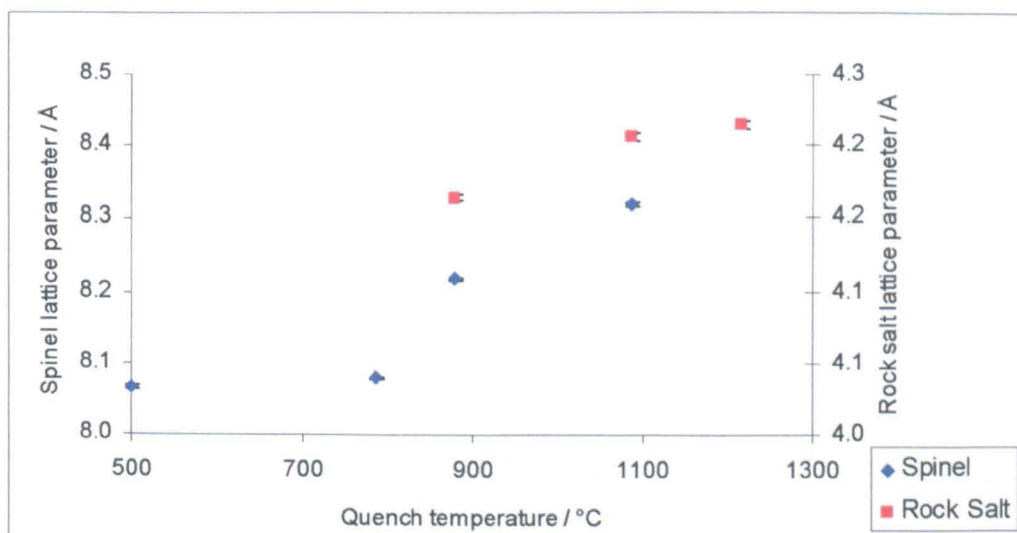


**Figure 5.23** - Variation in lattice parameter of spinel and rock salt phases for  $x = 0.40$  in  $Li_{1-x}Co_{1+2x}Mn_{1-x}O_4$ .



## 5.5 ‘Li<sub>1-x</sub>Co<sub>1/2+6x/5</sub>Mn<sub>1.5-x/5</sub>O<sub>4</sub>’ – phase relations in the LiCo<sub>0.5</sub>Mn<sub>1.5</sub>O<sub>4</sub> – Co<sub>1.7</sub>Mn<sub>1.3</sub>O<sub>4</sub> system

### 5.5.1 Solid solution studies

Samples with compositions  $0.00 \leq x \leq 1.00$  on the join Li<sub>1-x</sub>Co<sub>1/2+6x/5</sub>Mn<sub>1.5-x/5</sub>O<sub>4</sub> were prepared. The end-member Co<sub>1.7</sub>Mn<sub>1.3</sub>O<sub>4</sub> ( $x = 1.00$ ) was selected since this is the limit of the Co<sub>3-x</sub>Mn<sub>x</sub>O<sub>4</sub> cubic spinel solid solution at 800 °C. No studies on this binary join have been reported previously, though the join lies close to that (Li<sub>4</sub>Mn<sub>5</sub>O<sub>12</sub> – Co<sub>2</sub>MnO<sub>4</sub>) studied previously by West *et al.*<sup>12</sup>

Single phase cubic spinels were obtained over the full range of compositions,  $0.00 \leq x \leq 1.00$ , with lattice parameter data presented in Table 5.6 and Figure 5.25.

**Table 5.6** – Lattice parameter data for  $0.00 \leq x \leq 1.00$  for Li<sub>1-x</sub>Co<sub>1/2+6x/5</sub>Mn<sub>1.5-x/5</sub>O<sub>4</sub>.  
Estimated standard deviations are presented in parentheses.

$x$ in Li <sub>1-x</sub> Co <sub>1/2+6x/5</sub> Mn <sub>1.5-x/5</sub> O <sub>4</sub>	Stoichiometry	$a_{\text{spinel}} / \text{Å}$
0.00	LiCo <sub>0.5</sub> Mn <sub>1.5</sub> O <sub>4</sub>	8.1316 (8)
0.24	Li <sub>0.76</sub> Co <sub>0.788</sub> Mn <sub>1.452</sub> O <sub>4</sub>	8.1929 (8)
0.50	Li <sub>0.5</sub> Co <sub>1.1</sub> Mn <sub>1.4</sub> O <sub>4</sub>	8.2425 (7)
0.80	Li <sub>0.2</sub> Co <sub>1.46</sub> Mn <sub>1.34</sub> O <sub>4</sub>	8.2938 (16)
1.00	Co <sub>1.7</sub> Mn <sub>1.3</sub> O <sub>4</sub>	8.3214 (14)

**Figure 5.25** – Lattice parameter data for  $0.00 \leq x \leq 1.00$  for Li<sub>1-x</sub>Co<sub>1/2+6x/5</sub>Mn<sub>1.5-x/5</sub>O<sub>4</sub>

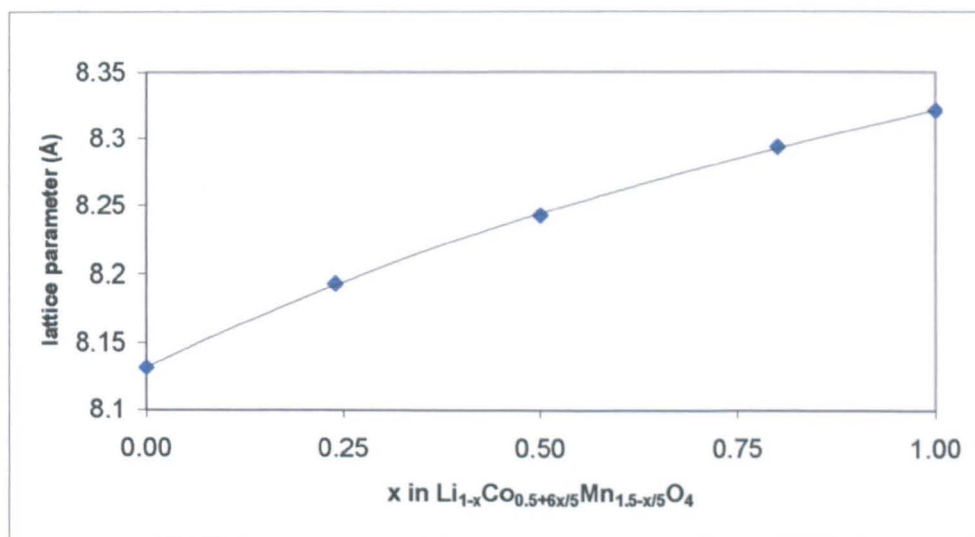


**Figure 5.26** – TG and DTA data for  $\text{Li}_{0.76}\text{Co}_{0.788}\text{Mn}_{1.452}\text{O}_4$  ( $x = 0.24$ ).

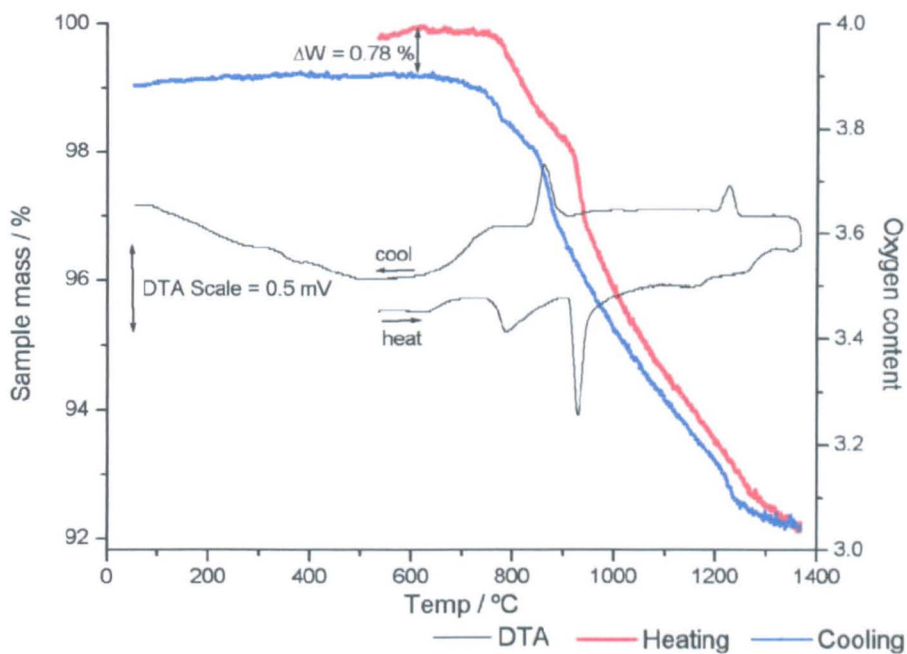


**Figure 5.27** – TG and DTA data for  $\text{Li}_{0.5}\text{Co}_{1.1}\text{Mn}_{1.4}\text{O}_4$  ( $x = 0.50$ ).

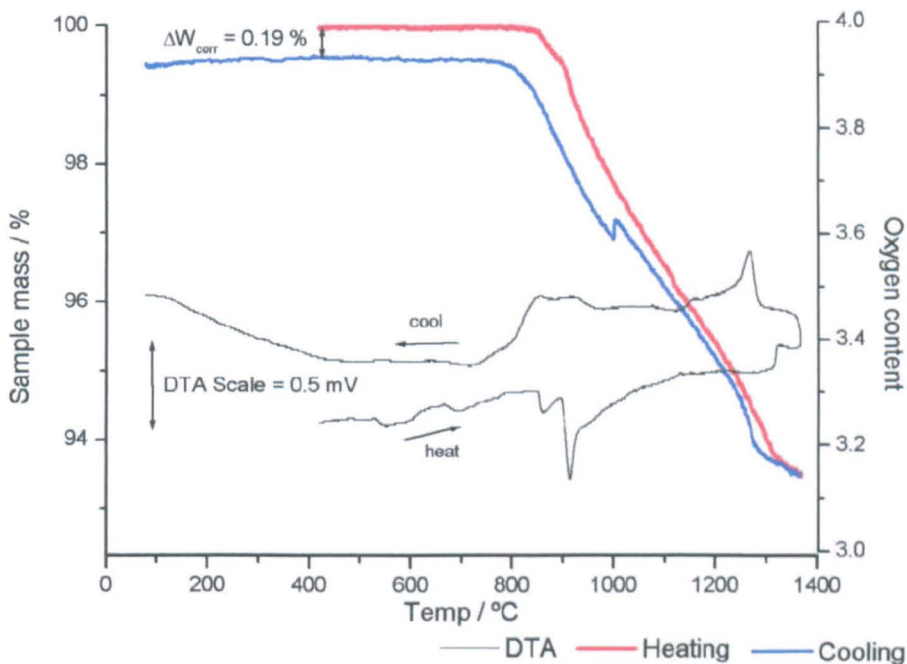
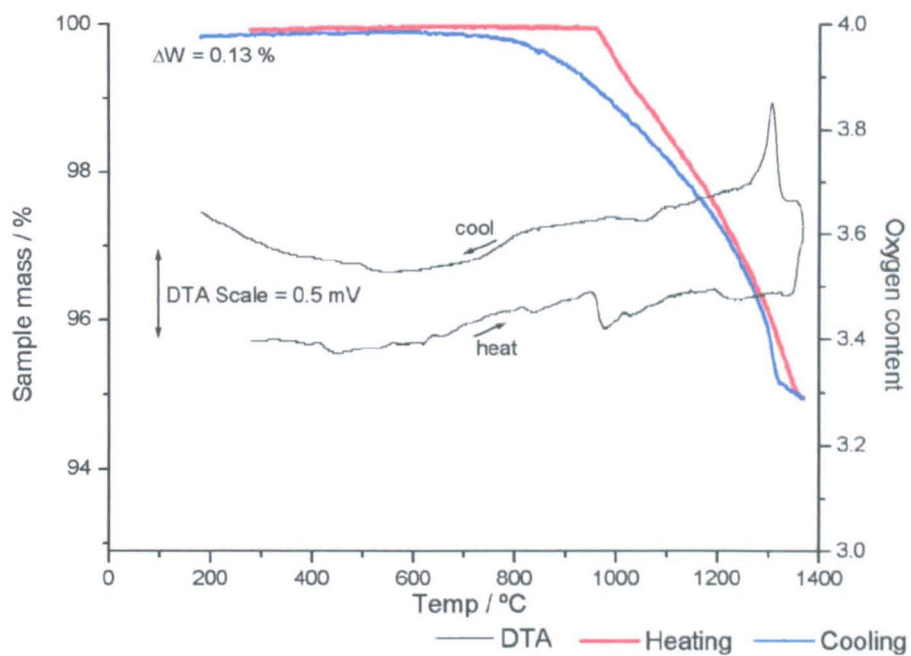


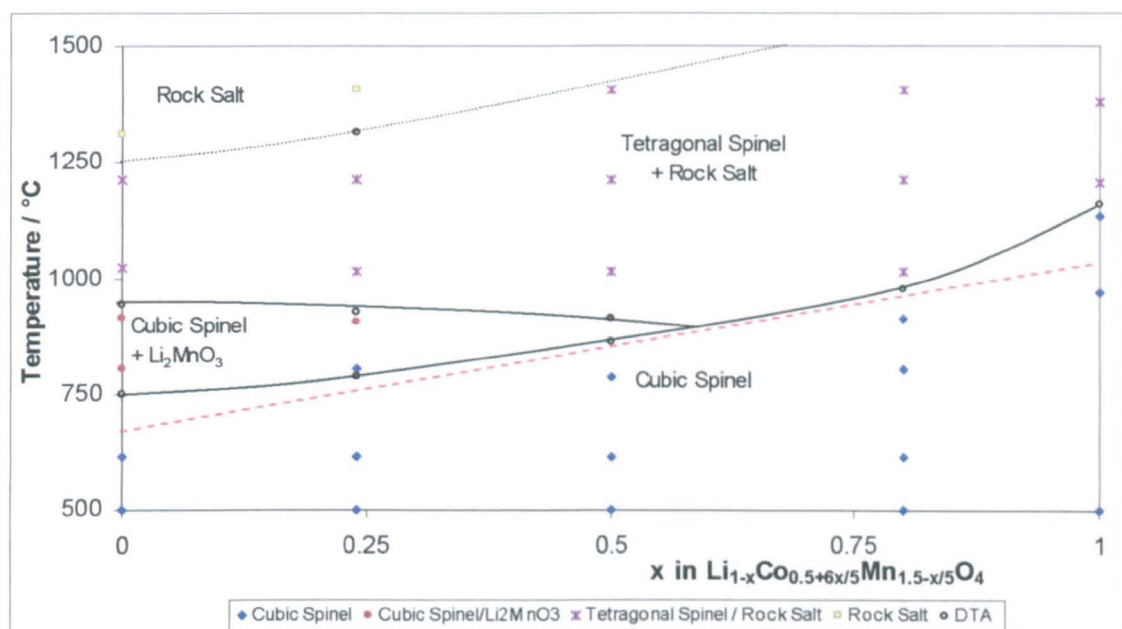
Figure 5.28 – TG and DTA data for  $\text{Li}_{0.2}\text{Co}_{1.46}\text{Mn}_{1.34}\text{O}_4$  ( $x = 0.80$ ).



### 5.5.3 Binary Phase Diagram for $\text{Li}_{1-x}\text{Co}_{1/2+6x/5}\text{Mn}_{1.5-x/5}\text{O}_4$ join

Samples were quenched from  $\sim 600 - 1400$  °C to attempt the stabilisation of high temperature phases to room temperature. The phase analysis work is presented, along with relevant TG and DTA data, in the form of a phase diagram in Figure 5.29.

**Figure 5.29** – The  $\text{Li}_{1-x}\text{Co}_{1/2+6x/5}\text{Mn}_{1.5-x/5}\text{O}_4$  phase diagram (in air). Red dotted line indicates temperature at which the onset of weight loss is observed in TG data.



The spinel structure was retained to at least 750 °C for the whole compositional range, though the stability range extended to higher temperatures as  $x$  increased (e.g.  $x = 1.30$  was stable to  $\sim 1100$  °C).

A pair of two phase regions were identified. For  $x < 0.50$ , samples quenched from temperatures inside the area enclosed by two sets of DTA peaks were found to give a mixture of  $\text{Li}_2\text{MnO}_3$  and a cubic spinel. At temperatures above the second DTA peak, and above the single DTA peak observed for  $x \geq 0.51$ , a mixture of tetragonal spinel and simple disordered cubic rock salt was observed. Single phase cubic rock salt was obtained for  $x \leq 0.24$ ; for  $x = 0.24$ , this phase had lattice parameter  $a = 4.2534$  (10). Single phase rock salts may form for  $x > 0.24$ , but the high temperatures required ( $> 1450$  °C) were beyond the range of the quench furnace available.

occurring over a single curve (e.g. as observed for  $\text{Co}_3\text{O}_4$ , in Figure 5.19). Quenches made, of any sample, from temperatures above that of the TG inflexion gave mixtures of spinel and disordered rock salt. It is likely that the presence of this inflexion in TG data is indicative of the decomposition of  $\text{Li}_2\text{MnO}_3$ .

Figures 5.31 – 5.36 show the decrease in compositional extent of the cubic spinel solid solution area as temperature increases; note that these limits are interpreted from TG data, i.e. a single phase cubic spinel may continue to exist at higher temperatures than indicated here, but that TG data indicate that weight loss is occurring (i.e. samples are likely to be oxygen-deficient). The black dotted lines indicate the probable boundary of the cubic spinel solid solution area.

These data essentially show a minimum in thermal stability centred at  $\sim \text{LiCoMnO}_4$ . This presents grave difficulties in the preparation of this composition as a single phase by high temperature solid state reaction routes. The assumption that the as-prepared samples were fully oxygenated, i.e. that  $\text{LiCoMnO}_4$  has formed as opposed to  $\text{LiCoMnO}_{4-\delta}$ , must be taken with some caution. It is strongly recommended that future research seek a viable low temperature synthesis route.

**Figure 5.31** – Extent of oxygen-stoichiometric cubic spinel at 550 °C. The green dotted line indicates the Mn-rich end of the  $\text{Li}_4\text{Mn}_5\text{O}_{12}$  –  $\text{Co}_2\text{MnO}_4$  cubic spinel solid solution reported by West et al.<sup>12</sup>

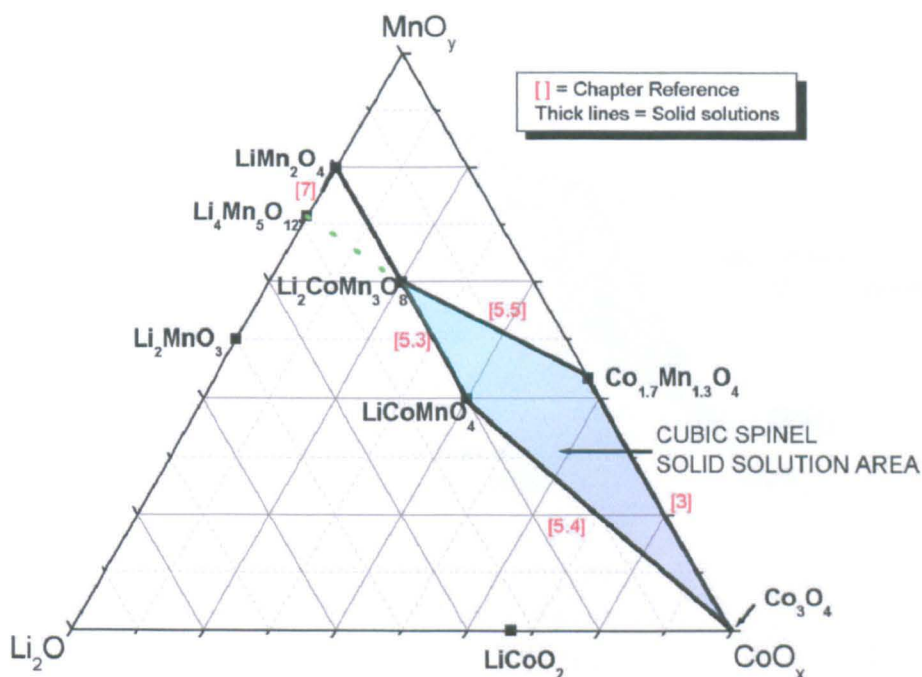


Figure 5.32 – Extent of oxygen-stoichiometric cubic spinel at 600 °C.

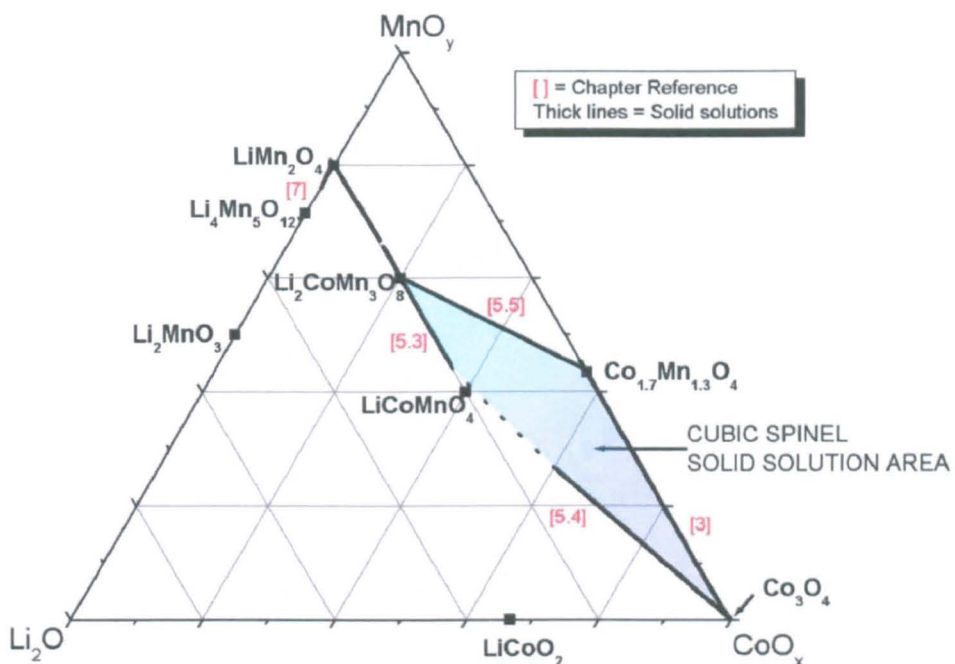


Figure 5.33 – Extent of oxygen-stoichiometric cubic spinel at 700 °C.

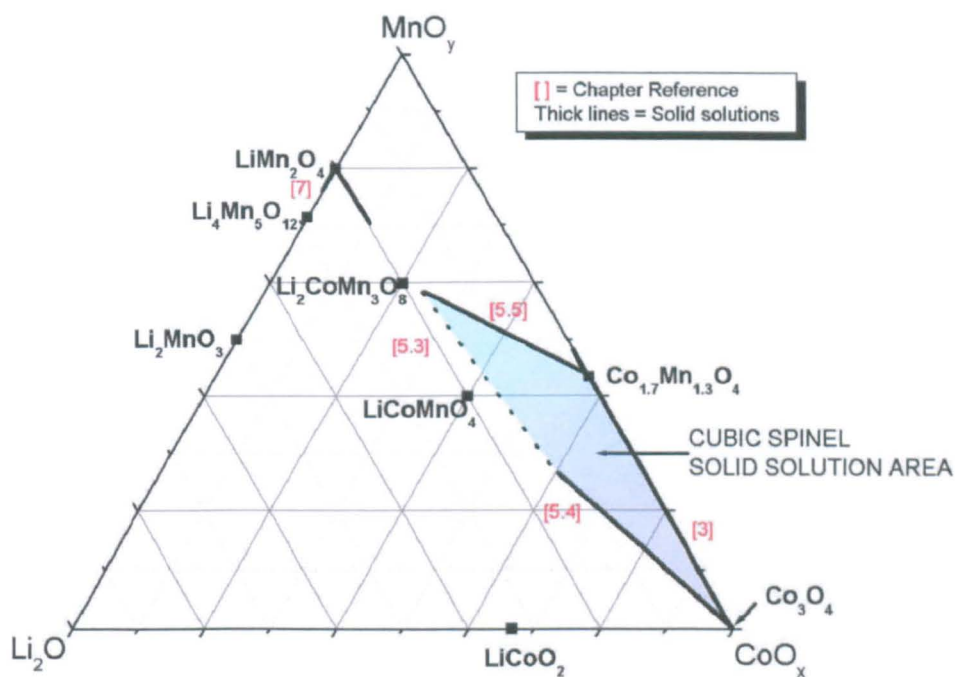


Figure 5.34 – Extent of oxygen-stoichiometric cubic spinel at 800 °C.

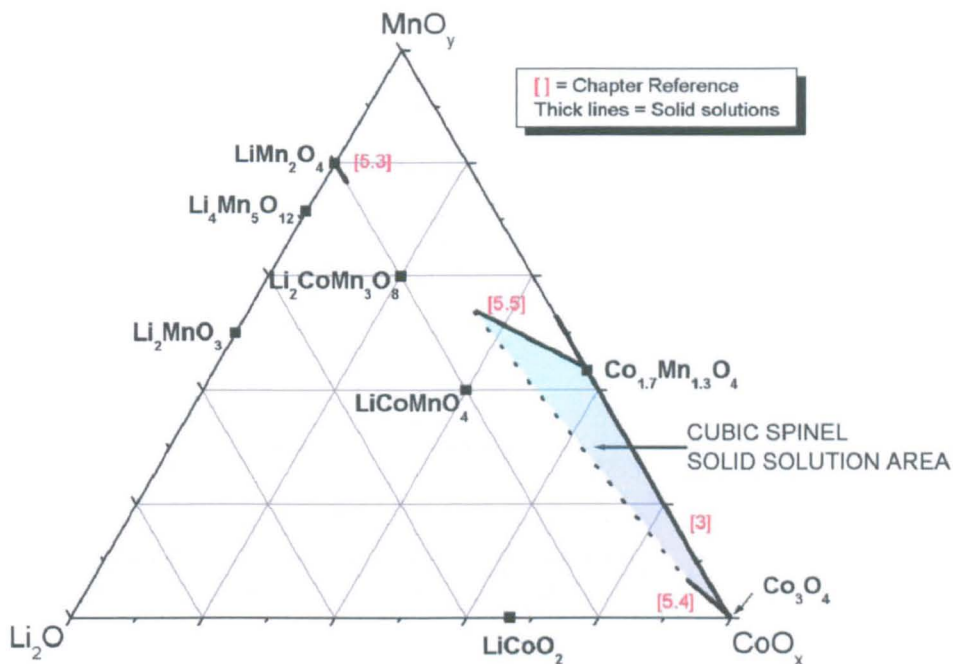


Figure 5.35 – Extent of oxygen-stoichiometric cubic spinel at 900 °C.

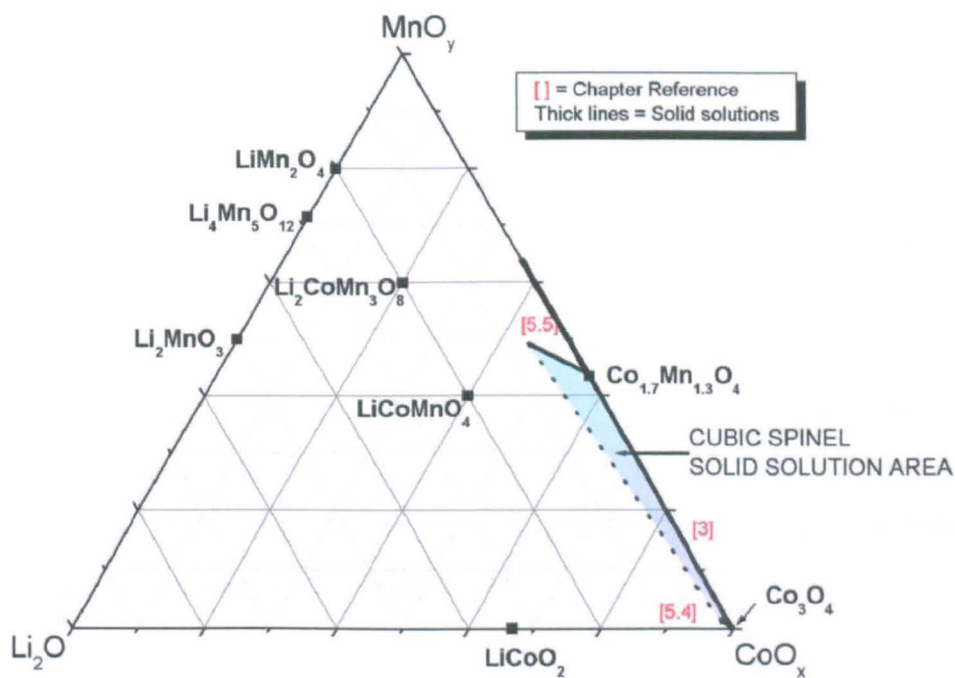
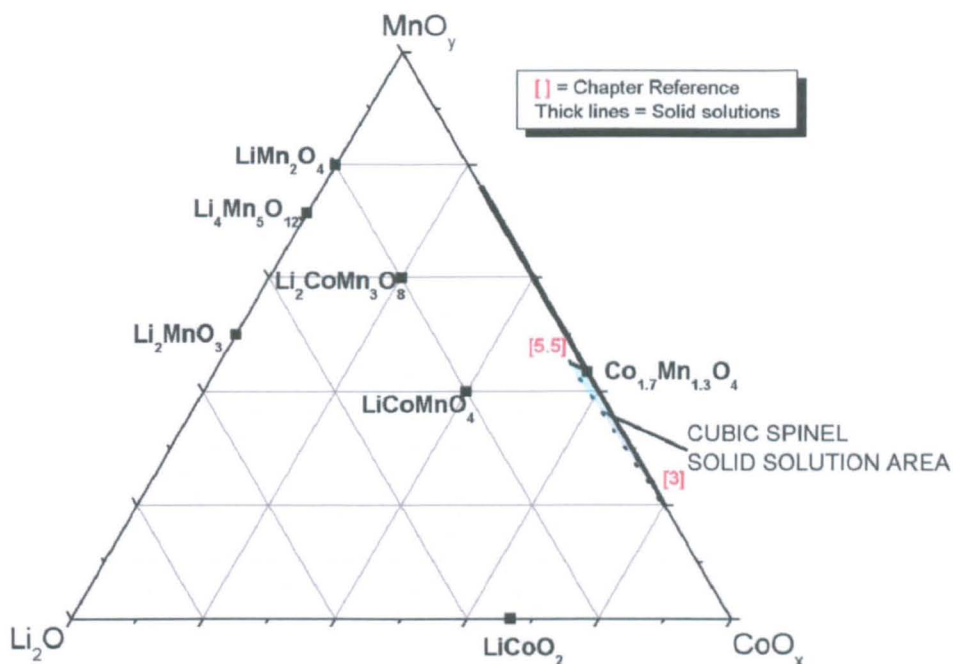


Figure 5.36 – Extent of oxygen-stoichiometric cubic spinel at 1000 °C.



### 5.6.3 Effect of temperature on rock salt solid solution area

The rock salt obtained as a single phase at the lowest temperature was CoO, at 950 °C. As the treatment temperature increased further, single phase rock salts could be isolated at other compositions, forming a rock salt solid solution area. The extent of this rock salt solid solution area at 1000 °C, 1150 °C and 1350 °C is shown in Figures 5.37 – 5.39. As the temperature increases, the extent of the solid solution area also increases, extending further out from CoO.

This rock salt solid solution area also overlaps part of the lower temperature cubic spinel solid solution area, and is likely to be more extensive at temperatures above 1350 °C; studies at such high temperatures were limited due to the risk of damage to equipment from Li, Co and/or Mn volatilization.

Figure 5.37 – Extent of single phase rock salt at 1000 °C.

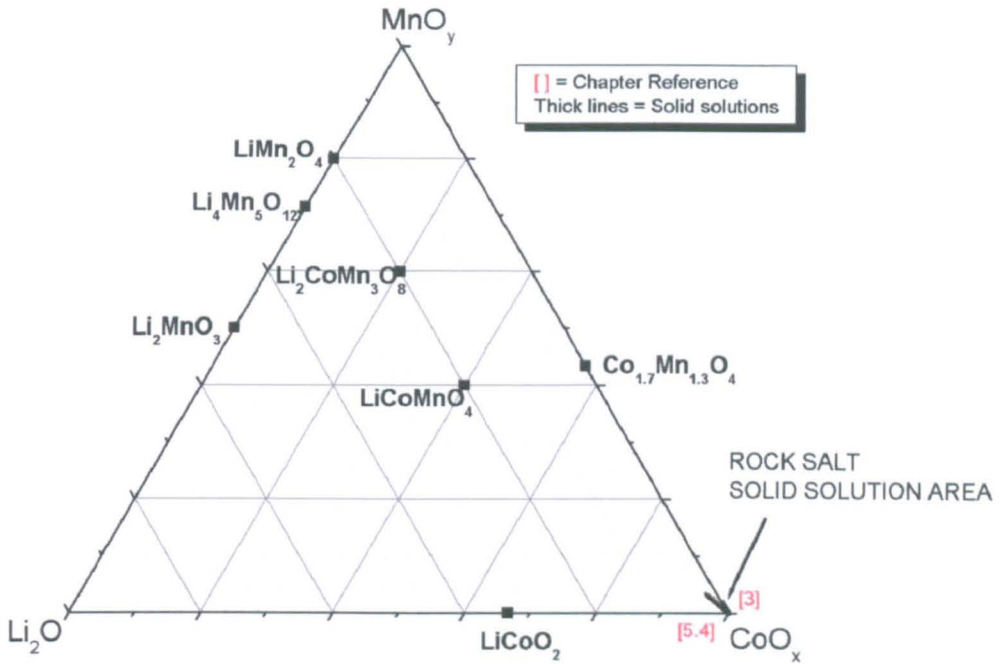


Figure 5.38 – Extent of single phase rock salt at 1150 °C.

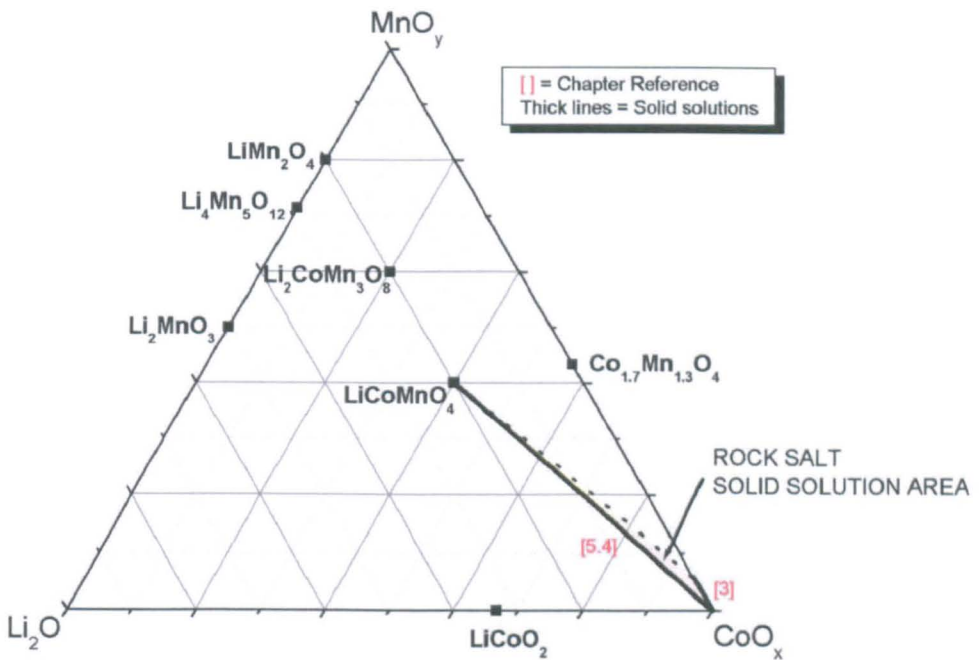
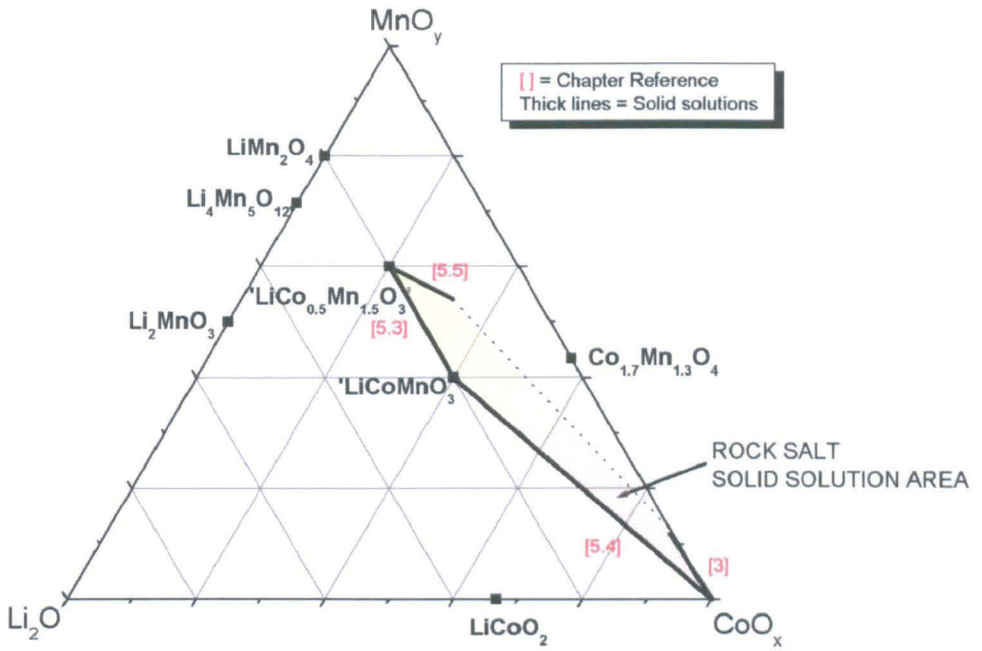
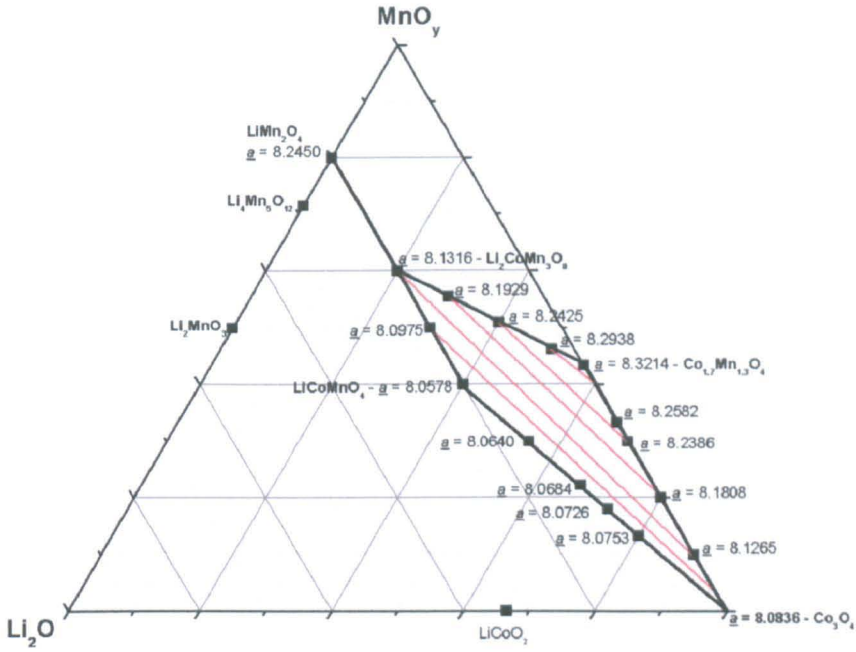


Figure 5.39 – Extent of single phase rock salt at 1350 °C.



**Figure 5.40** – Lattice parameters (in Å) for various cubic spinel compositions annealed at 500 °C. Red contour lines indicate compositions of equal lattice parameter.



**Figure 5.41** – Lattice parameters (in Å) for various high temperature rock salt compositions. Red contour lines indicate compositions of equal lattice parameter.

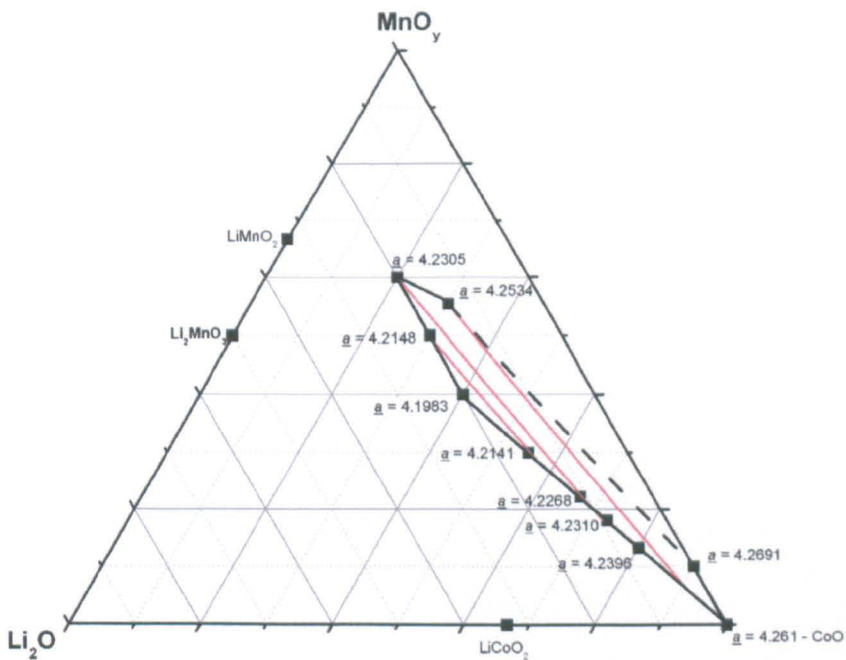


Figure 6.2 – Arrhenius plot for  $\text{Li}_{1-x}\text{Co}_{1+2x}\text{Mn}_{1-x}\text{O}_4$ .

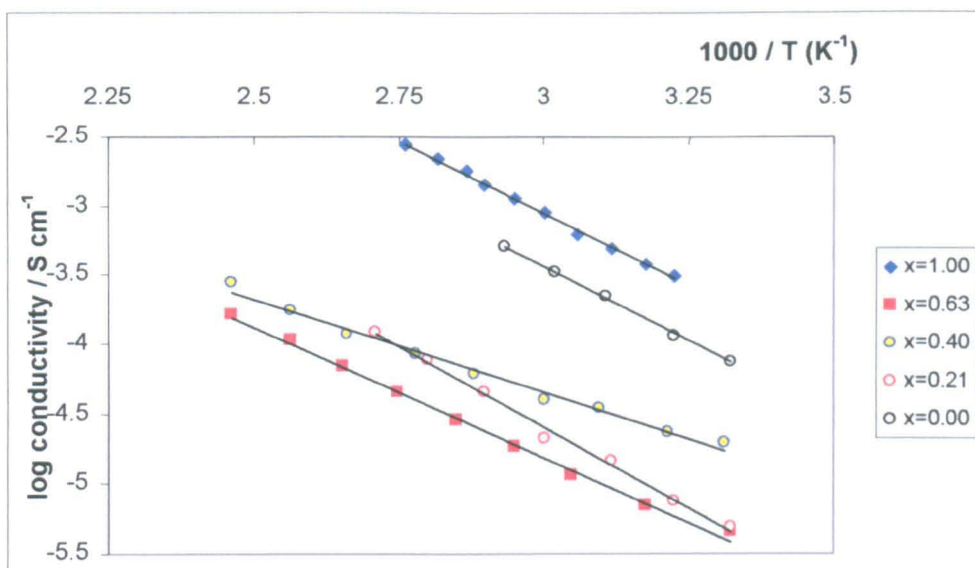
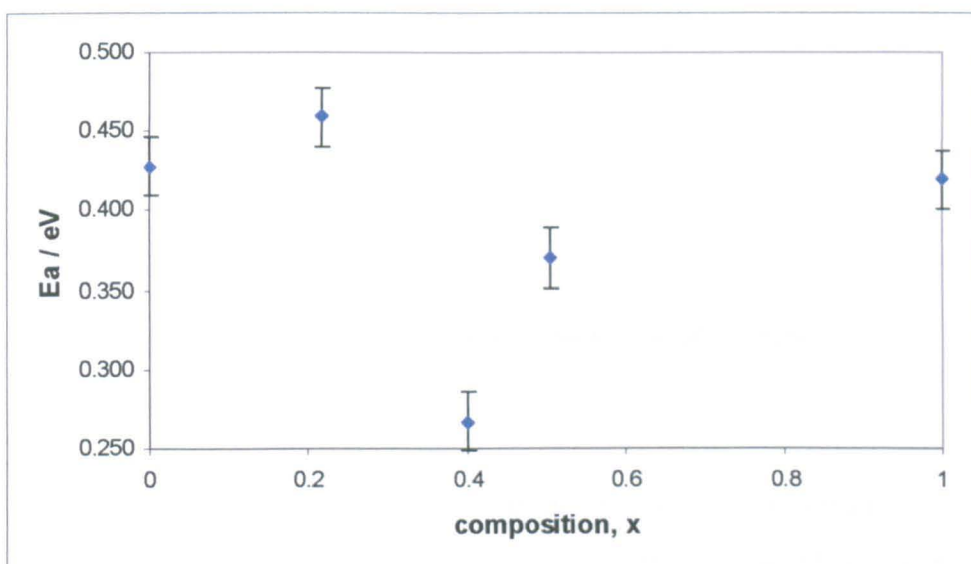


Figure 6.3 – Calculated activation energies for  $\text{Li}_{1-x}\text{Co}_{1+2x}\text{Mn}_{1-x}\text{O}_4$ .



The modest levels of semiconductivity observed for compositions with  $0.00 \leq x \leq 1.00$  are consistent with an electron hopping mechanism in a material containing mixed valence transition metal cations. The reason for the apparent random variation in bulk conductivity and activation energy with composition, however, is unclear. It is possible that the compositions of the samples have been altered during the sintering process, and not re-obtained during the annealing step at 500 °C; *i.e.* they are no longer single phase spinels but instead may also contain an amount of the disordered rock salt or  $\text{Li}_2\text{MnO}_3$  phases.

Figure 6.5 – Arrhenius plot for  $\text{Li}_{1-x}\text{Co}_{1/2+6x/5}\text{Mn}_{1.5-x/5}\text{O}_4$ .

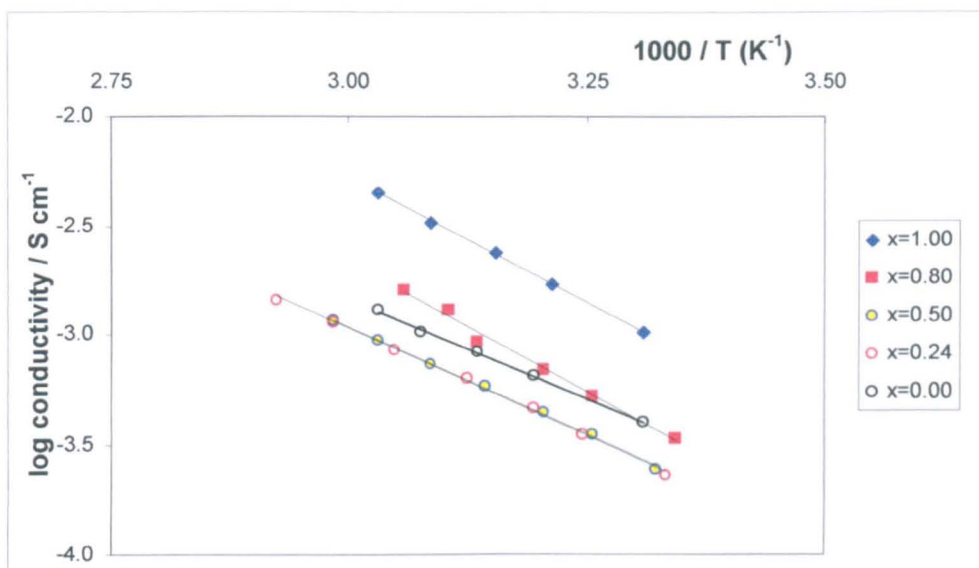
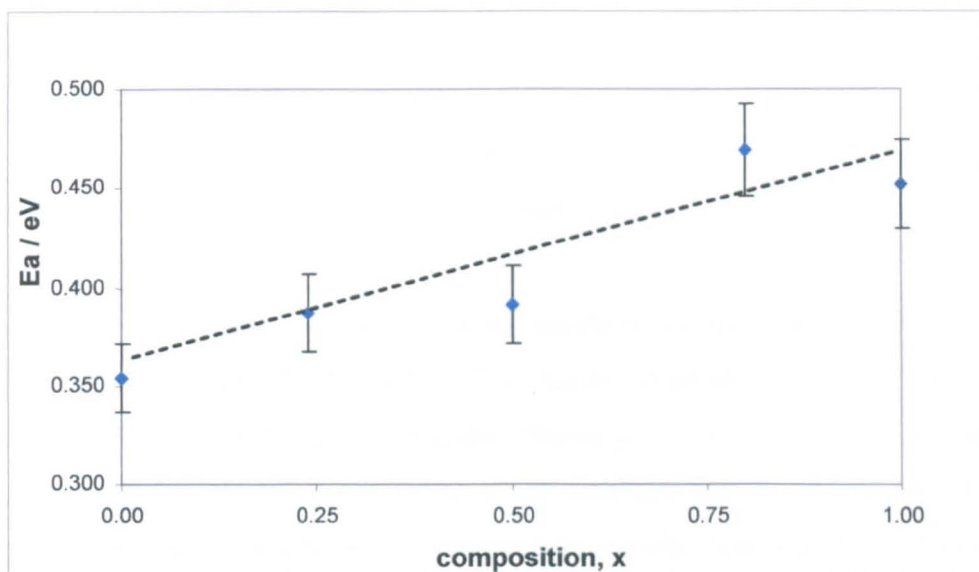


Figure 6.6 – Calculated activation energies for  $\text{Li}_{1-x}\text{Co}_{1/2+6x/5}\text{Mn}_{1.5-x/5}\text{O}_4$ .



The modest levels of semiconductivity observed for compositions with  $0.00 \leq x \leq 1.00$  are consistent with an electron hopping mechanism in a material containing mixed valence transition metal cations. The reason for the pattern observed here in the conductivity and activation energy data is unclear; the conductivity maxima coincident with the end-members may suggest some special stability for compositions with  $x = 0.00$  and  $1.00$ , where the structures are possibly more ordered, *i.e.*:



**Figure 6.7** – Potential profile for cell with  $\text{LiCoMnO}_4$  ( $x = 0.00$ ) as active material, cycled in range 3.0 – 5.1 V at C/10 rate.

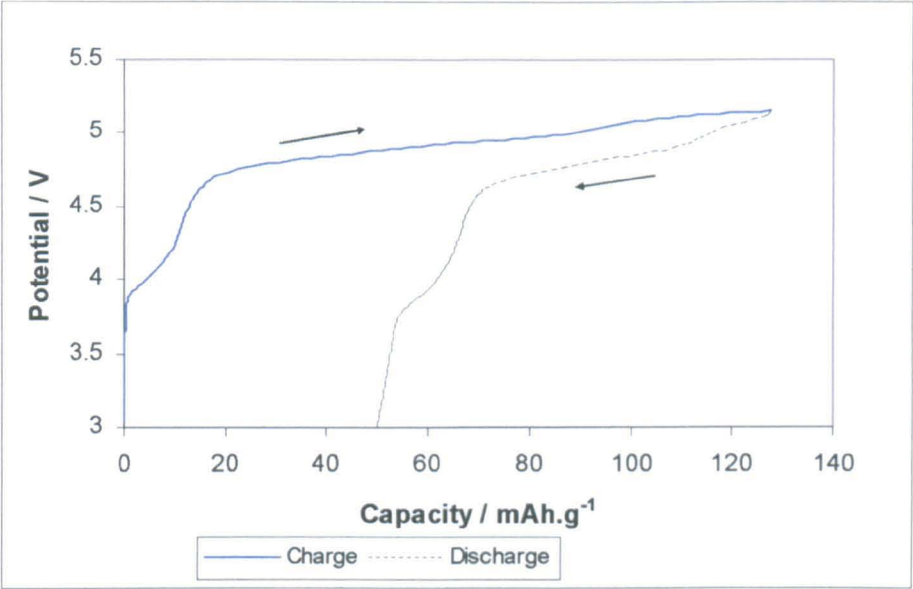


**Figure 6.8** – Discharge (Li insertion) profiles for  $\text{LiCoMnO}_4$  ( $x = 0.00$ ) for first 5 cycles, in the range 0.25 – 2.5 V at C/5 rate.

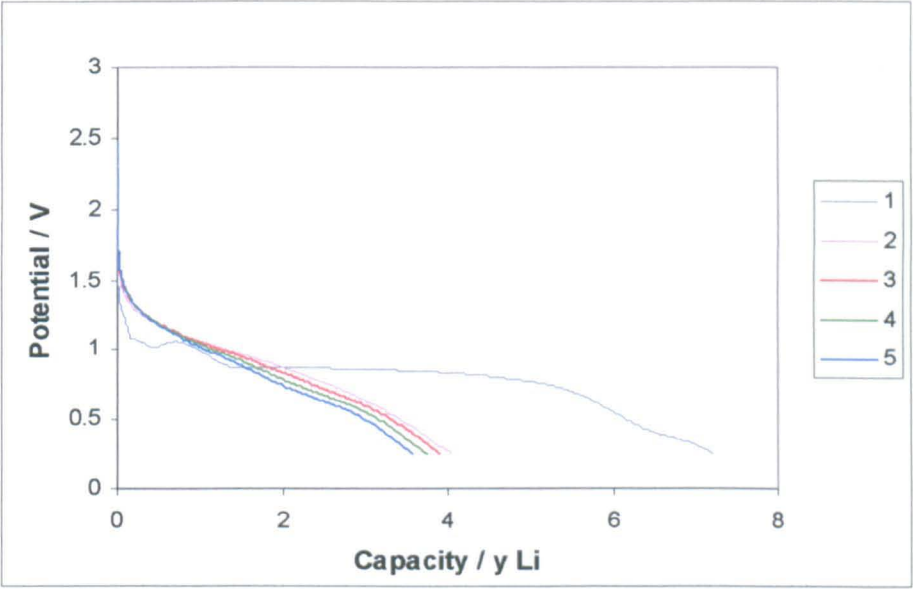


**Figure 6.9** – Potential profile for cell containing  $\text{Li}_{0.49}\text{Co}_{2.02}\text{Mn}_{0.49}\text{O}_4$  ( $x = 0.51$ ) as the active material, cycled in the range 3.0 – 5.1 V at C/10 rate.

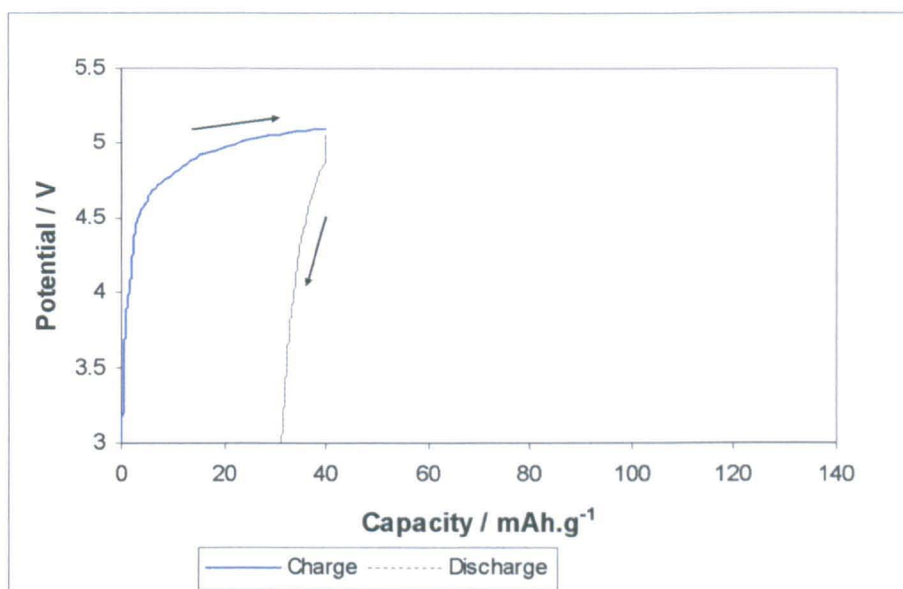


**Figure 6.10** – Discharge (Li insertion) profiles for  $\text{Li}_{0.49}\text{Co}_{2.02}\text{Mn}_{0.49}\text{O}_4$  ( $x = 0.51$ ) for first 5 cycles, in the range 0.25 – 2.5 V at C/5 rate.

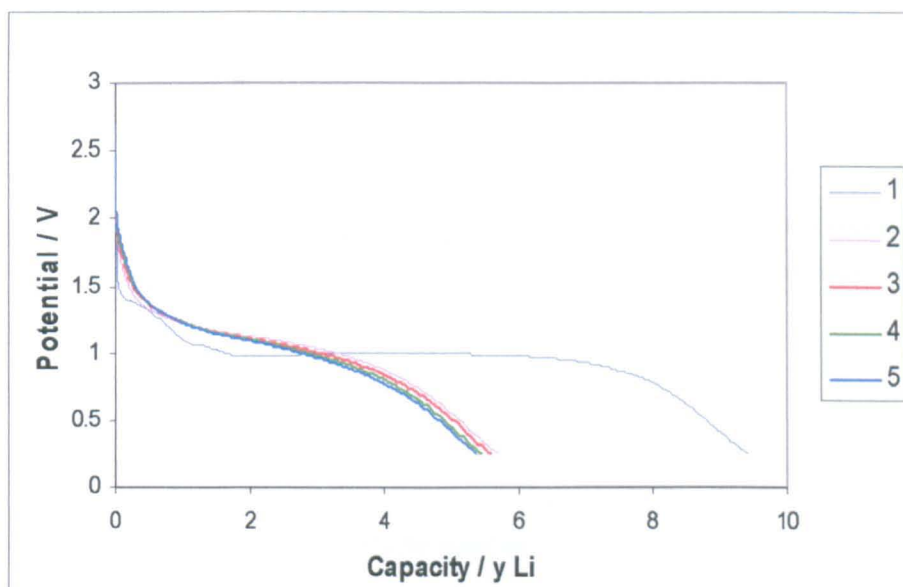


**Figure 6.13** – Specific charge capacity at ~ 5.0 or ~ 4.5 V after 10 cycles for cells with active material of composition  $0.00 \leq x \leq 1.00$  ( $\text{Li}_{1-x}\text{Co}_{1+2x}\text{Mn}_{1-x}\text{O}_4$ ), cycled over range 3.0 – 5.1 V at C/10 rate.

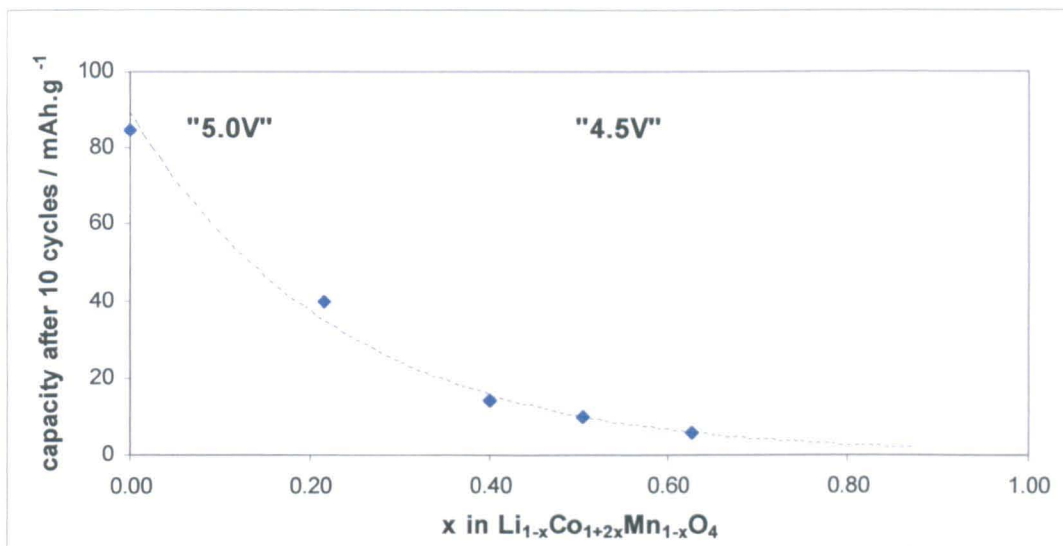


**Figure 6.14** – Variation in discharge capacity (y Li) with composition ( $0.00 \leq x \leq 1.00$  in  $\text{Li}_{1-x+y}\text{Co}_{1+2x}\text{Mn}_{1-x}\text{O}_4$ ) after 1 and 10 cycles.

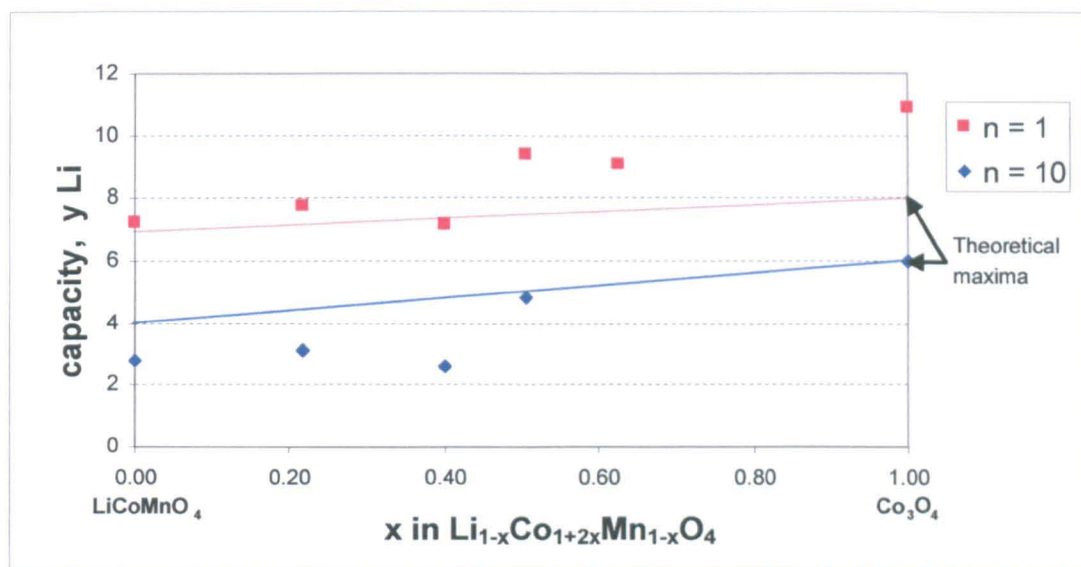


**Figure 6.15** – Theoretical specific capacity for insertion of 1 Li into  $\text{Li}_{1-x+y}\text{Co}_{1+2x}\text{Mn}_{1-x}\text{O}_4$  (where  $0.00 \leq x \leq 1.00$ ,  $y = 1 \text{ Li}$ ).

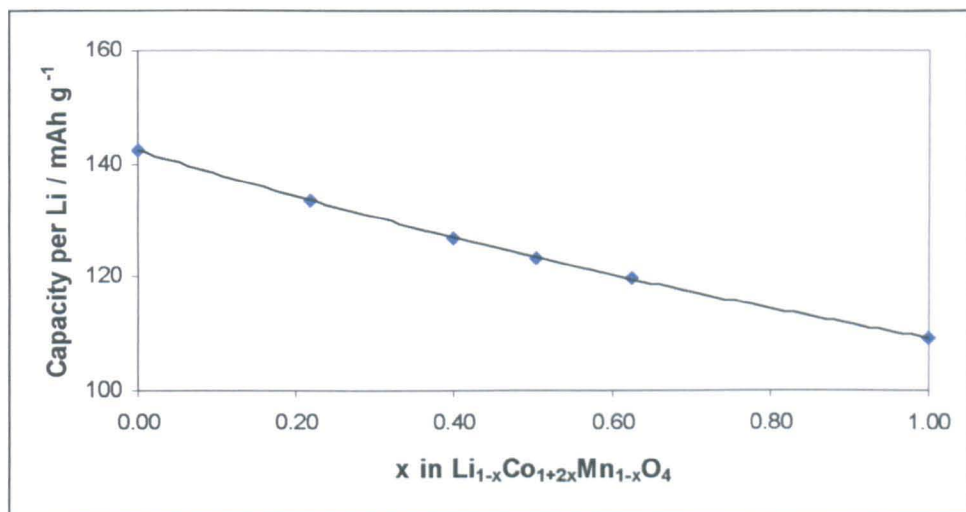


**Figure 6.16** - Potential profile for cell with  $\text{Li}_2\text{CoMn}_3\text{O}_8$  ( $x = 0.00$ ) as active material, cycled in range 3.0 – 5.1 V at C/10 rate.

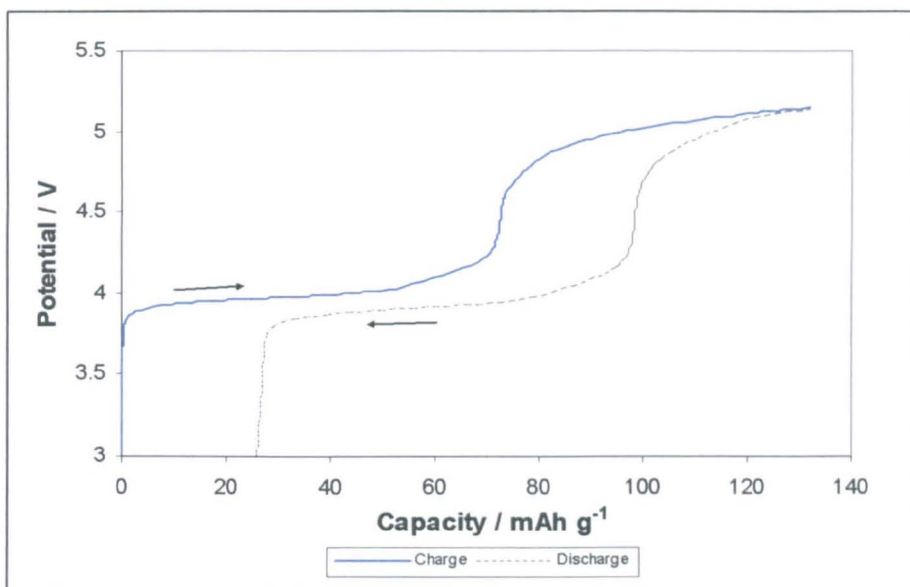


**Figure 6.17** – Discharge (Li insertion) profiles for  $\text{Li}_2\text{CoMn}_3\text{O}_8$  ( $x = 0.00$ ) for first 5 cycles, in the range 0.25 – 2.5 V at C/5 rate.

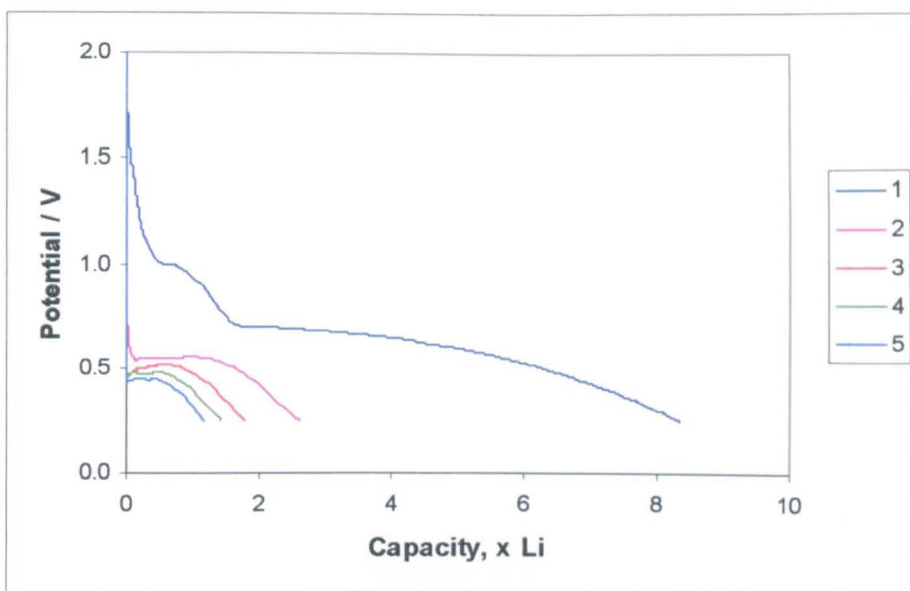


**Figure 6.18** – Potential profile for cell containing  $\text{Li}_{0.5}\text{Co}_{1-x}\text{Mn}_{1.4}\text{O}_4$  ( $x = 0.50$ ) as the active material, cycled in the range 3.0 – 5.1 V at C/10 rate.

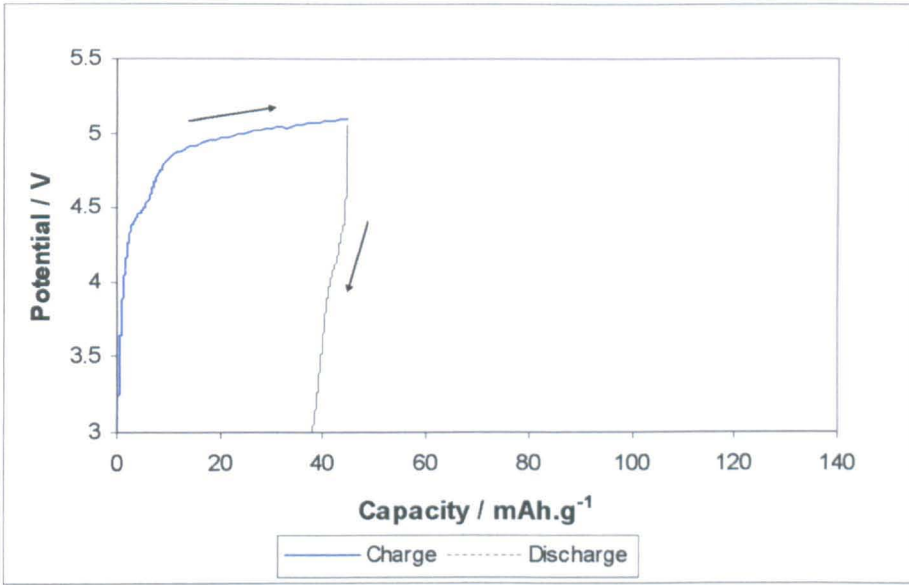


**Figure 6.19** – Discharge (Li insertion) profiles for  $\text{Li}_{0.5}\text{Co}_{1-x}\text{Mn}_{1.4}\text{O}_4$  ( $x = 0.50$ ) for first 5 cycles, in the range 0.25 – 2.5 V at C/5 rate.

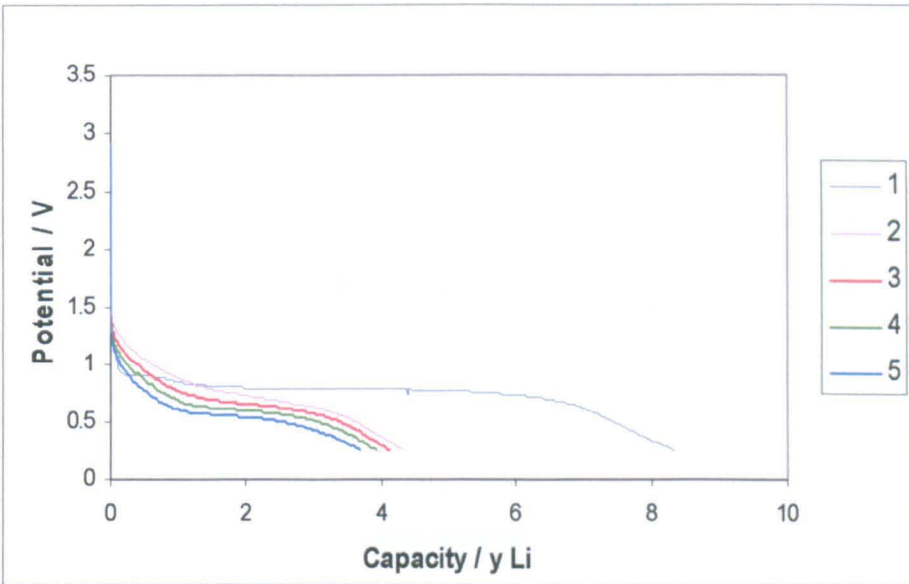


**Figure 6.20** – Variation in discharge/charge specific capacity of plateau centred on  $\sim 1.0$  V upon cycling for  $\text{Li}_2\text{CoMn}_3\text{O}_8$  ( $x = 0.00$ ).

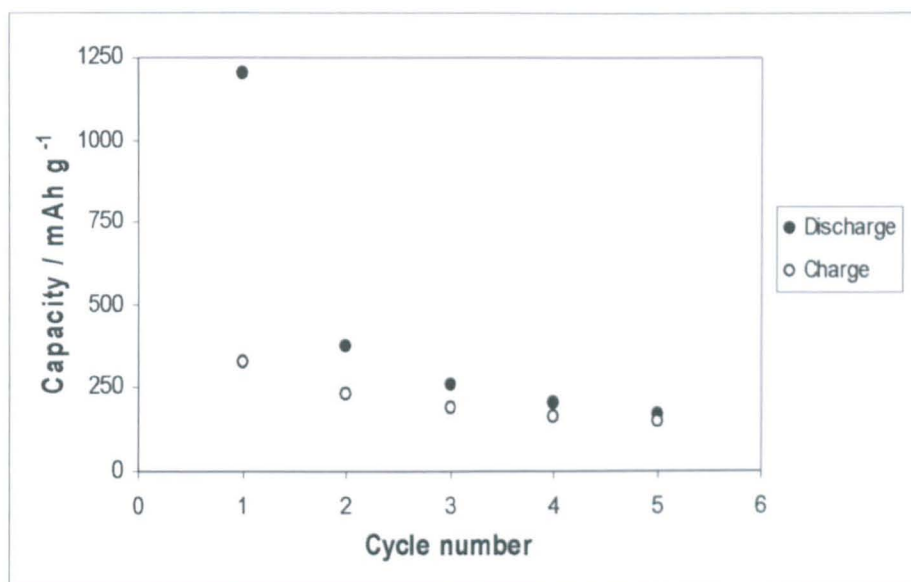


**Figure 6.21** – Variation in discharge/charge specific capacity of plateau centred on  $\sim 1.0$  V upon cycling for  $\text{Li}_{0.5}\text{Co}_{1.1}\text{Mn}_{1.4}\text{O}_4$  ( $x = 0.50$ ).

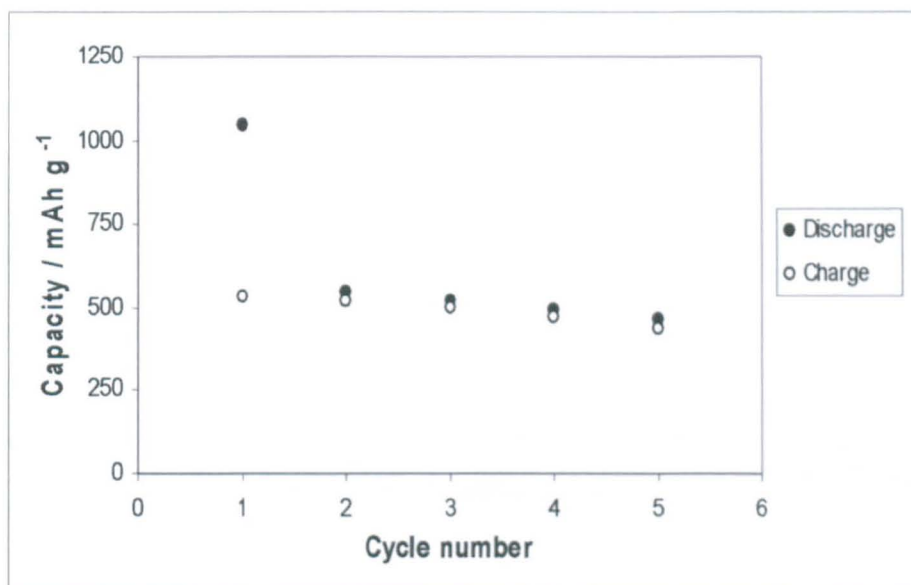


**Figure 6.22** – Specific charge capacity at ~ 5.0 or ~ 4.5 V after 10 cycles for cells with active material of composition  $0.00 \leq x \leq 1.00$  ( $\text{Li}_{1-x}\text{Co}_{1/2+6x/5}\text{Mn}_{3/2-x/5}\text{O}_4$ ), cycled over range 3.0 – 5.1 V at C/10 rate.

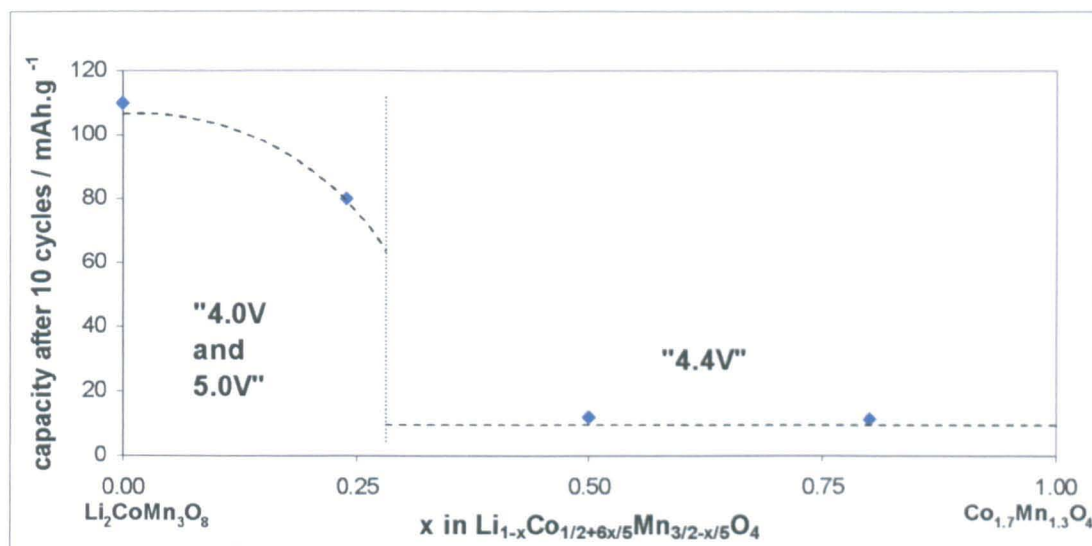


**Figure 6.23** – Variation in discharge capacity (y Li) with composition ( $0.00 \leq x \leq 1.00$  in  $\text{Li}_{1-x+y}\text{Co}_{1/2+6x/5}\text{Mn}_{3/2-x/5}\text{O}_4$ ) after 1 and 10 cycles.

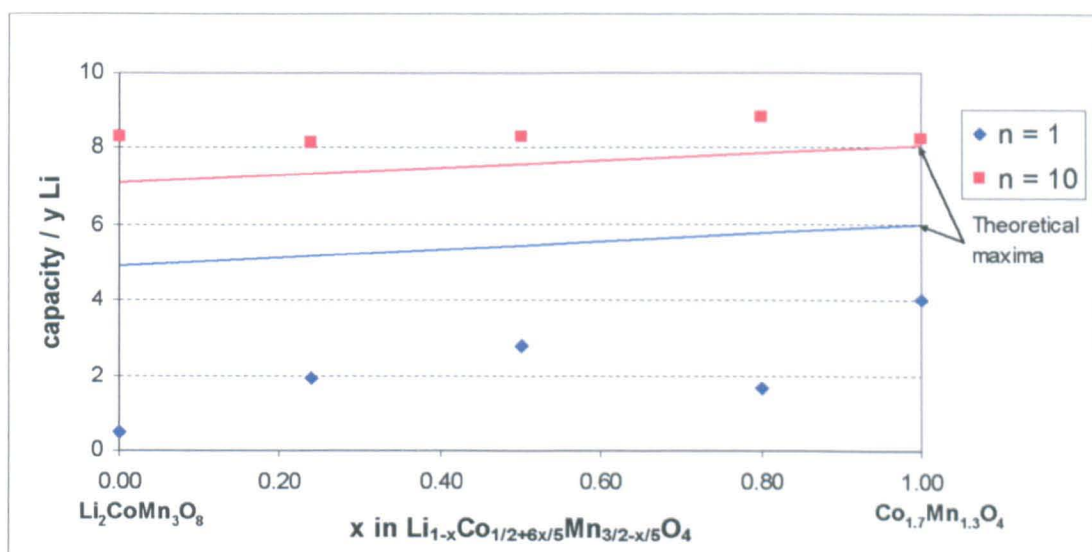


**Figure 6.24** – Theoretical specific capacity for insertion of 1 Li into  $\text{Li}_{1-x+y}\text{Co}_{1/2+6x/5}\text{Mn}_{3/2-x/5}\text{O}_4$   
(where  $0.00 \leq x \leq 1.00$ ,  $y = 1$ ).

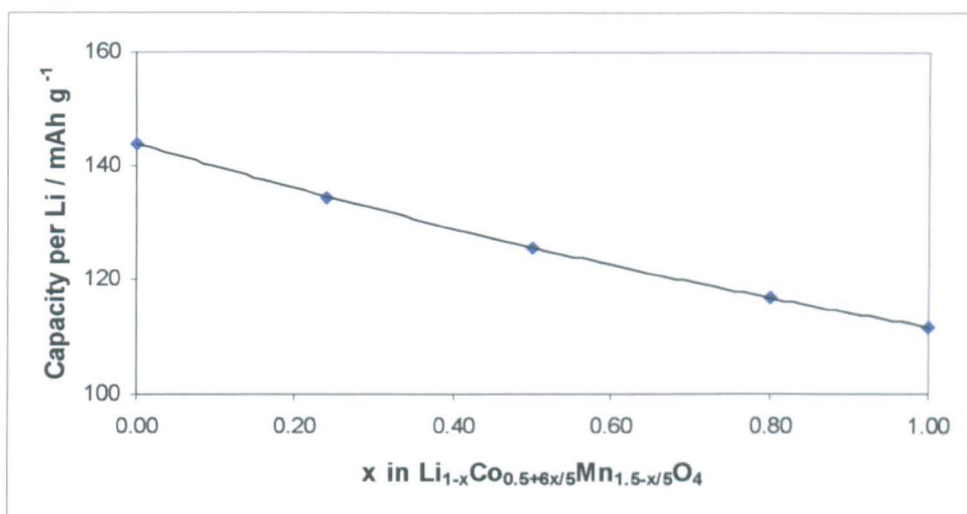


**Figure 7.2** – TG and DTA data for  $\text{LiMn}_2\text{O}_4$

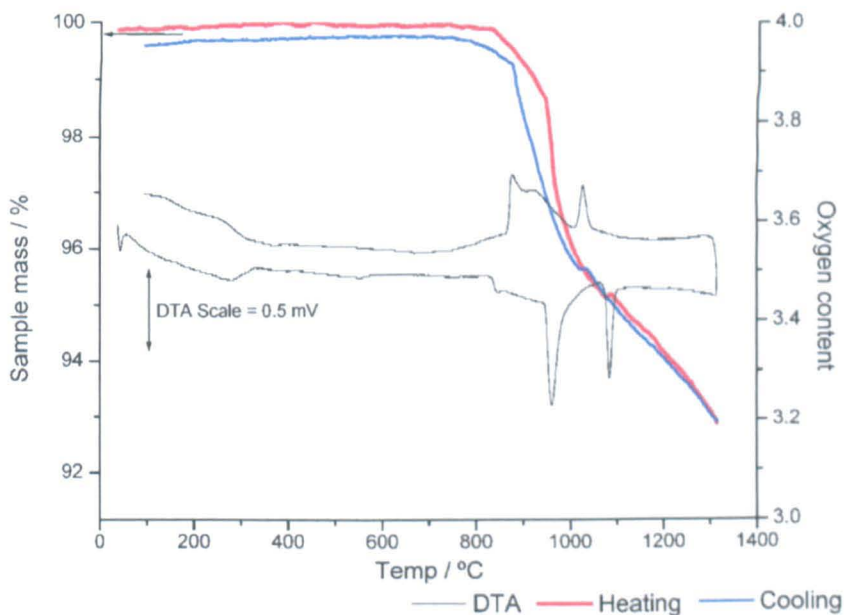
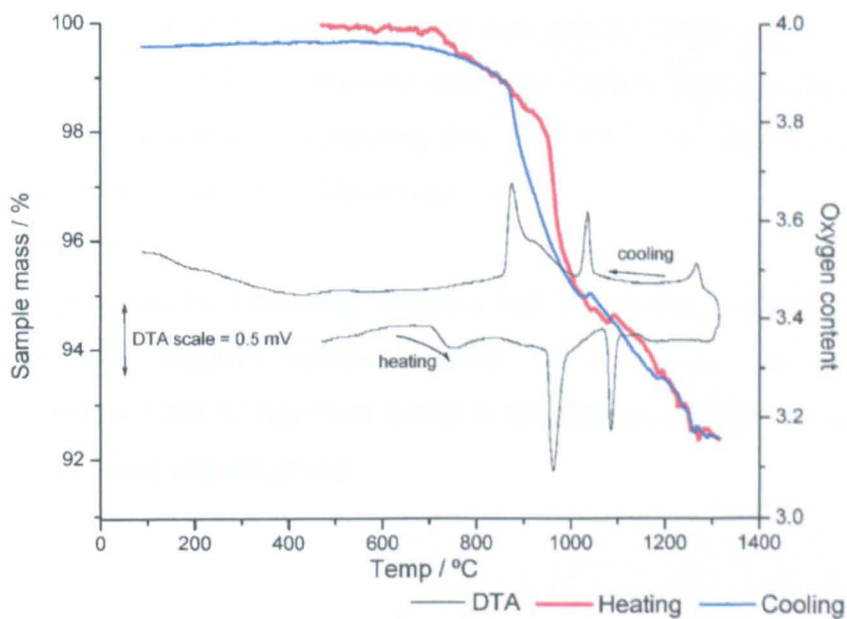
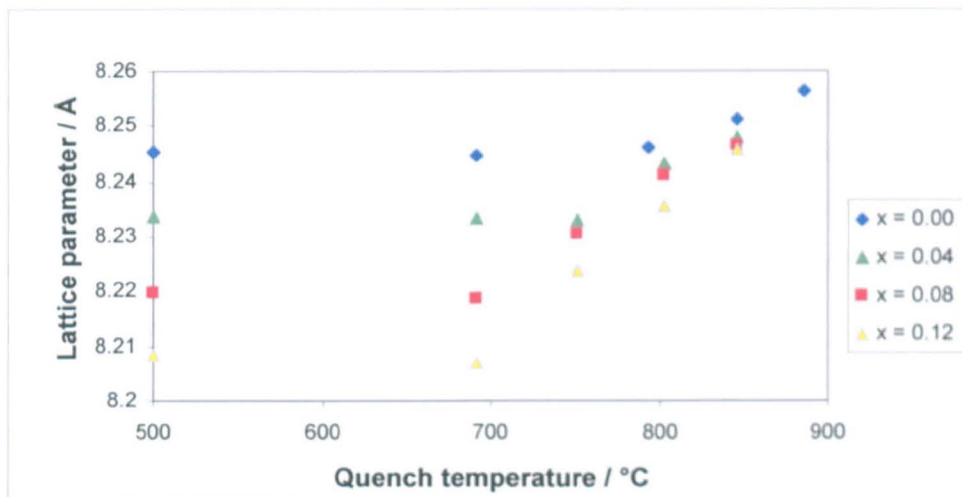


**Figure 7.3** – TG and DTA data for  $\text{Li}_{1.08}\text{Mn}_{1.92}\text{O}_4$



Samples from this compositional range were quenched into mercury from elevated temperatures and studied by XRD. For all compositions, the cubic structure was retained in samples quenched up to 846 °C; an increase in lattice parameter was noted for all compositions as quench temperatures increased (Figure 7.3).

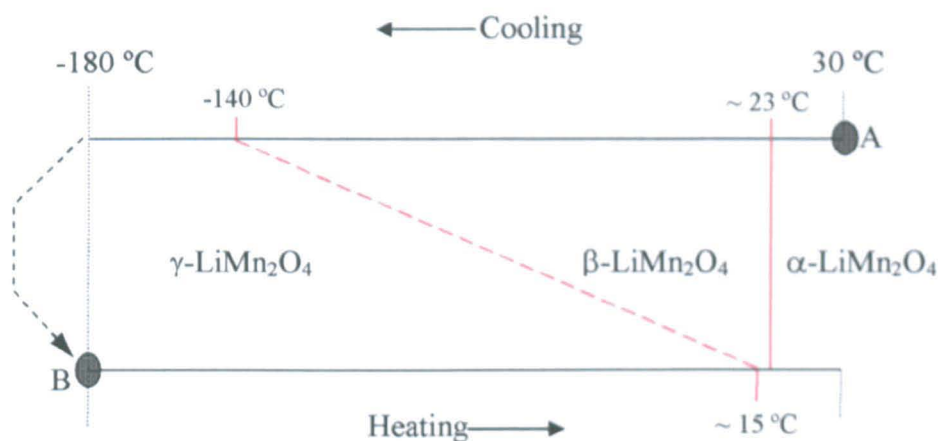
*Figure 7.3 – Cubic spinel lattice parameters for quenched  $\text{Li}_{1-x}\text{Mn}_{2-x}\text{O}_4$ .*



A mixture of  $\text{Li}_2\text{MnO}_3$  and a spinel phase was observed in samples quenched from 900 – 962 °C. In samples quenched above 962 °C, a mixture of  $\text{LiMnO}_2$  and a spinel phase was observed. No single phase materials were observed in samples quenched from over 900 °C. Annealing these quenched samples re-obtained the single phase cubic spinel. Quenches from as high as 1400 °C showed very poor quality XRD patterns, with peak broadening and loss of intensity, suggesting that lithia loss does occur at significantly higher temperatures than studied by Thackeray.

The mechanism proposed by Thackeray, where a high temperature ' $\text{Li}_{0.6}\text{Mn}_{2.4}\text{O}_4$ ' spinel phase was suggested, requires significant lithia loss to occur. No evidence for significant loss below 1200 °C has been found in the data presented here, and no high temperature spinel phase was observed.

**Figure 7.7** – Schematic diagram indicating the large hysteresis effect in  $\beta \rightarrow \gamma$  phase transition in  $\text{LiMn}_2\text{O}_4$  on cooling to  $-180\text{ }^\circ\text{C}$  and subsequent heating. DSC experiment: cool from A to  $-180\text{ }^\circ\text{C}$ ; heat from B at  $10\text{ }^\circ\text{C min}^{-1}$ . Not shown to scale.



The low temperature polymorphism of  $\text{LiMn}_2\text{O}_4$  has not been resolved in the literature. Four possibilities have been raised, and these are listed in Table 7.3.

**Table 7.3** – Reported possible low temperature phase transitions in  $\text{LiMn}_2\text{O}_4$ .

Proposed transitions on cooling	Authors
cubic $\rightarrow$ orthorhombic	Rousse et al., <sup>8,9</sup> Tomeno <sup>11</sup>
cubic $\rightarrow$ tetragonal	Wills <sup>14</sup>
cubic $\rightarrow$ tetragonal + cubic	Yamada <sup>15</sup>
cubic $\rightarrow$ orthorhombic $\rightarrow$ tetragonal ( $< 60\text{ K}$ )	Takada <i>et al.</i> <sup>5,10,12</sup>

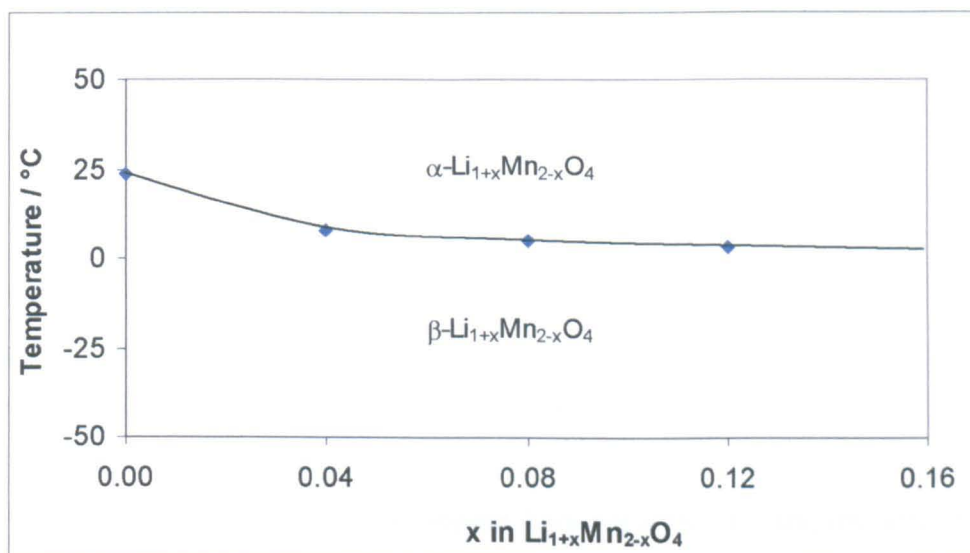
The DSC data presented here clearly indicate that two distinct phase transitions occur in  $\text{LiMn}_2\text{O}_4$  at sub-ambient temperatures, though a significant hysteresis effect occurs for the  $\gamma \rightleftharpoons \beta$  transition.

It is likely that one of these phases will have tetragonal symmetry, whilst the other will have orthorhombic symmetry, in agreement with the works of Takada et al. However, the transition to  $\gamma\text{-LiMn}_2\text{O}_4$  (possibly Takada's tetragonal phase) is observed at a much higher temperature here ( $\sim 133\text{ K}$  rather than  $\sim 60\text{ K}$ ). The likely cause of both transitions is the distorting effect of Jahn-Teller active  $\text{Mn}^{3+}$  ions; partial charge ordering may occur just below room temperature, with complete charge ordering occurring on further cooling.

### 7.3.3b Untreated $\text{Li}_{1+x}\text{Mn}_{2-x}\text{O}_4$

DSC data were recorded on heating for  $x = 0.04, 0.08$  and  $0.12$  after initially cooling to  $-60$  and  $-180$  °C. A single DSC peak was observed for all compositions on cooling to  $-60$  °C. The intensity, and temperature, of this peak decreased as  $x$  increased (*i.e.* as  $\text{Mn}^{3+}$  content decreased). A simple phase diagram for the  $\text{Li}_{1+x}\text{Mn}_{2-x}\text{O}_4$  binary join cooled to  $-60$  °C is presented in Figure 7.8.

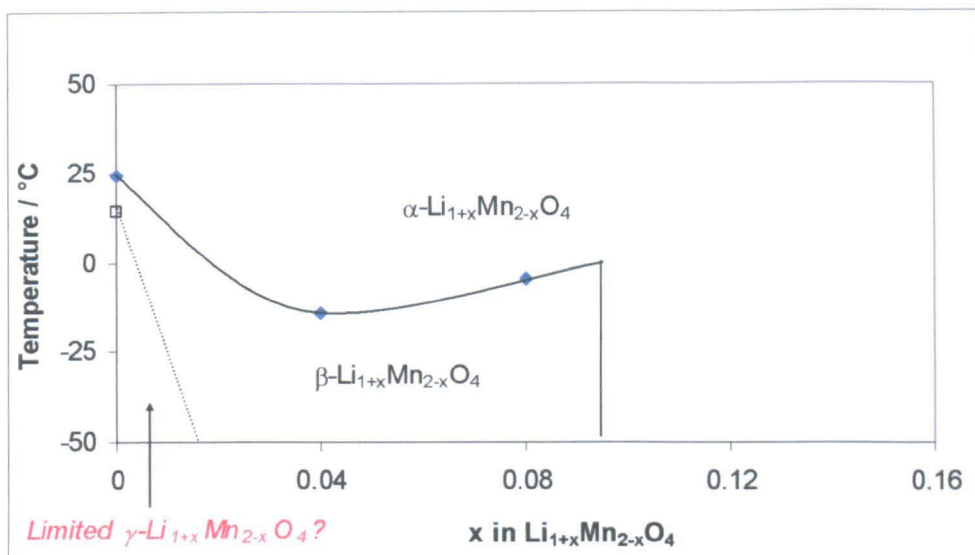
**Figure 7.8** – DSC peak maxima for  $\text{Li}_{1+x}\text{Mn}_{2-x}\text{O}_4$  binary join cooled to  $-60$  °C.



When the initial cooling was conducted to  $-180$  °C, a similar pattern was observed (Figure 7.9). Only a single peak was observed for  $x = 0.04$  and  $0.08$ ; *i.e.* no transition to a  $\gamma$ -phase occurred in  $\text{Li}_{1+x}\text{Mn}_{2-x}\text{O}_4$  for  $x \geq 0.04$ . It is possible that a limited range of compositions could show the  $\beta \rightarrow \gamma$  transition as suggested in Figure 7.9.

It is not understood why no peak was observed for  $x = 0.12$  after cooling to  $-180$  °C, though any cooperative Jahn-Teller distortions may be limited by the low  $\text{Mn}^{3+}$  content at this composition.

Figure 7.9 - DSC peak maxima for  $\text{Li}_{1+x}\text{Mn}_{2-x}\text{O}_4$  binary join cooled to  $-180^\circ\text{C}$ .



### 7.3.3c Heat-treated $\text{Li}_{1+x}\text{Mn}_{2-x}\text{O}_4$

Samples with composition  $x = 0.00, 0.04, 0.08$  and  $0.12$  were quenched from  $692^\circ\text{C}$  and  $846^\circ\text{C}$ . DSC data were then recorded on heating after initially cooling to  $-180^\circ\text{C}$ .

The TG data showed that minimal oxygen loss occurred in samples with  $x \leq 0.08$  quenched from  $692^\circ\text{C}$ . A small oxygen loss was recorded for  $x = 0.12$  at  $692^\circ\text{C}$ , suggesting a stoichiometry of  $\text{Li}_{1.12}\text{Mn}_{1.88}\text{O}_{3.98}$  at this temperature. However, all samples were shown to have begun losing weight by  $\sim 800^\circ\text{C}$ ; calculated stoichiometries for the materials quenched from  $846^\circ\text{C}$  are presented in Table 7.4.

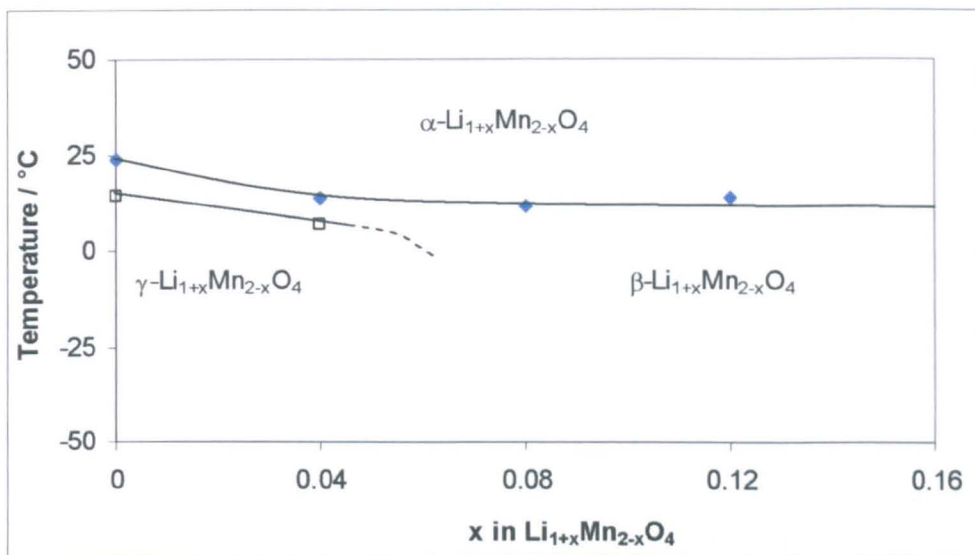
**Table 7.4** – Oxygen contents calculated from TG data for  $\text{Li}_{1+x}\text{Mn}_{2-x}\text{O}_{4-\delta}$  samples quenched from  $846^\circ\text{C}$ ; Mn oxidation state calculated with assumption that phases had  $\text{Li}_{1+x}\text{Mn}_{2-x}\text{O}_4$  stoichiometry before heating and that all weight loss is due to oxygen volatilisation.

$x$	$\delta$	Stoichiometry	Calculated Mn oxidation state
0.00	0.03	$\text{LiMn}_2\text{O}_{3.97}$	3.47
0.04	0.07	$\text{Li}_{1.04}\text{Mn}_{1.96}\text{O}_{3.93}$	3.48
0.08	0.12	$\text{Li}_{1.08}\text{Mn}_{1.92}\text{O}_{3.88}$	3.48
0.12	0.14	$\text{Li}_{1.12}\text{Mn}_{1.88}\text{O}_{3.86}$	3.51

In samples of  $x = 0.00$  and  $0.04$  quenched from  $692^\circ\text{C}$ , two peaks were observed in the DSC data on heating. Only one peak was observed in data for  $x = 0.08$  and  $0.12$ . From

these data it was possible to construct a low temperature phase diagram for  $\text{Li}_{1+x}\text{Mn}_{2-x}\text{O}_4$  quenched at 692 °C and cooled to -180 °C (Figure 7.10).

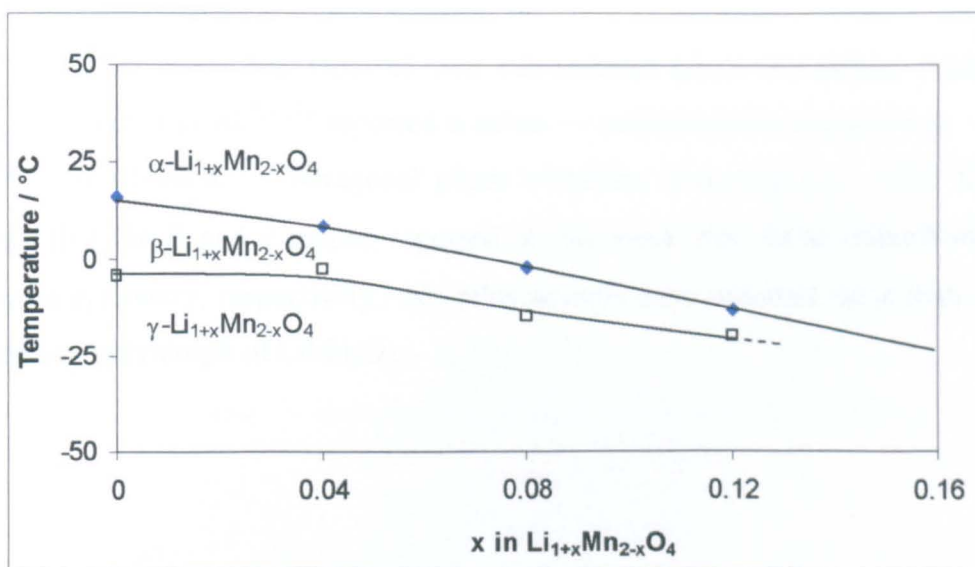
**Figure 7.10** - Low temperature phase diagram for  $\text{Li}_{1+x}\text{Mn}_{2-x}\text{O}_4$  quenched from 692 °C and cooled to -180 °C.



Both the intensity and temperature of the DSC peaks decrease with decreasing Mn content.

Samples from the whole composition range studied ( $x = 0.00$  to 0.12) showed two DSC peaks when quenched from 846 °C. Both DSC peaks moved to lower temperatures (Figure 7.11) and became less intense as Mn content decreased.

**Figure 7.11** - Low temperature phase diagram for  $\text{Li}_{1+x}\text{Mn}_{2-x}\text{O}_4$  quenched from 846 °C and cooled to -180 °C.



The decrease in DSC peak intensity and temperature observed for samples quenched from 692 and 846 °C can be related to the Mn content in the samples; the distortion effectively decreases as the Li/Mn ratio increases, *i.e.* as there is less Mn present. The average oxidation state of Mn in these samples quenched from 846 °C, calculated from TG data (Table 7.4), remains constant with  $x$ , and hence all compositions show the two transitions.

From these data, it can be seen that two phase transitions occur for  $\text{LiMn}_2\text{O}_4$ , and that these phase transitions can also be stabilised in lithium-excess materials in the  $\text{Li}_{1+x}\text{Mn}_{2-x}\text{O}_4$  solid solution. This stabilisation can be achieved by quenching in oxygen vacancies, thereby increasing the overall  $\text{Mn}^{3+}$  concentration. As the average Mn oxidation state approaches  $\text{Mn}^{3.5+}$  it becomes more likely that cooperative Jahn-Teller distortions will occur. Since both of the low temperature phase transitions in the  $\text{Li}_{1+x}\text{Mn}_{2-x}\text{O}_4$  materials show a strong dependence on the  $\text{Mn}^{3+}$  content, it can be concluded that both are related to the Jahn-Teller effect. It is therefore likely that the higher temperature  $\alpha \rightleftharpoons \beta$  transition involves partial charge ordering, and that further charge ordering occurs on further cooling to enable the  $\beta \rightleftharpoons \gamma$  transition. It also appears that a critical average manganese valence of  $\sim \text{Mn}^{3.5+}$  must be reached for the  $\beta \rightleftharpoons \gamma$  to occur. Low temperature diffraction studies are needed to enable identification of the symmetry of the  $\beta$ - and  $\gamma$ - $\text{Li}_{1+x}\text{Mn}_{2-x}\text{O}_4$  phases.

The large hysteresis observed for the  $\gamma \rightarrow \beta$  transition suggests that this is not a first order transition. It may be that this is a more displacive second order, martensitic transition. This would be consistent with a gradual increase in charge ordering.

Only one other group has reported two sub-ambient phase transitions occurring in  $\text{LiMn}_2\text{O}_4$ ; Takada *et al.*<sup>5,10,12</sup> reported a cubic  $\rightarrow$  orthorhombic transition at  $\sim 10$  °C, with an orthorhombic  $\rightarrow$  tetragonal phase transition occurring at  $\sim -200$  °C. It is possible that the  $\beta$  and  $\gamma$  phases reported in this work may have orthorhombic and tetragonal symmetry, respectively. No other authors have reported more than one low temperature polymorph of  $\text{LiMn}_2\text{O}_4$ .

## 7.4 Conclusion

Compositions were prepared on the  $\text{Li}_{1+x}\text{Mn}_{2-x}\text{O}_4$  solid solution, where Li replaces  $\text{Mn}^{3+}$  as  $x$  increases. These materials had the cubic spinel structure at room temperature.

The cubic spinel structure was retained for  $0.00 \leq x \leq 0.12$  in samples quenched from up to 846 °C; TG-DTA data showed these quenched materials to be oxygen-deficient at this temperature, resulting in a decrease in the overall Mn oxidation state as  $\text{Mn}^{3+}$  content increased.

The low temperature phase diagram of  $\text{LiMn}_2\text{O}_4$  was investigated by DSC; two low temperature phase transitions were observed. One, at  $\sim 23$  °C on heating, has been widely reported, though the symmetry changes involved are not yet satisfactorily understood. The second transition occurred at  $\sim -140$  °C on cooling, and  $\sim 15$  °C on heating; this significant hysteresis suggests that the transition may be second-order, possibly martensitic in nature; this is consistent with an increase in charge ordering in the  $\beta \rightarrow \gamma$  transition.

The ' $\alpha \rightarrow \beta$ ' transition at room temperature was also observed for compositions with  $0.04 \leq x \leq 0.12$ . The second, ' $\beta \rightarrow \gamma$ ' transition was absent for untreated samples, consistent with a decrease in  $\text{Mn}^{3+}$  content. When steps were taken to increase  $\text{Mn}^{3+}$  content such that the average manganese oxidation state fell to  $\text{Mn}^{3.5+}$ , *i.e.* when oxygen-deficient samples were prepared by quenching from elevated temperatures, the ' $\beta \rightarrow \gamma$ ' transition was observed for the whole range of compositions studied,  $0 \leq x \leq 0.12$ . This second transition has not been clearly identified in the literature, and has not been studied by DSC previously. Previous studies have only considered magnetic ordering at  $\leq 60$  K; no structural changes are reported to accompany this.

The likely cause for both transitions is the distortions caused by Jahn-Teller active  $\text{Mn}^{3+}$  cations, and charge ordering occurring on cooling. These data may be consistent with the findings of Takada *et al.*,<sup>5,10,12</sup> *i.e.* the ' $\alpha \rightarrow \beta$ ' and ' $\beta \rightarrow \gamma$ ' transitions reported here may correspond to cubic  $\rightarrow$  orthorhombic and orthorhombic  $\rightarrow$  tetragonal transitions respectively.

## 7.5 References

- (1) Thackeray, M. M.; Mansuetto, M. F.; Dees, D. W.; Vissers, D. R. *Materials Research Bulletin* **1996**, *31*, 133.
- (2) Thackeray, M. M.; Mansuetto, M. F.; Johnson, C. S. *Journal of Solid State Chemistry* **1996**, *125*, 274.
- (3) Thackeray, M. M.; Rossouw, M. H. *Journal of Solid State Chemistry* **1994**, *113*, 441.
- (4) Paulsen, J. M.; Dahn, J. R. *Chemistry of Materials* **1999**, *11*, 3065.
- (5) Takada, T.; Hayakawa, H.; Kumagai, T.; Akiba, E. *Journal of Solid State Chemistry* **1996**, *121*, 79.
- (6) Sugiyama, J.; Atsumi, T.; Hioki, T.; Noda, S.; Kamegashira, N. *Journal of Alloys and Compounds* **1996**, *235*, 163.
- (7) Mandal, S.; Rojas, R. M.; Amarilla, J. M.; Calle, P.; Kosova, N. V.; Anufrienko, V. F.; Rojo, J. M. *Chemistry of Materials* **2002**, *14*, 1598.
- (8) Rouse, G.; Masquelier, C.; Rodriguez-Carvajal, J.; Elkaim, E.; Lauriat, J.-P.; Martinez, J. L. *Chemistry of Materials* **1999**, *11*, 3629.
- (9) Paolone, A.; Roy, P.; Rouse, G.; Masquelier, C.; Rodriguez-Carvajal, J. *Solid State Communications* **1999**, *111*, 453.
- (10) Takada, T.; Hayakawa, H.; Enoki, H.; Akiba, E.; Sleg, H.; Davidson, I.; Murray, J. *Journal of Power Sources* **1999**, *81-82*, 505.
- (11) Tomeno, I.; Kasuya, Y.; Tsunoda, Y. *Physical Review B* **2001**, *64*, 1.
- (12) Hayakawa, H.; Takada, T.; Enoki, H.; Akiba, E. *Powder Diffraction* **2000**, *15*, 19.
- (13) Tabuchi, M.; Masquelier, C.; Kobayashi, H.; Kanno, R.; Kobayashi, Y.; Maki, Y.; Kageyama, H.; Nakamura, O. *Journal of Power Sources* **1997**, *68*, 623.
- (14) Wills, A. S.; Raju, N. P.; Greedan, J. E. *Chemistry of Materials* **1999**, *11*, 1510.
- (15) Yamada, A.; Tanaka, M.; Tanaka, K.; Sekai, K. *Journal of Power Sources* **1999**, *81-82*, 73.
- (16) Masquelier, C.; Tabuchi, M.; Ado, K.; Kanno, R.; Kobayashi, Y.; Nakamura, O.; Goodenough, J. B. *Journal of Solid State Chemistry* **1996**, *123*, 255.
- (17) Yamada, A.; Miura, K.; Hinokuma, K.; Tanaka, M. *Journal of the Electrochemical Society* **1995**, *142*, 2149.
- (18) Sugiyama, J.; Atsumi, T.; Koiwai, A.; Sasaki, T.; Hioki, T.; Noda, S.; Kamegashira, N. *Journal of Physics: Condensed Matter* **1997**, *9*, 1729.

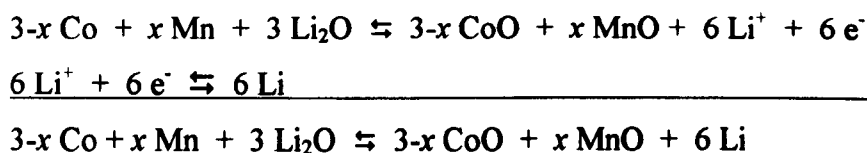
## Chapter 8

### Conclusions and Further Work

#### 8.1 Conclusions

The  $\text{Co}_{3-x}\text{Mn}_x\text{O}_4$  phase diagram (with  $0.00 \leq x \leq 3.00$ ) has been studied. A cubic spinel solid solution was found at 500 °C for compositions in the range of  $0.00 < x < 1.30$ . This extended across the whole compositional range of the phase diagram at temperatures increasing with Mn content. Single phase spinel materials could be prepared with any Co:Mn ratio by simple heat treatments.

Lithiation of samples of composition  $\text{Co}_{3-x}\text{Mn}_x\text{O}_4$  has been successfully attempted, though cycling likely proceeds via (de)lithiation of the individual rock salts:



The observed practical discharge capacities for Mn-doped materials were significantly lower ( $\sim 475 \text{ mAh.g}^{-1}$ ) than for  $\text{Co}_3\text{O}_4$  ( $\sim 800 \text{ mAh.g}^{-1}$ ), but in good agreement with the proposed mechanism. Manganese doping led to cells with impressive performance in terms of cyclability, better specific capacity than the graphite anode materials currently used, low potential vs. Li ( $\sim 0.6 \text{ V}$  for  $x = 2.60$  vs.  $\sim 1.0 \text{ V}$  for  $x = 0.00$  (*i.e.*  $\text{Co}_3\text{O}_4$ )), and cost / health benefits over the  $\text{Co}_3\text{O}_4$  anodes currently attracting much interest in the literature.

Three joins in the  $\text{Li}_2\text{O-CoO}_x\text{-MnO}_y$  phase diagram have been studied, extending from  $\text{LiMn}_2\text{O}_4$  to  $\text{LiCoMnO}_4$  ( $\text{LiCo}_x\text{Mn}_{2-x}\text{O}_4$ ),  $\text{Li}_2\text{CoMn}_3\text{O}_8$  to  $\text{Co}_{1.7}\text{Mn}_{1.3}\text{O}_4$  ( $\text{Li}_{1-x}\text{Co}_{1/2+6x/5}\text{Mn}_{1.5-x/5}\text{O}_4$ ) and  $\text{LiCoMnO}_4$  to  $\text{Co}_3\text{O}_4$  ( $\text{Li}_{1-x}\text{Co}_{1+2x}\text{Mn}_{1-x}\text{O}_4$ ). In each case, a solid solution was identified for the compositional range  $0.00 \leq x \leq 1.00$ .

These joins most likely form three sections through a solid solution area, *i.e.* an area of compositions that form single phase cubic spinels with variable lithium, cobalt and manganese ratios. It was found that all of these phases lost oxygen on heating;

compositions centred around  $\text{LiCoMnO}_4$  and  $\text{Co}_3\text{O}_4$  were found to lose  $\sim 1$  oxygen and form disordered rock salts after heating to at least  $1000\text{ }^\circ\text{C}$ . The compositional extent of this high temperature rock salt solid solution area increased with temperature, overlapping the area of the  $\text{Li}_2\text{O-CoO}_x\text{-MnO}_y$  phase diagram covered by the cubic spinel solid solution area at  $500\text{ }^\circ\text{C}$ .

$\text{LiCoMnO}_4$  has great potential as a cathode material for the next generation of Li-ion batteries. Two plateaux are observed in the electrochemical data; at  $4.0\text{ V}$  (the reason for this is unknown, but may be due to a  $\text{Mn}^{3+} \rightleftharpoons \text{Mn}^{4+}$  redox couple) and at  $\sim 5.0\text{ V}$  (most likely due to the  $\text{Co}^{3+} \rightleftharpoons \text{Co}^{4+}$  redox couple). The results of the phase diagram studies suggest that oxygen non-stoichiometry may be problematic for  $\text{LiCoMnO}_4$ , and this may explain the persistence of the unexpected  $\sim 4\text{ V}$  plateau. The  $5\text{ V}$  plateau is also observed to have an inflexion at about half-discharge; this may be related to the ordering of lithium ions over tetrahedral sites after  $50\%$  of the lithium has been removed

Compounds on the  $\text{Li}_{1-x}\text{Co}_{1+2x}\text{Mn}_{1-x}\text{O}_4$  solid solution show significant capacities for lithium insertion. The best performance was observed for  $x = 0.51$ , where specific capacities of  $\sim 750\text{ mAh g}^{-1}$  were obtained, with good capacity retention over the first five cycles. This offers a significant improvement over the graphite anodes used in the current generation of lithium-ion cells.

On first discharge, insertion of over  $8\text{ Li}$  into  $\text{Li}_{1-x}\text{Co}_{1/2+6x/5}\text{Mn}_{3/2-x/5}\text{O}_4$  samples was found to be possible. However, the capacity on subsequent cycles was found to be extremely limited; the reasons for the poor performance are not understood.

No significant capacities were obtained for lithium extraction from any of the materials with  $x > 0.00$  on either of the  $\text{Li}_{1-x}\text{Co}_{1+2x}\text{Mn}_{1-x}\text{O}_4$  or  $\text{Li}_{1-x}\text{Co}_{1/2+6x/5}\text{Mn}_{3/2-x/5}\text{O}_4$  solid solutions.

The sub-ambient phase diagram of  $\text{LiMn}_2\text{O}_4$  has been studied. While numerous sources in the literature report a single sub-ambient phase transition for  $\text{LiMn}_2\text{O}_4$ , the DSC data presented here indicated two transitions. It is proposed that a  $\beta\text{-LiMn}_2\text{O}_4$  phase exists between  $15\text{ }^\circ\text{C}$  and  $-140\text{ }^\circ\text{C}$ ; a  $\gamma\text{-LiMn}_2\text{O}_4$  phase exists below  $-140\text{ }^\circ\text{C}$ . The structures of these phases have not yet been characterised but work on this is in

progress. These transitions were observed in  $\text{Li}_{1+x}\text{Mn}_{2-x}\text{O}_4$  when oxygen vacancies were introduced by quenching, and reducing the average Mn valence to below  $\text{Mn}^{3.5+}$ .

## 8.2 Further Work

The following areas are considered by the author to be important for future study:

*The cobalt oxide-manganese oxide phase diagram:*

- use different experimental conditions to try and obtain greater range of rock salt compositions.

*The application of cobalt manganese oxides as anodes*

- Study of cells containing (Co,Mn)O rock salts as the active material, to eliminate issues regarding the capacity loss on first discharge observed for the spinel materials.
- Study other transition metal oxides, particularly those with spinel or rock salt structure. While countless examples are possible, this study should be limited to atoms of relatively low weight, e.g. the oxides of atoms up to, and including, those of the first row of the transition metals.

*The  $\text{Li}_2\text{O-CoO}_x\text{-MnO}_y$  phase diagram*

- Research low temperature synthesis routes for  $\text{LiCoMnO}_4$  (and, in general, spinels with compositions in the  $\text{Li}_2\text{O-CoO}_x\text{-MnO}_y$  phase diagram) to avoid issues of oxygen non-stoichiometry. Such routes may yield fully oxygenated phases with low particle size, with improved battery performance.
- Look for similar solid solution area phenomena and spinel  $\rightleftharpoons$  rock salt transitions in other spinel systems.

*Battery studies of interest as a result of the studies on lithium cobalt manganate spinels*

- Study the effect of annealing conditions on the  $\sim 4$  V capacity observed for  $\text{LiCoMnO}_4$ .

- Further study of compounds on the solid solution between  $\text{Li}_2\text{CoMn}_3\text{O}_8$  and  $\text{Co}_{1.7}\text{Mn}_{1.3}\text{O}_4$  to determine why their electrochemical performance as anodes falls short of the theoretical capacities.
- Study rock salts with stoichiometry  $(\text{Li}_x\text{Co}_y\text{Mn}_z)\text{O}$  (where  $x + y + z = 1$ ) for possible anode materials.
- Study the join between  $\text{Li}_2\text{CoMn}_3\text{O}_8$  and  $\text{Co}_3\text{O}_4$  for potential candidate cathode and anode materials.
- Look for possible anodic behaviour in related systems (e.g. replace Co with Fe) and look for other oxides (including those containing lithium) as possible anode materials.
- Further study the effects of cycle rate and other experimental conditions.
- Study the effect of particle size.

*The sub-ambient polymorphism of  $\text{LiMn}_2\text{O}_4$*

- Gather low temperature neutron diffraction data, and perform Rietveld refinement to fully characterise the structures of the possible low temperature polymorphs of  $\text{LiMn}_2\text{O}_4$ .